



## Aboveground biomass estimation of individual trees with airborne Lidar data

**Author:**

Liu, Li

**Publication Date:**

2019

**DOI:**

<https://doi.org/10.26190/unsworks/3824>

**License:**

<https://creativecommons.org/licenses/by-nc-nd/3.0/au/>

Link to license to see what you are allowed to do with this resource.

Downloaded from <http://hdl.handle.net/1959.4/64210> in <https://unsworks.unsw.edu.au> on 2024-05-02

# **Aboveground Biomass Estimation of Individual Trees with Airborne Lidar Data**

**Li LIU**

A thesis in fulfilment of the requirements for the degree of Doctor of Philosophy



School of Civil & Environmental Engineering

Faculty of Engineering

April 2019



## **ORIGINALITY STATEMENT**

‘I hereby declare that this submission is my own work and to the best of my knowledge it contains no materials previously published or written by another person, or substantial proportions of material which have been accepted for the award of any other degree or diploma at UNSW or any other educational institution, except where due acknowledgement is made in the thesis. Any contribution made to the research by others, with whom I have worked at UNSW or elsewhere, is explicitly acknowledged in the thesis. I also declare that the intellectual content of this thesis is the product of my own work, except to the extent that assistance from others in the project's design and conception or in style, presentation and linguistic expression is acknowledged.’

Signed .....

Date .....

## **COPYRIGHT STATEMENT**

'I hereby grant the University of New South Wales or its agents the right to archive and to make available my thesis or dissertation in whole or part in the University libraries in all forms of media, now or here after known, subject to the provisions of the Copyright Act 1968. I retain all proprietary rights, such as patent rights. I also retain the right to use in future works (such as articles or books) all or part of this thesis or dissertation.

I also authorise University Microfilms to use the 350 word abstract of my thesis in Dissertation Abstract International (this is applicable to doctoral theses only).

I have either used no substantial portions of copyright material in my thesis or I have obtained permission to use copyright material; where permission has not been granted I have applied/will apply for a partial restriction of the digital copy of my thesis or dissertation.'

Signed .....

Date .....

## **AUTHENTICITY STATEMENT**

'I certify that the Library deposit digital copy is a direct equivalent of the final officially approved version of my thesis. No emendation of content has occurred and if there are any minor variations in formatting, they are the result of the conversion to digital format.'

Signed .....

Date .....

### INCLUSION OF PUBLICATIONS STATEMENT

UNSW is supportive of candidates publishing their research results during their candidature as detailed in the UNSW Thesis Examination Procedure.

**Publications can be used in their thesis in lieu of a Chapter if:**

- The student contributed greater than 50% of the content in the publication and is the "primary author", i.e. the student was responsible primarily for the planning, execution and preparation of the work for publication
- The student has approval to include the publication in their thesis in lieu of a Chapter from their supervisor and Postgraduate Coordinator.
- The publication is not subject to any obligations or contractual agreements with a third party that would constrain its inclusion in the thesis

Please indicate whether this thesis contains published material or not.

- This thesis contains no publications, either published or submitted for publication. If this box is checked, you may delete all the material on page 2.*
- Some of the work described in this thesis has been published and it has been documented in the relevant Chapters with acknowledgement. If this box is checked, you may delete all the material on page 2.*
- This thesis has publications (either published or submitted for publication) incorporated into it in lieu of a chapter and the details are presented below*

#### CANDIDATE'S DECLARATION

I declare that

- I have complied with the Thesis Examination Procedure
- where I have used a publication in lieu of a Chapter, the listed publication(s) below meet(s) the requirements to be included in the thesis.

Name	Signature	Date (dd/mm/yy)
Li Liu	Li Liu	01/04/19

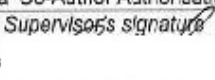
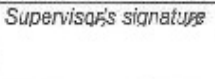
#### Postgraduate Coordinator's Declaration (to be filled in where publications are used in lieu of Chapters)

I declare that

- the information below is accurate
- where listed publication(s) have been used in lieu of Chapter(s), their use complies with the Thesis Examination Procedure
- the minimum requirements for the format of the thesis have been met.

PGC's Name	PGC's Signature	Date (dd/mm/yy)
Hamid Valipour	Hamid Valipour	08/04/19

For each publication incorporated into the thesis in lieu of a Chapter, provide all of the requested details and signatures required

<b>Details of publication #1:</b>				
<i>Full title: A voxel-based multiscale morphological airborne lidar filtering algorithm for digital elevation models for forest regions</i>				
<i>Authors: Li Liu &amp; Samsung Lim</i>				
<i>Journal or book name: Measurement</i>				
<i>Volume/page numbers: Volume 123, Pages 135-144</i>				
<i>Date accepted/ published: July 2018</i>				
<b>Status</b>	Published	<input checked="" type="checkbox"/> Accepted and In press	<input type="checkbox"/> In progress (submitted)	<input type="checkbox"/>
<b>The Candidate's Contribution to the Work</b>				
Li Liu performed analysis on the data, interpreted the results and drafted the manuscript				
<b>Location of the work in the thesis and/or how the work is incorporated in the thesis:</b>				
Chapter 4				
<b>Primary Supervisor's Declaration</b>				
I declare that:				
<ul style="list-style-type: none"> <li>the information above is accurate</li> <li>this has been discussed with the PGC and it is agreed that this publication can be included in this thesis in lieu of a Chapter</li> <li>All of the co-authors of the publication have reviewed the above information and have agreed to its veracity by signing a 'Co-Author Authorisation' form.</li> </ul>				
<i>Supervisor's name</i>	<i>Supervisor's signature</i>	<i>Date (dd/mm/yy)</i>		
Samsung Lim		8/4/19		
<b>Details of publication #2:</b>				
<i>Full title: A multiscale morphological algorithm for improvements to canopy height models</i>				
<i>Authors: Li Liu, Samsung Lim, Xuesong Shen, and Marta Yebra</i>				
<i>Journal or book name: Computers and Geosciences</i>				
<i>Volume/page numbers: N/A</i>				
<i>Date accepted/ published: N/A</i>				
<b>Status</b>	Published	<input type="checkbox"/> Accepted and In press	<input type="checkbox"/> In progress (submitted)	<input checked="" type="checkbox"/>
<b>The Candidate's Contribution to the Work</b>				
Li Liu performed analysis on the data, interpreted the results and drafted the manuscript				
<b>Location of the work in the thesis and/or how the work is incorporated in the thesis:</b>				
Chapter 5				
<b>Primary Supervisor's Declaration</b>				
I declare that:				
<ul style="list-style-type: none"> <li>the information above is accurate</li> <li>this has been discussed with the PGC and it is agreed that this publication can be included in this thesis in lieu of a Chapter</li> <li>All of the co-authors of the publication have reviewed the above information and have agreed to its veracity by signing a 'Co-Author Authorisation' form.</li> </ul>				
<i>Supervisor's name</i>	<i>Supervisor's signature</i>	<i>Date (dd/mm/yy)</i>		
Samsung Lim		8/4/19		
<b>Details of publication #3:</b>				
<i>Full title: Assessment of Tree Attributes Extraction Algorithms</i>				
<i>Authors: Li Liu &amp; Samsung Lim</i>				
<i>Journal or book name: IGARSS 2018 - 2018 IEEE International Geoscience and Remote Sensing Symposium</i>				
<i>Volume/page numbers: 4503-4506</i>				

<i>Date accepted/ published: 05 November 2018</i>			
<b>Status</b>	<i>Published</i>	<input checked="" type="checkbox"/> <i>Accepted and In press</i>	<input type="checkbox"/> <i>In progress (submitted)</i>
<b>The Candidate's Contribution to the Work</b>			
Li Liu performed analysis on the data, interpreted the results and drafted the manuscript			
<b>Location of the work in the thesis and/or how the work is incorporated in the thesis:</b>			
Chapter 6			
<b>Primary Supervisor's Declaration</b>			
I declare that:			
<ul style="list-style-type: none"> <li>the information above is accurate</li> <li>this has been discussed with the PGC and it is agreed that this publication can be included in this thesis in lieu of a Chapter</li> <li>All of the co-authors of the publication have reviewed the above information and have agreed to its veracity by signing a 'Co-Author Authorisation' form.</li> </ul>			
<i>Supervisor's name</i>	<i>Supervisor's signature</i>	<i>Date (dd/mm/yy)</i>	
<i>Samsung Lim</i>	<i>[Signature]</i>	<i>8/9/19</i>	

<b>Details of publication #4:</b>			
<i>Full title: A hybrid method for segmenting individual trees from airborne lidar data</i>			
<i>Authors: Li Liu, Samsung Lim, Xuesong Shen, and Marta Yebra</i>			
<i>Journal or book name: Computers and Electronics in Agriculture</i>			
<i>Volume/page numbers: N/A</i>			
<i>Date accepted/ published: N/A</i>			
<b>Status</b>	<i>Published</i>	<input type="checkbox"/> <i>Accepted and In press</i>	<input checked="" type="checkbox"/> <i>in progress (submitted)</i>
<b>The Candidate's Contribution to the Work</b>			
Li Liu performed analysis on the data, interpreted the results and drafted the manuscript			
<b>Location of the work in the thesis and/or how the work is incorporated in the thesis:</b>			
Chapter 7			
<b>Primary Supervisor's Declaration</b>			
I declare that:			
<ul style="list-style-type: none"> <li>the information above is accurate</li> <li>this has been discussed with the PGC and it is agreed that this publication can be included in this thesis in lieu of a Chapter</li> <li>All of the co-authors of the publication have reviewed the above information and have agreed to its veracity by signing a 'Co-Author Authorisation' form.</li> </ul>			
<i>Supervisor's name</i>	<i>Supervisor's signature</i>	<i>Date (dd/mm/yy)</i>	
<i>Samsung Lim</i>	<i>[Signature]</i>	<i>8/9/19</i>	

## **Abstract**

This thesis presents a framework of the aboveground biomass (AGB) estimation for individual trees from airborne lidar data. To reduce the impact of topography on object points, a voxel-based multiscale morphological airborne lidar filtering algorithm is proposed to distinguish ground points from object points and normalise the height values of identified object points. Because of the presence of pits demonstrating abnormally lower elevation values than the surroundings in the canopy height model (CHM), a multiscale morphological algorithm is proposed to rectify the pits and improve the accuracy of the CHM. Once the pits in the CHM are rectified, a hybrid method is proposed to segment lidar points into individual trees. A modified CHM-based tree segmentation algorithm is used to identify highly accurate tree tops, which are served as seeds in a point-based profile analysis to segment individual trees meanwhile recognising understory trees. Due to the lack of points representing breast height of individual trees, diameter at breast height (DBH) cannot be extracted from segmented trees directly. Hence, a DBH regression model is generated based on extracted tree height and crown width. The principal component analysis and the ridge regression are conducted to investigate if multicollinearity exists in the input variables for AGB regression model generation and remove the irrelevant variables. Three existing generalised AGB allometric models are exploited to compute the AGB estimates as the reference, respectively since the field samples of the AGB estimates are not available. Once the input variables are set, the AGB regression models are generated by various machine learning techniques to examine which technique has the best performance in regression model generation, including random forest, support vector regression, multilayer perceptron and radial basis function. The qualities of the various AGB regression models are assessed by model efficiency index, adjusted coefficient of determination, leave-one-out cross validation, Akaike information criterion, and normalised-mean-square-errors of the AGB estimates. According to the results, the best AGB regression model can explain up to 99% of the variation of the AGB estimates. In conclusion, random forest yields the most accurate AGB regression models and is most robust in regression model generation.

## **Acknowledgement**

Foremost, I would like to express my sincere gratitude to my supervisor Prof. Samsung Lim and my joint-supervisor Dr. Xuesong (Johnson) Shen for their warm support, constructive suggestions and hard work, which assists me to complete the PhD program in time.

I would like to convey my appreciation to Dr. Yincai Zhou for his help with installing GIS software, to Mrs. Patricia McLaughlin for her support in annual reviews, to Mrs. Maria Lee and Mrs. Warassamon Kate Brown for providing me with some work opportunities and to other staff in the School of Civil and Environmental Engineering for their devotion to ensure the workplaces are enjoyable and nice.

Special thanks go to my fellow graduate students in the Lidar and GIS Group, Ms. Yang Zhang, Mr. Hossein Asefi, Mr. Mohammad Ridhwan Tamjis, Ms. Zeyuan Qi, Ms. Zetty Haji Abdul Hamid, Ms. Xuefen Liu, Ms. Qishuo Qao, Ms. Jinyi Sun, Ms. Zi Chen, and Mr. Bingnan Li, for their kind help and warm guidance. Wish them all the best for their research and future.

I would like to acknowledge Dr. Marta Yebra. It is such a pleasure to communicate with her about the research. She always responds to my questions promptly and is very generous to offer the research data, provide guidelines about the research experiments and comment on the manuscripts of the paper, which helps me to conduct the research smoothly.

I would like to attribute my thanks to my friends in Sydney, especially Nikhil Zote for everything he has done for me. He took the initiative to help with my spoken English, introduced me to other professionals when I was job hunting, and cheered me up when I was under the weather. I also thank Esther Wang for her guidance about life in Australia; and Joe Ding and Yun Hou for their inspiration. They made my life in Sydney much easier.

I also want to convey my gratitude to my friends far back in China. They are always on my side to show solidarity and support, in the face of long distance. Their experiences with life help me to avoid the same problems and shed a light on my future path.

Financial support from University of New South Wales (UNSW) is also deeply appreciated for providing me with the chance to complete my Phd degree. Simultaneously, I also thank Postgraduate Research Student Support (PRSS) for the financial support for the IGARSS 2018 conference in Valencia, Spain.

Most of all, I want to express my gratitude to my families, for their support and love.

## **Publications**

### **Conference Proceedings:**

Liu, L. & Lim, S. 2018. Assessment of Tree Attributes Extraction Algorithms. In: IGARSS2018. Valencia, Spain, 23-27<sup>th</sup> July 2018.

### **Journal Papers:**

Liu, L. & Lim, S. 2018. A voxel-based multiscale morphological airborne lidar filtering algorithm for digital elevation models for forest regions. *Measurement*, 123:135-144.

Liu, L., Lim, S., Shen, X., and Yebra, M., 2019. A multiscale morphological algorithm for canopy height model improvement. *Computers and Geosciences*, 130:20-31.

Liu, L., Lim, S., Shen, X., and Yebra, M., 2019. A hybrid method for segmenting individual trees from airborne lidar data. *Computers and Electronics in Agriculture*, 163: 104871.

Liu, L., Lim, S., Shen, X., and Yebra, M., 2019. Generalized allometric models for aboveground biomass estimation: a case study in Australia. *Small-scale Forestry*. (under review)

## Table of Contents

Abstract.....	I
Acknowledgement .....	II
Publications.....	III
Table of Contents.....	IV
List of Figures.....	VII
List of Tables .....	X
List of Symbols, Abbreviations and Nomenclature .....	XI
Chapter 1 : Introduction.....	1
1.1 Motivation.....	1
1.2 Objectives of the study.....	3
1.3 Contributions of the study.....	6
1.4 Outline of thesis .....	9
Chapter 2 : Aboveground Biomass Estimation from Remote Sensing Data .....	12
2.1 AGB estimation from optical sensor data.....	13
2.2 AGB estimation from radar sensor data.....	16
2.3 AGB estimation from lidar data.....	18
2.4 Uncertainties and errors of AGB estimation from remote sensing data .....	22
2.5 Summary .....	24
Chapter 3 : Study Region and Methodology .....	26
3.1 Study region and data.....	26
3.1.1 Study region.....	26
3.1.2 Data description .....	26
3.2 Methodology .....	29
3.3 Summary .....	30
Chapter 4 : A Voxel-based Multiscale Morphological Airborne Lidar Filtering Algorithm for Forest Regions .....	31
4.1 Ground filtering from airborne lidar data .....	31
4.2 Methodology .....	34
4.2.1 Height distribution analysis .....	36
4.2.2 Convexity constraint .....	37
4.2.3 Morphological filtering.....	38
4.2.4 Moving-window voxel filtering.....	38
4.2.5 Otsu segmentation.....	40

4.3	Experiments and discussions .....	41
4.3.1	Study region .....	41
4.3.2	Filtering results .....	41
4.3.3	Analysis of the filtering results of the ISPRS benchmark datasets .....	42
4.3.4	Analysis of the filtering results of the Black Mountain Dataset .....	45
4.3.5	Analysis of critical parameters in the algorithm .....	48
4.4	Summary .....	53
Chapter 5 : A Multiscale Morphological Algorithm for Improvements to Canopy Height Models.....		55
5.1	Improving the accuracy of CHM .....	55
5.2	Methodology .....	57
5.2.1	A multiscale Laplacian operator .....	58
5.2.2	A multiscale morphological closing operator .....	60
5.2.3	A multiscale median filtering operator .....	62
5.2.4	Validation.....	66
5.3	Results and discussion .....	68
5.3.1	Analysis of the choices of parameters.....	72
5.3.2	Analysis of the multiscale morphological closing operator.....	76
5.3.3	Analysis of the multiscale median filtering operator .....	76
5.3.4	Analysis of the impact of the spatial resolution of the base CHM.....	77
5.4	Summary .....	77
Chapter 6 : Assessment of Tree Parameters Extraction Algorithms.....		80
6.1	Introduction.....	80
6.2	Tree parameter extraction algorithms .....	83
6.2.1	Fixed-window local maxima algorithm .....	83
6.2.2	Popescu and Wynne’s local maxima algorithm.....	84
6.2.3	Variable area local maxima algorithm .....	84
6.2.4	Individual-tree-crown delineation algorithm .....	84
6.2.5	Li’s point-based segmentation algorithm.....	85
6.3	Evaluation methodology .....	85
6.4	Results and discussion .....	87
6.5	Summary .....	92
Chapter 7 : A Hybrid Method for Segmenting Individual Trees from Airborne Lidar Data...		94
7.1	Methodology .....	94
7.1.1	Identification of LM.....	95

7.1.2	Segmentation of individual trees.....	98
7.1.3	Detection of understorey trees .....	104
7.2	Results and discussion .....	106
7.3	Summary .....	109
Chapter 8	: The Generation of Aboveground Biomass Regression Model for Individual Trees. .....	112
8.1	Methodology .....	112
8.1.1	Generating the DBH allometric model .....	113
8.1.2	Generating the AGB regression model .....	118
8.2	Results and discussion .....	120
8.3	Summary .....	127
Chapter 9	: Concluding Remarks and Recommendations .....	130
9.1	Concluding remarks .....	130
9.2	Recommendations.....	133
References	.....	136

## List of Figures

Figure 3.1 The study region in Black Mountain, Canberra, Australia indicated by the red rectangle box. Colours depict the elevation values of a 1-m resolution DSM over the study region. The red dots represent the locations of the sample plots.....	28
Figure 3.2 The flowchart of the framework.....	30
Figure 4.1 The flowchart of the proposed airborne lidar filtering algorithm.....	36
Figure 4.2 Visual assessment of the results: (a)-(e) are the DTMs derived from VF, LT, TS, MCC and SMRF, respectively.....	46
Figure 4.3 Visual assessment of the points-based results of the region in the red rectangle in Figure 4.2 : (a)-(e) are the classified points by VF, LT, TS, MCC and SMRF, respectively. Brown pixels represent ground and black pixels represent objects.....	47
Figure 4.4 Quantitative Analysis of $CSizeZ$ .....	49
Figure 4.5 Quantitative Analysis of $CSize_x/y$ .....	50
Figure 4.6 Quantitative Analysis of $CSize_{max}$ .....	52
Figure 5.1 Detailed flow chart of each step of the proposed algorithm (the number denotes the order of steps in the algorithm), MLO means multiscale Laplacian operator, MMCO means multiscale morphological closing operator and MMFO means multiscale median filtering operator.....	58
Figure 5.2 Laplacian operators of different window sizes.....	59
Figure 5.3 Various window morphological closing operators.....	61
Figure 5.4 Procedures of replacing pit pixels.....	64
Figure 5.5 The 1-m resolution CHM of the Black Mountain Reserve before and after the improvement.....	65
Figure 5.6 Extracted individual trees derived from the 1-m resolution CHM before and after the improvement for different algorithms (the red polygons show the crown boundaries).....	68
Figure 5.7 The robustness test of the algorithm.....	70

Figure 5.8 The 1-m resolution CHM of the mixed forest in Canberra before and after the improvement.....	71
Figure 5.9 The histograms of the differences between the matching cell values and field records for various CHMs.....	75
Figure 6.1 The differences of tree height for various algorithms.....	89
Figure 6.2 The differences of crown width for various algorithms.....	90
Figure 6.3 The tree height differences between various ITC results and the reference.....	92
Figure 7.1 The flowchart of the proposed method.....	95
Figure 7.2 The concept of Otsu segmentation.....	98
Figure 7.3 The identification of nearest local maxima in eight directions.....	100
Figure 7.4 The concept of segmenting individual trees.....	101
Figure 7.5 Gap identification.....	102
Figure 7.6 The identification of crown boundary points.....	103
Figure 7.7 Height histogram analysis of a tree segment.....	105
Figure 7.8 Three tree segments at individual tree level.....	106
Figure 7.9 The distributions of the differences of tree height and crown width for various conditions.....	108
Figure 8.1 Flowchart of the methodology.....	113
Figure 8.2 The relationship between predicted DBH values and field DBH observations for various models.....	121
Figure 8.3 The ridge trace values of different input variables.....	124
Figure 8.4 The relationships between the predicted AGB estimates by various approaches and the reference AGB estimates from Paul's Model.....	126
Figure 8.5 The relationships between the predicted AGB estimates by various approaches and the reference AGB estimates from Williams' Model.....	126

Figure 8.6 The relationships between the predicted AGB estimates by various approaches and the reference AGB estimates from Jucker's Model.....127

## List of Tables

Table 3.1 A summary of the field measurements.....	28
Table 4.1 Quantitative analysis of $E_{T_I}$ , and $E_{T_{II}}$ for various algorithms.....	43
Table 4.2 Quantitative analysis of $E_{T_t}$ and $E_C$ for various algorithms.....	44
Table 4.3 $E_M$ and $E_S$ analysis result for DTMs generated by various algorithms.....	48
Table 5.1 Analysis of the accuracy of extracted individual trees.....	69
Table 5.2 The RMSEs of the improved CHMs with varying weights and thresholds (compared with the RMSE of the original CHM <sub>1</sub> being 0.699 m) .....	72
Table 5.3 The mean absolute errors of the improved CHMs with varying weights and thresholds (compared with the mean absolute error of the original CHM <sub>1</sub> being 0.364 m).....	72
Table 5.4 The standard deviations of the improved CHMs with varying weights and thresholds (compared with the standard deviation of the errors for original CHM <sub>1</sub> being 0.685) .....	72
Table 6.1 The Analysis of the results for various algorithms.....	89
Table 6.2 The Analysis of the impact of resolution on the accuracy of the results.....	91
Table 7.1 The results of the proposed method in various conditions.....	108
Table 8.1 The accuracy analysis of the predicted DBH values generated by various models.....	121
Table 8.2 Eigen values of the original input variables.....	125
Table 8.3 The analysis of the qualities of various generated AGB regression models.....	125

## List of Symbols, Abbreviations and Nomenclature

3D	Three-Dimensional
ACR	Allometric Canopy Ratio
AGB	Aboveground Biomass
AIC	Akaike Information Criterion
ARVI	Atmospherically Resistant Vegetation Index
ASTER	Advanced Spaceborne Thermal Emission And Reflection Radiometer
AVHRR	Advanced Very High Resolution Radiometer
BGB	Belowground Biomass
BI	Brightness Index
CBERS	China-Brazil Earth Resources Satellite
CHM	Canopy Height Model
CNN	Convolutional Neural Network
CV	Leave-One-Out Cross Validation
CW	Crown Width
DAM	Dry Aboveground Biomass
DBH	Diameter at Breast Height
DEM	Digital Elevation Model
DR	Detection Rate
DSM	Digital Surface Model
DTM	Digital Terrain Model
DVI	Difference Vegetation Index
$E_c$	Cohen's Kappa Coefficient
EGI	Excess Green Index
EI	Model Efficiency Index
ETM+	Enhanced Thematic Mapper Plus
ExBVI	Excess Blue Vegetation Index
ExRVI	Excess Red Vegetation Index
FLM	Fixed-Window Local Maxima Algorithm
GAI	Green Area Index
GCI	Green Chlorophyll Index
GIS	Geographic Information System
GLAS	Geoscience Laser Altimeter System
GLCM	Grey Level Co-occurrence Matrix

GLI	Green Leaf Index
GNN	Gradient Nearest Neighbour
GPG	Good Practice Guidance
GPS	Global Positioning System
GRVI	Green Red Vegetation Index
GVI	Green Vegetation Index
H	Tree Height
$H_{fb}$	The Height of the First Branch
$H_{mean}$	Mean Height
IKAW	Kawashima Index
InSAR	Interferometry SAR
IPCC	The Intergovernmental Panel on Climate Change
IRS	Indian Remote Sensing Satellites
ICESat	Ice, Cloud, and Land Elevation Satellite
ITCD	The Individual Tree Crown Delineation Algorithm
JERS	Japan Earth Resources Satellite
KNN	K-Nearest Neighbour
Lidar	Light Detection and Ranging
LM	Local Maxima
LMM	Linear Mixed Effects Model
LO	Laplacian Operator
LoG	Laplacian of Gaussian
LPS	Li's Point-Based Segmentation Algorithm
LULUCF	Land Use, Land-Use Change, and Forestry
MAE	Mean Absolute Error
MCC	Multiscale Curvature Classification
MCO	Morphological Closing Operator
MFO	Median Filtering Operator
MGRVI	Modified Green Red Vegetation Index
MH	Mean Height
MLP	Multilayer Preceptron
MLO	Multiscale Laplacian Operator
MMCO	Multiscale Morphological Closing Operator
MMFO	Multiscale Median Filtering Operator
MMT	Most Matching Tree

MNDVI	Modified Normalised Difference Vegetation Index
MODIS	Moderate Resolution Imaging Spectroradiometer
MSAVI	Modified Soil Adjusted Vegetation Index
MST	Metabolic Scaling Theory
NDVI	Normalised Difference Vegetation Index
NMSE <sub>AGB</sub>	Normalised Mean Square Error of Aboveground Biomass
NOAA	National Oceanic and Atmospheric Administration
NRVI	Normalised Ratio Vegetation Index
<i>OI</i>	Object Index
OLI	Operational Land Imager
PCA	Principal Component Analysis
PMF	Progressive-Morphological-Filter
PMT	Potential Matching Tree
PTIN	Progressive-Triangulated-Irregular-Network
PWLM	Popescu and Wynne's Local Maxima Algorithm
QMH	Quadratic Mean Height
$\bar{R}^2$	Adjusted Coefficient of Determination
RBF	Radial Basis Function
R-CNN	Region-based Convolutional Neural Network
RECI	Red Edge Chlorophyll Index
RED	The Red Waveband
RF	Random Forest
RMSE	Root-Mean-Square Error
RT	Reference Tree
RVI	Ratio Vegetation Index
SAR	Synthetic Aperture Radar
SAVI	Soil Adjusted Vegetation Index
SMA	Spectral Mixture Analysis
SMRF	The Simple Morphological Filter
SPOT	Satellite Pour L'observation De La Terre
SR	Simple Ratio
SVI	Simple Vegetation Index
SVR	Support Vector Regression
TCT	Tasseled Cap Transform
TIN	Triangular Irregular Network

TM	Thematic Mapper
TVI	Transformed Vegetation Index
UAV	Unmanned Aerial Vehicle
VARI	Visible Atmospherically Resistant Index
VLM	Variable Area Local Maxima Algorithm
WI	Wetness Index
WiFS	Wide Field Sensors
WLS	Weighted-Linear-Least-Squares
$\delta_H$	Standard Deviation of Height

# **Chapter 1 : Introduction**

## **1.1 Motivation**

Deforestation and forest degradation can lead to climate and environmental change because forests act as a major carbon source to the atmosphere and play a critical role in global carbon cycling (Achard et al., 2004; Hese et al., 2005; Houghton, 2005; Hansen et al., 2013). Consequently, concerns with global climate change and ecosystem functions are leading to increasing attention to accurate forest biomass estimation and the examination of its dynamics (Le Toan et al., 2011). The estimation of forest biomass provides insights into greenhouse gas inventories and terrestrial carbon accounting and contributes to many ecological investigations of such subjects as carbon cycles and vegetation growth (Crow, 1978; Houghton et al., 2000; Fang et al., 2001; Burrows et al., 2003). For example, the estimation of forest biomass assists in the characterisation of biomes and ecosystems, in measuring forest productivity and grazing pressure, and investigating pool sizes of nutrients and energy content. For undisturbed forests, biomass estimation helps to understand the carbon loss during land cover change processes. For desertified regions, periodical biomass estimation not only shows the growth trend of the vegetation but also assists in studying the carbon cycle, evaluating the effects of ecological restoration in desertified areas, and maintaining the sustainable development of desert ecosystems (Yan et al., 2015). For forest managers and policy makers, calculating the amount of forest biomass helps them to make decisions about forest logging, thinning, pruning, and other activities to improve the forest health and reduce wildfires.

Generally, forest biomass includes aboveground biomass (AGB) and belowground biomass (BGB). AGB includes trees, shrubs, and vines, whereas BGB are living roots, dead fine and coarse litter in the soil. Because of the difficulty of measuring belowground biomass, the majority of research on forest biomass focuses on AGB. In this thesis, forest biomass indicates only aboveground forest biomass unless additional information is provided.

Traditional methods for AGB estimation require destructive harvesting of randomly chosen plants or quadrats. However, these methods have multiple drawbacks such as being time-consuming, labour-intensive, and inefficient (Segura and Kanninen, 2005; Seidel et al., 2011; Wang et al., 2011). Moreover, the randomly selected plants or quadrats may represent the spatial variation of the AGB estimates poorly. Geographic Information System (GIS)-based AGB estimation is another approach which uses environmental variables to obtain biomass estimates, but the results are less accurate because AGB is not strongly correlated to environmental variables (Lu, 2006; Chen, 2013). Process-based ecosystem models analyse the AGB estimates based on

biogeochemical processes, such as photosynthesis, and carbon allocation (Smyth et al., 2013). To generate a comprehensive model, scholars usually combine various factors such as hydrology, soil, biology, anthropogenic effects, and climate. Nonetheless, the limited availability of data sources e.g. climate data and soil, and inaccuracy of the models often lead to inaccurate biomass estimates (Rivington et al., 2006; Larocque et al., 2008; Zhang et al., 2012). Moreover, process-based ecosystem models are based on the assumption of homogeneous stands, which may not hold in practice, therefore lacking the ability to demonstrate the spatial variability of the AGB.

The advantages of remotely sensed images, such as data availability, advanced image processing techniques, and the strong correlations between spectral bands and vegetation parameters, make remote sensing images an ideal source for large-area AGB estimation, especially in areas of difficult access. The Intergovernmental Panel on Climate Change, Good Practice Guidance (IPCC GPG, IPCC, 2003) points out that remote sensing images are appropriate to verify the national Land Use, Land-Use Change, and Forestry (LULUCF) carbon pool estimates - especially the AGB estimates. Consequently, many authors have utilised coarse spatial resolution optical images, including National Oceanic and Atmospheric Administration (NOAA) - Advanced Very High Resolution Radiometer (AVHRR) (Häme et al., 1997) and Moderate Resolution Imaging Spectroradiometer (MODIS) (Baccini et al., 2004), to estimate AGB continentally and/or globally. However, using coarse spatial resolution images for AGB estimation has limited effectiveness due to mixed pixels and the mismatch between the size of the ground reference data and the grid size of the satellite image. Some scholars utilised satellite images with finer spatial resolutions to enhance the AGB estimation at regional scale, including Landsat Thematic Mapper (TM) images (Krankina et al., 2004; Turner et al., 2004) and Advanced Spaceborne Thermal Emission and Reflection Radiometer (ASTER) (Muukkonen and Heiskanen, 2007). Nevertheless, one of the vulnerabilities of optical sensor images is data saturation, especially in forest sites with high biomass density, which leads to poor AGB estimation performance.

Because of the capability of lidar to depict physical structural information on the tree or forest canopy, AGB estimation using lidar data remains a hot topic. Results show that biomass estimation with lidar data leads to more accurate results than optical images (Cao et al., 2018), and various lidar metrics have been exploited to estimate the biomass, such as mean height and quadratic mean height. These metrics can be extracted based on either individual trees or polygon areas. Area-based methods yield statistical metrics from lidar point clouds or Canopy Height Models (CHMs) created from the point clouds, while individual-tree-based methods recognise tree parameters such as the treetop (Popescu et al., 2002; Chen et al., 2006) and crown width (Popescu et al., 2003) and generate metrics based on individual trees. AGB estimation with area-based approaches requires AGB reference data measured at the plot level, which can introduce

errors. For instance, lidar pulses may not penetrate tree canopies to describe snags, woody debris, and understorey vegetation accurately, while the reference AGB records may be measured consisting of these features (Næsset, 2005). Compared with the commonly-used area-based methods, individual-tree-based methods can demonstrate the spatial variation of AGB at individual tree level regardless of the size of the sampling area. However, individual-tree-based methods are more challenging because of the difficulties in segmenting individual trees especially in closed or multilayer forests. Consequently, the AGB estimation in such forests demonstrates lower accuracy for complex canopy surfaces than sparse forests or homogeneous forests and requires more lidar-based variables to achieve promising results. Hence, there is a need to develop a framework for AGB estimation at individual tree level.

In this thesis, the main aim is to develop a framework to estimate the aboveground biomass of individual trees with airborne lidar data collected over a forest in Australia. Various algorithms are proposed in this thesis to obtain accurate AGB results. More detailed objectives are presented in Section 1.2.

## 1.2 Objectives of the study

The main objectives of this study are listed below with detailed description:

1. To develop an effective lidar filtering algorithm for forest regions (Chapter 4)

Lidar filtering is fundamental in forest applications because it is essential to classify the lidar points into vegetation points and ground points before further processing and the knowledge of an accurate digital terrain model (DTM) generated by the classified ground points helps to minimise the impact of topography on vegetation points. However, in most cases, large forests are in rural areas where mountainous regions are predominant. Slopes vary greatly in these regions, leading to poor performance of the existing airborne lidar filtering algorithms. What is worse, the dense point clouds of forests may lead to high omission errors of ground points and misclassification of object points as ground. Hence, there is a need to develop an effective airborne lidar filtering algorithm to filter out the object points in forest regions, which generates an accurate DTM.

2. To improve the accuracy of the canopy height model (Chapter 5)

The accuracy of the CHM has an impact on the number of individual trees extracted and the accuracy of the generated tree parameters, such as individual tree height ( $H$ ), and the crown width ( $CW$ ), when CHM-based tree segmentation algorithms are applied. However, a CHM is subject to multiple inherent errors and uncertainties. For instance, a CHM is generated by

subtracting the digital surface model (DSM) from the corresponding DTM pixel-wise. Consequently, the accuracy of a CHM is dependent on the accuracy of the DSM and the DTM. Although common practices assume that the first return of a lidar pulse represents the top of the tree, while the last return represents the ground surface, this assumption is not always valid in practice, which may lead to the underestimation of the tree heights when using CHM-based products. In addition, the penetration of lidar pulses into the canopy may result in pits, which are abnormally lower pixel values than the surroundings in a CHM. Therefore, it is essential to improve the accuracy of the CHM before further processing.

3. To segment individual trees from random lidar points and separate subdominant trees from dominant trees (Chapter 7)

To compute the AGB of individual trees, it is essential to retrieve individual tree parameters such as tree height and crown width. However, the presence of subdominant trees can cause the overestimation of individual tree parameters. Because of the dense canopies, subdominant trees are usually blocked by dominant trees and only few existing tree segmentation methods succeeded in distinguishing subdominant trees from dominant trees. To extract accurate individual tree parameters for AGB estimation, it is critical to detect subdominant trees accurately.

4. To examine the performance of existing generalised AGB allometric models and to investigate the performance of various machine learning algorithms in the generation of regression models (Chapter 8)

The accuracy of the AGB regression model is associated with the input parameters. Conventionally, the generation of the AGB regression model requires the field samples of AGB estimates to calibrate with individual tree parameters. However, field measurements of the AGB estimates are not always available because some forests are inaccessible to collect field measurements. In this case, existing generalised AGB allometric models will be used to compute the AGB estimates as the reference data. Generalised AGB allometric models are models to reflect the relationships between the AGB and individual tree parameters within one relationship regardless of the study region and tree species. However, the performance of the existing generalised AGB allometric models is rarely examined. Hence, there is a need to investigate if the existing generalised AGB allometric models are applicable in our study region, including AGB allometric models generated by Paul et al., (2015), Williams et al., (2005) and Jucker et al., (2017). The three AGB allometric models are referred to as Paul's model, Williams' model and Jucker's model, respectively hereafter,

Besides the input parameters, the accuracy of the AGB regression model also depends on the regression methods. Although a large amount of work has been conducted to generate AGB regression models for individual trees, there is little consensus on the statistical method or set of input variables because of the wide range of forest conditions (Lu, 2006). One common approach is to generate the regression model by machine learning algorithms because of their robustness against noise. To test the performance of different machine learning methods in generating the AGB regression model for individual trees, four widely used machine learning approaches are tested, including support vector regression (SVR), random forest (RF), multilayer perceptron (MLP) and radial basis function (RBF).

The study aims to answer the following questions:

1. Is there an effective lidar filtering method suitable for forest areas?

In order to achieve promising results in forest regions, many lidar filtering algorithms are based on mathematical morphological operations such as opening and closing operations in multiple spatial scales. However, it is still challenging to remove large and small objects simultaneously. In this thesis, the height distribution of lidar points, the convexity constraint, and voxel-based filtering will be explored to distinguish ground points from object points and develop an effective lidar filtering algorithm for forest regions.

2. Will the refinement of CHM assist in capturing better tree parameter results?

The penetration of lidar pulses is believed by many scholars to be the cause of pits in a CHM. These abnormally lower pixel values than the neighbourhood will degrade the accuracy of the CHM and impact the CHM-based individual tree segmentation and modelling. In this thesis, the author will take advantage of the features of pits, namely their irregular shape and discrete distribution and the fact that they are mainly present on canopy surfaces in the CHM, to identify pits and replace them with meaningful values. Two individual tree segmentation algorithms including the variable-area-local-maxima algorithm (VLM, Swetnam and Falk, 2014) and the individual-tree-crown delineation algorithm (ITCD, Dalponte et al., 2015) are applied to the CHM before and after the improvement, respectively, to examine if the improvement promotes the accuracy of the extracted individual tree height.

3. Can subdominant trees be extracted with airborne-based lidar data?

Subdominant trees are generally blocked by the dominant species in the forest and many CHM-based individual tree segmentation algorithms fail to identify subdominant trees. Moreover, the recognised local maxima (LM) by the CHM-based tree segmentation algorithms may suffer

from omission error when applied to a CHM with a large grid cell size whereas the recognised LM may generate high commission errors when applied to a CHM with a small grid cell size. Although lidar-point-based tree segmentation algorithms can identify subdominant trees, they lack efficiency and may suffer from oversegmentation in dense forests. To identify highly accurate tree top as well as the understory trees, a CHM-based and a point-based individual tree segmentation algorithm will be integrated by using the LM derived from the CHM-based algorithm as seeds in the point-based individual tree segmentation algorithm. Field measurements of individual tree heights and crown widths will be compared with the results derived from the proposed algorithm to check if the proposed algorithm can detect subdominant trees and if the extracted individual tree parameters are accurate.

4. Will the existing generalised AGB allometric models be useful to calculate the AGB estimates in a different forest?

Generalised AGB allometric models are produced to reflect the relationships between AGB and the input variables within one relationship, irrespective of the site locations and tree species. These generalised AGB allometric models use numerous field observations of various tree species in different locations and are supposed to minimise the uncertainty in AGB estimation. However, few studies have investigated the performance of these generalised allometric models. In this study, the performance of three existing generalised AGB allometric models will be examined by analysing the correlation between the AGB estimates derived from these generalised AGB allometric models and the lidar-based individual tree parameters in the study region. Whether these generalised AGB allometric models are applicable to other forests and achieve promising results will also be investigated.

### **1.3 Contributions of the study**

In summary, the contributions of the study are as follows:

1. A voxel-based multiscale morphological airborne lidar filtering algorithm for DTMs for forest regions

In this thesis, a voxel-based morphological filtering algorithm is proposed to generate very accurate DTMs over forest regions. Height distribution analysis, convexity constraints, morphological filtering, and moving-window voxel-based filters are exploited to detect object points in different spatial resolutions. Instead of removing the recognised object points at each spatial scale, which may lead to high commission errors, an object index is introduced to label the classified lidar points in each iteration. We exploit the return number and the total number of

returns in lidar data to calculate the weight of the object index. Otsu segmentation is applied to compute the threshold of the object indices. If the indices are above the threshold, the corresponding lidar points are regarded as objects and removed. The novelty of the algorithm includes: 1) the introduction of an object index to minimise the misclassification of lidar points in different spatial resolutions; 2) the introduction of the information of the return number and the total number of returns in lidar-processing algorithms; 3) the proposal of a moving-window voxel-based filtering method.

## 2. A multiscale morphological algorithm for improvements to CHMs

Pixels with distinctively lower elevation values than the surrounding pixels in a CHM, e.g. pixels representing a pit, often lead to the underestimation of tree heights. To rectify the underestimation, this thesis presents a novel multiscale CHM improvement algorithm. We assume that: 1) most of the pits are distributed in the canopy regions; 2) trees in the study area demonstrate different sizes and species; and 3) the top view of a tree canopy shows a circle. Based on these assumptions, a multiscale Laplacian operator is applied to identify potential pits including pits and valid canopy gaps. A multiscale morphological closing operator is used to distinguish the pits from canopy gaps and a multiscale median filtering operator is applied to replace pit pixels with correct values. Different from existing CHM improvement algorithms, the proposed algorithm utilises multiscale operators in each step to deal with various canopy conditions. Meanwhile, to minimise the impact of possible inappropriate selection of window sizes on the final results, the results created by the multiscale operators in each step are also fused. These are the novelty of the present algorithm.

## 3. A hybrid method for segmenting individual trees from airborne lidar data

Segmentation of individual trees from airborne lidar data makes use of either the point cloud directly or CHMs. Point-based segmentation is generally known to be more accurate than CHM-based segmentation but is sensitive to the point density and often requires a high overhead cost of computing. CHM-based segmentation can be easily implemented but is impractical for the detection of understory trees. To identify highly accurate tree tops as well as understory trees, this thesis proposes a hybrid method by modifying a CHM-based individual tree crown delineation (ITCD) algorithm and integrating the modified algorithm into a point-based algorithm. A multiscale local maxima (LM) algorithm is developed to improve the accuracy of LM obtained from CHMs in different spatial resolutions. The improved LM are used as seeds to segment the lidar point cloud into individual trees. For each tree, histogram analysis is applied to investigate the presence of understory trees. Three metrics, namely the number of points, the maximum height of points within a particular layer and the ratio of the overlapped area between the top layer

and the understorey layer to the area of the top layer, are introduced to reduce the risk of misclassifying an outward-extending branch of a tree as a separate tree during the histogram analysis of the lidar points to segment understorey trees.

The novelties of the proposed method include the following: 1) a multiscale LM analysis is proposed to identify LM at different spatial resolutions to select LM that are strongly correlated to the tree apices; 2) a moving-window analysis is proposed to investigate the vertical profile of the lidar points in a local region to delineate the tree crown boundaries quickly; 3) three metrics are introduced to limit the misidentification of an outward-extending branch of a tree as a separate tree during the histogram analysis of the lidar points for understorey trees detection, including the number of points, the maximum height of points within a particular layer and the ratio of the overlapped area between the top layer and the understorey layer to the area of the top layer.

4. Testing the performance of four machine learning techniques on the generation of the regression model and examining the performance of three existing generalised AGB allometric models

In this thesis, three existing generalised AGB allometric models for individual trees are tested, namely Paul's model, Williams' model and Jucker's model. Since the diameter at breast height (DBH) of a tree is a crucial parameter for AGB estimation and most tree segmentation algorithms fail to extract the DBH from individual trees directly as few lidar points are present at the breast height, a localised DBH regression model is generated by lidar-based tree height and crown width and field observations of DBH. Four machine learning techniques, namely random forest, support vector regression, multilayer perceptron and radial basis function, are used to generate the DBH regression model respectively to investigate which technique yields the most accurate DBH results. The predicted DBH values that deviate least from the observations are chosen as input for AGB estimation. To generate the AGB regression model, AGB estimates are computed by the aforementioned three existing generalised AGB allometric models respectively to be used as reference to calibrate with lidar-based tree parameters. Principal component analysis (PCA, Lever et al., 2017) is applied to examine the presence of multicollinearity in the input variables for AGB estimation. Ridge regression is applied to remove the less important variables if multicollinearity exists. The aforementioned four machine learning techniques are applied respectively to generate the AGB regression model.

The novelties of the work include the following: (1) four machine learning algorithms are examined on their performance in the generation of regression models; (2) a site-specific DBH regression model is generated based on field observations and lidar-based metrics and compared with two existing generalised DBH allometric models; (3) instead of selecting the input variables

for regression manually or relying on the machine learning techniques to select the useful variables, the PCA is used to investigate the multicollinearity in the variables and use the ridge regression to remove the less important variables; (4) the performance of three existing generalised AGB allometric models are compared.

## **1.4 Outline of thesis**

This thesis is structured in line with the main contributions as shown above.

Chapter 2 reviews a large number of previous studies on AGB estimation, from field measurements collection to lidar-based estimation. A wide range of methodologies and algorithms have been exploited and analysed. Although estimating AGB based on field measurements is most accurate, the long time and intensive labour force required prohibit the collection of field measurements from extensive usage. Because of the ability to capture land surface features over a large region consistently, remote sensing images prove to be reliable data sources for AGB estimation. Many scholars explored remote-sensing reflectance and various vegetation indices to map the distribution of AGB at continental and global scale because of the good trade-off between spatial resolution, image coverage and temporal resolution of the image. However, the mixed pixels and the huge difference between the ground reference data and cell size of the satellite image make it difficult to get accurate results with coarse spatial resolution images. Although some scholars utilised optical images with better spatial resolution to enhance the results, data saturation in optical sensor data is quite common, especially in forests with high biomass density, leading to the poor performance of AGB estimation. The advance of lidar technology makes lidar data a good source for AGB estimation, as the point clouds can accurately depict the physical characteristics of the canopy surface such as the quantile heights of trees. These physical characteristics are correlated with the AGB, and can be used as input variables to obtain general AGB models. However, although great efforts have been made to estimate the AGB with lidar data based on plots, not much work has been done to estimate the AGB at individual tree level. Some researchers computed the AGB based on individual trees, but the tree parameters such as tree height and crown width derived from a CHM may be overestimated due to the failure to extract subdominant trees from a CHM. In addition, the presence of pits in a CHM will affect the accuracy of the extracted tree parameters as well, but little work has been conducted to replace the pits before further processing during the AGB estimation based on individual trees. Moreover, existing airborne lidar filtering algorithms fail to achieve promising results in forest regions because of dense canopies, leading to underestimation of tree heights, which also affects the accuracy of the AGB estimation for individual trees. Hence, there is a need to minimise these

errors to develop a comprehensive framework for the AGB estimation of individual trees with airborne lidar data.

To compute the AGB estimates of individual trees accurately, Chapter 3 presents the overview of the methodology of the framework. The characteristics of the study region are also briefly described as well as the associated lidar data and the field measurements.

To distinguish object points from ground points accurately in forest regions, Chapter 4 presents a voxel-based multiscale morphological airborne lidar filtering algorithm. A height distribution analysis is applied to remove outliers; a convexity constraint is applied to detect object points; a morphological filtering algorithm and a moving-window voxel algorithm are applied to remove building rooftops and low vegetation. Instead of removing detected object points in each iteration, an object index is introduced to label them. Once the iteration is done, the points with the object index above the threshold derived from Otsu Segmentation are regarded as object points and removed.

As mentioned above, the pits present in the CHM are another source of errors, which will degrade the accuracy of the CHM and affect the accuracy of individual tree parameters derived from the CHM. To replace the pits with correct values and improve the accuracy of the CHM, Chapter 5 presents a multiscale morphological algorithm. A multiscale Laplacian operator, a multiscale morphological closing operator and a multiscale median filtering operator are applied to detect and replace pits with meaningful values.

Inaccurate individual tree parameters will lead to AGB estimation for individual trees with low accuracy. Traditionally, CHM-based and point-based algorithms are two common techniques to segment individual trees from airborne lidar data. In general, point-based algorithms process lidar points directly but suffer from intensive computation, while CHM-based algorithms are efficient but fail to extract sub-dominant trees in dense canopies and their performance relies on the resolution of the CHM. To test which existing algorithm yields the most accurate results, Chapter 6 compares the fixed-window local maxima algorithm (FLM, Silva et al., 2017), Popescu and Wynne's local maxima algorithm (PWLM, Popescu and Wynne, 2004), the variable area local maxima algorithm (VLM, Swetnam and Falk, 2014), the individual-tree-crown delineation algorithm (ITCD, Dalponte et al., 2015) and Li's point-based segmentation algorithm (LPS, Li et al., 2012). To testify if CHMs with better spatial resolution promote the accuracy of extracted tree heights and crown widths since they provide more details, CHM-based algorithms are also applied to CHMs with different resolutions.

As shown in Chapter 6, although CHM-based tree segmentation algorithms can detect LM efficiently, they cannot detect understory trees and the accuracy of extracted tree parameters depends on the spatial resolution of the CHM, whereas point-based tree segmentation algorithms can identify understory trees, they are not computationally-efficient and may suffer from oversegmentation in dense canopies. To capture accurate tree height and crown width simultaneously meanwhile maintaining a high detection rate and identify understory trees, Chapter 7 proposes a hybrid method for segmenting individual trees from airborne lidar data. A modified ITC algorithm is applied to improve the accuracy of LM obtained from CHMs in different spatial resolutions. The improved LM are used as seeds to segment the lidar point cloud into individual trees. For each tree, histogram analysis is applied to investigate the presence of understory trees.

After the extraction of individual tree parameters, the next step is to estimate the AGB of individual trees. However, since field observations of the AGB of individual trees are not available, Chapter 8 applies three existing generalised AGB allometric models respectively to compute the AGB estimates as the reference. Firstly, a localised diameter at breast height (DBH) regression model is generated based on lidar-based tree parameters and field observations of the DBH, since the DBH of a tree is a function of the corresponding tree height and crown width. Various machine learning techniques will be applied separately to generate the DBH regression model to demonstrate which technique achieves the best performance. The most accurate DBH values, namely least deviated from the field measurement of DBH will serve as input variables in the AGB estimation. Secondly, the aforementioned three generalised AGB allometric models are explored to compute the AGB estimates as the reference in the generation of the AGB regression model, respectively. Thirdly, in case of multicollinearity in the input variables, the PCA analysis is applied to examine the presence of multicollinearity and ridge regression is then applied to remove less important variables. Lastly, after the selection of the input variables, the AGB regression model is developed by different machine learning techniques using different sets of AGB estimates as the reference, respectively.

The thesis ends with concluding remarks and outlooks in Chapter 9.

## **Chapter 2 : Aboveground Biomass Estimation from Remote Sensing Data**

Previous studies have examined various AGB estimation techniques extensively (Lu, 2006; Lu et al., 2012). Common approaches include: 1) empirical model-based, 2) biomass expansion/conversion factor or coefficient-based, 3) process model-based, and 4) integration of plot and remotely sensed data. McRoberts et al. (2013) validated that remote sensing-based models yield more accurate AGB estimates than other models such as GIS-based empirical models or process-based ecosystem models. This chapter reviews the existing algorithms employed for the AGB estimation from remote sensing data, ranging from optical satellite images to lidar point clouds. Although the existing algorithms demonstrate a wide range of methodologies and techniques, various categories of AGB estimation algorithm using remote sensing data can be grouped based on the available data sources and the methods adopted. In this chapter, the data source is set as the categorisation criterion, therefore classifying the current algorithms into three classes: (i) AGB estimation from optical satellite images, (ii) AGB estimation from radar images and (iii) AGB estimation from lidar point clouds. Instead of exploring the algorithms extensively, this chapter will focus on the most commonly used techniques.

Section 2.1 presents the state-of-the-art algorithms for AGB estimation from optical satellite images. The strengths and weaknesses of the existing algorithms are examined in detail and the drawbacks inherent in the algorithms for AGB estimation from optical satellite images are discussed comprehensively. Due to the ability to penetrate forest canopy to some extent, weather independency and the sensitivity to water content in vegetation, synthetic aperture radar (SAR) is another reliable source for AGB estimation and many scholars have studied SAR images for AGB estimation (Dobson et al., 1995; Kasischke et al., 1997; Le Toan et al., 2011; Huang and Chen, 2013). In Section 2.2 of this chapter, different algorithms for AGB estimation from SAR images are investigated. For each algorithm, the corresponding advantages and disadvantages are analysed and the problems associated with the SAR images are explored. As a cutting-edge technology, lidar provides another opportunity to estimate AGB since the lidar pulses can accurately depict the physical characteristics of trees, which are strongly correlated to AGB. Section 2.3 explores various algorithms for AGB estimation from lidar point clouds and examines the pros and cons of each algorithm. The optical sensor, radar, and lidar have their own strengths and weaknesses, leading to difficulties in AGB estimation from remotely-sensed data. In Section 2.4 of the chapter, therefore, the challenges of AGB estimation from remotely sensed data are described and analysed in detail. Section 2.5 presents a summary of the literature review and analyses the problems in the current framework of AGB estimation of individual trees.

## 2.1 AGB estimation from optical sensor data

A large volume of optical sensor data has been used for AGB estimation, from platforms including Landsat, Satellite Pour l'Observation de la Terre (SPOT), QuickBird, ASTER, MODIS, China-Brazil Earth Resources Satellite (CBERS), and AVHRR (Lu, 2006; Luther et al., 2006; Fuchs et al., 2009; Lu et al., 2012; Song, 2013; Du et al., 2014; Tian et al., 2017). For instance, Verbesselt et al. (2006) monitored herbaceous biomass in South Africa using a time series of vegetation indices derived from SPOT images. Ji et al. (2012) mapped the AGB in the Yukon Flats region at a 30-m resolution with Landsat images and field measures and found that the mean absolute error of AGB estimates was 21.8 Mg/ha and the mean bias error was 5.2 Mg/ha. The AGB estimation results indicate that the spatial pattern of the AGB estimates on the generated AGB estimation map was correlated to the distribution of the vegetation species. It is essential to apply effective methods to extract variables to generate the AGB regression model, since optical sensor images have various spatial and spectral resolutions. Popular methods, including texture measures, image transform algorithms (e.g. PCA; and tasseled cap transform, TCT), vegetation indices, and spectral mixture analysis (SMA), have been applied for AGB estimation from optical multispectral images (Lu, 2006).

One of the most commonly used methods is grey level co-occurrence matrix (GLCM)-based texture measures (Lu and Batistella, 2005; Kayitakire et al., 2006; DeGrandi et al., 2009; Sarker et al., 2012). For instance, various GLCM-based texture measures were employed Lu and Batistella (2005) to investigate the relationships between biomass and textural measures for secondary forest and mature forest in Rondônia State, Brazil, such as mean, entropy, contrast, homogeneity, second moment, variance, dissimilarity, and correlation. These texture measures were generated by multiple spectral bands like Landsat TM spectral bands 2, 3, 4, 5, and 7 with various moving-window sizes (e.g.  $5 \times 5$ ,  $7 \times 7$ ,  $9 \times 9$ ,  $11 \times 11$ ,  $15 \times 15$ ,  $19 \times 19$ , and  $25 \times 25$ ). According to the results, in mature forest, textural images are more correlated to the biomass than the original spectral bands because of the complex forest stand structure, but the secondary forest shows reverse relationships because of the relatively simple stand structure. Lu (2005) revealed that, although textural measures play more significant roles than spectral measures (spectral bands or vegetation indices) in complicated forest stand structures, spectral responses such as vegetation indices and spectral bands are more influential in biomass estimation for simple forest stand structures. The author also acknowledged that, compared to using only spectral measures or textural measures, combining spectral measures and textural measures could improve the AGB estimation performance.

Using various vegetation indices is another widely applied approach for AGB estimation (Häme et al., 1997; Boyd et al., 1999; Huete et al., 2002; Zheng et al., 2004; Claverie et al., 2012). For example, Todd et al. (1998) examined the relationship between biomass and brightness index (BI), the Tasseled Cap green vegetation index (GVI), normalised difference vegetation index (NDVI), the red waveband (RED), and wetness index (WI) on grazed and ungrazed rangelands in the north-central region of Colorado, USA using TM images. To demonstrate the changes of AGB estimates between 1984 and 1990, Ikeda et al. (1999) exploited time-series Landsat TM images as well as climate data from 1984 to 1990 to generate an AGB estimation growth model. The results show that, compared with the NDVI, TM2/TM3 performs better at AGB estimation. Using different vegetation indices generated by Landsat Enhanced Thematic Mapper Plus (ETM+) images, Zheng et al. (2004) applied multiple regression analysis to calculate AGB estimates in Wisconsin, USA. The AGB for pine forests shows strong correlation with the corrected NDVI and, when hardwoods are separated from pine forests, the performance of AGB estimations substantially improves in contrast to those obtained without separating the hardwoods.

Mutanga and Skidmore (2010) examined whether the narrow band vegetation indices, such as Simple Ratio (SR), Modified Normalised Difference Vegetation Index (MNDVI), and Transformed Vegetation Index (TVI) were applicable to characterise the biomass of *Cenchrus ciliaris* grass in high canopy density. The results demonstrate that the MNDVI performs better in estimating biomass than the standard NDVI. Comparing the three vegetation indices, SR demonstrates a higher correlation to biomass than other two vegetation indices. The results confirm that saturation of vegetation indices can be tackled by narrow band indices to estimate the biomass in regions of dense vegetation.

Mutanga et al. (2012) estimated the biomass in a wetland area covered by dense vegetation using NDVIs computed from WorldView-2 imagery, and the random forest regression method was used to predict the biomass. The NDVIs computed by the red band and near infrared band in the WorldView-2 imagery improve the accuracy of AGB compared with the traditional NDVIs.

Yan et al. (2015) analysed the spatiotemporal pattern of the AGB in a desert ecosystem in China using MODIS and Landsat TM images. Various vegetation indices were explored to generate the AGB model, including NDVI, Soil Adjusted Vegetation Index (SAVI), Modified Soil Adjusted Vegetation Index (MSAVI), Difference Vegetation Index (DVI), and Ratio Vegetation Index (RVI). A time-series of AGB spectra between 2000 and 2012 fitted by the least-squares method shows the trends of AGB throughout these years. Spatial variations of AGB based on time series indicate that the AGB is increasing in most regions, which is correlated to precipitation. The

relationship between the AGB and precipitation demonstrates that precipitation contributes significantly to AGB variation.

Optical sensors with coarse spatial resolution, such as MODIS, have proven to be useful to map the AGB continentally and globally (Baccini et al., 2004) because of the balance between spatial resolution, image coverage and temporal resolution (Lu, 2006). Nonetheless, a coarse resolution pixel usually receives responses from multiple homogeneous forest stands because of the large cell size, which makes the direct AGB estimation problematic at local and/or regional scales (Hyypä and Hyypä, 2001). Hence, when quantifying AGB at local to regional scales, it is a must to utilise the finer spatial resolution data such as ASTER to integrate the coarse images with ground truth data. Tomppo et al. (2002) validated that the AGB estimation models generated by Landsat TM data could be used to relate ground measurements with coarse resolution IRS (Indian Remote Sensing Satellites)-1C Wide Field Sensors (WiFS) data. Muukkonen and Heiskanen (2007) utilised ASTER and MODIS satellite images to estimate the AGB over a large area in southern Finland. Stand-wise forest inventory data and moderate resolution ASTER images were first used to generate a regression model, which was then used to estimate the AGB for a larger region with coarser resolution MODIS images. The relative root-mean-squared error (RMSE) of the results is 9.9%, indicating that the obtained estimates are identical to the district-level mean values provided by the Finnish National Forest Inventory. Dang et al. (2019) applied random forest regression algorithm to the Sentinel-2 imagery to estimate forest AGB. Spectral indices such as Atmospherically Resistant Vegetation Index (ARVI), Green Chlorophyll Index (GCI), and Red Edge Chlorophyll Index (RECI), and GLCM-based texture measures such as mean, correlation, variance, entropy, homogeneity, second moment, contrast, and dissimilarity are extracted to predict the AGB. The combination of 132 spectral and texture variables can predict accurate AGB estimation with RMSE of 18.3%. Another way to map AGB regionally is by using auxiliary data. Baccini et al. (2004) combined MODIS images with topographic and climate data such as elevation, precipitation, and temperature to map AGB at regional scales in a National Forest in California. The results indicate that, with the help of topographic and climate variables, coarse resolution images can be applied to map AGB over broad regions with promising accuracy. However, this kind of auxiliary data is not always available.

In summary, even though optical sensor images are the primary data source to compute the AGB estimation, they suffer from data saturation if the biomass density of the forest regions is high (Lu et al., 2012). For instance, when the biomass density is up to 100-150 t/ha, data saturation will happen in the Landsat TM imagery (Foody et al., 2003; Lu et al., 2012). In addition, vegetation spectral variables are influenced by vegetation characteristics and complicated biophysical environments, such as atmosphere, vegetation phenology, and soil moisture; therefore, AGB

estimation models generated by optical spectral measures are site-specific (Foody et al., 2003; Lu, 2005). Another vulnerability of optical sensor data is the impact of weather, which makes it hard to estimate AGB in tropical regions with optical sensor images. Overall, although optical images provide meaningful information about horizontal vegetation structures like canopy cover and vegetation types, they fail to provide vertical vegetation structures for instance canopy height, canopy mean height, which are critical parameters for AGB estimation.

## **2.2 AGB estimation from radar sensor data**

In contrast to optical sensors, SAR is able to penetrate the forest canopy, sensitive to water content in vegetation, and free of the impact of bad weather, and is therefore a promising method for AGB estimation (Le Toan et al., 1992, 2011; Kasischke et al., 1997; Sun et al., 2002; Patenaude et al., 2005; Nafiseh et al., 2011). Important factors including the wavelength such as X-band, C-band, L-band, and P-band, polarisation e.g. HH, HV, VV, and VH, land cover, incidence angle, and terrain characteristics like dielectric constant and roughness will affect the backscattering coefficient of land cover surfaces. Consequently, various radar data have different characteristics associated with forest stand parameters (Leckie, 1998).

Longer wavelength radar generally penetrates the forest canopy more deeply and provides more information about the vertical structure of the canopy. Previous research has proven that the short wavelength bands such as X- or C-band are appropriate for low biomass estimation because the short wavelength interacts mainly with canopies, whereas the long-wavelength bands such as L- or P-bands are suitable for high biomass estimation because the long wavelength can interact with branches and trunks (Saatchi and Moghaddam, 1999; Patenaude et al., 2005). Multiple studies have proven L-band images to be useful to compute AGB estimates (Sader, 1987; Kurvonen et al., 1999). In terms of polarisation, Beaudoin et al. (1994) validated that the HH return is correlated to both crown and trunk biomass, and the VV and HV returns are related to crown biomass. Harrell et al. (1997) assessed four methods to calculate AGB estimates in pine stands using SIR C- and L-band multipolarisation radar images and the results demonstrated that the L-band HH polarisation data are critical for the estimation of the AGB. The results also indicated that the combination of C-band HV or HH polarisation data in the regression equations would enhance the performance of the AGB estimation. For AGB estimation from radar sensors, common techniques include the interferometry technique related to backscattering phases and amplitudes (Balzter et al., 2007), and regression techniques related to backscattering amplitudes (Santos et al., 2002; Sandberg et al., 2011; Rahman and Sumantyo, 2013).

Kuplich et al. (2000) estimated the AGB of regenerating forests using Japan Earth Resources Satellite (JERS)-1/SAR data and pointed out that the SAR image is useful to compute AGB estimates for young, regenerating forests after block logging. Castel et al. (2002) recognised the relationships between the stand biomass of a pine plantation and the backscatter coefficient of JERS-1/SAR data and found that, in comparison to AGB estimation for old stands, the JERS-1/SAR data performed better on young stands. Similarly, Santos et al. (2002) analysed the relationships between the AGB and backscatter signals with JERS-1/SAR data, which are influenced by the forest structural-physiognomic characteristics as well as the volume and double-bounce scattering of the radar.

Hussin et al. (1991) estimated slash pine biomass based on L-band polarimetric SAR images and found that the maximum coefficient of determination was achieved with HV polarised SAR data. Le Toan et al. (1991) investigated the relationship between the stem biomass and multi-band polarimetric SAR images, and VV, VH, and HH polarisations in the P band were proven to show strong correlations between the backscattering coefficient and the biomass of stems. To analyse large natural forests in the Eurasian part of the boreal forest zone, Rauste et al. (1994) tested the applicability of polarimetric SAR in forest biomass estimation and the maximum correlation was found near the linear HV polarisation in the P band.

Imhoff (1995) investigated the relationship between radar backscatter and biomass saturation and determined the radar signal saturation limits in biomass estimation for different forest types. Radar signal saturation affects the biomass estimates by about 100 tons/ha for the P band, 40 tons/ha for the L-band, and 20 tons/ha for the C-band. The results indicate that the C-band is useful to measure biomass in biomes covering 25% of the vegetation surface area throughout the world, the L-band in biomes covering 37%, and the P-band in biomes covering 62%.

Luckman et al. (1997) investigated the relationship between the mean backscattering coefficient and the areal density of AGB in a tropical forest. The L-band, according to the results, is useful to distinguish different levels of forest biomass up to 60 tonnes per hectare, while the C-band is limited to differentiating between vegetation and bare dry soil.

However, data saturation in radar data still occurs in complex forest stand structures, such as a mature forest (Lucas et al., 2007; Solberg et al., 2014). To solve this problem, many scholars refer to interferometry SAR (InSAR, Balzter, 2001; Nafiseh et al., 2011), because InSAR can extend the range of saturation to some extent, therefore improving the performance of AGB estimation (Saatchi et al., 2011). According to Saatchi et al. (2011), when integrating InSAR with backscattering values, the saturation point of the L-band increases to 200 tons/ha. In addition, InSAR has the stereo-viewing capability and can provide vegetation height information, which is

suitable for large-scale biomass estimation because the vegetation canopy height is strongly correlated to the biomass. This provides a solution for AGB estimation in tropical and subtropical regions because optical sensors cannot solve the cloud-cover issue (Solberg et al., 2014). Although InSAR can tackle the issue of data saturation, the accuracy of the results based on InSAR estimation depends on external factors for instance temperature, moisture, and wind speed (Pulliainen et al., 2003).

The analyses of the existing algorithm of AGB estimation from radar data show that radar data only demonstrate the roughness of land cover surfaces, but it cannot be used to distinguish vegetation types. Another vulnerability associated with radar data is speckle. Proper filtering methods are required to remove the speckles in radar data to enhance the AGB estimation performance (Kellndorfer et al., 2004).

### **2.3 AGB estimation from lidar data**

Lidar data are a great data source to estimate the AGB since lidar pulses can penetrate the forest canopies and demonstrate the physical features of the canopy surface accurately such as tree height, which are highly correlated with biomass (Salas et al., 2010; Zhao et al., 2009). Area-based AGB estimation is a widely used method which explores statistical techniques to analyse descriptors of forests like the number of lidar returns, canopy height, and ratios of returns from lidar data. These descriptors are commonly used for the AGB estimation (Næsset & Økland, 2002; Popescu et al., 2002, 2004; Næsset, 2004; Anderson et al., 2006; Donoghue et al., 2007; Hawbaker et al., 2010; Ioki et al., 2010).

Drake et al. (2003) examined the generality of the relationships between lidar-based metrics and forest structural features, such as AGB, mean stem diameter and basal area in different regions with different precipitation patterns. The results demonstrate different patterns of relationships between lidar-based metrics and the AGB in these two regions, even after the adjustment of leaf drop. The differences in the relationships may result from the differences in the underlying allometric relationships between the AGB and the stem diameter in tropical wet and moist forests.

Kronseder et al. (2012) estimated AGB for different forest types at various degradation levels in Central Kalimantan based on lidar data. Statistics of the lidar-based metrics and the forest inventory plots are employed to generate AGB-prediction models for different forest types. The generated regression models can explain 83% of the AGB variation in lowland dipterocarp forest plots, whereas the models can only explain 32% of the AGB variation in peat swamp forest. The experiments validate the ability of lidar to quantify the deforestation and the forest degradation in different forest ecosystems.

Krofcheck et al. (2016) estimated the AGB of woody vegetation in a juniper savanna in central New Mexico based on airborne lidar points and existing allometries. The authors proposed two hypotheses: first, the difficulties in crown delineation because complex clumping patterns of juniper-dominated forests can be solved by segmenting multiple crowns into single trees; second, three-dimensional lidar-based structural metrics are more closely related to field-measured AGB than CHM-based metrics. The first hypothesis was examined by comparing the accuracy of the AGB derived from single-crown allometric estimation and from clumped-crown allometric estimation. The second hypothesis was tested by comparing the fit of AGB regression models generated by lidar-based and CHM-based structural metrics, respectively. According to the results, single-crown segmentation is not required to estimate the AGB accurately, whereas by including the canopy segment point density, the AGB regression model developed by lidar-based structural metrics describes the relationship between the field-measured AGB and the structural metrics better.

The studies using lidar data to generate general AGB models over broad regions, regardless of the data format, including airborne waveform (Lefsky et al., 2002) and discrete-return (Asner et al., 2009, 2012; Asner and Mascaro, 2014), indicate that the mean height is significant for AGB estimation. More specifically, multiplying the mean height by the number of CHM grid cells equals the geometric volume of the total forest canopy, which can be used to indicate the three-dimensional (3D) canopy volume over the study region (Chen et al., 2007). The model based on canopy geometric volume performs better in estimating the stem volume, a significant measure associated with the stem biomass and total AGB, than more complex models generated by other lidar metrics which are selected by stepwise regression (Chen et al., 2007). The quadratic mean height (QMH) is another meaningful lidar metric for AGB estimation. According to Brown et al. (2005), tree biomass does not demonstrate a linear relationship with tree height and taller trees have a disproportionately larger biomass. The QMH can show the nonlinear relationship and is therefore one of the best biomass predictors for AGB estimation (Lefsky et al., 1999).

Some scholars analysed the impact of statistical techniques on the accuracy of AGB estimates using lidar data. Powell et al. (2012) compared three statistical techniques for modelling biomass to understand the impact of modelling techniques on the biomass dynamics, including reduced major axis regression, Gradient Nearest Neighbour (GNN) imputation, and RF regression trees. Models generated by different methods are applied to time-series Landsat images for 20 years to obtain biomass trajectories. The generated biomass dynamics maps are integrated with the location and timing maps of forest disturbance and regrowth to demonstrate the biomass over large areas and long time periods. According to the results, the three modelling techniques achieve similar results, depending upon various validation measures and scales.

Mauya et al. (2015) modelled the AGB of the miombo woodlands in Tanzania with airborne lidar data. Two different methods, namely linear mixed effects model (LMM) and k-nearest neighbour (KNN), are used to generate the model, respectively. The results indicate that the AGB model generated by LMM has better prediction accuracy than the KNN-based AGB model.

Gleason and Im (2012) evaluated machine learning approaches - RF, SVR, and Cubist ® regression trees - to calculating the forest biomass estimates at both individual tree and plot levels based on high point density airborne lidar data. The comparisons of the results indicate that modelling at the plot level can improve the biomass estimation accuracy and that SVR generated the most accurate biomass model. However, when estimating the biomass at the individual tree level, all the models yielded similar results.

Although multiple studies demonstrate that biomass estimation from lidar data performs better than individual optical or radar data (Clark et al., 2011), lidar data has limited spectral information to classify different vegetation species. Hence, many researchers have fused images with lidar data to enhance the AGB estimates. Anderson et al. (2008) and Vaglio Laurin et al. (2014) integrated lidar data with hyperspectral data and obtained more accurate biomass estimation results in a temperate mixed forest in the eastern USA and a tropical forest in Africa.

Næsset et al. (2011) estimated the AGB at three geographical levels from a stand to a district using airborne lidar data and InSAR as auxiliary information. A model-based estimation was conducted at the stand level while model-assisted estimators were used at the local community level and the district level. The results show a considerable improvement in biomass estimates when lidar data serves as auxiliary information. In addition, the results yielded by InSAR also improve when an accurate terrain model is provided.

Su et al. (2016) estimated the AGB and the corresponding spatial distribution for the forests in China based on a combination of optical imagery, Geoscience Laser Altimeter System (GLAS)/Ice, Cloud, and Land Elevation Satellite (ICESat) data, climate surfaces, ground inventory records, and topographic data. To minimise the impact of uncertainty of plot locations, an uncertainty field model is introduced during the estimation of the AGB. The results indicate that the uncertainty field model can reduce up to 10% of the uncertainty in the AGB estimates and can explain 75% of the variation in the AGB estimation.

Phua et al. (2017) computed the AGB of the tropical rainforests in Malaysia based on airborne lidar points, Landsat 8 Operational Land Imager (OLI) images, and the combination of lidar points and OLI images. Height percentile and laser penetration variables, namely the ratio of the last to the total number of the returns, are computed based on lidar data, while vegetation indices are

calculated based on OLI images, including TVI, Normalised Ratio Vegetation Index (NRVI), RVI, Simple Vegetation Index (SVI), SAVI, NDVI, and DVI. Eight texture variables, including the mean, dissimilarity, variance, second moment, entropy, correlation, homogeneity, and contrast, and three Tasseled Cap transformations including brightness, greenness and wetness are also computed to serve as predictors in the AGB estimation. According to the results, laser penetration variables have a moderate correlation with the AGB. In addition, texture measures are strongly correlated with the AGB, with the Pearson's correlation coefficient ranging from 36.6% to 51.9%. The results also indicate that the integrated use of lidar data and OLI images can improve the accuracy of AGB estimates.

Zolkos et al. (2013) reviewed more than 70 refereed articles about biomass estimation and analysed the corresponding reported biomass accuracy estimates on the basis of different remote sensing platforms, including airborne and spaceborne, and various sensor types including optical, radar, and lidar. Based on the analysis, the AGB models generated by airborne lidar metrics demonstrate a better accuracy than those derived from radar or passive optical data. Although the AGB models generated by multi-sensor metrics produce a greater range of results than lidar-only models, multi-sensor-based models do not guarantee better biomass estimates. Their research also indicates that the model accuracy is related to the forest type and plot size. Apart from the lidar sensor, both the allometric equations for biomass estimation (Zhao et al., 2012) and related stand structure variables like stem density, wood-specific gravities, height, and canopy volume, will contribute to the performance variability.

Lu et al. (2019) used RGB imagery and point cloud data to predict AGB estimation of wheat with a low-cost unmanned aerial vehicle (UAV) system. Vegetation indices such as Visible Atmospherically Resistant Index (VARI), Excess Green Index (EGI), Excess Red Vegetation Index (ExRVI), Excess Blue Vegetation Index (ExBVI), Modified Green Red Vegetation Index (MGRVI), Green Leaf Index (GLI), Kawashima Index (IKAW), Green Red Vegetation Index (GRVI), and canopy height metrics including mean height, median height, percentile height, standard deviation of height and coefficient of variation are explored to generate the regression model. The authors pointed out the combination of vegetation indices and canopy height metrics can yield more accurate AGB estimation results than using vegetation indices or canopy height metrics alone.

However, when generating area-based AGB models, the reference biomass data should be measured at the plot level, which is subject to errors. For example, when calculating the reference biomass, understorey vegetation, woody debris, and snags may be included, whereas lidar first returns may not penetrate the canopy to show these features (Næsset, 2005). An alternative to the

area-based approach is the individual tree-based approach. Different from the area-based approach, individual tree-based approach requires the extraction of individual tree parameters such as the treetop (Popescu et al., 2002; Chen et al., 2006), crown radius (Popescu et al., 2003), or crown boundary (Zhen et al., 2014). Van Aardt et al. (2006) assessed an object-based approach to AGB modelling using lidar points. Objects were segmented based on a lidar-derived CHM and the results were compared with stand-based modelling. The results demonstrate a distinct improvement when using object-based models. Nonetheless, segmenting individual trees from lidar data requires high point density and is challenging in dense canopies.

## 2.4 Uncertainties and errors of AGB estimation from remote sensing data

The core of AGB estimation from remotely sensed data is to infer the AGB of interest from measurements collected by various remote sensing sensors, which can be expressed by the mathematic model in Eq. (2.1):

$$y = f(x) + e \quad (2.1)$$

where:  $y$  denotes the AGB of the target,  $x$  denotes the measurements from remote sensing sensors,  $f$  represents the unknown estimation approach and  $e$  represents the deviation resulting from random noises contributing to the errors of AGB estimation.

As such, the task of the retrieval of  $y$  is to determine the estimation approach  $f$  as close as possible to the truth (Ali et al., 2015). However, the task is challenging since variations in the chemical, physical and biological features of a target can lead to a change in the target's electromagnetic response in terms of absorption, emission, transmission, or reflection (Ulaby et al., 1986). On the other hand, electromagnetic radiation of the same target may demonstrate a non-uniform sensitivity based on various wavelengths and acquisition geometries (Twomey, 1997). Moreover, the electromagnetic response of a target is a function of multiple variables and each one contributes differently to the total electromagnetic response based on the chemical, physical and biological characteristics. As a result, different geo-/bio-physical variable configurations can yield a similar electromagnetic response, which is denoted as parameter ambiguity (Beven and Freer, 2001). Hence, AGB estimation from remote sensing data is subject to various errors and uncertainties. Identifying and quantifying the errors and uncertainties involved in AGB estimation is crucial to improve the performance (Wang et al., 2009, 2011; Lu et al., 2012). Consequently, plenty of work has been conducted to examine these uncertainties (Heath and Smith, 2000; Chave et al., 2004; Sierra et al., 2007; Larocque et al., 2008; Asner et al., 2009; Wang et al., 2009). For example, Saatchi et al. (2007) reported that the uncertainty could be up to 20% for total AGB mapping. Keller et al. (2001) analysed all the uncertainties that may be generated in the AGB

estimation procedures. These uncertainties include allometric models, the sampling, and ratios used to estimate biomass, where the primary source of uncertainty is the allometric models. Meanwhile, the accuracy of AGB estimates will increase by 10% if the size of the sample plots increases from 0.25 ha to 1 ha to minimise the sampling errors. Chave et al. (2004) confirmed that allometric models are the major source of uncertainties. Asner et al. (2011) and Mascaro et al. (2011) indicated that lidar-derived AGB estimates had errors ranging from 17 to 40 Mg per ha (1Mg = 1,000 kg) in tropical forests. Montesano et al. (2014) also analysed the uncertainty of AGB estimates obtained based on lidar and SAR data from both airborne and spaceborne platforms in different countries. According to the results, it is difficult to achieve a low relative error because of the differences between the scale of biomass at the site level and the spatial resolution of current spaceborne sensors. Wang et al. (2011) and Zhang et al. (2013) both investigated how the location errors of sample plots affected the accuracy of AGB estimates by randomly changing the coordinates of the sample plots. The authors acknowledged that the location errors did not influence the mean estimates greatly but the changes would reduce the correlation between the AGB and Landsat TM spectral variables. However, the authors also pointed out that, when a coarser spatial resolution was used, the impacts of the plot location errors would be mitigated. Sun et al. (2019) exploited the impact of three factors on the quality of prediction models, including cross-validation methods, the sizes of field measurements, and regression methods. Six commonly-used regression methods used to estimate the forest AGB include partial least squares regression, Gaussian processes, stepwise linear regression, support vector machine, nonlinear regression using a logistic model, and random forest. According to the results, regression methods are the major factor to determine the quality of the prediction models and among the six regression methods, random forest yields the most accurate result.

Analyses of the uncertainties and errors involved in AGB estimation allow them to be grouped into the following categories:

- 1) field measurements of tree variables such as DBH and height have errors, including measurement, grouping, recording and sampling errors;
- 2) the sample plots may not be representative of all conditions throughout large areas in a forest, which will affect the extrapolation of biomass estimates or measurements;
- 3) the remote sensing images are subject to errors; for instance, spectral values are inaccurate because of poor weather conditions, and improper spatial interpolation techniques are chosen for geometrical and radiometric corrections;
- 4) the sample plots and the cells representing the sample plots in the remotely sensed data are mismatched because of global positioning system (GPS) uncertainties, especially in dense forests;

- 5) the sizes of sample plots and image pixels are different, leading to the presence of mixed pixels, namely a single pixel representing multiple sample plots;
- 6) field measurements and remote sensing data are recorded at different time.

According to the reported studies, the range of the relative errors of the estimates is between 5% and 30% and the relative errors are relevant to the forest ecosystems, topography, remotely sensed data and the adopted methods (Chen et al., 2000; Keller et al., 2001; Nabuurs et al., 2008; Mascaro et al., 2011). In general, the level of accuracy of AGB estimates required for forest management depends on the scale of the study region. For instance, the accuracy is required to be higher than 90% at regional scale, while an accuracy of 80% is also acceptable at continental and global scales.

## 2.5 Summary

This chapter has reviewed the existing algorithms of AGB estimation from remote sensing data. Multiple methods have been examined and their weaknesses and strengths have been discussed. According to the analyses of these algorithms, optical images are a valuable data source because a large amount of images are ready to use, image processing algorithms are advanced and vegetation parameters have a strong correlation with spectral bands. However, optical images suffer from data saturation, especially in forests with high biomass density. In addition, optical sensors cannot overcome the cloud-cover problem. In comparison, SAR can penetrate the canopy to some extent, therefore providing vertical information on vegetation. Meanwhile, SAR is sensitive to the water content in the vegetation but is not influenced by bad weather. Consequently, a SAR image is an alternative data source for AGB estimation. However, data saturation still exists in SAR images, especially in a mature forest, and the speckles in the SAR images are another problem.

The advent of the lidar technique provides an opportunity to estimate AGB accurately since lidar data can accurately depict the 3D structure of the forest, which is critical for the AGB estimation of a forest. Previous studies have shown that AGB estimation based on lidar metrics performs better than optical images alone (Cao et al., 2018). Common strategies for AGB estimation based on lidar data include area-based and individual-tree-based. Because area-based approaches require an AGB reference recorded at the plot level, they may introduce errors. In addition, when measuring the AGB at the plot level, snags, woody debris, and understorey vegetation may be included, but lidar pulses may not penetrate the canopies deeply enough to describe these features. Moreover, compared to individual-tree-based methods, the mismatch between the reference data and the lidar-based metrics due to the uncertainties of GPS has a more profound impact on the results. Although individual-tree-based methods can show the spatial variation of the AGB at

single tree level and are not affected by the size of the sample plot, they are quite challenging, since it is difficult to segment individual trees from randomly placed points, especially in dense forests. Therefore, the aim is to develop a framework to estimate the AGB of individual trees for a forest in Australia. In Chapter 3, the study region will be described, and the methodology of the framework will be presented in details.

## **Chapter 3 : Study Region and Methodology**

The examination of existing algorithms for AGB estimation from remote sensing data indicates that individual-tree-based approaches can compute the AGB estimates accurately and show the spatial variations of the AGB estimates at individual-tree level but it is difficult to segment a large amount of lidar points into individual trees, especially in dense canopies. To compute the AGB estimates of individual trees accurately from airborne lidar data, a comprehensive framework is developed. In this chapter, the study region will be illustrated and the methodology of the framework will be discussed with the structure of the chapter as follows: Section 3.1 presents the study region, describes the associated airborne lidar data and field measurements while Section 3.2 demonstrates the methodology of the framework with a brief summary in Section 3.3.

### **3.1 Study region and data**

#### *3.1.1 Study region*

A forest (35°16'S, 149°05'E) of approximately 137.49 ha, located in the Black Mountain Nature Reserve, Canberra, Australia, is chosen for this study as shown in Figure 3.1. It is chosen because of the availability of the field measurements. This forest is a key element of the preservation of plant diversity in the region since it houses around 500 plant pieces and is characterised by different types of gum trees, shrubs and herbaceous flora. The predominant tree species include scribbly gum (*Eucalyptus rossii*), brittle gum (*Eucalyptus mannifera*), yellow box (*Eucalyptus melliodora*) and red stringybark (*Eucalyptus macrorhyncha*). The elevations of the study region range from about 567 m to about 848 m from the sea level.

#### *3.1.2 Data description*

The associated airborne lidar data were collected by a Leica ALS50-II lidar system. Each transmitted lidar pulse obtained up to seven returns. After decomposing the lidar full waveforms, the lidar data consist of 31,916,135 points. The configured scan angle is  $\pm 30^\circ$  from nadir and the reported accuracy is 10 cm horizontally and 7 cm vertically. Overall, the data set has an average point density of 23.2 point/m<sup>2</sup>. The processing of lidar data was run in Matlab R2013b (MathWorks, 2015) using the Intel (R) Core(TM) i7-472 4900 CPU with the installed memory of 16 GB.

Field measurements were established in 23 circular plots (about 900 m<sup>2</sup> each). All plots were georeferenced with a Global Positioning System (GPS) device with differential correction

capability. The accuracy of the GPS device is up to 3 m due to the multipath effect caused by tall trees. For all trees within the 23 circular plots, the height of the first branch ( $H_{fb}$ ) and tree height ( $H$ ) were recorded using a standard clinometer and distance tape method. At least two measures were taken from different viewpoints. Every two of the viewpoints was separated by at least  $90^\circ$  to ensure uncorrelated measures. Although all trees in each plot were measured, if the difference between two height measurements was larger than 1 m, the tree was discarded to ensure confidence in the accuracy of the field measurements. A crown width (CW) is the horizontal distance from edge to edge of the crown. Drip lines of the outermost edges are used to measure CWs. The average of the horizontal distances along different axes in different directions was regarded as the crown width of a tree. The diameter at breast height ( $DBH$ ) was recorded as the diameter of the trunk of a tree at 1.30 m from the ground. Overall, the total number of field observations was 176. After the statistical analysis of the 176 records, the maximum, minimum, mean and standard deviation of the tree height and crown width are selected and the statistical metrics are listed in Table 1, which aims to provide a brief overview of the trees in the plots..

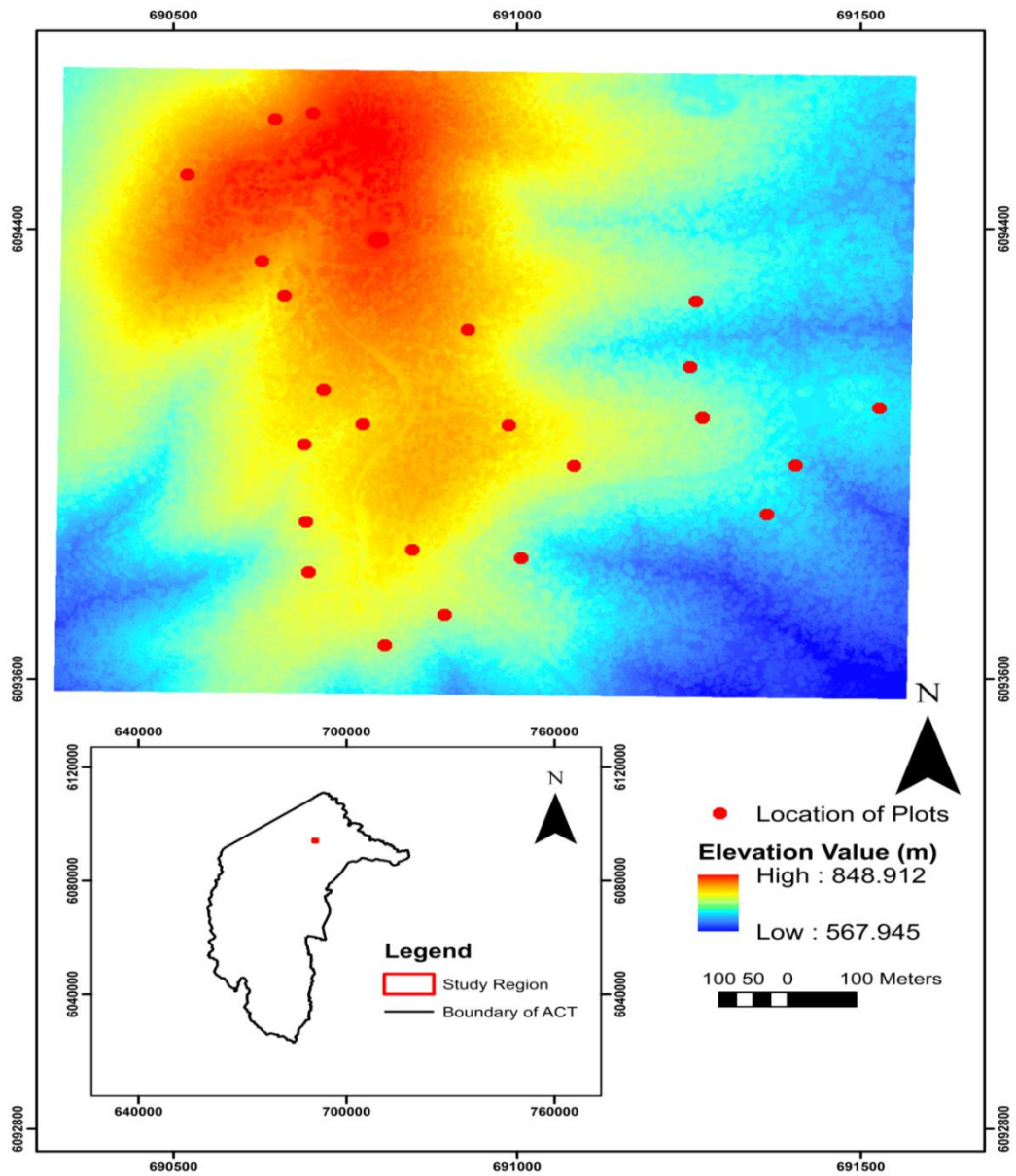


Figure 3.1 The study region in Black Mountain, Canberra, Australia indicated by the red rectangle box. Colours depict the elevation values of a 1-m resolution DSM over the study region. The red dots represent the locations of the sample plots.

Table 3.1 A summary of the field measurements

	Min	Max	Mean	Std
$H_{fb}$ (m)	0.40	9.89	5.17	1.90
$H$ (m)	4.47	16.61	10.04	2.68
CW (m)	0.66	12.30	4.95	2.42
DBH (cm)	5.73	62.10	22.58	11.28

## 3.2 Methodology

To estimate the AGB of individual trees from airborne lidar data, it is critical to segment lidar points into individual trees and extract accurate individual tree parameters such as tree height, crown width, and DBH. However, because lidar points contain both object points and ground points, it is a must to distinguish object points from ground points and normalise the height values of the identified object points to remove the impact of topography. Hence, a voxel-based multiscale morphological airborne lidar filtering algorithm is firstly applied to recognise object points. The identified ground points within each  $1\text{ m} \times 1\text{ m}$  grid cell are interpolated to generate a 1-m resolution DTM. The classified object points are treated as vegetation because no other objects are in the study region. A 1-m resolution DSM is created by the vegetation points with the highest elevation values in each grid. The 1-m resolution CHM is created by subtracting the 1-m resolution DTM from the corresponding DSM pixel-wisely. However, because of pits present in the CHM, which will degrade the accuracy of the CHM, it is essential to recognise and replace the pits with correct values. As such, a multiscale morphological algorithm is used to rectify the pits and improve the accuracy of the CHM. Once the improvement of the CHM is done, a hybrid individual tree segmentation algorithm is utilised to segment the vegetation points with normalised height values into individual trees. After the segmentation of individual trees and the extraction of individual tree parameters, different machine learning algorithms are applied to generate the AGB regression model based on field measurements and lidar-based individual tree parameters, respectively. The flowchart of the framework is shown in Figure 3.2.

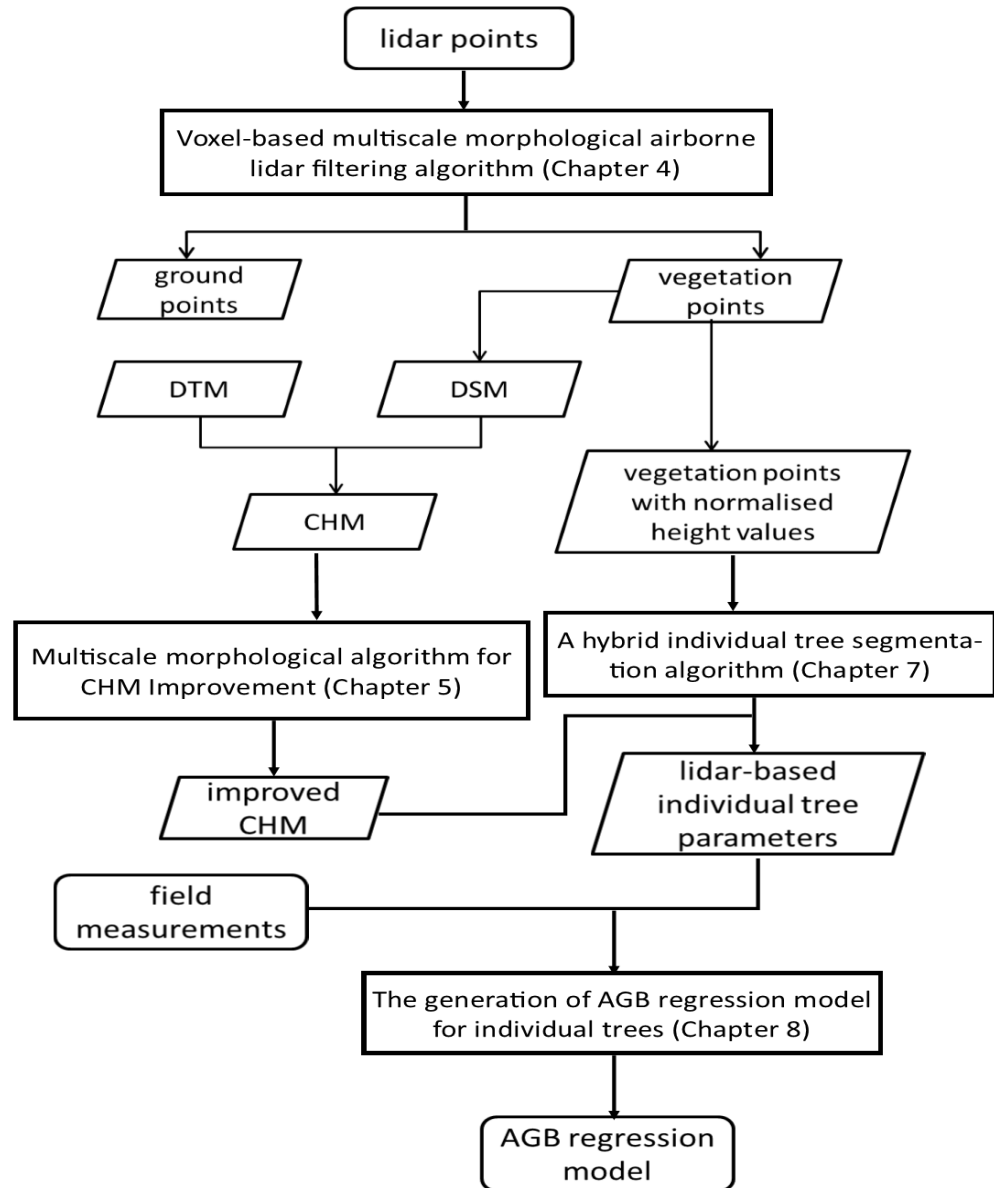


Figure 3.2 The flowchart of the framework

### 3.3 Summary

Chapter 3 mainly describes the characteristics of the study region, the corresponding airborne lidar data and field measurements, and demonstrates the methodology of the framework briefly. As stated, it is critical to first distinguish object points from ground points and normalise the height values of the identified object points, therefore minimising the impact of topography on the vegetation points. Consequently, a voxel-based multiscale morphological airborne lidar filtering algorithm is proposed to identify object points, and the details are present in Chapter 4.

## **Chapter 4 : A Voxel-based Multiscale Morphological Airborne Lidar Filtering Algorithm for Forest Regions**

As stated in Chapter 3, the first step of the framework is to classify the airborne lidar points into ground points and non-ground points. The classified ground points will be used to generate the DTM and the height values of the non-ground points will be normalised by subtracting the corresponding DTM to remove the impact of topography in further processing. Retrieving significant knowledge of the DTM alongside other objects requires labelling of the unorganised 3D datasets, which is often subject to intensive analysis (Biosca and Lerma, 2008; Vosselman et al., 2004; Ural and Shan, 2016). Starting with a set of 3D geospatial coordinates, the labelling analysis exploits various features such as slope, curvature, and elevation to distinguish ground points from object points, which is generally referred to as ground filtering.

In this chapter, a voxel-based multiscale morphological airborne lidar data filtering algorithm is presented, which takes advantage of the height distribution of points, the convexity of points, the relative height difference between a point and its surroundings in multiple spatial scales. To reduce the misclassification of ground points in each iteration, this algorithm introduces an object index to label object points in different spatial scales. The information of the return number and the total number of returns in lidar data is used to compute the weight of the object index and the Otsu segmentation is exploited to calculate the threshold of object index automatically. If the corresponding object index of a point is above the threshold, it is regarded as an object point and removed.

The chapter is structured as follows: Section 4.1 reviews existing ground filtering algorithms; Section 4.2 deals with the detailed information about the proposed algorithm; Section 4.3 presents the experiments, evaluation of the results and analyses of the parameters followed by a brief summary in Section 4.4.

### **4.1 Ground filtering from airborne lidar data**

As an important source of geospatial information, DTMs play an essential role in a variety of geospatial applications. Reliable knowledge of DTM allows road designs, flood controls, and military operations (Gong et al., 2000) and help mining, surveying, and city planning more efficient and effective. Conventional approaches such as field surveying and photogrammetry serve to yield highly accurate DTM products; however, the intensive labour required and monetary cost prohibit more extensive applications of these methods. One promising alternative to the acquisition of a highly accurate DTM is airborne lidar. The appealing feature of the

availability of highly accurate 3D geospatial coordinates has drawn much attention (Habib et al., 2005). Consequently, numerous research works have been undertaken to generate accurate DTMs using airborne lidar data, and the work is well examined by Sithole and Vosselman (2004), Liu (2008), Meng et al. (2010) and Zhang et al. (2018). Based on the adopted strategies, the existing ground filtering approaches can be mainly categorised into four domains (Kraus and Pfeifer, 1998; Axelsson, 1999; Pfeifer et al., 1999; Vosselman, 2000; Zhang et al., 2003; Brovelli et al., 2004; Shan and Sampath, 2005; Sithole and Vosselman, 2005; Meng et al., 2009; Mongus et al., 2014), namely, slope-based, interpolation-based, mathematical-morphology-based, and segmentation-based algorithms. Recent advances in computer science also allow statistical analysis and machine learning to be employed in ground filtering algorithms.

The basic concept behind slope-based algorithms is that the bare ground is smooth and the slope between ground and objects is distinctive from the slope between ground points (Vosselman, 2000; Roggero, 2001; Sithole, 2001; Shan and Sampath, 2005). On the basis of this assumption, the slope of a lidar point and its surroundings is computed and the point is labelled as an object if the slope exceeds the predefined threshold. If the threshold is set large, more object points will be accepted as ground, whereas a small threshold will lead to the removal of ground points in hilly regions. Since the results are heavily reliant on the slope threshold, slope-based algorithms achieve promising results in comparatively flat regions and the performances worsen sharply in mountainous areas as slopes in these regions vary. Although Vosselman (2000) suggested that a solution can be provided by the integration of the knowledge of terrains derived from training datasets, it is impractical to capture all types of terrains in a study region, especially if the study area is a forest region.

An interpolation-based algorithm generates an approximate terrain surface and identifies ground points based on some measurements, such as the residual (i.e. the normal distance from the point to the generated surface) or the angle (Kraus and Pfeifer, 1998; Pfeifer et al., 1998, 1999; Axelsson, 2000; Sohn and Dowman, 2002; Nie et al., 2017). However, these methods are prone to misclassifying non-ground points with low-elevation values as ground points. To improve the performance, many researchers adopted a multiscale strategy (Evans and Hudak, 2007; Mongus and Žalik, 2012; Chen et al., 2013; Hu et al., 2014), that is, estimation of the approximate terrain surface and the residual at various spatial scales. However, the implementation of these methods is time-consuming. Moreover, the multiscale strategy cannot ensure the removal of low-elevation object points.

Based on mathematical morphological operations such as opening and closing operators, morphology-based filters identify ground points in a greyscale image. They assume that the grey

values of objects are distinctive from the ground when the points are converted to a greyscale image according to the elevation since the heights of object points are greater than those of surroundings (Zhang et al., 2003, Chen et al., 2007; Pingel et al., 2013; Mongus et al., 2014). Being sensitive to window sizes, the morphology-based filters require tuning of the parameters to achieve optimal results. Large window sizes will degrade rugged terrain attributes such as peaks, while small window sizes may compromise the performance of removing objects.

Starting with segmenting lidar points by features such as a smoothness constraint (Tóvári and Pfeifer, 2005) or slope (Filin and Pfeifer, 2006), segmentation-based algorithms then calculate geometric attributes (e.g. size, shape) and merge different segments on the basis of topological relations, which are explored to remove objects (Jacobsen and Lohmann, 2003; Sithole, 2005; Sithole and Vosselman, 2005; Tóvári and Pfeifer, 2005). However, the challenge of these algorithms is the accuracy of the segmentation results, especially in boundary regions.

Statistical-analysis-based algorithms are based on the assumption that the elevation of ground points will demonstrate a normal distribution whereas the presence of objects will disturb the normal distribution. Hence, by computing the skewness and/or kurtosis of lidar datasets and removing points with high height or intensity values iteratively until the skewness and/or kurtosis is balanced, the DTM is created (Bartels et al., 2006; Bartels and Hong, 2006; Bao et al., 2008; Bartels and Hong, 2010; Crosilla et al., 2013). However, the computation is intensive and the algorithms may fail to wipe out low-elevation outliers. On the other hand, machine-learning-based algorithms (e.g. conditional random field, AdaBoost, random forest, artificial neural network, deep learning) classify lidar points into various categories such as ground, building, and grass (Niemeyer et al., 2013; Lodha et al., 2007; Lu et al., 2009; Jahromi et al., 2011; Hu and Yuan, 2016) simultaneously. However, the performance of the algorithms depends on the extensive training data.

In general, the aforementioned algorithms have their own strengths and weaknesses with respect to computational efficiency, overall accuracy, ease of implementation, and adaptability (Ural and Shan, 2016). The majority of these approaches achieve good accuracy in relatively flat regions. However, problems occur when mountainous terrains, cliffs, ridges, and forest areas are mixed with man-made objects. However, problems occur in mountainous terrains, cliffs, ridges, and forest areas mixed with man-made objects. To obtain accurate DTMs in forest regions, a multiscale-curvature-classification (MCC) was introduced by Evans and Hudak (2007). It iteratively identifies a point as an object if it is above positive curvature thresholds in various scales. However, the authors acknowledged that the presence of low-elevation vegetation would negatively impact the performance of the algorithm. Guan et al. (2014) proposed a cross-section-

plane (CSP) analysis to filter out object points in wooded mountain areas. Firstly, the raw lidar points are partitioned into 3D voxels, based on the points in each voxel, multi-directional CSPs are generated; secondly, for each CSP, potential ground points are selected according to the lidar point characteristics, such as the number of returns, intensity, and height; thirdly, initial ground points are detected in each CSP based on the slope and distance, and fourthly, the detected initial ground points are refined by a merging-or-intersecting strategy. Zhao et al. (2016) proposed an improved progressive triangular irregular network (TIN) densification filtering algorithm. Firstly, a morphological opening operator is applied to obtain potential ground seeds; secondly, ground seed points are identified by a translation plane fitting method; finally, iterative TIN densification is performed to generate an accurate DTM. However, the selection of the lowest point within a grid to represent the true ground in the generation of a coarse terrain surface in the first step is subject to errors because of systematic and random uncertainties in the lidar data acquisition. Moreover, a lidar pulse may not penetrate the dense canopy to hit the ground. Silva et al. (2018) compared weighted-linear-least-squares (WLS), MCC, progressive-morphological-filter (PMF), and progressive-Triangulated-Irregular-Network (PTIN) in a forest environment in Washington State, the United States, with distinctive land use and land cover. The results indicate that WLS, MCC, and PTIN obtain similar classification results whereas PMF identifies a smaller number of points as terrain compared to other algorithms. The results also demonstrate that MCC generates a DTM with higher elevation values whereas PMF tends to underestimate the DTM. However, the authors also acknowledged that the four algorithms should be evaluated over complex forest environments.

Although morphology-based algorithms tend to perform well in steep-sloped regions given a well-chosen window size, detecting large and small objects is, however, still challenging (Özcan and Ünsalan, 2016). To overcome the aforementioned problems, this chapter presents a voxel-based multiscale morphological airborne lidar filtering algorithm, which is denoted by VF hereafter. Instead of removing object points in multiple spatial scales, the proposed algorithm labels these points in each iteration by introducing an object index, which aims to minimise the misclassification of ground points as object points.

## **4.2 Methodology**

To distinguish object points from ground points, firstly, a set of cell sizes needs to be selected, and then points can be projected into different cells according to the spatial coordinates. Because of the presence of outliers (i.e. isolated points with high elevations or lower elevations than the surroundings), a height distribution analysis is typically employed to detect and remove these outliers before further processing. Once the outliers are removed, a convexity constraint can

be applied to calculate the convexity of each cell to detect object points. However, the convexities of building roofs and low vegetation can be small, and therefore the convexity constraint may compromise the removal of building rooftops and low vegetation. To tackle this problem, a morphological filtering algorithm and a moving-window voxel algorithm are proposed. To avoid the impact of misclassification on further procedures, an object index ( $OI_i$ ) is also introduced to label the classified object points. In addition, different weights are assigned to the object index on the basis of the number of returns and the return numbers since multiple returns contribute less to ground points. That is, if a point is classified as an object, the object index of the point will increase by the sum of one and the difference between the number of returns and the return number, which is denoted as Rule 1 hereafter. The whole process will be repeated until the cell size becomes above the maximum threshold. Once this is done, an Otsu segmentation algorithm is used to compute the threshold for the object indices, and the points with object indices higher than the threshold are recognised as objects and removed. The detailed procedures are listed below and illustrated in Figure 4.1:

- Step 1. Select a set of cell sizes and set the minimum as the current one;
- Step 2. Project the lidar points into different cells according to the coordinates;
- Step 3. For each cell, apply height analysis to the points within the cell and remove outliers;
- Step 4. For each cell, apply the convexity constraint and label the points within the cell as objects if the convexity of the cell is above the threshold. For the classified object points, the corresponding  $OI_i$  increases according to Rule 1;
- Step 5. For each cell, apply morphological filtering. If a point is recognised as an object point, the corresponding object index of the point increases based on Rule 1;
- Step 6. For each cell, apply moving-window voxel filtering; as a result, the object indices of the classified object points increase by the weights calculated by Rule 1;
- Step 7. If the cell size reaches the maximum, go to Step 8; otherwise, set another cell size as the current one and repeat Steps 2–6;
- Step 8. Apply Otsu segmentation to the object indices of all lidar points excluding outliers; therefore the points with object indices above the threshold are regarded as objects and removed.

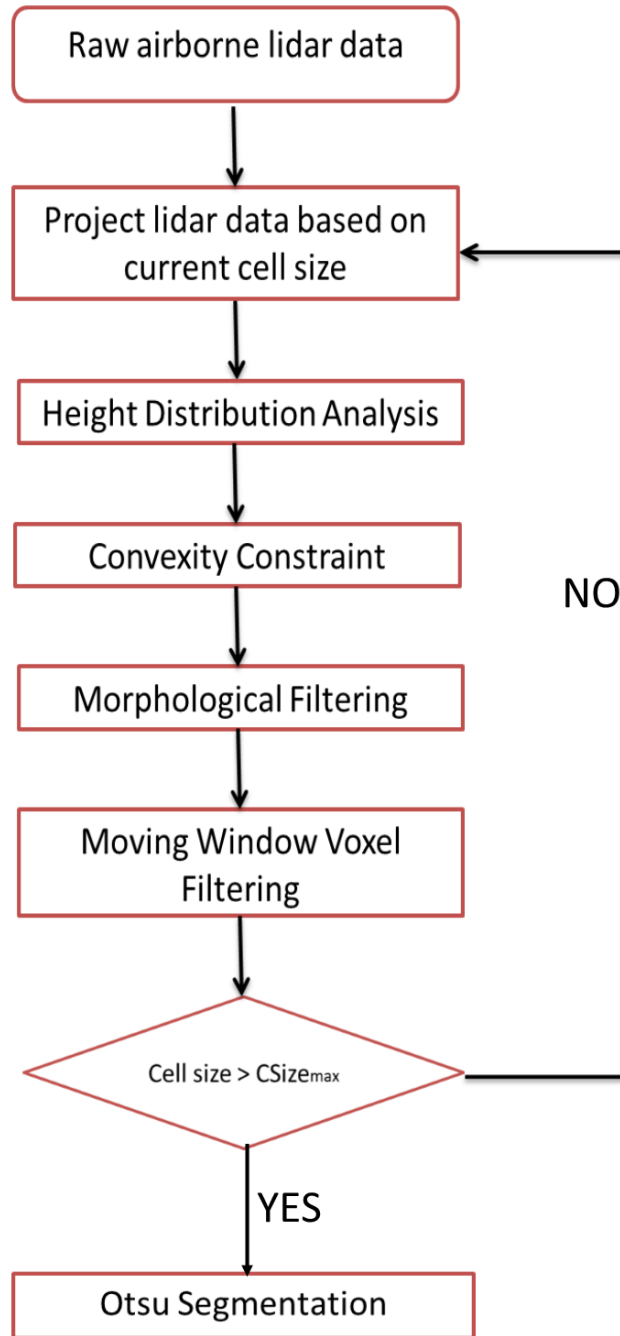


Figure 4.1 The flowchart of the proposed airborne lidar filtering algorithm

#### 4.2.1 Height distribution analysis

Since outliers have a negative impact on the result accuracy, it is desirable to delete outliers before further processing. According to Crosilla et al. (2013), the height distribution of ground points will follow the normal distribution whereas the presence of other points will disturb it. In this study, the height distribution analysis is explored to recognise and eliminate outliers. For each cell, the mean height ( $H_{mean}$ ) and the standard deviation ( $\sigma_H$ ) are computed. According

to the Three Sigma Rule (Pukelsheim, 1994), points with heights less than  $3\sigma_H$  from  $H_{mean}$  are regarded as outliers and the corresponding object indices will be set to -1. The points with the value of -1 for the corresponding object indices will not be processed in further stages. In case of ground points in highly-elevated regions, points with heights greater than  $3\sigma_H$  from  $H_{mean}$  are labelled as objects and the corresponding object indices increase by Rule 1. The mathematical formula for this method is expressed as Eq. (4.1):

$$\begin{aligned} H_{mean} &= Mean(\sum_1^n H_i) & \sigma &= \sqrt{\sum_1^n (H_i - H_{mean})^2 / n} \\ OI_i &= \begin{cases} -1; & \text{if } H_i < H_{mean} - 3\sigma \\ OI_i + (T_R - R_N + 1); & \text{if } H_i > H_{mean} + 3\sigma \end{cases} \end{aligned} \quad (4.1)$$

where  $H_{mean}$  is the mean height of the points within a cell;  $H_i$  represents the height of the point  $i$  ( $i = 1, 2 \dots n$ ) in the cell;  $Mean$  is the mean function;  $n$  is the total number of points in the cell;  $\sigma$  is the standard deviation of the height in the cell;  $OI_i$  represents the object index of the point  $i$ ;  $T_R$  denotes the total number of returns; and  $R_N$  denotes the return number.

#### 4.2.2 Convexity constraint

The convexity constraint, proposed by Zhao and You (2012), was originally exploited to separate roofs from trees since the majority of roofs are convex in a local region. For the node  $v_0$ , any two consecutive nodes alongside  $v_0$  will generate a facet  $F_t$ . Consequently, a region with  $3 \times 3$  cells will form eight facets  $\{F_1, F_2, \dots, F_8\}$ . A  $3 \times 3$  moving window is chosen since a small-sized moving window does not cover large areas to ensure accurate estimation of convexity and will compromise the computational efficiency, whereas a large window will take into account remote regions that have little impact on local convexity. For each facet  $F_T$  with nodes  $\{v_0, v_i, v_{i+1}\}$ , based on their distances from the current facet, the other nodes can be grouped into the positive or negative distance group. The maximum absolute distances in each class are compared and the smaller value is assigned to  $F_T$ , as shown in Eq. (4.2). As such, the convexity of the node  $v_0$  is defined as the maximum value assigned to eight facets, which is demonstrated in Eq. (4.3).

$$d_{F_T} = \begin{cases} d_{pos}; & \text{if } \text{abs}(d_{pos}) \geq \text{abs}(d_{neg}) \\ d_{neg}; & \text{if } \text{abs}(d_{pos}) < \text{abs}(d_{neg}) \end{cases} \quad (4.2)$$

where  $d_{F_T}$  denotes the distance from the neighbour to facet  $F_T$ ;  $d_{pos}$  and  $d_{neg}$  represent the maximum distance in the positive and negative distance groups, respectively; and  $\text{abs}$  denotes the absolute value of the input.

$$\text{Con}_{v_0} = \max(d_{F_1}, d_{F_2}, \dots, d_{F_8}) \quad (4.3)$$

where  $\text{Con}_{v_0}$  demonstrates the convexity at node  $v_0$ , and  $d_{F_1}, d_{F_2}, \dots, d_{F_8}$  represent the assigned values of each facet, and  $\max$  is the function that returns the largest value of the input.

For a smooth region, such as ground or a building roof, the convexity is small, whereas the convexity of a tree canopy should be large since the heights of points on a canopy vary greatly. The threshold of the convexity constraint should be properly chosen since a small threshold will result in the misclassification of ground points, whereas object points can be categorised as ground if a large threshold is given. The mathematical formula for this method is expressed as Eq. (4.4):

$$QI_i = \begin{cases} QI_i; & \text{if } \text{Con}_{v_0} \leq \alpha \\ OI_i + (T_R - R_N + 1); & \text{if } \text{Con}_{v_0} > \alpha \end{cases} \quad (4.4)$$

where  $\alpha$  is the threshold for convexity.

#### 4.2.3 Morphological filtering

Due to the presence of low vegetation and building rooftops, the convexity constraint may fail to eliminate all object points. To delete low vegetation and buildings, a morphological filtering (Zhang et al., 2003) is exploited. The concept of the morphological filtering is to compare the elevation difference between a point and the minimum surface grid. If the difference is above the threshold, the point is regarded as an object. For the convenience of computation, instead of determining the threshold adaptively as Zhang et al. (2003), a constant value of 3 cm is set. The selection of parameters should be carefully determined since a large threshold may fail to remove low vegetation points whereas a small parameter can cause the deletion of ground points. Once a point is treated as an object point, the corresponding object index of the point will be processed according to Eq. (4.5):

$$QI_i = \begin{cases} QI_i; & \text{if } (H_i - H_s) \leq \theta_h \\ OI_i + (T_R - R_N + 1); & \text{if } (H_i - H_s) > \theta_h \end{cases} \quad (4.5)$$

where  $H_s$  is the elevation of the minimum surface grid, and  $\theta_h$  denotes the threshold for elevation difference.

#### 4.2.4 Moving-window voxel filtering

Morphological filtering may fail to recognise small and large objects at the same time. Building rooftops may remain after the morphological filtering. Hence moving-window voxel filtering is explored to remove building rooftops. This algorithm takes advantage of the elevation differences between ground and objects. If the elevations of points are greater than those of the

surroundings, the points will be identified as objects. The details of the moving-window voxel filtering are listed as follows:

Step 1. Given the presence of points in the current cell  $p_{s,t}$  ( $s = 1, 2, \dots, nr$ ;  $t = 1, 2, \dots, nc$ , where  $nr$  is the total number of rows and  $nc$  is the total number of columns), get the minimum value in the  $z$  direction within a  $3 \times 3$  window according to Eq. (4.6);

$$\begin{aligned} H_{s,t} &= \min(H_i) \\ H_{\min} &= \min(H_{a,b}) \quad a = s - 1, \dots, s + 1; \quad b = t - 1, \dots, t + 1 \end{aligned} \quad (4.6)$$

where  $H_{s,t}$  represents the minimum height in cell  $p_{s,t}$ ;  $H_{\min}$  represents the minimum height in a  $3 \times 3$  neighbourhood of cell  $p_{s,t}$ .

Step 2. For each cell within the  $3 \times 3$  window, calculate the voxel index for the points in the cell based on Eq. (4.7) and allocate the points to corresponding voxels; the voxels with the same row and column numbers but different height numbers form a bin:

$$VI_i = \text{floor}((H_i - H_{\min}) / \text{CSize}_z) + 1 \quad (4.7)$$

where:  $VI_i$  is the voxel index of a point in  $z$  direction;  $\text{floor}$  represents the function that rounds the input value to the nearest integer no larger than the input value, and  $\text{CSize}_z$  denotes the height size of a voxel.

Step 3. For the bin derived from the current cell  $p_{s,t}$ , search for the minimum serial number ( $V_{p_{s,t}}$ ) in the  $z$  direction containing points and label the points whose voxel indices in the  $z$  direction are larger than the minimum one as objects, as shown in Eq. (4.8):

$$QI_i = \begin{cases} QI_i; & \text{if } VI_i \leq V_{p_{s,t}} \\ OI_i + (T_R - R_N + 1); & \text{if } VI_i > V_{p_{s,t}} \end{cases} \quad (4.8)$$

where  $V_{p_{s,t}}$  indicates the minimum serial number in the  $z$  direction of the bin derived from cell  $p_{s,t}$ .

Step 4. Identify the smallest serial number in the  $z$  direction that contains points for every other bin generated within the window. The removable index ( $RI_{p_{s,t}}$ ) of cell  $p_{s,t}$  increases by 1 if  $V_{p_{s,t}}$  is larger than the surroundings, as expressed by Eq. (4.9):

$$RI_{p_{s,t}} = RI_{p_{s,t}} + 1; \quad \text{if } V_{p_{s,t}} > V_{p_{a,b}} + \varepsilon \quad (4.9)$$

where  $V_{p_{a,b}}$  indicates the minimum serial number in the  $z$  direction of the bin derived from cell  $p_{a,b}$  ( $a = s - 1, \dots, s + 1; b = t - 1, \dots, t + 1; p_{ab} \neq p_{st}$ ); and  $\varepsilon$  is a constant value to minimise the effect of elevation change.

For a  $3 \times 3$  window,  $p_{s,t}$  is surrounded by eight neighbouring cells. Hence, if  $RI_{p_{s,t}}$  is larger than 4, it is assumed that the points within  $p_{s,t}$  are higher than the neighbours and should be treated as objects. However, given a large window size, high-elevation ground points will be assigned a large voxel index and will therefore be removed, especially in hilly regions. In this case, if the window size is too large, go to Step 5 for further processing. Otherwise, go to Step 6.

Step 5. Divide a cell into small region in case of the removal of ground points in hilly regions.

The small region should be able to cover a building rooftop while avoiding the elimination of ground points with great height values. Hence, 25 m is set based on experimentation. For each small region, Steps 1–4 are repeated with a  $2 \times 2$  window to analyse the heights of the points in the region compared to the heights of the surroundings. A  $2 \times 2$  window is set to minimise the effect of elevation changes.

Step 6. The points with the minimum serial number in the bin derived from  $p_{s,t}$  should be processed according to Eq. (4.10):

$$QI_i = \begin{cases} QI_i; & \text{if } RI_{p_{s,t}} \leq (m^2 - 1)/2 \\ QI_i + (T_R - R_N + 1); & \text{if } RI_{p_{s,t}} > (m^2 - 1)/2 \end{cases} \quad (4.10)$$

where  $m$  is the size of the moving window.

Step 7. Repeat Steps 1–6 until all cells are visited.

Instead of partitioning all lidar points, only points within the moving window are allocated into various voxels for the ease of computation and avoiding the allocation of empty voxels. An appropriate voxel height is essential since a larger value may fail to recognise object points, whereas a small value may result in the removal of ground points even though it enhances the removal of object points. In terms of the size of the moving window, a small value may not cover a building rooftop, therefore fails to capture roof points, whereas a large-sized window may remove ground points due to the great elevation changes in mountainous regions. Taking these factors into account, a  $3 \times 3$  moving window is selected.

#### 4.2.5 Otsu segmentation

Once the iteration is complete, the corresponding object indices of points are assigned to different values. To distinguish object points from ground points, Otsu segmentation (Otsu, 1979) is exploited to calculate the threshold due to its automatic computation and ease of implementation.

As the chosen threshold should maximise the variance among distinctive features, it should be applied to the mathematical model expressed by Eq. (4.11). Hence, for each object index, the variance of the result is computed and the object index with the largest variance is set as the threshold. Points with larger object indices than the threshold are treated as object points and removed.

$$\begin{cases} \theta^2 = \omega_0(\varepsilon_0 - \varepsilon_L)^2 + \omega_1(\varepsilon_1 - \varepsilon_L)^2 \\ \omega_0 = \sum_{r=0}^k P_{OI_r}; \text{ where: } P_{OI_r} = g_{OI_r}/g \\ \omega_1 = \sum_{r=k+1}^L P_{OI_r}; \\ \varepsilon_0 = \sum_{r=0}^k rP_{OI_r}/\omega_0; \\ \varepsilon_1 = \sum_{r=k+1}^L rP_{OI_r}/\omega_1; \\ \varepsilon_L = \sum_{r=0}^L rP_{OI_r}; \end{cases} \quad (4.11)$$

where  $k$  is the current object index value;  $r = 0, 1, \dots, k, \dots, L$ ;  $L$  is the maximum value of the object index;  $\theta^2$  is the class variance when the object index value is  $k$ ;  $\omega_0$  is the possibility of the presence of object index values with levels ranging from 0 to  $k$ ;  $\omega_1$  is the possibility of the presence of object index values with levels ranging from  $k + 1$  to  $L$ ;  $P_{OI_r}$  is the possibility of the presence of object index value  $r$ ;  $g_{OI_r}$  indicates the total number of points with an object index value of  $r$ ;  $g$  represents the total number of points excluding outliers;  $\varepsilon_0$  is the mean value of object indices ranging from 0 to  $k$ ;  $\varepsilon_1$  is the mean value of object indices ranging from  $k + 1$  to  $L$ ; and  $\varepsilon_L$  is the mean value of the whole object indices.

### 4.3 Experiments and discussions

#### 4.3.1 Study region

To examine the performance of the proposed voxel-based multiscale morphological airborne lidar filtering algorithm, the airborne lidar data covering the study region were used to conduct the experiment. To validate the robustness of the algorithm, the airborne lidar benchmark datasets representing different scenarios from ISPRS (ISPRS, 2017) were also used for the test.

#### 4.3.2 Filtering results

When selecting a set of cell sizes, small cell sizes were chosen to ensure the elimination of vegetation points, while large cell sizes should be able to envelop a building rooftop. If the minimum cell size is selected, a too small minimum cell size may result in the deletion of ground points and compromise the computational efficiency whereas a large value can hinder the recognition of low-elevated vegetation. Another factor to consider is that omission error can increase if a large maximum cell size is chosen, while a small maximum size can fail to detect object points. Taking these factors into account as well as the computation convenience, the minimum cell size was computed based on Cho et al. (2004). Because of the small coverage of data and sparse point density, the maximum cell size for the ISPRS datasets was 25 m, and other cell sizes were 2, 5, 10, and 20 m. For the study region, the maximum cell size was assigned as 70 m and other cell sizes were 0.5, 1, 2, 5, 10, 20, 40, 50 and 60 m. The determination of the cell sizes is often based on experimentation.  $H_{\text{mean}}$  and  $\delta$  for the height distribution analysis were computed according to the statistical analysis. The initial value of an object index was set to 0. The convexity constraint threshold was set to 0.25 m for the ISPRS datasets because of the sparse point density whereas it was set to 0.03 m for the study region based on experimentation results. As discussed above,  $\theta_h$  was set to 3 cm for the study region. However, it was set to 5 cm for the ISPRS datasets due to the low point density. Because of various point densities and different scenarios in the ISPRS datasets, the values of  $CSize_z$  for the ISPRS datasets were determined based on experimentation. For the Black Mountain datasets, the  $CSize_z$  for moving-window voxel filtering was determined to be 0.25 m. The threshold for the object index was calculated automatically based on Otsu segmentation. Natural neighbour interpolation was adopted to interpolate since it yields a smoother approximation result (Sibson, 1981). The resolution for the DTMs was 1 m.

### 4.3.3 Analysis of the filtering results of the ISPRS benchmark datasets

A common approach to examining the filtering results is to calculate Type I error ( $E_{T_I}$ ), Type II error ( $E_{T_{II}}$ ), and total error ( $E_{T_t}$ ). The mathematical models for these metrics are shown in Eqs (4.12)-(4.14).

$$E_{T_I} = T_{FG}/T_G \quad (4.12)$$

$$E_{T_{II}} = T_{FO}/T_O \quad (4.13)$$

$$E_{T_t} = (T_{FG} + T_{FO})/(T_G + T_O) \quad (4.14)$$

where  $T_{FG}$  is equal to the amount of ground points that are recognised as object points;  $T_G$  indicates the total number of ground points;  $T_{FO}$  denotes the number of object points that are misclassified as ground points; and  $T_O$  denotes the total number of object points.

Cohen's kappa coefficient ( $E_C$ ) (Cohen, 1960) for each sample was also computed to indicate the similarity between the filtering results and the reference data. Cohen's kappa coefficient was chosen since it is more robust than other calculations of percentage agreement. In addition, the filtered results generated by some software applications, namely, Lastools (denoted by LT, Lastools, 2016), MCC, and the simple morphological filter (SMRF) (SMRF, 2016) of Pingel et al. (2013), are also compared with the reference to verify the performance of the proposed algorithm. Because only the reference data for the ISPRS benchmark datasets is available, the point-based analysis was only conducted on the results of first set of datasets. Tables 4.1-4.2 indicate the statistics of  $E_{T_I}$ ,  $E_{T_{II}}$ ,  $E_{T_t}$ , and  $E_C$  for the results obtained with different algorithms, respectively.

Table 4.1 Quantitative analysis of  $E_{T_I}$ , and  $E_{T_{II}}$  for various algorithms

Sample No.	$E_{T_I}$ (%)				$E_{T_{II}}$ (%)			
	<i>VF</i>	<i>LT</i>	<i>MCC</i>	<i>SMRF</i>	<i>VF</i>	<i>LT</i>	<i>MCC</i>	<i>SMRF</i>
11	31.83	40.53	27.63	7.88	3.75	1.20	8.19	8.81
12	11.57	31.27	14.10	2.57	2.14	0.70	8.92	3.30
21	9.25	34.21	5.03	0.26	1.53	1.39	13.15	4.07
22	28.50	33.65	7.71	2.57	6.11	0.86	30.68	5.07
23	17.57	35.25	19.64	3.21	4.18	1.40	17.65	6.17
24	17.30	39.22	10.32	2.25	3.50	1.55	14.67	6.90
31	12.41	25.67	6.36	0.39	3.43	0.29	17.56	1.52
41	32.01	47.63	33.45	3.64	6.02	1.39	12.36	8.17
42	13.06	33.76	14.54	0.27	1.76	1.52	6.80	1.98
51	10.57	14.48	5.74	0.59	6.47	1.05	7.68	4.44
52	21.38	35.60	18.10	3.09	6.14	1.57	13.34	10.08
53	18.44	36.41	16.78	1.18	6.91	0.43	5.18	31.97
54	7.46	24.73	20.46	2.51	3.37	0.56	5.34	2.05
61	7.36	19.21	3.02	0.51	3.73	0.50	2.57	10.70
71	17.05	25.59	3.73	0.99	2.20	1.58	18.64	6.84

Table 4.2 Quantitative analysis of  $E_{T_t}$  and  $E_C$  for various algorithms

Sample No.	$E_{T_t}$ (%)				$E_C$ (%)			
	VF	LT	MCC	SMRF	VF	LT	MCC	SMRF
11	19.84	23.74	19.33	8.28	61.38	57.04	61.90	83.12
12	6.97	16.36	11.57	2.92	86.09	67.51	76.87	94.15
21	7.54	26.93	6.83	1.10	80.33	45.22	80.53	96.77
22	21.52	23.42	14.87	3.35	56.60	54.55	64.01	92.21
23	11.23	19.23	18.70	4.61	77.65	62.15	62.58	90.73
24	13.51	28.87	11.52	3.52	70.02	44.98	72.18	91.13
31	8.27	13.97	11.52	0.91	83.49	72.48	76.64	98.17
41	11.95	24.45	22.88	5.91	85.10	51.05	54.21	88.18
42	5.07	10.96	9.07	1.48	87.44	70.99	78.23	96.48
51	9.67	11.55	6.16	1.43	74.54	71.40	82.75	95.76
52	19.78	32.04	17.60	3.82	40.80	26.93	42.30	81.04
53	17.97	34.96	16.31	2.43	24.37	12.29	27.06	68.12
54	5.26	11.74	12.34	2.27	89.40	75.99	74.93	95.44
61	7.24	18.56	3.00	0.86	44.90	22.31	67.64	87.22
71	15.37	22.88	5.41	1.65	41.57	38.97	74.23	91.81

According to the statistics, SMRF has the smallest  $E_{T_t}$ s for all the samples at the expense of high  $E_{T_{II}}$ s. Meanwhile,  $E_{T_t}$ s and  $E_C$ s for SMRF are also low because the majority of the points in these samples are ground points. This can be validated by the fact that  $E_{T_t}$ s of Samples 21-22 for MCC are smaller than those for VF even though  $E_{T_{II}}$ s for VF in the two samples are much smaller than those for MCC. In contrast,  $E_{T_{II}}$ s for LT are lowest for all datasets despite of their highest  $E_{T_t}$ s. For instance, in Samples 11 and 41, more than 40% of ground points are removed. Consequently,  $E_{T_t}$ s and  $E_C$ s for LT are higher than other algorithms given that more ground points are present in the samples. One exception is Sample 42 where the number of object points outnumbers that of ground points. Hence,  $E_C$  of Sample 42 for LT is relatively small. Because of multiple constraints, our algorithm also achieved low  $E_{T_{II}}$ s ranging from 1.53% to 6.91% at the expense of relatively high  $E_{T_t}$ s. However,  $E_{T_t}$ s and  $E_C$ s for our algorithm are larger than those for MCC and SMRF in most cases because more ground points than object points are present in most samples. Meanwhile, the convexity constraint fails to work in Samples 22, 31, 51 and 54, and  $E_{T_{II}}$ s of these samples for VF are slightly larger than those for SMRF probably because of the

low point density. As for MCC, its performance varies and, while it obtained low  $E_{TII}$ s for some samples, it achieved small  $E_{T_I}$ s for others.

The small  $E_{TII}$ s of all samples for VF validate that our algorithm can identify and remove object points in various scenarios. However, the ISPRS benchmark datasets focus on urban and rural regions and none of these datasets contain dense forests. Moreover, the majority of the points in these datasets are ground points. But in the forest datasets, object points would outnumber ground points. To verify if the algorithm works well in dense forests, the analyses of the results of the Black Mountain datasets are conducted.

#### *4.3.4 Analysis of the filtering results of the Black Mountain Dataset*

Because of the absence of the reference data for the Black Mountain dataset, DTMs from the classified ground points by VF, LT, MCC, SMRF and Terrasolid (denoted by TS, Terrasolid, 2016) were compared with each other, and the similarities between the DTMs were assessed. Figure 4.2 show the DTMs of the study region generated by the aforementioned algorithms. The visual assessment indicates that the majority of DTMs generated by the given algorithms are smooth except that the maximum elevation value of the DTM generated by SMRF in Figure 4.2 (e) is obviously greater than other DTMs, which may suggest that SMRF fails to achieve promising results in this dataset.

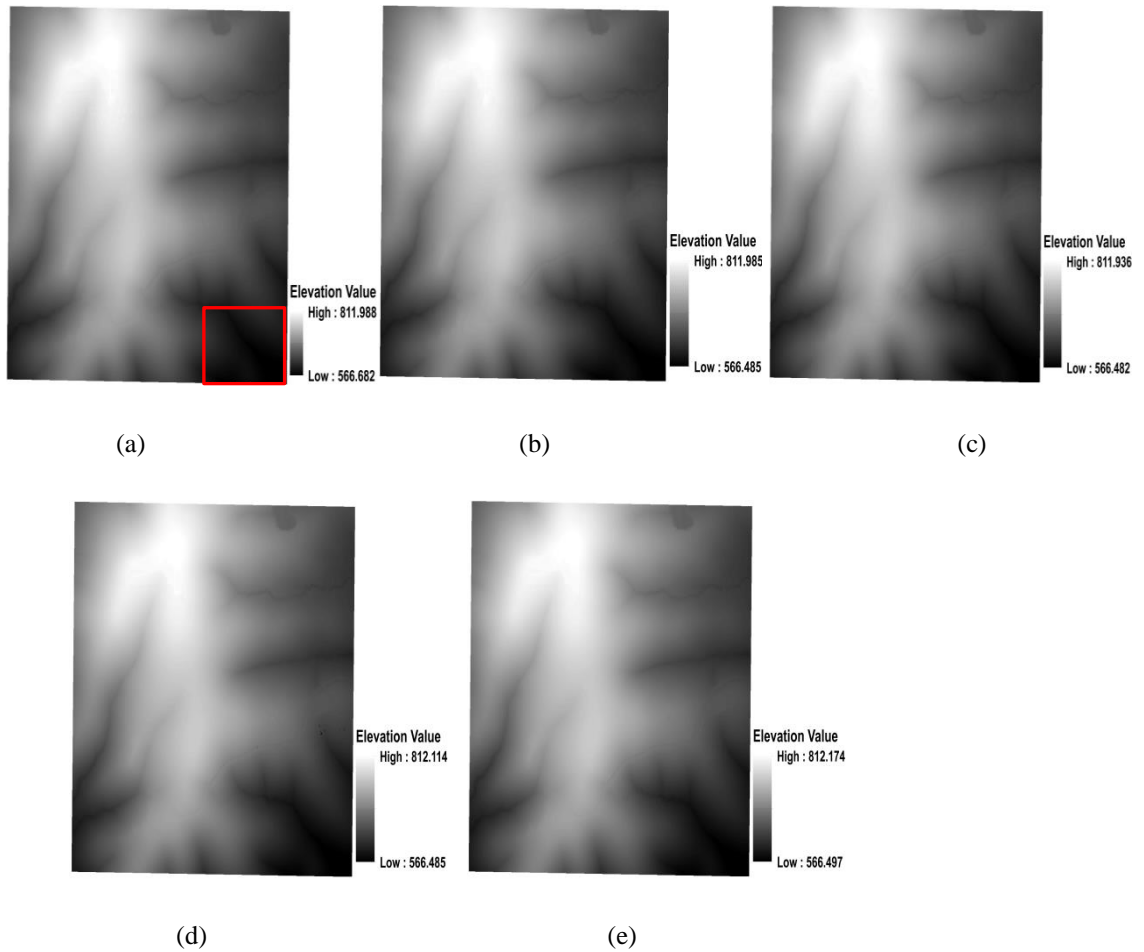


Figure 4.2 Visual assessment of the results: (a)-(e) are the DTMs derived from VF, LT, TS, MCC and SMRF, respectively.

To verify the statement that SMRF overestimates the bare earth, a further investigation of the results is conducted. Figure 4.3 shows the object points in the red rectangle in Figure 4.2 classified by the given algorithms with brown pixels representing ground and black representing objects. As shown in Figure 4.3 (c), compared with other results, TS identifies more points as objects. In contrast, more points are labelled as ground points by SMRF. It means SMRF is likely to overestimate the ground whereas TS tends to underestimate the ground.

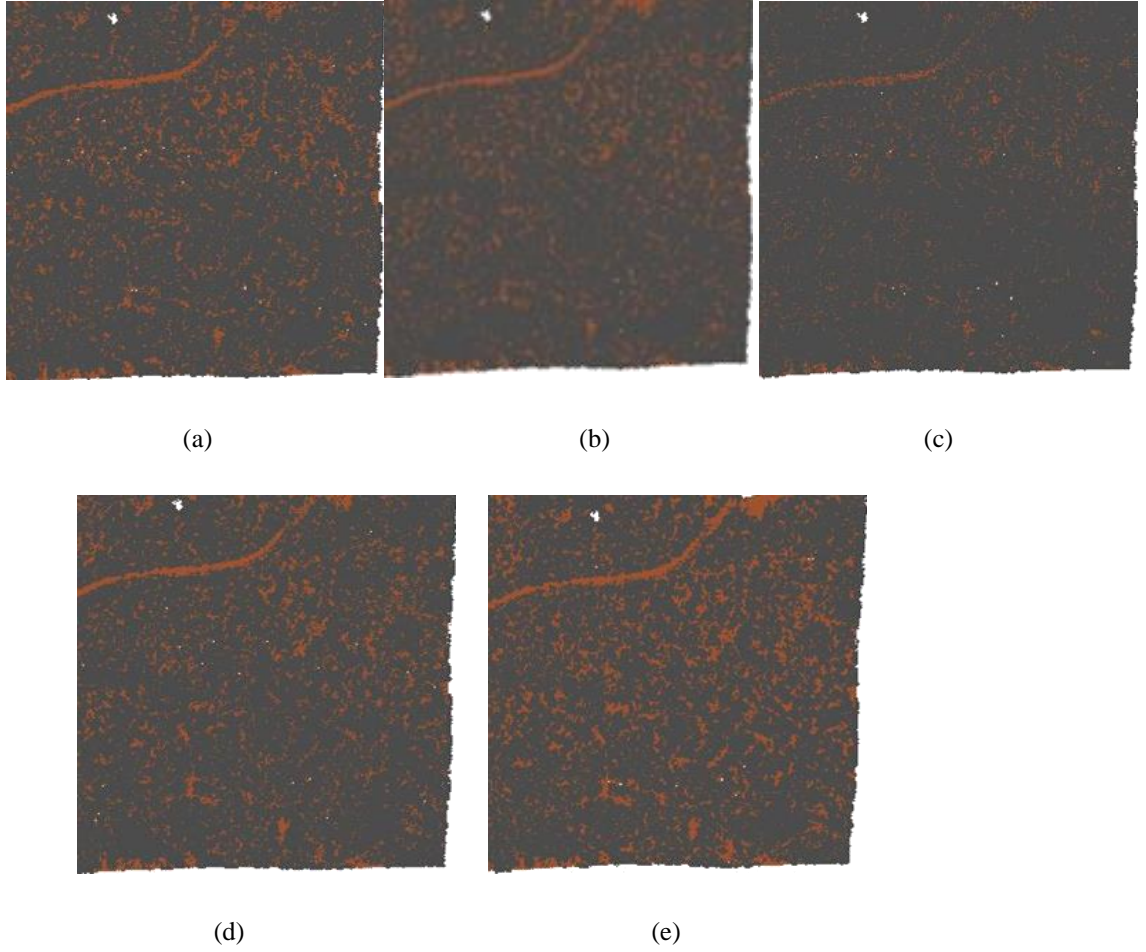


Figure 4.3 Visual assessment of the points-based results of the region in the red rectangle in Figure 4.2 : (a)-(e) are the classified points by VF, LT, TS, MCC and SMRF, respectively. Brown pixels represent ground and black pixels represent objects.

To compare the similarity between the DTMs, the mean difference ( $E_M$ ) and the mean standard deviation ( $E_S$ ) were computed. More specifically, with the DTM derived from one algorithm as the reference, the mean value ( $E_M$ ) and the standard deviation ( $E_S$ ) of the differences between the reference and the DTM generated by other algorithms were calculated, respectively. The mathematical models for  $E_M$  and  $E_S$  are shown in Eqs. (4.15)-(4.16).

$$E_M = \text{Mean}(DEM_T - DEM_R) \quad (4.15)$$

$$E_S = \text{STD}(DEM_T - DEM_R) \quad (4.16)$$

where:  $DEM_T$  and  $DEM_R$  are the test DTM and the reference DTM, respectively; and STD represents the function that returns the standard deviation of the input.

Based on Eqs. (4.15)-(4.16), the results were computed and presented below in Table 4.3. The values in each column indicate that  $E_M$ s and  $E_S$ s are generated using the head of column as the

reference whereas the values in each row represented by  $E_M$ s and  $E_S$ s are generated using the first column in that row as the reference.

Table 4.3  $E_M$  and  $E_S$  analysis result for DTMs generated by various algorithms

	$DEM_{TS}$		$DEM_{VF}$		$DEM_{LT}$		$DEM_{MCC}$		$DEM_{SMRF}$	
	$E_M$ (cm)	$E_S$ (cm)								
$DEM_{TS}$	-	-	4.6	31.4	2.6	17.5	3.0	32.4	5.6	11.3
$DEM_{VF}$	-4.6	31.4	-	-	-2.1	37.6	-1.6	37.6	1.0	30.9
$DEM_{LT}$	-2.6	17.5	2.1	26.2	-	-	0.4	31.5	3.1	17.6
$DEM_{MCC}$	-3.0	32.4	1.6	37.6	-0.4	31.5	-	-	2.7	32.8
$DEM_{SMRF}$	-5.6	11.3	-1.0	30.9	-3.1	17.6	-2.7	32.8	-	-

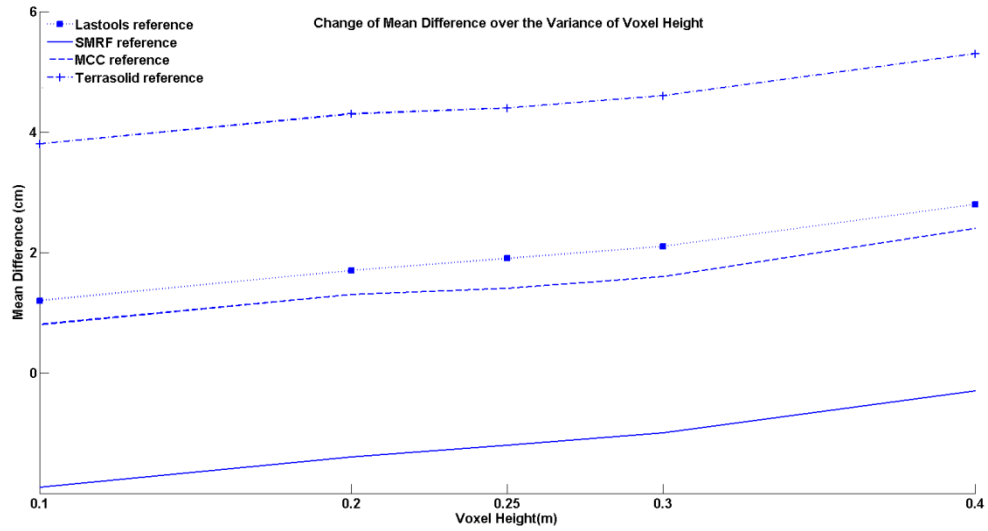
According to Table 4.3, the DTMs generated by VF, MCC, LT and SMRF are similar as the absolute values of  $E_M$ s are less than 2.1 cm, which indicates the performance of our algorithm is comparable to these three algorithms. In particular, the DTM derived from MCC is identical to that of LT since the absolute values of the  $E_M$ s are less than 1 cm. Nonetheless, the DTMs yielded by SMRF are higher than other DTMs, which is validated by the fact that their  $E_M$ s are lower than zero. In contrast, the DTMs created by TS are lower than those by other algorithms since their  $E_M$ s are greater than zero.

#### 4.3.5 Analysis of critical parameters in the algorithm

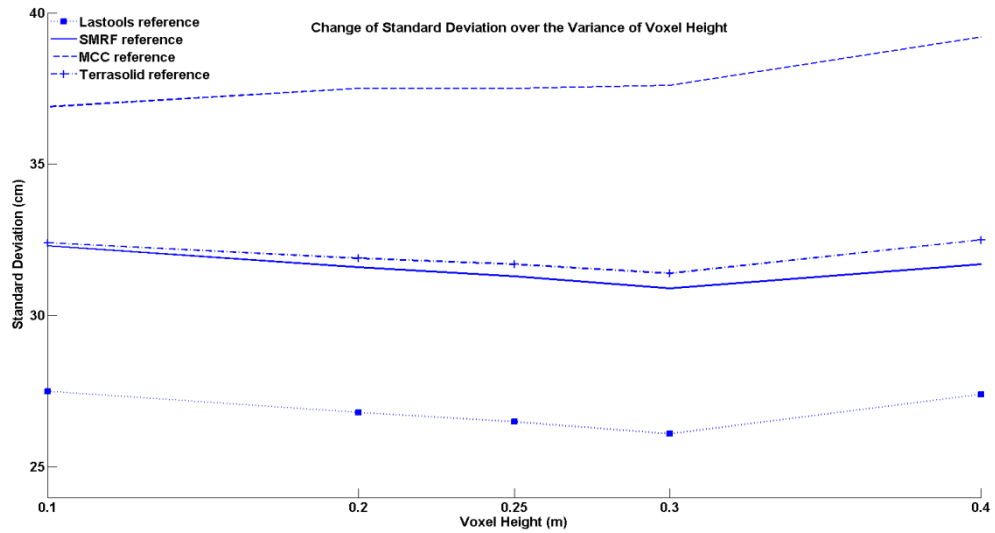
To understand the impacts of some parameters on the accuracy of the final results, several experiments were conducted by tuning the parameters. Since the ISPRS datasets are sparse and out-of-date, only the Black Mountain datasets were employed for these experiments. That is, the results generated by using different parameters are investigated based on DTM-based quantitative assessment, and  $E_M$ s and  $E_S$ s are computed in order to show how the results change over a variety of different values of the parameters.

##### 4.3.5.1 Analysis of the $CSize_z$ for moving-window voxel filtering

The value of  $CSize_z$  for the moving-window voxel filtering is critical since a large value may fail to eliminate object points whereas a small value may remove the ground points with high elevation values. To analyse its impact on the final result, five different parameters were chosen, namely 0.1, 0.2, 0.25, 0.3, and 0.4 whereas other parameters were set to default values.  $E_M$  and  $E_S$  of the proposed algorithm (VF) with respect to various algorithms are shown in Figure 4.4.



(a) Change of  $E_M$  depending on  $CSize_Z$



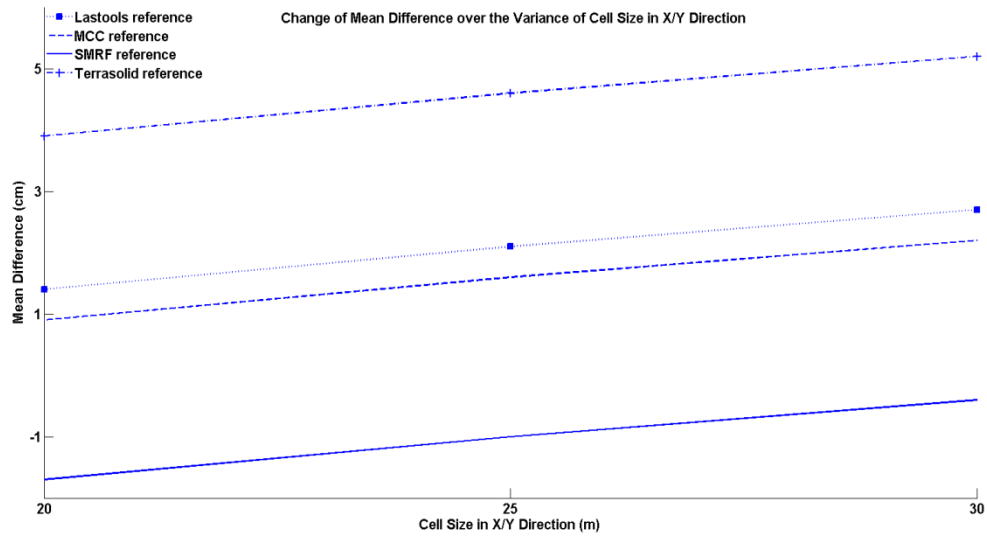
(b) Change of  $E_S$  depending on  $CSize_Z$

Figure 4.4 Quantitative Analysis of  $CSize_Z$

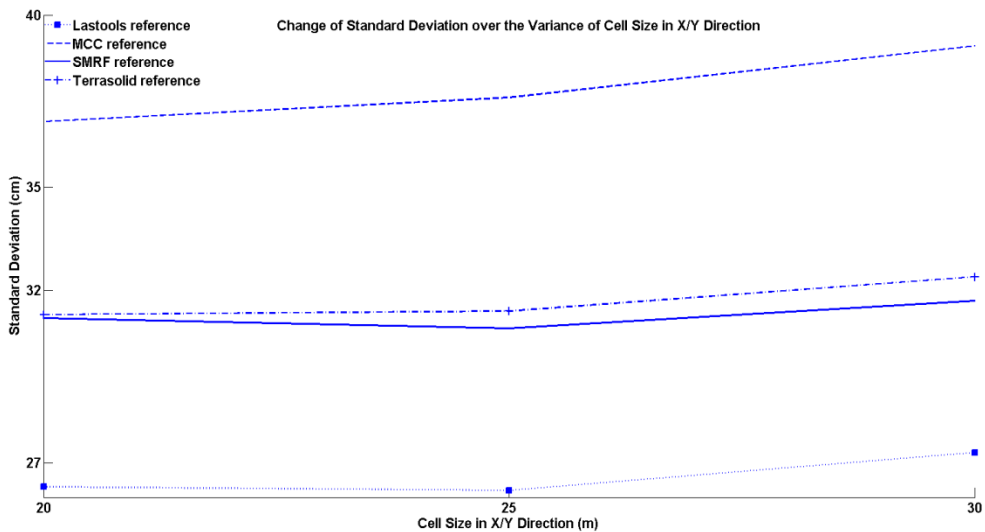
According to Figure 4.4,  $E_M$  increases as  $CSize_Z$  increases. This means that a small  $CSize_Z$  works better than a large  $CSize_Z$ . The differences between the DTMs generated by VF and LT, by VF and TS, or by VF and MCC increase when  $CSize_Z$  continues to increase. However, the differences between the DTMs generated by VF and SMRF become smaller when  $CSize_Z$  increases, and they are most small when  $CSize_Z$  is 0.4 m. The pattern of  $E_S$  is more complex. When  $CSize_Z$  increases, it decreases in the beginning followed by an increase. One exception is that  $E_S$  increases continuously when the MCC DTM is used as the reference.

#### 4.3.5.2 Analysis of the cell size in the x and y direction in Step 5 for moving-window voxel filtering

To avoid highly elevated ground points being removed, a large cell was divided into small regions and the moving-window voxel filtering was applied within small regions. To examine the influence of the cell size in the x and y direction ( $CSize_{x/y}$ ) on the accuracy of the final results, a set of experiments with three different values, namely 20, 25, and 30 m, were conducted while other parameters were set to the same in the Section 4.2. The results are investigated and illustrated in Figure 4.5.



(a) Change of  $E_M$  depending on  $CSize_{x/y}$



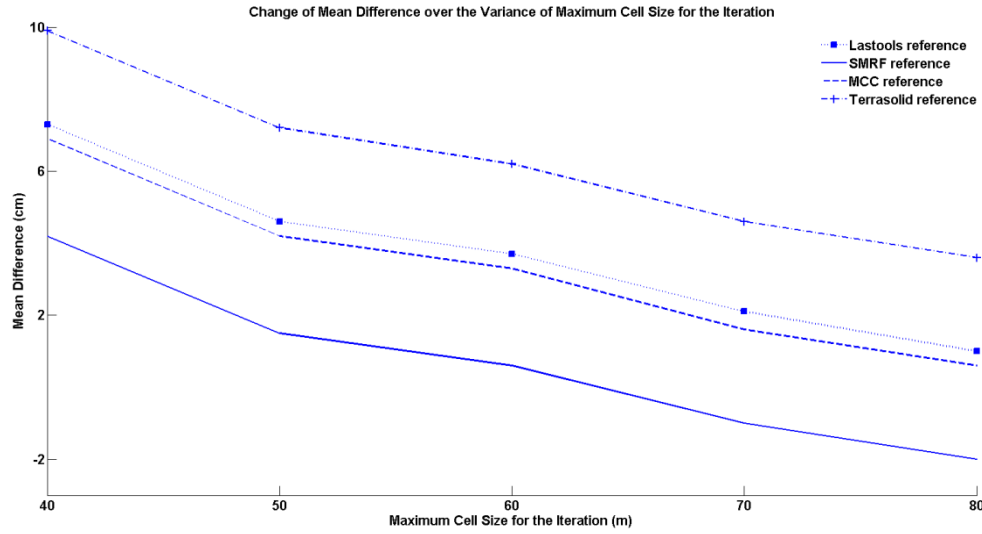
(b) Change of  $E_S$  depending on  $CSize_{x/y}$

Figure 4.5 Quantitative Analysis of  $CSize_{x/y}$

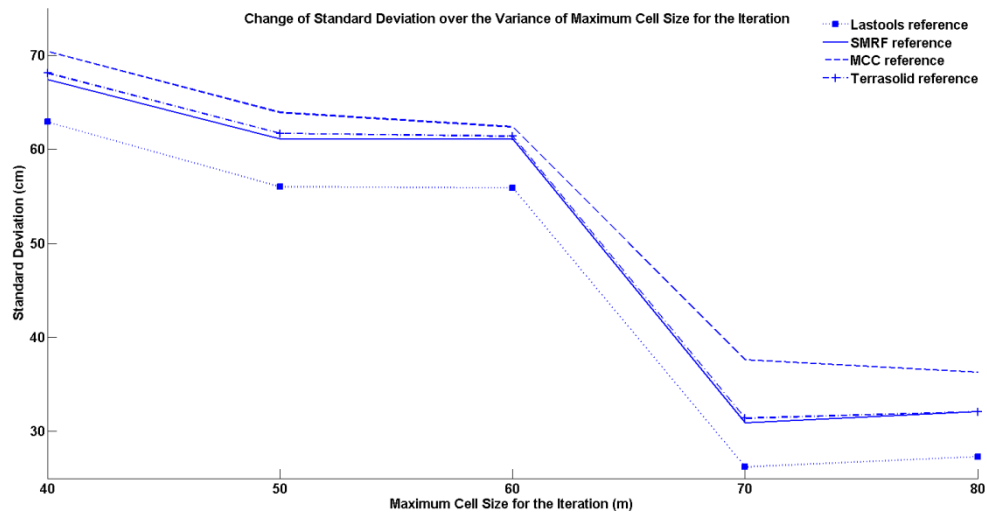
The examination of Figure 4.5 indicates that  $E_M$  increases as  $CSize_{x/y}$  increases. However,  $E_S$  generally decreases first and then increases when  $CSize_{x/y}$  continues to increase. The only exception is when DTM generated by MCC is used as the reference where  $E_S$  increases continuously. The combination of Figures 4.5(a)-(b) indicates that the DTM generated by VF is rather similar to the DTM created by SMRF when  $CSize_{x/y}$  equals 30 m because the corresponding absolute values of  $E_M$  and  $E_S$  are smaller compared with those when  $CSize_{x/y}$  is 20 m or 30 m. In contrast, the differences between the DTMs derived from VF and LT, VF and TS, VF and MCC are the smallest when  $CSize_{x/y}$  is 20 m.

#### 4.3.5.3 Analysis of the maximum cell size for the iteration

To examine the effect of the maximum cell size on the final filtering results, the maximum cell size ( $CSize_{max}$ ) was set to 40, 50, 60, 70, and 80 m for the respective experiments. These final results with different  $CSize_{max}$  while other parameters being the same values in Section 3.2 were statistically analysed in terms of  $E_M$  and  $E_S$ . The analysis results for the corresponding parameters are shown in Figure 4.6.



(a) Change of  $E_M$  depending on  $CSize_{max}$



(b) Change of  $E_S$  depending on  $CSize_{max}$

Figure 4.6 Quantitative Analysis of  $CSize_{max}$

According to Figure 4.6, the increase of  $CSize_{max}$  leads to the steady decline of  $E_M$  and a huge decrease of  $E_S$  followed by a slight increase when  $CSize_{max}$  continues to increase. The smallest differences between the VF DTM and the TS DTM are demonstrated when  $CSize_{max}$  is 80 m. Conversely, the DTM generated by VF is most similar to those generated by SMRF when  $CSize_{max}$  equals 70 m. For the DTMs derived from LT and MCC, they are more similar to VF DTMs when  $CSize_{max}$  is 80 m, with  $E_M$ s being 1.0 cm and 0.6 cm, respectively.

Throughout the analyses in Sections 4.3.5.1-4.3.5.3, DEMs acquired by VF are found to be more similar to those generated by TS when more restrictions are applied whereas they are more

identical to those created by SMRF when fewer restrictions are applied. Considering that SMRF yields higher commission errors than the proposed algorithm in the ISPRS datasets, SMRF tends to overestimate the elevation of bare earth in dense forests as shown in Section 4.3. On the other hand, TS seems to suffer from the underestimation of ground (see Section 4.3) because applying more restrictions means more removal of ground points.

#### 4.4 Summary

In this chapter, a lidar data filtering algorithm that explores the features of object points at various spatial scales was proposed. For each spatial scale, object points are detected by investigating height distribution, convexity constraints, and the elevation difference between objects and ground. Instead of removing object points in each iteration, an object index for each point was introduced to avoid the elimination of misclassified ground points. When a point is identified as an object point, the corresponding object index will increase by the sum of one and the difference between the number of returns and the return number, since a point may contribute less to the ground surface if the associated number of returns and the return number are highly deviated. Once the iteration is complete, the Otsu segmentation is applied to select the threshold for the object index, and points with object indices higher than the threshold are treated as objects.

The point-based quantitative analyses of the results for the ISPRS benchmark datasets demonstrate that the proposed algorithm manages to achieve low commission errors in different scenarios ranging from 1.53% to 6.91%. To verify if the algorithm works well in dense forests, it is compared with other commercially available lidar filtering algorithms, such as Terrasolid, Lastools, MCC and SMRF in terms of the mean difference and mean standard deviation between the DTMs. The results indicate that the performance of the proposed algorithm is comparable with that of SMRF as the mean difference between the two is 0.1 cm. The proposed algorithm requires a high density of points since the convexity constraint may not work well with a low point density. The selection of parameters is also critical. For instance, the cell size in the z direction to locate the points in various voxels influences the accuracy of the results, since a small cell size tends to delete highly elevated ground points whereas a large cell size in the z direction will overestimate the bare earth.

Once the ground points and object points are identified, the classified ground points are interpolated to a 1-m spatial resolution DTM. Since there are no buildings in the study region, the object points are regarded as vegetation points without further identification. From the classified vegetation points, the points of the maximum height within each  $1\text{ m} \times 1\text{ m}$  grid cell are selected and rasterised to create a 1-m spatial resolution DSM. Consequently, a 1-m resolution CHM

(denoted by  $CHM_1$ ) is generated by subtracting the 1-m DTM from the 1-m DSM pixel by pixel. However, there are pixels in the CHM demonstrating abnormally lower elevation values than the surroundings because of the penetration of lidar pulses into the tree canopies, which is known as pits. Since an accurate CHM is essential for individual tree segmentation and modelling, it is essential to identify these pits and replace them with correct values. Hence, in Chapter 5, a multiscale morphological algorithm to improve the accuracy of the CHM will be presented.

## **Chapter 5 : A Multiscale Morphological Algorithm for Improvements to Canopy Height Models**

CHMs represent the differences between canopy surface models and the corresponding underlying ground surface models (Zhao and Popescu, 2007). A CHM can be useful for the estimation of forest structure parameters (e.g. canopy density and canopy cover) and the extraction of individual tree parameters. As such, great attention has been drawn for segmenting CHMs to identify individual trees (Popescu et al., 2002), and mapping canopy gaps (Gaulton and Malthus, 2010) from CHM-based products. However, as a raster image, a CHM has multiple inherent errors and uncertainties (Li et al., 2012). One of these errors is the pits demonstrating abnormal lower elevation values than the surroundings. To replace the pits with correct values and improve the accuracy of the CHM, a multiscale morphological algorithm is proposed in this chapter. A multiscale Laplacian operator, a multiscale morphological closing operator and a multiscale median filtering operator are applied to detect and replace pits. The chapter is structured as follows: Section 5.1 analyses the errors and uncertainties associated with the CHM and reviews the existing algorithms to improve the accuracy of the CHM; Section 5.2 describes the methodology comprehensively. In Section 5.3, the performance of the proposed algorithm is investigated by applying it to the study region, the accuracies of the CHM of the study region before and after the improvement are compared and the impact of different parameters on the accuracy of the final results is analysed with a summary of this chapter in Section 5.4.

### **5.1 Improving the accuracy of CHM**

As stated above, a CHM is associated with different inherent errors and uncertainties. Firstly, the accuracy of a CHM is largely dependent on the accuracy of the digital surface model (DSM) and the corresponding digital terrain model (DTM). The first return of a lidar pulse is generally assumed to be coming from the top of the canopy whereas the last return is expected to be from the ground. However, these assumptions are not always valid in practice, and therefore tree heights derived from a CHM can be often lower than the ground truth (Chasmer et al., 2006) or be overestimated, given a large terrain slope (Alexander et al., 2018). This inaccuracy affects the estimation of biomass and fuel loads (Hudak et al., 2012). Secondly, the interpolation process applied to a DTM is prone to errors that will be propagated to the CHM during the generation process when subtracting a DSM by the corresponding DTM. Thirdly, there are pixel values demonstrating abnormally lower values than the surroundings in a CHM. These abnormal values typically represent pits. Pixels representing pits, i.e. pit pixels will create “holes” if not properly processed. Because of their presence, tree parameters derived from a CHM can deviate from the

true values. Accurate CHMs are of great significance for individual tree extraction and modelling (Jing et al., 2012; Hu et al., 2014). Hence it is essential to improve CHMs before further applications. An effective way to improve the accuracy of a CHM would be assigning reasonable values to pit pixels.

Axelsson (1999) claimed that multiple elevation values with similar spatial coordinates in an x/y direction in lidar data might cause pits. Persson et al. (2002) suggested that pits in a tree crown may be derived from the penetration of lidar pulses through the tree. Gaveau and Hill (2003) confirmed that the penetration into the upper canopy causes pits. The interpolation of lidar points when creating CHMs would propagate these errors. Leckie et al. (2003) stated that combing data from different flight lines could also be a cause of pits. Therefore, Leckie et al. (2003) assigned all lidar returns into 25-cm grid cells and used only the highest value from each cell to generate a surface model. Although this approach removed multiple ground returns within the canopy, the authors acknowledged that some remaining ground returns caused artefacts in the surface model. Also, when the point density was low, some grids were void because of no returns. Chen et al. (2006) recommended a large grid cell size to minimise the impact of pits in crowns. However, multiple tree crowns can be represented by a single cell if a too large cell size is used. Some studies took advantage of image smoothing methods (i.e. mean, median, Gaussian filters) to replace pits and smooth CHMs (Hosoi et al., 2012). However, smoothing a CHM without prior detection of pits can lead to the omission of treetops, hence degrading the accuracy of tree heights. Ben-Aire et al. (2009) proposed a statistical approach to manage pits. A Laplacian operator (LO) was applied to a CHM, and a self-defined threshold was then employed to identify the pits from the Laplacian-filtered image. Once the pits were recognised, a median filtering operator (MFO) was applied to replace these pits. However, the threshold was defined based on visual assessment, and is therefore prone to errors. Zhao and Popescu (2007) utilised Gaussian and wavelet filters to smooth the original CHMs and replace the pits. Although wavelet filters tend to preserve local features such as treetops, they could not replace the pits effectively because some relatively large pits were still present after the wavelet filter. Meanwhile, a Gaussian filter may blur the image despite its ability to replace the pits. Zhao et al. (2013) extended the method of Ben-Aire et al. (2009) by introducing a canopy control algorithm. A morphological closing operator (MCO) was applied to the original CHM to identify the canopy regions based on the assumption that a tree crown forms a circle in a vertical view. If a circle is identified and the associated height is above the threshold, it is regarded as a canopy region. The potential pits detected by a LO were treated as pits if they are located in the canopy regions and then smoothed by an MFO. Although Zhao et al. (2013) modified the algorithm of Ben-Aire et al. (2009), their fixed-window operators (i.e. LO, MCO and MFO) cannot manage canopies with different sizes, especially when tree species

vary. Shamsoddini et al. (2013) proposed an adaptive mean filter approach to replace pits. A similar index is introduced to detect pits within a  $3 \times 3$  window. Once a pit is identified, a mean filter with a preset window size is used to replace it. However, it is difficult to determine the optimal window size. Khosravipour et al. (2014) assumed that pits appear when lidar pulses penetrate a tree crown, hence the authors generated partial CHMs using subsets of lidar points and created a pit-free CHM by stacking the partial CHMs based on height values. However, the generation of partial CHMs may also introduce pits during the interpolation process.

To overcome the abovementioned problems, in this chapter, a novel multiscale CHM improvement algorithm is proposed on the basis of three assumptions: 1) pits are mainly present in the canopy regions; 2) trees in the study area vary in size and species; and 3) the canopy shape of a tree from the top view is a circle. Different from Zhao et al. (2013), multiscale operators are proposed in each step to deal with various canopy conditions. The results yielded by the multiscale operators in each step are also fused to minimise the impact of possible inappropriate selection of window sizes on the final results. The influence of various parameters on the accuracy of the final result is analysed extensively. Field measurements (i.e. tree heights and tree coordinates) are used to assess the accuracies of the CHMs before and after the improvement, to validate the effectiveness of the proposed algorithm quantitatively, and to demonstrate whether the improved CHM increases the estimation accuracy of individual tree heights when applied to a single tree extraction algorithm.

## **5.2 Methodology**

Pits show abnormally lower heights than their surroundings, which can be exploited to differentiate them from tree pixels. However, valid canopy gaps showing low elevation values due to the loss or removal of trees are also present in the forest. Unlike valid canopy gaps which have a minimum area and a minimum height of gap closure (Gaulton and Malthus, 2010), pits are irregularly shaped, discrete and distributed mainly on canopy surfaces. Therefore our strategy is to identify potential pits which may include not only pits but also canopy gaps if the pixel value is distinctively lower than the neighbourhood in a local region, and then to distinguish pits from canopy gaps. As pits are irregularly shaped and isolated, these properties are useful to differentiate pits from the detected potential pits. The recognised pits will be replaced with reasonable values. The core steps of this method are illustrated in Figure 5.1 and explained comprehensively in the following sections.

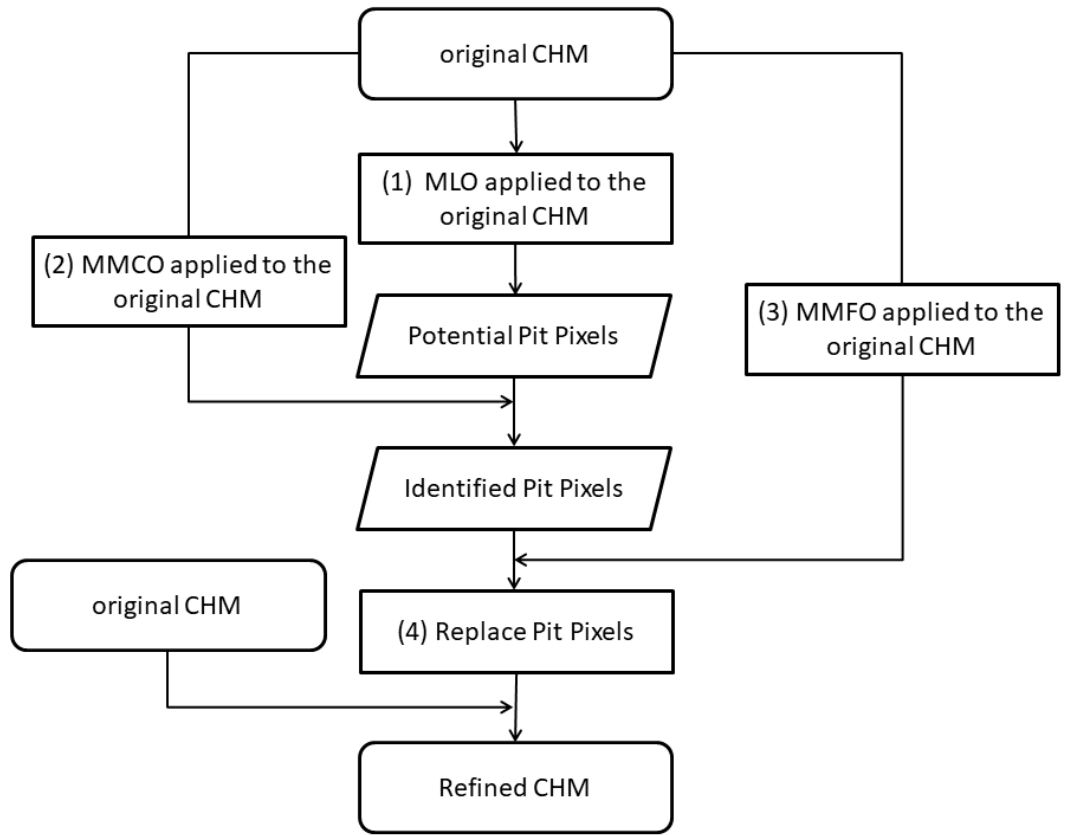


Figure 5.1 Detailed flow chart of each step of the proposed algorithm (the number denotes the order of steps in the algorithm), MLO means multiscale Laplacian operator, MMCO means multiscale morphological closing operator and MMFO means multiscale median filtering operator.

### 5.2.1 A multiscale Laplacian operator

LOs are widely used in edge detection (Santhi et al., 2016), however; it is difficult to determine the optimal window size of a LO because a large window size may falsely detect normal values as pits, whereas a small window size may fail to detect some pits. Although applying a particular LO iteratively can alleviate this problem if a small window size is used, the number of repetitions will affect the final results because a large number of repetitions may falsely detect pits. Taking these factors into account, a multiscale Laplacian operator (MLO) is introduced by applying LOs with various window sizes to a  $CHM_1$  and fusing the individual LO-filtered images. A large window LO (e.g., a  $7 \times 7$  LO) is likely to misclassify normal values, which can lead to over-smoothness, hence  $3 \times 3$  and  $5 \times 5$  LOs (denoted by  $LO_3$  and  $LO_5$ , respectively) are selected in this study as illustrated in Figure 5.2. Some pits may be omitted in the  $LO_3$ -filtered image if  $LO_3$  is small for  $CHM_1$ , whereas the  $LO_5$ -filtered image may misclassify normal values, and therefore the two LO-filtered images are fused to achieve a balance between the omission of potential pit pixels (in case  $LO_3$  is too small for  $CHM_1$ ) and the misclassification of normal values (in case  $LO_5$  is too small for  $CHM_1$ ). The fusion of the Laplacian-filtered images is carried out

using Eq. (5.1). That is, for each grid cell in the fused image, its cell value is calculated by the weighted sum of the corresponding cell values in the two LO-filtered images.

$$I_{MLO} = w_{LO_3} \times I_{LO_3} + (1 - w_{LO_3}) \times I_{LO_5} \quad (5.1)$$

where  $I_{MLO}$  denotes the fused Laplacian-filtered image;  $I_{LO_3}$  denotes the Laplacian-filtered image yielded by  $LO_3$ ;  $I_{LO_5}$  denotes the Laplacian-filtered image yielded by  $LO_5$ ;  $w_{LO_3}$  denotes the weight of  $I_{LO_3}$  in the fusion process.

-1	-1	-1
-1	+8	-1
-1	-1	-1

-1	-1	-1	-1	-1
-1	-1	-1	-1	-1
-1	-1	+24	-1	-1
-1	-1	-1	-1	-1
-1	-1	-1	-1	-1

(a)  $LO_3$

(b)  $LO_5$

Figure 5.2 Laplacian operators of different window sizes

However, the choice of  $w_{LO_3}$  should be carefully considered since a large  $w_{LO_3}$  may fail to detect some potential pits whereas a small  $w_{LO_3}$  can misclassify normal values. To obtain the optimal results, a series of values in the range of 0 and 1 are tested. Based on the experimental results,  $w_{LO_3}$  is set to 2/3. The main principle of selecting the weight in Eq. (5.1) is that, if the canopies are generally large,  $w_{LO_3}$  should be set to a large value; and if the canopies are small,  $w_{LO_3}$  should be given to a small value. Since crown boundaries will also be detected when the MLO filtering is applied, a threshold (denoted by  $T_{MLO}$ ) is introduced to distinguish potential pits from crown boundaries. If the value of a pixel is below the threshold, it is regarded as a potential pit pixel. Since the proposed algorithm is based on the assumption that pits are present in the canopy regions, the height difference that separates a tree canopy and the ground should be carefully considered. A small value of the height difference will lead to the misclassification of normal values as potential pits whereas a large value will lead to the omission of some pits. Considering the given tree species, the height difference is considered to be 3 m. Now the threshold of  $LO_5$  (denoted by  $T_{LO_5}$ ) is calculated as  $-72$  m using Eq. (5.2). Similarly, the threshold of  $LO_3$  (denoted by  $T_{LO_3}$ ) is calculated as  $-24$  m.

$$T_{LO_5} = \sum_{i=0}^4 \sum_{j=0}^4 C_{5_{i,j}} LO_{5_{i,j}} = -72 m$$

$$C_5 = \begin{bmatrix} 3 & 3 & 3 & 3 & 3 \\ 3 & 3 & 3 & 3 & 3 \\ 3 & 3 & 0 & 3 & 3 \\ 3 & 3 & 3 & 3 & 3 \\ 3 & 3 & 3 & 3 & 3 \end{bmatrix}, \quad LO_5 = \begin{bmatrix} -1 & -1 & -1 & -1 & -1 \\ -1 & -1 & -1 & -1 & -1 \\ -1 & -1 & 24 & -1 & -1 \\ -1 & -1 & -1 & -1 & -1 \\ -1 & -1 & -1 & -1 & -1 \end{bmatrix} \quad (5.2)$$

where  $C_5$  is a  $5 \times 5$  weight matrix for the candidate pit pixel's neighbors,  $C_{5_{i,j}}$  and  $LO_{5_{i,j}}$  indicate the elements of the corresponding matrices in the  $i$ -th row and  $j$ -th column, respectively. And the threshold for the MLO (i.e.  $T_{MLO}$ ) is computed using Eq. (5.3).

$$T_{MLO} = w_{LO_3} \times T_{LO_3} + (1 - w_{LO_3}) \times T_{LO_5} \quad (5.3)$$

### 5.2.2 A multiscale morphological closing operator

Since the MLO detects not only pits but also valid canopy gaps, it is better to separate the canopy gaps from the detected potential pits. In contrast to the canopy gaps that are mostly located near or on the edge of canopies, pits are often placed within the canopy regions. We propose a multiscale morphological closing operator (MMCO) that makes use of this property. The main concept of the MMCO is to identify various sizes of canopy regions with adaptive MCOs while minimizing the influence of the improper choice of the size of each MCO by fusing the results. Instead of applying various window-size MCOs to a particular CHM, various window-size MCOs are applied to various CHMs with different cell sizes to improve the detection of canopies with different sizes meanwhile minimizing the misidentification. For instance, if both a  $3 \times 3$  window MCO ( $MCO_3$ ) and a  $5 \times 5$  window MCO ( $MCO_5$ ) are applied to  $CHM_1$  to recognise the canopy regions, the maximum width of the identified canopy will be 5 m. On the other hand, if  $MCO_3$  is applied to a 2-m resolution CHM ( $CHM_2$ ) and  $MCO_5$  is applied to  $CHM_1$ , the maximum width of the identified canopy will be 6 m. Although larger canopies in  $CHM_1$  can be identified with a larger MCO (e.g., a  $7 \times 7$  window MCO denoted by  $MCO_7$ ), it increases misclassification of non-canopy regions as canopies. In addition, a CHM with a large cell size can eliminate the presence of pits. Taking these factors into consideration, different MCOs are applied to various CHMs with different spatial resolutions. Although a CHM with a large cell size can limit the presence of pits in the CHM, it can blur the crown boundaries and merge multiple crowns into one pixel if the canopies are small. Hence, the maximum cell size is set to 2 m. However, the accuracy of the fused morphologically filtered image will degrade because of the introduction of a CHM with a large cell size. Hence, a CHM with a small cell size is also included to enhance the accuracy of the fused morphologically-filtered image. In general, a CHM with a small cell size increases the number of pits. To keep the balance between the accuracy and the presence of pits, the minimum cell size is set to 50 cm. Because of these reasons,  $CHM_1$ ,  $CHM_2$  and a 50-cm resolution CHM

(denoted by  $CHM_{0.5}$ ) were used in the MMCO filtering process. The main steps of MMCO are described as follows. Firstly,  $MCO_3$  is applied to  $CHM_2$ ,  $MCO_5$  is applied to  $CHM_1$  and  $MCO_7$  is applied to  $CHM_{0.5}$ .  $MCO_3$ ,  $MCO_5$ , and  $MCO_7$  are illustrated in Figure 5.3. These MCOs are used because of the assumption that the canopy of a tree is a circle shape from the top view. If  $MCO_3$  is applied to  $CHM_1$ , it may fail to identify pits clustered in a large area, therefore  $MCO_3$  is applied to  $CHM_2$ . On the other hand, if  $MCO_7$  is applied to  $CHM_1$ , it may misclassify normal values isolated in a small region, therefore  $MCO_7$  is applied to  $CHM_{0.5}$ . The images generated by  $MCO_3$ ,  $MCO_5$ , and  $MCO_7$  are denoted as  $I_{MCO_3}$ ,  $I_{MCO_5}$  and  $I_{MCO_7}$ , respectively. Secondly, once the morphologically-closing filtering is done,  $I_{MCO_3}$  and  $I_{MCO_7}$  are resampled into 1-m resolution images by bilinear resampling and the resulting images are denoted as  $I_{MCO_{R3}}$  and  $I_{MCO_{R7}}$ , respectively. Bilinear resampling is chosen because it utilises the neighborhood information. Thirdly,  $I_{MCO_{R3}}$ ,  $I_{MCO_5}$  and  $I_{MCO_{R7}}$  are fused based on Eq. (5.4) to balance the trade-off between the omission of pits in a large region (in case the selected MCO is small) and misclassification of normal values in a small region (in case the selected MCO is large). That is, the cell value of the fused morphologically-filtered image is the weighted sum of the corresponding cell values in  $I_{MCO_{R3}}$ ,  $I_{MCO_5}$ , and  $I_{MCO_{R7}}$ .

$$I_{MMCO} = w_{MCO_3} \times I_{MCO_{R3}} + (1 - w_{MCO_{R3}} - w_{MCO_{R7}}) \times I_{MCO_5} + w_{MCO_7} \times I_{MCO_{R7}} \quad (5.4)$$

where  $I_{MMCO}$  is the fused morphologically-filtered image,  $w_{MCO_3}$  and  $w_{MCO_7}$  denote the weights of  $I_{MCO_3}$  and  $I_{MCO_7}$ , respectively.

0	1	0	0	1	1	1	0	0	1	1	1	1	1	0	
			1	1	1	1	1	1	1	1	1	1	1	1	
			1	1	1	1	1	1	1	1	1	1	1	1	1
			1	1	1	1	1	1	1	1	1	1	1	1	1
			1	1	1	1	1	1	1	1	1	1	1	1	1
0	1	0	0	1	1	1	0	0	1	1	1	1	1	0	
			1	1	1	1	1	1	1	1	1	1	1	1	
			0	1	1	1	0	0	1	1	1	1	1	0	

(a)  $MCO_3$

(b)  $MCO_5$

(c)  $MCO_7$

Figure 5.3 Various window morphological closing operators

If  $w_{MCO_3}$  is large and  $w_{MCO_7}$  is small,  $I_{MMCO}$  may misclassify normal values covering a small region. If  $w_{MCO_3}$  is small and  $w_{MCO_7}$  is large,  $I_{MMCO}$  may fail to identify pits covering a large area. A base CHM is defined as the CHM whose spatial resolution is most frequently used in the improvement algorithm. In this paper,  $CHM_1$  is treated as the base CHM so that all weights for

Eq. (5.4) are chosen to make sure the weight for  $I_{\text{MCO}_5}$  is not smaller than other weights. One can notice that, if the canopies are large,  $w_{\text{MCO}_3}$  can be large since  $\text{CHM}_2$  is used to capture large canopies. If the canopies are small,  $w_{\text{MCO}_7}$  can be set to a large value because  $\text{CHM}_{0.5}$  is used to enhance the accuracy of  $I_{\text{MMCO}}$ . Taking these factors and the vegetation species into account, various values between 0 and 1 for  $w_{\text{MCO}_3}$  and  $w_{\text{MCO}_7}$  are analysed. Based on experimentation,  $w_{\text{MCO}_3}$  and  $w_{\text{MCO}_7}$  are set to 1/3 and 1/6, respectively. To identify the canopy regions after the MMCO filtering is applied, the threshold for  $I_{\text{MMCO}}$  (denoted by  $T_{\text{MMCO}}$ ) is introduced. For each pixel in the fused CHM generated by the MMCO filtering, it is regarded as a canopy region if the value of the cell is above  $T_{\text{MMCO}}$ . The selection of the threshold has an influence on the accuracy of the detected canopy regions because a small  $T_{\text{MMCO}}$  detects under-canopy regions whereas a large  $T_{\text{MMCO}}$  can fail to detect some possible canopy regions. Zhao et al. (2013) stated that  $T_{\text{MMCO}}$  is related to the height of the first branch and selected 10 m as an optimal threshold. In this study, however, an empirical value of 5 m is chosen based on the field measurements.

### 5.2.3 A multiscale median filtering operator

Once the pits are identified, they should be replaced with some meaningful values. As mentioned above, mean filters and Gaussian filters will blur the image whereas a fixed-window median filter cannot replace various size pits with meaningful values at the same time. To overcome this problem, a multiscale median filtering operator (MMFO) is proposed. The basic theory of the MMFO is to smooth CHMs in various spatial resolutions by applying variable window-size MFOs and then fusing the filtered images. Variable window-size MFOs were applied to various CHMs in different spatial resolutions to deal with pits in various sizes. Compared to applying variable window-size MFOs to a CHM with a particular spatial resolution, MMFO can remove pits in various sizes meanwhile minimising the filling of canopy gaps. For example, if both a  $3 \times 3$  window MFO ( $\text{MFO}_3$ ) and a  $5 \times 5$  window MFO ( $\text{MFO}_5$ ) are applied to  $\text{CHM}_1$ , the maximum size of pits that can be replaced is 5 m. However, when  $\text{MFO}_3$  is applied to  $\text{CHM}_2$  and  $\text{MFO}_5$  is applied to  $\text{CHM}_1$ , a 6-m pit can be replaced. As the introduction of a CHM with a large cell size will degrade the accuracy of the fused median-filtered image, a CHM with a small cell size is included to enhance the accuracy of the fused image. The maximum and minimum cell sizes of the CHM used in MMFO should be carefully chosen because a large cell size can limit the number of pit pixels and it can also blur the crown boundaries. On the other hand, a CHM with a smaller cell size can have too many pit pixels. Taking these factors as well as the tree species into account,  $\text{CHM}_{0.5}$ ,  $\text{CHM}_1$  and  $\text{CHM}_2$  are used in MMFO. Firstly,  $\text{MFO}_3$  is used to smooth  $\text{CHM}_2$ ,  $\text{MFO}_5$  is applied to  $\text{CHM}_1$  and  $\text{MFO}_7$  is applied to  $\text{CHM}_{0.5}$ . In comparison with  $\text{MFO}_5$ ,  $\text{MFO}_3$  may fail to smooth isolated pit pixels that cover a large area while  $\text{MFO}_7$  may

oversmooth non-isolated pit pixels that cover a small region if applied to  $CHM_1$ . Hence applying  $MFO_3$  to  $CHM_2$  aims to minimise undersmoothness of the isolated pit pixels, and applying  $MFO_7$  to  $CHM_{0.5}$  aims to minimise the oversmoothness of non-isolated pit pixels. The results are denoted as  $I_{MFO_3}$ ,  $I_{MFO_5}$  and  $I_{MFO_7}$ , respectively. Secondly,  $I_{MFO_3}$  and  $I_{MFO_7}$  are resampled into 1-m resolution images via bilinear resampling and are denoted by  $I_{MFO_{R3}}$  and  $I_{MFO_{R7}}$ , respectively. Thirdly,  $I_{MFO_{R3}}$ ,  $I_{MFO_5}$ , and  $I_{MFO_{R7}}$  are fused by computing the weighted sum of the cell values according to Eq. (5.5) because the median-filtered images may suffer from oversmoothness of non-isolated pixels covering a small region given a large MFO or undersmoothness of isolated pixel clusters covering a large region given a small MFO. Because  $CHM_1$  is selected as the base CHM in this paper, the introduction of  $CHM_2$  in MMFO is to replace large pits whereas the introduction of  $CHM_{0.5}$  is to enhance the accuracy of the fused result. The main principle of choosing the weights in Eq. (5.5) is to ensure that the weight for  $I_{MFO_5}$  is not smaller than other weights. In addition, if the canopy width is large,  $w_{MFO_3}$  can be large so that large pits can be replaced. If the canopy width is small,  $w_{MFO_3}$  should be set to a small value in case of blurring the canopy boundaries in the fused median-filtered image. Considering these factors and the tree species,  $w_{MFO_3}$  and  $w_{MFO_7}$  in the range of 0 and 1 are examined. Based on experimentation, the optimal choices of  $w_{MFO_3}$  and  $w_{MFO_7}$  are 1/4 and 1/4, respectively.

$$I_{MMFO} = w_{MFO_3} \times I_{MFO_{R3}} + (1 - w_{MFO_3} - w_{MFO_7}) \times I_{MFO_5} + w_{MFO_7} \times I_{MFO_{R7}} \quad (5.5)$$

where  $I_{MMFO}$  is the fused median-filtered image,  $w_{MFO_3}$  and  $w_{MFO_7}$  denote the weights of  $I_{MFO_{R3}}$  and  $I_{MFO_{R7}}$ , respectively.

Once pits are separated from potential pit pixels and the MMFO filtering is carried out, the identified pits are replaced with the corresponding values in  $I_{MMFO}$  as illustrated in Figure 5.4. That is, if the cell value in  $I_{MLO}$  is below  $T_{MLO}$  while the corresponding value in  $I_{MMCO}$  is above  $T_{MMCO}$ , the cell value in the  $CHM_1$  is replaced with the corresponding cell value in  $I_{MMFO}$ ; otherwise, the cell value in the  $CHM_1$  remains the same. This process produces the final improved CHM which is referred to as  $CHM_{R1}$ . CHMs before and after improvement (i.e.  $CHM_1$  and  $CHM_{R1}$ ) are provided in Figure 5.5. Some differences between the CHMs before and after the improvement in an enlarged region of the black rectangle in Figure 5.5(a) are highlighted by red circles in Figure 5.5(c)-(d). As can be seen from Figure 5.5(c)-(d), most small and isolated pixels in the red circles which must be pits in Figure 5.5(c) have been removed. Quantification of the removal rate was unavailable because the number of actual pits is unknown and unpractical to survey in the field.

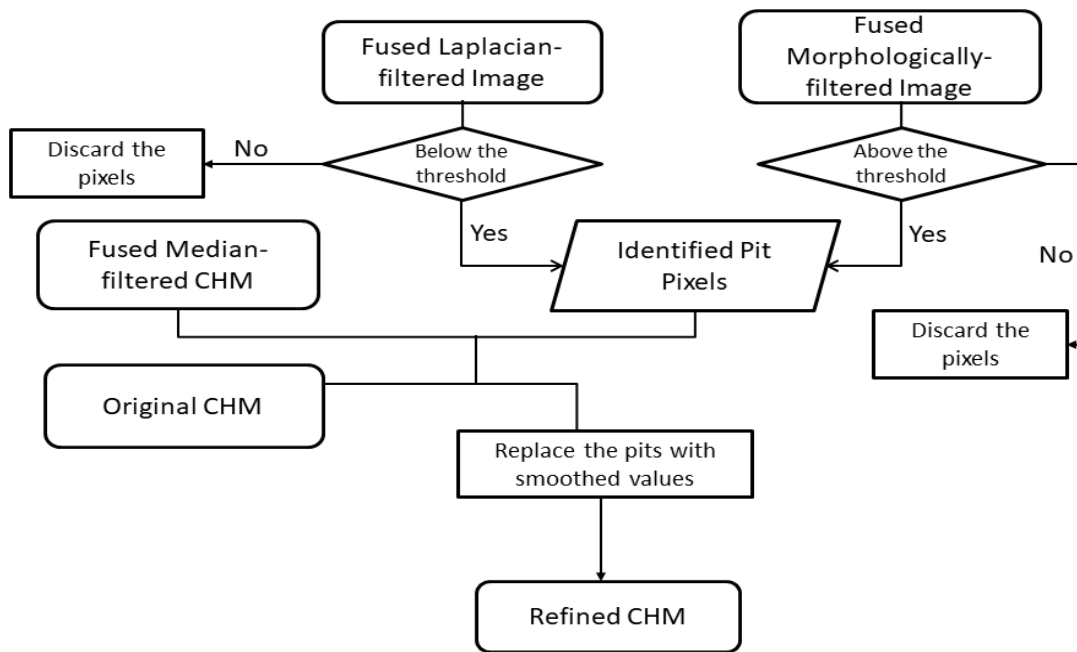
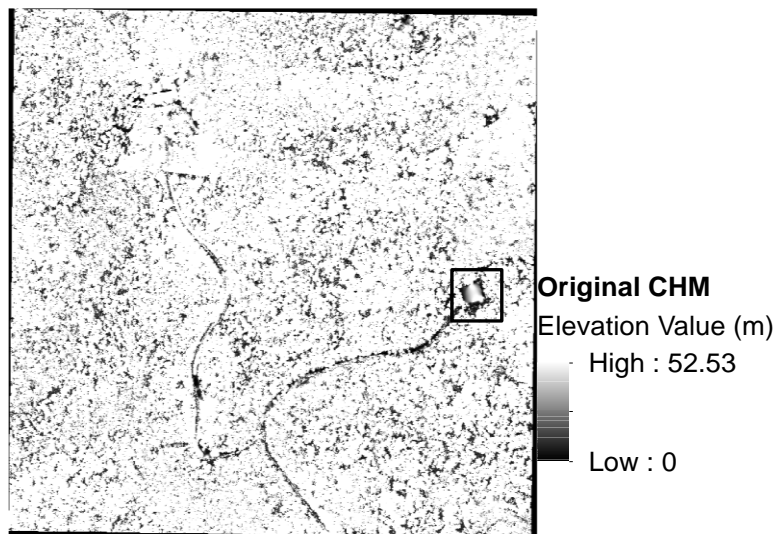
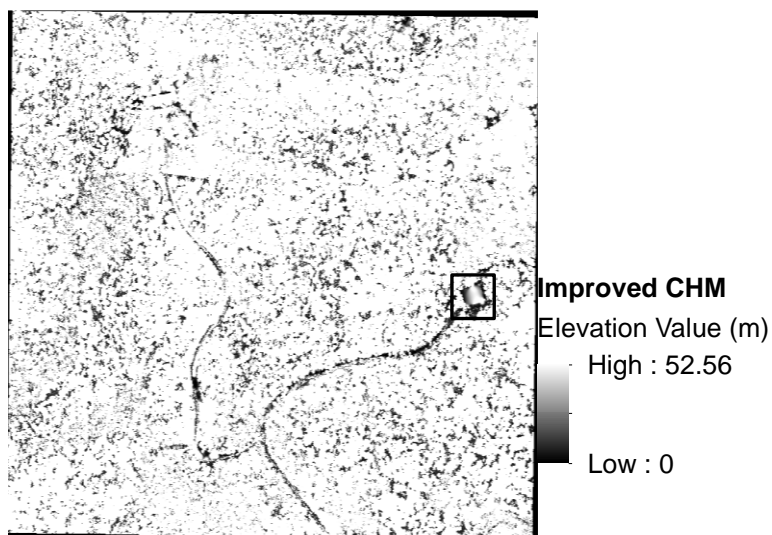


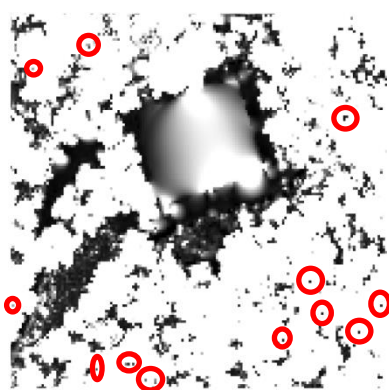
Figure 5.4 Procedures of replacing pit pixels



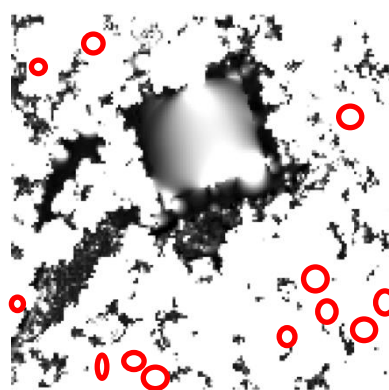
(a) Original 1-m resolution CHM



(b) 1-m resolution CHM after improvement



(c) A part of CHM1 in the black box in (a)



(d) A part of CHMR1 in the black box in (b)

Figure 5.5 The 1-m resolution CHM of the Black Mountain Reserve before and after the improvement

#### 5.2.4 Validation

To verify if the proposed algorithm improved the accuracy of the CHM, the RMSEs of  $CHM_I$  and  $CHM_{R1}$ , are computed respectively as follows: the column and row serial numbers of each record are calculated based on the coordinates, then the closest matching cell value is searched within a neighbourhood of a 10-m radius, i.e. the absolute difference between the cell value and the height of the recorded tree is minimal within the neighbourhood. In case small cell values are used multiple times, an index is assigned to the cell when the corresponding cell value is matched with the height of a recorded tree and the cell will not be used in further processing. Therefore, the absolute difference between the matching cell value and the height of the recorded tree is used for computing the RMSE. The mean absolute error (denoted by MAE) and the standard deviation of the differences (denoted by  $\sigma$ ) between the matching cell values and the corresponding heights of the recorded trees are also computed. Paired t-tests ( $t_{pair}$ ) are also conducted between the matching cell values derived from the CHMs (i.e.  $CHM_I$  and  $CHM_{R1}$ ) and the recorded trees, respectively to show which cell values are more close to the recorded results. The mathematical models for the RMSE, MAE and  $t_{pair}$  are shown in Eqs. (5.6)-(5.10).

$$MAE = \sum_{i=1}^n |C_i - H_i| / n \quad (5.6)$$

$$RMSE = \sqrt{\sum_{i=1}^n (C_i - H_i)^2 / n} \quad (5.7)$$

$$E = \sum_{i=1}^n (C_i - H_i) / n \quad (5.8)$$

$$\sigma = \sqrt{\sum_{i=1}^n (C_i - H_i - E)^2 / n} \quad (5.9)$$

$$t_{pair} = (\sqrt{n} \times E) / \sigma \quad (5.10)$$

where:  $n$  is the total number of trees,  $H_i$  is the height of the recorded tree  $i$  while  $C_i$  is the corresponding matching cell value, and  $E$  is the mean difference between the matching cell values and the corresponding heights of the recorded trees.

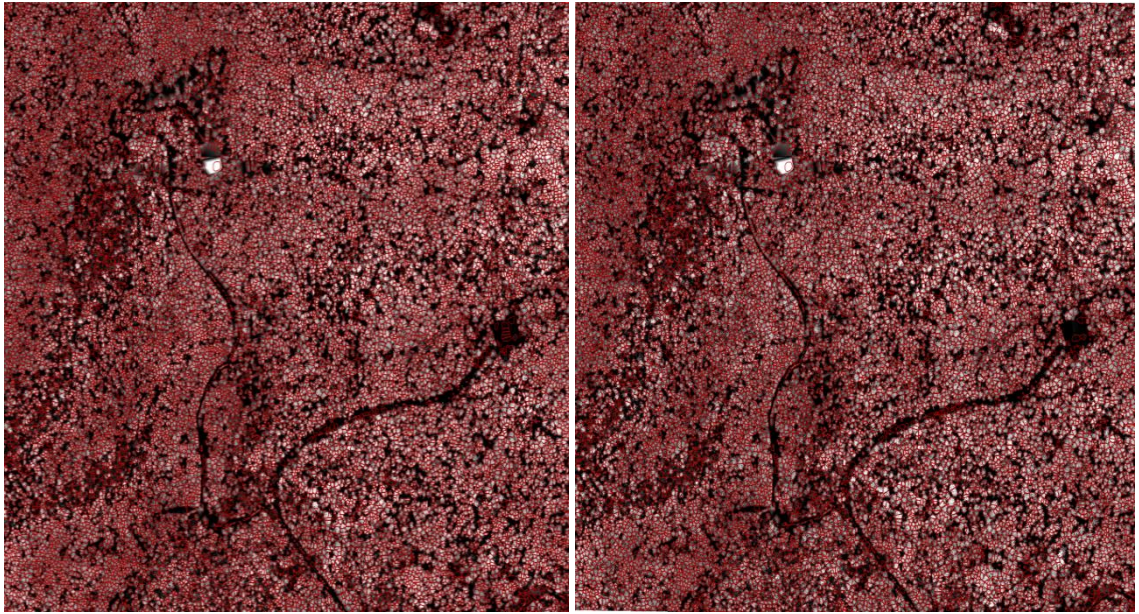
To investigate if the improvement of the CHM can increase the accuracy of individual tree segmentation, two commonly used individual tree extraction algorithms, namely the variable-area-local-maxima algorithm (VLM, Swetnam and Falk, 2014) and the individual-tree-crown delineation algorithm (ITCD, Dalponte et al., 2015) are applied to  $CHM_I$  and  $CHM_{R1}$ , respectively. The results are compared with the field measurements. These two algorithms are selected because of their ability to extract accurate treetops. For each reference tree (RT) in the field measurements, the most matching tree (MMT) from the extracted individual trees is searched. That is, if the horizontal distance between a reference tree and an extracted tree is within

10 m, the extracted tree is regarded as a potential matching tree (PMT), and if the height difference between an extracted tree and a PMT is the least, the PMT is treated as the MMT. The horizontal distance is set to 10 m because of the GPS errors in dense canopies. Once the MMTs are identified, the height differences between the MMTs and the corresponding RTs are computed. The average and the RMSE of the differences are computed according to Eqs. (5.11)-(5.12) and compared to check if the improvement of the CHM improves the accuracy of the extracted tree height. The results derived from CHM<sub>R1</sub> by VLM and ITCD are denoted by VLM<sub>R1</sub> and ITCD<sub>R1</sub>, respectively whereas the results derived from CHM<sub>1</sub> by VLM and ITCD are denoted by VLM<sub>1</sub> and ITCD<sub>1</sub>, respectively. The results derived from the 1-m resolution CHM before and after the improvement for different algorithms are illustrated in Figure 5.6.

$$E_H = \sum_{i=1}^{N_M} (H_i - H_{R_i}) / N_M \quad (5.11)$$

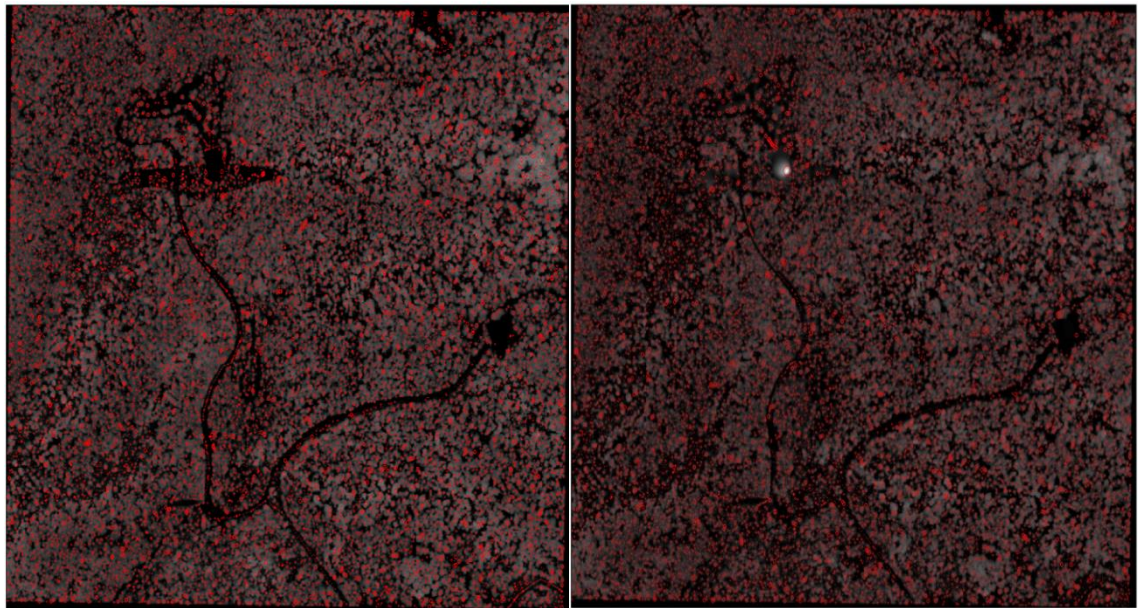
$$RMSE_H = \sqrt{\sum_{i=1}^{N_M} (H_i - H_{R_i})^2 / N_M} \quad (5.12)$$

where  $H_i$  and  $H_{R_i}$  are the height of the extracted tree and the corresponding MMT<sub>*i*</sub> ( $i=1,2,\dots, N_M$ ), respectively;  $E_H$  is the average of differences between  $H_i$  and  $H_{R_i}$ , and  $RMSE_H$  is the RMSE of the height differences between the extracted trees and the corresponding MMTs.



(a) Extracted Individual Trees for ITCD<sub>1</sub>

(b) Extracted Individual Trees for ITCD<sub>R1</sub>



(c) Extracted Individual Trees for VLM<sub>1</sub>

(d) Extracted Individual Trees for VLM<sub>R1</sub>

Figure 5.6 Extracted individual trees derived from the 1-m resolution CHM before and after the improvement for different algorithms (the red polygons show the crown boundaries)

### 5.3 Results and discussion

As stated above,  $w_{LO_3}$  in the fusion process was set to  $2/3$  based on trial and error and  $T_{MLO}$  was set to  $-40$  m based on Eq. (5.3). In terms of  $T_{MMCO}$ , it was set to  $5$  m based on the field measurements. The experiment was carried out in Matlab R2013b (MathWorks, 2015) using

the Intel (R) Core(TM) i7-472 4900 CPU with the installed memory of 16 GB. The processing time was 5 minutes and 16.2 seconds. The RMSEs of CHM<sub>1</sub> and CHM<sub>R1</sub> were 0.699 m and 0.390 m, respectively. The mean absolute errors of CHM<sub>1</sub> and CHM<sub>R1</sub> were 0.364 m and 0.243 m, respectively. The standard deviations for CHM<sub>1</sub> and CHM<sub>R1</sub> were 0.685 and 0.382, respectively. The  $t_{\text{Pair}}$  values for CHM<sub>1</sub> and CHM<sub>R1</sub> were 2.756 and 2.163, respectively. According to the t-test table (Statistical Tables, 2018), p value is 0.005 when the t value exceeds 2.609. Hence, the matching cell values yielded by CHM<sub>1</sub> were different from the field records while those derived from CHM<sub>R1</sub> were close to the field records.

The results of individual tree segmentation for VLM and ITCD are listed in Table 5.1. The comparisons of VLM<sub>1</sub> and VLM<sub>R1</sub>, ITCD<sub>1</sub> and ITCD<sub>R1</sub> indicate that the improvement of the CHM can increase the number of extracted trees and improve the accuracy of the height of an extracted individual tree. Although the differences in the total number of extracted trees for VLM<sub>1</sub> and VLM<sub>R1</sub> are relatively small,  $N_M$  for VLM<sub>R1</sub> is much higher than that for VLM<sub>1</sub>, and  $E_H$  for VLM<sub>R1</sub> is smaller than that for VLM<sub>1</sub>. A further investigation on VLM<sub>1</sub> and VLM<sub>R1</sub> shows that VLM may fail to extract all trees in the study region because, as shown in Figure 5.6, some places have no red polygons indicating that no trees are detected in this region. Because of the undersegmentation of trees, the differences of the total number of extracted trees for VLM<sub>1</sub> and VLM<sub>R1</sub> are small. The comparisons of  $N_M$  and  $E_H$  indicate the extracted trees derived from the improved CHM resemble the reference data more. In terms of ITCD<sub>1</sub> and ITCD<sub>R1</sub>, the total number of extracted trees for ITCD<sub>R1</sub> is much larger than that for ITCD<sub>1</sub>. Although  $N_M$  for ITCD<sub>1</sub> is slightly smaller than that for ITCD<sub>R1</sub>, the absolute value of  $E_H$  for ITCD<sub>1</sub> is much larger than that for ITCD<sub>R1</sub>. In addition, because of the presence of pits in the CHM<sub>1</sub>,  $E_H$  for ITCD<sub>1</sub> is negative. However, after replacing the pits with correct values,  $E_H$  for ITCD<sub>R1</sub> is positive, which confirms that the proposed algorithm can tackle the issue of underestimation of tree heights from the CHM.

Table 5.1 Analysis of the accuracy of extracted individual trees

Method	The number of extracted trees	$N_M$	$E_H$ (m)	$RMSE_{E_H}$ (m)
VLM <sub>1</sub>	18,380	114	0.191	0.663
VLM <sub>R1</sub>	18,812	140	0.032	0.649
ITCD <sub>1</sub>	20,325	146	-0.049	0.710
ITCD <sub>R1</sub>	33,925	148	0.012	0.568

To investigate the robustness of the proposed algorithm, different numbers of noises, namely pit values, were randomly added to the CHMs. After applying the proposed algorithm, the number

of removed noises in  $CHM_{R1}$  and the number of added noises in  $CHM_1$  were compared. Since the proposed algorithm assumes that pits are mainly present in the canopies regions, if the noises are added in the canopy gaps, the proposed algorithm will fail to identify them, which makes it an unfair comparison. Hence, only pixel values larger than 1.37 m were replaced with randomly generated low values and were regarded as noises. Based on the results as shown in Figure 5.7, 93.97% of the noises were removed if 0.5% of the total number of pixels were replaced with noises. 93.42% of the noises were removed if 1% of the total pixels were replaced with noises, 93.49% if 2% were replaced, 92.96% if 5% were replaced, and 91.92% if 10% were replaced. These results indicate the robustness of the algorithm.

To examine if the proposed algorithm can be applicable to other forests, the algorithm was tested with another forest in Canberra, a mixed forest with dominant tree species of oaks and Eucalypts. Lacking the reference data in this forest makes it difficult to compute MAE, RMSE, and  $\sigma$ , hence the robustness test was conducted. With  $w_{LO_3}$  set to  $2/3$  and  $T_{MMCO}$  set to 3 m, 83.83% - 87.53% of the noises were removed in the mixed forest when the percentages of noises ranged from 0.5% to 10%, as shown in Figure 5.7. The 1-m resolution CHMs of the mixed forest in Canberra before and after the improvement are demonstrated in Figure 5.8. The two robustness tests prove that the proposed algorithm is able to remove the majority of the noises in the CHMs. Moreover, with the same parameters applied to the mixed forest except that  $T_{MMCO}$  is set to 3 m, the proposed algorithm can be applicable to other forests with good results.

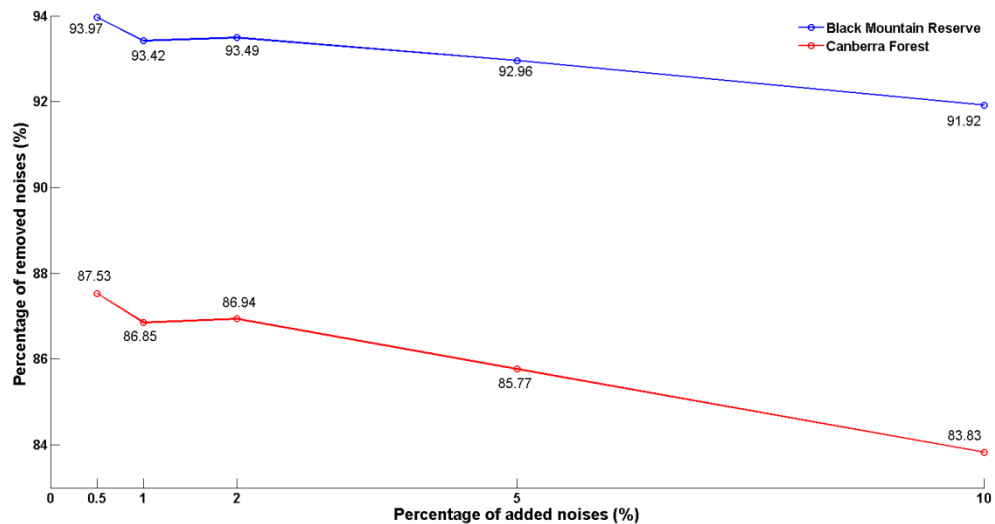
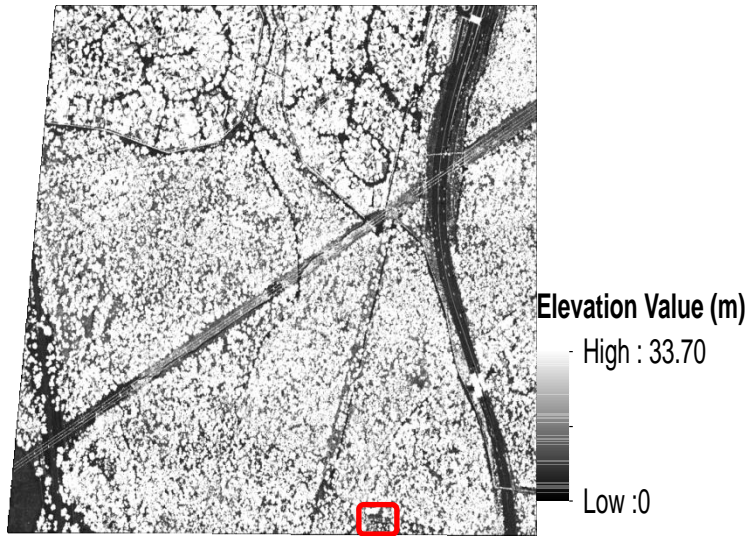
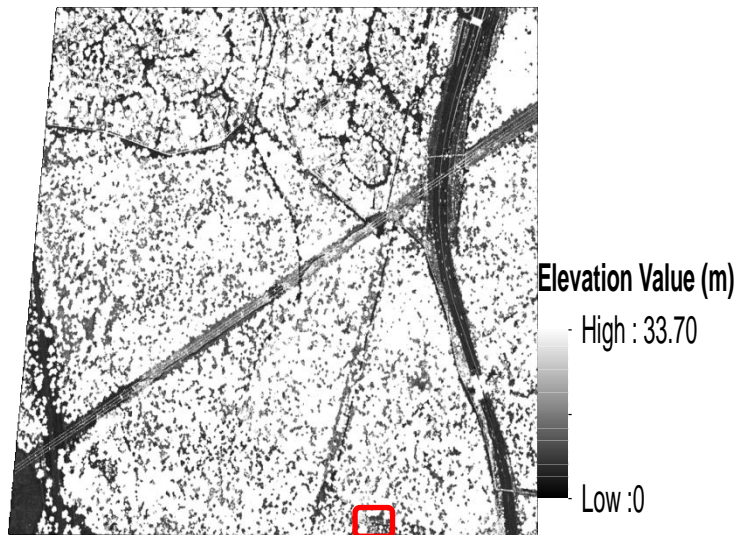


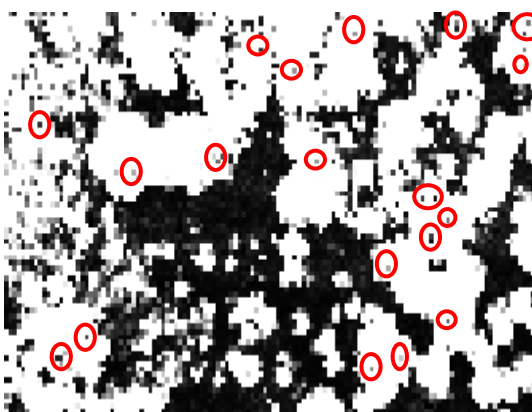
Figure 5.7 The robustness test of the algorithm



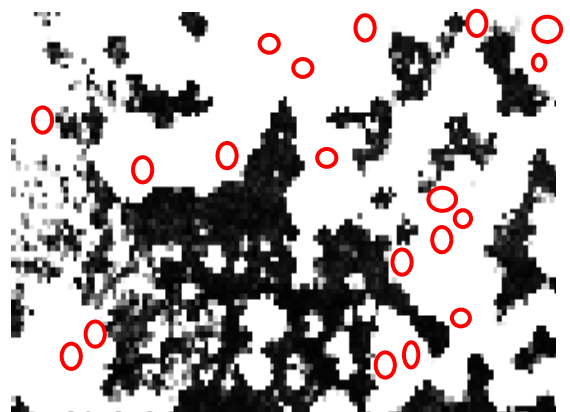
(a) Original 1-m resolution CHM of the mixed forest in Canberra



(b) 1-m resolution CHM of the mixed forest in Canberra after improvement



(c) A part of original 1-m resolution CHM in the red box in (a)



(d) A part of 1-m resolution CHM after refinement in the black box in (b)

Figure 5.8 The 1-m resolution CHM of the mixed forest in Canberra before and after the improvement

### 5.3.1 Analysis of the choices of parameters

To investigate the influence of the choices of parameters on the final result, different values of  $w_{LO_3}$  in the range of 0 and 1 in combination with different values of  $T_{MMCO}$  such as 1 m, 3 m, 5 m and 7 m were tested because around 95% of the heights of the first branch in the reference data are below 9 m. The corresponding RMSEs, MAE and  $\sigma$  are computed and listed in Tables 5.2-5.4, respectively.

Table 5.2 The RMSEs of the improved CHMs with varying weights and thresholds (compared with the RMSE of the original CHM<sub>1</sub> being 0.699 m)

$T_{MMCO}$ (m)	RMSE (m)				
	$w_{LO_3} = 0$	$w_{LO_3} = 1/3$	$w_{LO_3} = 1/2$	$w_{LO_3} = 2/3$	$w_{LO_3} = 1$
1	0.438	0.436	0.433	0.433	0.452
3	0.438	0.436	0.433	0.390	0.452
5	0.438	0.436	0.433	0.390	0.452
7	0.440	0.437	0.434	0.434	0.453

Table 5.3 The mean absolute errors of the improved CHMs with varying weights and thresholds (compared with the mean absolute error of the original CHM<sub>1</sub> being 0.364 m)

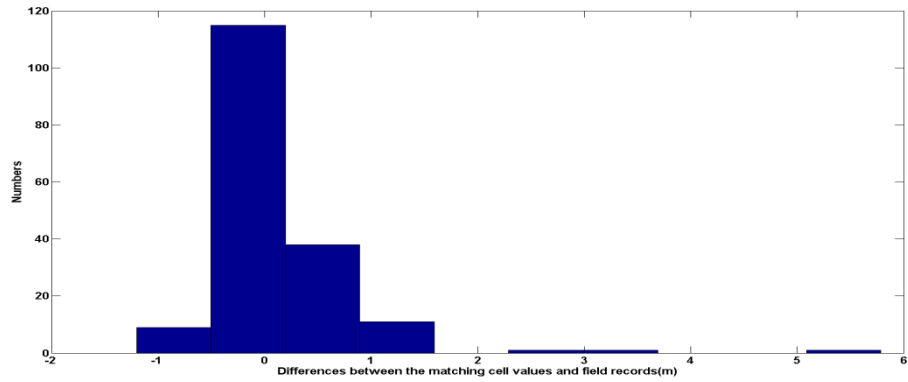
$T_{MMCO}$ (m)	MAE (m)				
	$w_{LO_3} = 0$	$w_{LO_3} = 1/3$	$w_{LO_3} = 1/2$	$w_{LO_3} = 2/3$	$w_{LO_3} = 1$
1	0.259	0.258	0.257	0.257	0.264
3	0.259	0.258	0.257	0.243	0.264
5	0.259	0.258	0.257	0.243	0.264
7	0.262	0.261	0.259	0.259	0.267

Table 5.4 The standard deviations of the improved CHMs with varying weights and thresholds (compared with the standard deviation of the errors for original CHM<sub>1</sub> being 0.685)

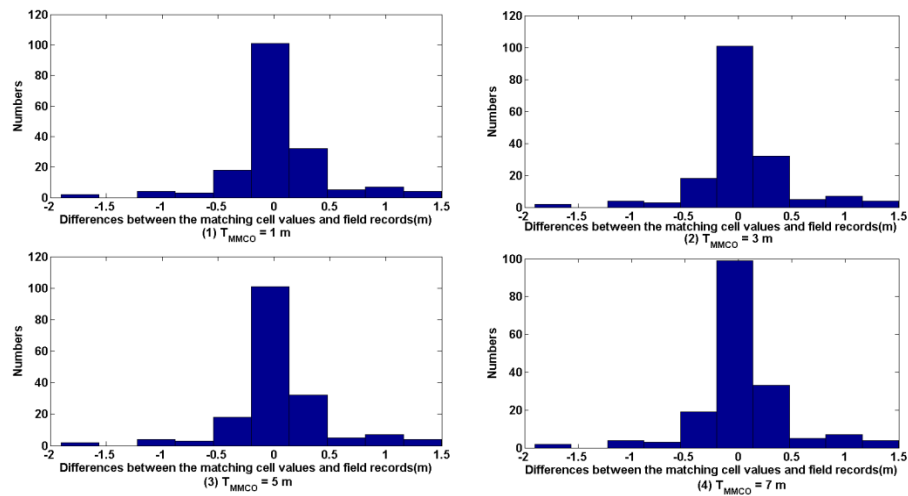
$T_{MMCO}$ (m)	$\sigma$ (m)				
	$w_{LO_3} = 0$	$w_{LO_3} = 1/3$	$w_{LO_3} = 1/2$	$w_{LO_3} = 2/3$	$w_{LO_3} = 1$
1	0.438	0.436	0.432	0.432	0.452
3	0.438	0.436	0.432	0.382	0.452
5	0.438	0.436	0.432	0.382	0.452
7	0.439	0.438	0.434	0.434	0.453

The comparisons before and after an improvement in terms of the RMSE and MAE demonstrate that the improvement with varying weights and thresholds increases the accuracy of the CHM. As seen in Table 5.2, if  $w_{LO_3}$  is 2/3 and  $T_{MMCO}$  is 3 m or 5 m, the corresponding RMSE is the lowest. In addition, if  $w_{LO_3}$  is a constant, the RMSE remains unchanged initially but increases when  $T_{MMCO}$  continues to increase except if  $w_{LO_3}$  is 2/3. A possible explanation for that is the initial increase of  $T_{MMCO}$  achieves a balance between the omission errors of pits and misclassifications of normal values. When  $T_{MMCO}$  increases, fewer potential pits will be classified as pits, leading to the increase of omission errors. However, the RMSE, MAE and  $\sigma$  remain stable when  $T_{MMCO}$  increases from 1 m to 5 m, which may result from the decrease of commission errors. Namely, fewer normal pixels are misclassified as pits as well when  $T_{MMCO}$  increases. If  $T_{MMCO}$  increases further, the omission errors increase, leading to the increase of the RMSE. To investigate why the RMSE, MAE, and  $\sigma$  remain unchanged when  $T_{MMCO}$  increases from 1 m to 5 m meanwhile  $w_{LO_3}$  is a constant, histograms of the differences between the matching cell values and the field records in various conditions were analysed as shown in Figure 5.9. According to Figure 5.9(b), when  $w_{LO_3}$  is 0, although the differences between the matching cell values and the corresponding field measurements become smaller compared with the differences for the original CHM in Figure 5.9(a), the distributions of the differences remain unchanged when  $T_{MMCO}$  varies from 1 m to 5 m. However, when  $T_{MMCO}$  increases from 5 m to 7 m, the number of the differences between about -1/6 m and about 1/6 m decreases while the number of the differences between about -0.50 m and about -1/6 m increases, which indicates some potential pits whose height values are less than 7 m are not treated as pits, therefore not being rectified. When  $w_{LO_3}$  is 2/3, the number of the differences between -0.50 m and 0.50 m increases greatly, as shown in Figure 5.9(c) while the number of the differences smaller than -0.50 m or larger than 0.50 m decreases given the value of  $T_{MMCO}$  ranging from 1 m to 5 m. However, when  $T_{MMCO}$  increases from 5 m to 7 m, the number of the differences smaller than -0.50 m or larger than 0.50 m increases again. Meanwhile, if  $w_{LO_3}$  is not properly chosen, the RMSE of the improved CHM will remain stable when  $T_{MMCO}$  varies from 1 m to 3 m. This indicates that the value of  $w_{LO_3}$  is very critical in the CHM improvement process. Conversely, providing a constant  $T_{MMCO}$ , the RMSE of the improved CHM will decrease initially followed by an increase if  $w_{LO_3}$  increases. A plausible explanation is that fewer normal values will be misclassified in the initial increase of  $w_{LO_3}$ , consequently lowering the RMSE. However, if  $w_{LO_3}$  increases further, omission errors of undetected pits increase and therefore the RMSE increases. One exception is when  $T_{MMCO}$  is 1 m or 7 m where the RMSE keeps decreasing. One possible explanation is that misclassified normal values outnumber unidentified pits and the increase of  $w_{LO_3}$  will reduce the commission errors significantly even if

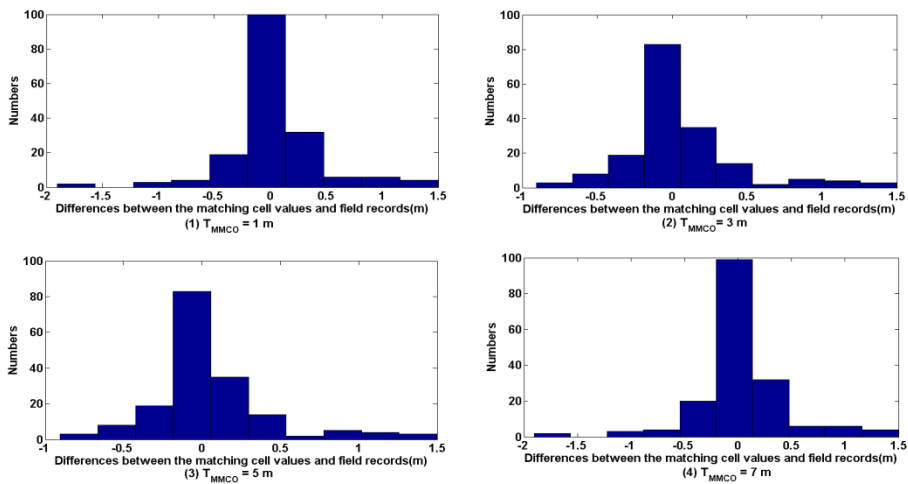
the omission errors increase. In addition, when  $T_{MMCO}$  equals to 1 m or 7 m, the RMSE does not change much if  $w_{LO_3}$  increases from 1/2 to 2/3, which may be a result from the small magnitude of the change. According to Tables 5.3-5.4, when  $w_{LO_3}$  is constant, the patterns of MAE and  $\sigma$  are the same as that of RMSE when  $T_{MMCO}$  increases, namely, MAE and  $\sigma$  remain stable initially before they increase when  $T_{MMCO}$  increases continuously. Meanwhile, when  $T_{MMCO}$  is constant, MAE and  $\sigma$  decrease initially before they increase again when  $w_{LO_3}$  increases. A reasonable explanation is that when  $w_{LO_3}$  increases initially, fewer normal values are misclassified, therefore leading to the decrease of MAE. However, when  $w_{LO_3}$  is too large, fewer pit pixels are identified so that the MAE will increase again. In Zhao et al. (2013), only  $LO_3$  is used in the detection of potential pit pixels and  $T_{MMCO}$  was set to 10 m, hence Zhao et al. (2013) is only a case of  $w_{LO_3} = 1$ . According to Tables 5.2-5.4, when  $w_{LO_3}$  is 1, the corresponding RMSE, MAE, and  $\sigma$  are larger than our best result, which validates the aforementioned statement that the usage of multiscale operators in the proposed algorithm can deal with pit pixels in different sizes.



(a) Original CHM



(b) The improved CHM when  $w_{L03}$  is 0



(c) The improved CHM when  $w_{L03}$  is  $2/3$

Figure 5.9 The histograms of the differences between the matching cell values and field records for various CHMs

### 5.3.2 Analysis of the multiscale morphological closing operator

To analyse the impact of MMCO on the accuracy of the final result, a fixed-window MCO (FMCO) and a various window-sized MCO (VMCO) were tested in comparison with MMCO. With other steps in Figure 5.1 being the same, FMCO only applies  $MCO_5$  to  $CHM_1$  in Step 2 instead of applying multiple MCOs; while VMCO applies  $MCO_3$ ,  $MCO_5$ , and  $MCO_7$  to the same CHM, i.e.  $CHM_1$  rather than applying different MCOs to different CHMs in different spatial resolution. For the comparison of the results,  $T_{MMCO}$  was set to 5 m and  $T_{MLO}$  was set to  $-40$  m. The RMSEs of the corresponding results for FMCO, VMCO, and MMCO were 0.433m, 0.433m, and 0.390 m, respectively. The MAEs of the corresponding results for FMCO, VMCO, and MMCO were 0.257 m, 0.257 m, and 0.243 m, respectively. The  $\sigma$ 's of the corresponding results for FMCO, VMCO, and MMCO were 0.433, 0.433, and 0.382, respectively. Since FMCO fails to identify various crown sizes due to its fixed window size while VMCO misidentifies non-crown regions due to the various window sizes, the RMSEs of the final improved CHMs yielded by FMCO and VMCO are greater than that of MMCO.

### 5.3.3 Analysis of the multiscale median filtering operator

MMFO was compared with a fixed-window MFO (FMFO) and a various window-sized MFO (VMFO). In terms of FMFO, with other steps in Figure 5.1 being the same, only  $MFO_5$  is applied to  $CHM_1$  in Step 3. In contrast, VMFO applies  $MFO_3$ ,  $MFO_5$ , and  $MFO_7$  to  $CHM_1$  only instead of applying  $MFO_3$ ,  $MFO_5$ , and  $MFO_7$  to  $CHM_2$ ,  $CHM_1$ , and  $CHM_{0.5}$ , respectively.  $T_{MLO}$  and  $T_{MMCO}$  were set to  $-40$  m and 5 m, respectively. The RMSEs of the corresponding results were 0.432 m for FMFO, 0.430 m for VMFO, and 0.390 m for MMFO, respectively. The MAEs of the corresponding results were 0.262 m for FMFO, 0.261 m for VMFO, and 0.243 m for MMFO, respectively. The  $\sigma$ 's of the corresponding results were 0.433 for FMFO, 0.430 for VMFO, and 0.382 for MMFO, respectively. As FMFO cannot smooth pits in various sizes simultaneously because of its fixed window size and VMFO may lead to the oversmoothness of some normal values because of its various window sizes, the corresponding results have greater RMSEs than that of MMFO. Meanwhile, in general the results from FMFO have a worse accuracy than the results from VMFO which indicates that the undersmoothness of pits in Step 3 is more affecting the improvement than the oversmoothness of normal values. Compared with the results in Tables 5.2-5.4, when  $w_{LO_3}$  is 0 or 1, only one LO is used in the improvement process. However, the accuracy of the improved CHM is lower than that of FMFO or FMCO when  $T_{MMCO}$  is 5 m while  $w_{LO_3}$  is 0 or 1, which indicates that MLO is most critical in the improvement process and the identification of potential pits is crucial to the accuracy of the improved CHM.

### 5.3.4 Analysis of the impact of the spatial resolution of the base CHM

To investigate if the spatial resolution of the base CHM has a noticeable impact on the improved result, the proposed algorithm was applied to different base CHMs, respectively, including CHM<sub>0.5</sub>, CHM<sub>1</sub>, CHM<sub>2</sub> and 3 m-resolution CHM (CHM<sub>3</sub>).  $T_{MLO}$  was set to  $-40$  m and  $T_{MMCO}$  was set to 5 m for a straightforward comparison with the result derived from the CHM<sub>1</sub>. When CHM<sub>0.5</sub> is served as the base CHM, a 25-cm resolution CHM and CHM<sub>1</sub> are used for MMCO and MMFO, respectively. When CHM<sub>2</sub> is served as the base CHM, CHM<sub>1</sub> and a 4-m resolution CHM (CHM<sub>4</sub>) are used for MMCO and MMFO, respectively. When CHM<sub>3</sub> is used as the base CHM, a 1.5-m resolution CHM and a 6-m resolution CHM are used in the improvement process. Before the improvement, the original RMSEs of CHM<sub>0.5</sub>, CHM<sub>1</sub>, CHM<sub>2</sub> and CHM<sub>3</sub> were 0.312 m, 0.699 m, 0.805 m, and 1.362 m, respectively. After the improvement, the corresponding RMSEs of CHM<sub>0.5</sub>, CHM<sub>1</sub>, CHM<sub>2</sub> and CHM<sub>3</sub> were 0.310 m, 0.390 m, 0.903 m, and 1.512 m, respectively. In addition, the MAEs of CHM<sub>0.5</sub> and CHM<sub>1</sub> decreased from 0.080 m to 0.066 m, and from 0.364 m to 0.243 m, respectively, but MAE increased from 0.379 m to 0.403 m for CHM<sub>2</sub>, and from 0.740 m to 0.874 m for CHM<sub>3</sub>, respectively. In terms of  $\sigma$ , it decreased from 0.319 to 0.310 for CHM<sub>0.5</sub>, decreased from 0.685 to 0.382 for CHM<sub>1</sub>, increased from 0.785 to 0.847 for CHM<sub>2</sub> and increased from 1.236 to 1.312 for CHM<sub>3</sub>, respectively. According to these results, when the cell size increases from 1 m to 3 m, the proposed algorithm fails to increase the accuracy of the CHM if the same parameters are used. For instance, if CHM<sub>1</sub>, CHM<sub>2</sub>, and CHM<sub>4</sub> are explored in MMFO and  $w_{MFO_3}$  and  $w_{MFO_7}$  are also set to  $1/4$ , separately, the maximum search region for MMFO is 12 m, which may lead to the overestimation of the replaced values. As a result, the accuracy of the fused median-filtered image will decrease. These results validate the aforementioned statement that when the crown canopies are small,  $w_{MFO_3}$  should be set to a small value in case of blurring the crown boundaries.

## 5.4 Summary

This chapter presented a multiscale morphological CHM improvement algorithm. A multiscale Laplacian operator is proposed to identify potential pit pixels. A multiscale morphological closing operator is proposed to identify the canopy regions and separate valid canopy gaps from the potential pit pixels. The identified pit pixels are replaced with the smoothed values obtained from a multiscale median filtering operator. Instead of applying multiscale operators to a CHM with particular cell size, the operators were applied to various CHMs with different cell sizes to deal with pits in different sizes, which is the major novelty of the proposed algorithm. Field measurements are used as a reference to compute the absolute mean errors, the

standard deviations of the errors and RMSEs of the CHMs before and after the improvement and to prove that the improvement of a CHM can increase the accuracy of extracted tree heights. According to the results, the proposed algorithm can reduce the absolute mean errors of the CHM from 0.364 m (before) to 0.243 m (after), the standard deviation of the mean errors of the CHM from 0.685 (before) to 0.382 (after) and the RMSE of the CHM from 0.699 m (before) to 0.390 m (after). Different percentages of noises ranging from 0.5% to 10% of the total number of pixels are added to the CHMs to investigate the robustness of the algorithm. After applying the proposed algorithm, 91.92% - 93.97% of the noises were removed.

To investigate if the improvement of the CHM can increase the accuracy of individual tree segmentation, two individual tree segmentation algorithms, ITCD and VLM, are applied to the CHMs before and after the improvement, respectively. The comparisons of the results derived from the CHMs before and after the improvement show an increase in the number of extracted trees and the accuracy of the tree heights for both algorithms. The multiscale Laplacian operator has a greater impact on the improvement process as concluded from the analysis of the thresholds of the multiscale Laplacian operator and multiscale morphological closing operator.

However, the proposed algorithm is based on the assumption that the canopy of a tree from the top view forms a circle. Therefore our algorithm can be effectively applied to different species and sizes whenever this assumption is applicable, but cannot be applied if tree canopies are not circular from the top view. For instance, for spindle-shaped trees whose canopies are oval from the top view, our MMCO with a circular kernel cannot be used to identify the canopies and the MMCO with a kernel of oval should be used instead. The input parameters of the algorithm should be carefully selected to achieve the optimal results. Because each forest has varying tree properties (e.g. crown diameter and height of the first branch), there are no universal parameters suitable for all forests. Generally, the weights for the base CHM should not be smaller than other weights. Meanwhile, if canopies are large, the weights for the CHM with a large cell size should be large enough to replace the large pits whereas the weights should be small if the canopies are small in case of blurring the canopy boundaries. Moreover, as CHMs have several inherent errors, the accuracy of a CHM is largely dependent on the accuracy of the DSM and the DTM. The proposed algorithm replaces the pits in the CHM with multiscale median filtered values. If prior knowledge of topography is provided, the CHM can be further improved.

After the improvement of the CHM, the next step is to segment individual trees and extract individual tree parameters for the AGB estimation. Generally, CHM-based and point-based algorithms are two commonly-used methods to segment individual trees from airborne lidar data. However, they are different pros and cons. For instance, CHM-based algorithms are easy to

implement but they cannot detect understory trees whereas point-based algorithms lack efficiency. To compare the performance of these two categories of algorithms, in Chapter 6, five existing individual tree segmentation algorithms will be assessed, consisting of Li's point-based segmentation algorithm (LPS, Li et al., 2012), the variable area local maxima algorithm (VLM, Swetnam and Falk, 2014), the fixed-window local maxima algorithm (FLM, Silva et al., 2017), the individual-tree-crown delineation algorithm (ITCD, Dalponte et al., 2015) and Popescu and Wynne's local maxima algorithm (PWLM, Popescu and Wynne, 2004).

## Chapter 6 : Assessment of Tree Parameters Extraction Algorithms

### 6.1 Introduction

After the improvement of the CHM, the next step of the framework is tree segmentation to obtain accurate three-dimensional (3D) structures of individual trees (e.g. crown width, crown height, tree height). Accurate knowledge of the 3D structures of individual trees is required for a variety of forest applications, for example, silviculture treatment, forest management, biodiversity assessment and forest planning (Hu et al., 2014; Paris et al., 2016). Field survey has been traditionally used to obtain individual tree parameters such as tree height, crown diameter and diameter at breast height (DBH), however, field survey is a time-consuming, labour-intensive and destructive sampling method which hinders broader sampling coverage. Compared to field sampling, remote sensing has been proven to be a reliable data acquisition technique to estimate forestry parameters at both individual and stand tree levels (Hyypä et al., 2001; Chen and Zhu, 2013; Wallace et al., 2014). As such, many efforts have been made to delineate individual crowns from remotely sensed data (Bunting and Lucas, 2006; Vastaranta et al., 2011; Hu et al., 2014), which has been well reviewed by Ke and Quackenbush (2011) and Zhen et al. (2016).

Common techniques for segmenting individual tree crowns from remotely sensed images include valley following (Gougeon, 1995), shadow recognition between trees (Warner et al., 1998), watershed segmentation (Chen et al., 2006; Hu et al., 2014), edge detection (Culvenor, 2002; Popescu et al., 2003; Koch et al., 2006), and 3D modelling (Gong et al., 2002). Although promising achievements have been accomplished by these studies, some issues still remain unresolved. Firstly, these methods work well in a particular forest environment but underperform in mixed forests where spacing between trees is irregular, tree sizes vary or tree crowns overlap intensively (Zhen et al., 2016); secondly, over-segmentation may occur if a branch of a tree extends outward widely and resembles a small tree; thirdly, the crowns of deciduous trees may overlap heavily, making the between-crown valleys invisible and leading to under-segmentation of the trees; fourthly, these methods generally underestimate tree heights (Chasmer et al., 2006).

The advent of airborne lidar has revolutionised the study of forest macrostructure across the landscape (Swetnam and Falk, 2014) because airborne lidar can record the vertical structures of trees accurately. As a result, numerous methods have been developed to estimate individual tree parameters from airborne lidar data (Brandtberg et al., 2003; Chen et al., 2006; Forzieri et al., 2009; Reitberger et al., 2009; Hu et al., 2014) and were reviewed thoroughly by Hyypä et al. (2008), Wulder et al. (2012) and Zhen et al. (2016). A common approach to segmenting individual trees from airborne lidar data is to take advantage of the methods developed to process remote

sensing images. Instead of exploring brightness and/or colour variations used in image-based methods, lidar-based methods make use of the height variation of a CHM. CHM-based methods usually assume that tree apices correlate with LM in the CHM and the reconstruction of a tree crown can be accomplished by using the geometrical parameters of the CHM (Vega et al., 2014). Well-known CHM-based methods for segmenting individual trees include the LM-based (Persson et al., 2002; Hyyppä et al., 2005), variable area window-based (Popescu et al., 2002; Popescu and Wynne, 2004; Swetnam and Falk, 2014; Coomes et al., 2017), watershed analysis (Chen et al., 2006; Kwak et al., 2007; Zhao and Popescu, 2007; Fang et al., 2016), spatial wavelet analysis (Falkowski et al., 2006, 2008) and template matching (Korpela et al., 2007).

The main problem with CHM-based algorithms is that the detection rate and the accuracy of segmenting tree crowns are heavily influenced by the spatial resolution of the CHM. Moreover, there is no general rule for selecting the optimal spatial resolution since it is specific to the properties of the lidar data and the forest type (Hengl, 2006). To resolve this issue, many scholars exploited multiscale analysis to enhance the segmentation accuracy. For example, Falkowski et al. (2006) made use of various two-dimensional (2D) Mexican hat wavelets with different sizes to filter CHMs. Wolf and Heipke (2007) used a series of Laplacian of Gaussian (LoG) filters to smooth a digital surface model (DSM) before applying a marker-controlled watershed segmentation method. The final individual tree crowns were derived from the multiple segmentation results. Using 3D crown models with identical shapes but different sizes, Holmgren et al. (2010) segmented tree crowns in accord with the correlation between the 3D models and CHMs. Incorporating the metabolic scaling theory (MST), Swetnam and Falk (2014) applied a variable-area-local-maxima algorithm (VLM) to reduce the commission error of false LM. Coomes et al. (2017) used moving windows with various sizes to segment individual tree crowns. Experiment results have shown that multiscale analysis outperforms single scale analysis (Jing et al., 2012) since multiscale analysis takes into consideration trees of different sizes.

Overall, the main advantage of CHM-based methods is the capability of image processing algorithms designed for edge detection and feature extraction. Moreover, their processing time can be reduced significantly by converting a large number of 3D points into a 2D raster image. Appropriate smoothing is required before identifying LM since it is essential to reduce/remove the noise in the CHM, however, mixed forests characterized by various crown widths make it difficult. In addition, CHM-based algorithms are vulnerable to commission and omission errors because detection of small tree apices is challenging if the segmentation scale is large, whereas many LM can be misidentified as tree apices if a smaller scale is applied, especially in deciduous or mixed forests (Vauhkonen et al., 2010). Moreover, CHM-based methods have the inherent

drawback of missing understorey trees because CHMs can only represent the outer surface of tree crowns.

One approach to overcoming the limitations of CHM-based methods is to segment individual trees from lidar points directly. Taking LM as initial seeds derived from the CHM, Morsdorf et al. (2004) proposed a voxel-based k-means clustering algorithm to segment trees. Similarly, Ferraz et al. (2012) clustered points using the mean-shift algorithm. Although good results were achieved with a well stratified vegetation layer, Ferraz et al. (2012) acknowledged that their method is unsuitable for more complex forest structures. Using a large number of training samples for supervised learning, Lee et al. (2010) introduced an adaptive clustering algorithm to segment individual trees directly from lidar points. Wang et al. (2008) applied a voxel-based hierarchical morphological algorithm to identify crown regions at each height interval and adopted a top-down routine to group crown regions at different height intervals. However, their method is prone to over- or under-segmentation because the height levels were uniformly applied without considering the tree height variations. Li et al. (2012) assumed that the space between two tree tops is large and proposed a region growing approach by segmenting trees sequentially. Vega et al. (2014) performed multiple segmentations at various scales and the best set of apices was then selected based on the shape of an ideal tree crown. Sačkov et al. (2017) used a moving window analysis to identify tree tops and applied a set of tree allometry rules such as tree distribution, relationships between tree heights, and relationships between tree heights and crown dimensions which were obtained from ground sample data. However, the complementary data used in the tree allometry rules are not always available. Hamraz et al. (2017) stratified lidar points into various layers by analysing the height histogram of the lidar points within a locale and then applied a segmentation method to each stratified layer. Harikumar et al. (2017) applied the marker-controlled watershed segmentation to segment the dominant tree crowns, projected each segment onto a 3D space separately and isolated subdominant trees from dominant trees by ten features, such as the crown surface height, the three spatial coordinates, and the number of points. Although segmenting individual trees directly from lidar points can improve the detection rate, a lack of efficiency is the major drawback because intensive computation is required to process a large number of 3D points. It is also challenging to segment accurate tree crowns from lidar points generated by different objects in a forest (Hu et al., 2014). Recently, the thriving of deep learning techniques in image classification or pattern recognition drives the application of deep learning algorithms to individual tree segmentation. Windrim and Bryson (2018) applied region-based convolutional neural networks (R-CNNs) and CNN-based 3D segmentation algorithms to segment individual trees. Vertical density raster images are generated by converting points into rasters. The Faster-RCNN object detector trained by vertical density raster images is applied to

segment points into individual trees. Weinstein et al. (2019) proposed a self-supervised deep learning neural network to delineate individual tree crowns in the true colour imagery. A CHM-based algorithm is applied to segment lidar data into individual trees, which can be served as the initial training data for the deep learning model. A small number of hand-annotated trees are also exploited to refine the model. Once the model is complete, it is applied to the true colour imagery to delineate the tree crowns. The results indicate the proposed approach improves the detection of individual trees. Although deep-learning based approaches yield promising results, the required large amount of training data remains a problem. A review of existing algorithms for segmenting individual trees from airborne lidar data indicates that CHM-based algorithms are easy to implement and computationally efficient but cannot detect understorey trees, and the resultant accuracy is not promising especially in deciduous or mixed forests. In addition, the results of CHM-based algorithms rely on the spatial resolution of the CHM. LM generated by a CHM with a large grid cell size may suffer from high omission errors while LM generated by a CHM with a small grid cell size may produce high commission errors. Conversely, point-based algorithms can identify understorey trees but are time-consuming in identifying tree apices and segmenting individual trees, and the accuracy is sensitive to the point density. To test which existing algorithm yields most accurate results, in this chapter, four CHM-based algorithms are compared, including the fixed-window local maxima algorithm (FLM, Silva et al., 2017), Popescu and Wynne's local maxima algorithm (PWLM, Popescu and Wynne, 2004), the variable-area-local-maxima algorithm (VLM, Swetnam and Falk, 2014), the individual-tree-crown delineation algorithm (ITCD, Coomes et al., 2017) and Li's point-based segmentation algorithm (LPS, Li et al., 2012). The five algorithms are selected since FLM identifies LM from the CHM with a fixed window while LPS reorganises lidar points from the highest to the lowest and clusters points based on the horizontal distances; PWLM computes the window size based on the cell value of CHM; and both VLM and LPS adopt the strategy of multiscale window size but VLM makes use of the MST to limit commission errors while ITCD identifies LM in multiscale. The extracted tree heights and crown widths are compared with the reference data to indicate the accuracies of various results. In addition, to investigate if CHMs with better spatial resolution promote the accuracy of the results, CHM-based algorithms are also applied to CHMs with different grid cell sizes.

## **6.2 Tree parameter extraction algorithms**

### *6.2.1 Fixed-window local maxima algorithm*

The algorithm identifies LM with a fixed moving window. Once the CHM is smoothed by a fixed-window mean filter, a fixed moving window is applied to recognise LM and a minimum height threshold is applied to remove the false ones. Once LM are identified, a variable

radius crown buffer is applied to delineate the initial crown region around the LM. After the individual crown polygons are merged by first area delimitation, the centroidal voronoi tessellation is employed to isolate individual crown polygon.

### 6.2.2 *Popescu and Wynne's local maxima algorithm*

The algorithm assumes higher values in a locale represent the peak of a tree crown and the crown size of a tree is related to its height. That is, a higher tree implies a larger crown size. Therefore, this algorithm checks the height value of each pixel and computes the window size according to Eq. (6.1). The local maximum within the window size is identified as a tree top. Once a tree top is identified, two perpendicular profiles of the CHM centered on the tree top are extracted and each profile is fitted to a fourth-degree polynomial. Critical points found around the tree tops based on the fitted function are measured and their distances are treated as the crown width.

$$C_w = 2.52503 + 0.00901H^2 \quad (6.1)$$

Where:  $C_w$  is the window size and  $H$  is the height of the pixel value.

### 6.2.3 *Variable area local maxima algorithm*

The algorithm employs predictions of the MST to reduce commission errors in LM. The core steps of the VLM are as follows, firstly, a local maximum algorithm is applied to identify LM pixels from the CHM; secondly, the LM that are too close to higher pixels are removed and the distance threshold is determined by the MST canopy radius model shown in Eq. (6.2); thirdly, remaining LM are treated as tree tops and the predicted canopy radius is treated as the crown width.

$$R_{can} = \beta h^\alpha \quad (6.2)$$

Where:  $R_{can}$  is the canopy radius,  $\beta$  is the normalisation constant,  $h$  is the tree height, and  $\alpha$  is a small value.

### 6.2.4 *Individual-tree-crown delineation algorithm*

The algorithm first locates LM within the CHM and the identified LM are regarded as tree tops and a decision tree is applied to grow crown regions around the tree tops. Firstly, a low-pass filter is applied to smooth the CHM; secondly, LM are recognised with a moving window of adaptive sizes; thirdly, the recognised LM are treated as tree tops and a decision tree approach is used to grow individual crowns around the tree tops; finally, the first return lidar points within

each crown region are extracted and the 2-D convex hull of the points are seen as the boundary of a crown region.

### 6.2.5 *Li's point-based segmentation algorithm*

LPS assumes the horizontal distance between the tops of two trees is large. Based on this assumption, the lidar points are reorganised from the highest to the lowest. The tallest points within a neighbourhood are treated as seeds in the further clustering steps. If the horizontal distance between a lower point and the seed of a cluster is within the threshold, the lower point is regarded as a part of the cluster. The clustering process is conducted iteratively until all the points are assigned to a cluster. Each cluster forms an individual tree and the maximum height of the point in the cluster is seen as the height of the tree. The 2-D convex hull of each cluster is recognised as a crown region.

## 6.3 Evaluation methodology

Although there is no standard for evaluating the results of individual tree segmentation (Yin and Wang, 2016), detection rate (DR), commission error ( $E_{com}$ ) and omission error ( $E_{om}$ ) are most commonly-used metrics for determining the tree detection accuracy. These metrics are shown in Eqs. (6.3)-(6.5).

$$DR = N_{TP}/N_R \quad (6.3)$$

$$E_{om} = N_{FN}/(N_{TP} + N_{FN}) \quad (6.4)$$

$$E_{com} = N_{FP}/(N_{TP} + N_{FP}) \quad (6.5)$$

where  $N_{TP}$  is the number of correctly located trees;  $N_R$  is the total number of reference trees;  $N_{FN}$  is the number of undetected reference trees; and  $N_{FP}$  is the number of falsely detected trees.

To compute the number of correctly located trees, the rules are set as follows: for each reference tree (RT), if the Euclidean distance between an extracted individual tree and the RT is within 3 m, the reference tree is regarded as detected; otherwise it is treated as undetected. We set a search buffer of 3 m because of the GPS errors. For each extracted tree, if the difference between the heights of the extracted tree and the corresponding RT is larger than 1 m, the tree is treated as falsely detected. In case that an extracted individual tree is matched with multiple RTs, once an extracted individual tree is matched with one RT, it will be labelled and not be processed in further steps. The mathematical model is illustrated in Eq. (6.6).

$$\begin{cases} D_{ref_{i,j}} = \sqrt{(x_j - x_{ref_i})^2 + (y_j - y_{ref_i})^2} \\ N_{TP} = N_{TP} + 1 & \text{if } \min(D_{ref_{i,j}}) \leq 3m \\ N_{FP} = N_{FP} + 1 & \text{if } \min(D_{ref_{i,j}}) \leq 3m \text{ and } |z_j - z_{ref_i}| > 1 \\ N_{FN} = N_{FN} + 1 & \text{if } \min(D_{ref_{i,j}}) > 3m \end{cases} \quad (6.6)$$

where  $(x_j, y_j, z_j)$  are the coordinates of the detected tree  $j$  ( $j = 1, 2, \dots, N_{DT}$ ),  $(x_{ref_i}, y_{ref_i}, z_{ref_i})$  are the coordinates of the RT  $i$  ( $i = 1, 2, \dots, 176$ ); and  $\min$  is the function to obtain the minimum value.

However, none of the three metrics,  $DR$ ,  $E_{om}$  and  $E_{com}$ , can demonstrate whether the tree attributes of a detected tree, such as tree height and crown width, are accurate or not. To measure the accuracy of the tree height and crown width derived from various algorithms, the most matching trees ( $MMTs$ ) are searched from the extracted trees, and the height ( $H$ ) and the crown width ( $CW$ ) of each  $MMT$  are compared with the corresponding reference data. The procedures of finding the  $MMTs$  are as follows. Because of the low accuracy of Global Positioning System ( $GPS$ ) in a dense forest, a buffer of 10m is set to search for the  $MMT$  for a reference tree ( $RT$ ). That is, for each reference tree, if the horizontal distance between an extracted individual tree and a  $RT$  is below 10m, the extracted individual tree is labelled as a potential matching tree ( $PMT$ ). The  $PMT$  whose height is most identical to the height of the  $RT$  is regarded as the  $MMT$ . After identifying the  $MMTs$ , the differences of the  $H$  and  $CW$  between the  $MMTs$  and the corresponding  $RTs$  are calculated. The average and the root-mean-square-error ( $RMSE$ ) of the differences are computed and recorded to indicate the accuracy of the algorithms. The mathematic models are shown in Eqs. (6.7)-(6.12):

$$E_H = \sum_{i=1}^{N_{TP}} (H_i - H_{R_i}) / N_{TP} \quad (6.7)$$

$$MAE_H = |\sum_{i=1}^{N_{TP}} (H_i - H_{R_i})| / N_{TP} \quad (6.8)$$

$$E_{CW} = \sum_{i=1}^{N_{TP}} (CW_i - CW_{R_i}) / N_{TP} \quad (6.9)$$

$$MAE_{CW} = |\sum_{i=1}^{N_{TP}} (CW_i - CW_{R_i})| / N_{TP} \quad (6.10)$$

$$RMSE_H = \sqrt{(\sum_{i=1}^{N_{TP}} (H_i - H_{R_i})^2) / N_{TP}} \quad (6.11)$$

$$RMSE_{CW} = \sqrt{(\sum_{i=1}^{N_{TP}} (CW_i - CW_{R_i})^2) / N_{TP}} \quad (6.12)$$

Where:  $H_i$  and  $CW_i$  are the height and the crown width of the  $MMT_i$  ( $i=1,2,\dots,N_{TP}$ ), respectively;  $H_{R_i}$  and  $CW_{R_i}$  denote the H and CW of the corresponding RT, respectively;  $E_H$  is the average of differences between  $H_i$  and  $H_{R_i}$ , whereas  $MAE_H$  is the average of the absolute differences between  $H_i$  and  $H_{R_i}$ ;  $E_{CW}$  is the average of differences between  $CW_i$  and  $CW_{R_i}$  while  $MAE_{CW}$  is the average of the absolute differences between  $CW_i$  and  $CW_{R_i}$ ;  $RMSE_H$  is the RMSE of the differences between the H of the MMTs and the RTs and  $RMSE_{CW}$  denotes the RMSE of the differences between the CW of the MMTs and the RTs.

## 6.4 Results and discussion

Due to the variations in forest conditions, the parameters of the five individual tree segmentation algorithms were tuned carefully to obtain optimal results. FLM was executed in R (R Core Team, 2016) with a  $5\times 5$  window based on the experimental results. The threshold for the maximum crown size was set to 15 m based on the field measurements. PWLM was performed by US Forest Service FUSION/LDV 3.50 software (McGauchey, 2016); the window size was computed based on the Eq. (6.1) automatically and the threshold for the minimum tree height was set to 1 m according to the field measurements. VLM was executed in Matlab R2013b based on the codes in Swetnam and Falk (2014) and the allometric canopy ratio (ACR) in the VLM was set to 0.25 empirically. ITCD was conducted in R as well with the `itcSegment` package (Dalponte, 2017). The search window size was set to  $5\times 5$  based on trial and error, the thresholds for the maximum crown size and the minimum tree height were set to 15 m and 1 m, respectively based on field measurements. In terms of LPS, it was applied in R; the spacing thresholds between two individual trees at upper level and lower level were relevant to a tree crown width, therefore setting them to 1 m and 3 m based on the field measurements. The maximum crown size was set to 15 m. The results for FLM, PWLM, VLM, ITCD, LPS are denoted by  $FLM_1$ ,  $PWLM_1$ ,  $VLM_1$ ,  $ITCD_1$  and LPS, respectively.

The total number of extracted individual trees ( $N_{DT}$ ) for  $FLM_1$ ,  $PWLM_1$ ,  $VLM_1$ ,  $ITC_1$  and LPS was 11868, 29649, 18380, 20325 and 62648, respectively. According to the core steps of identifying MMTs, the total number of the MMTs, denoted by  $N_{TP}$ , for  $FLM_1$ ,  $PWLM_1$ ,  $VLM_1$ ,  $ITCD_1$  and LPS was 109, 102, 74, 131 and 130, respectively. The total number of misidentified individual trees, denoted by  $N_{FP}$ , for  $FLM_1$ ,  $PWLM_1$ ,  $VLM_1$ ,  $ITCD_1$  and LPS was 23, 23, 17, 19 and 17, respectively.

Table 6.1 indicates the analysis results for various algorithms. According to the results, although LPS achieves the largest number of extracted individual trees and the lowest commission error,  $E_{CW}$  is not promising in comparison with the results for  $VLM_1$  and  $ITCD_1$ . One plausible

explanation can be that *LPS* suffers from oversegmentation. A further investigation of the results validates the explanation. As shown in Figure 6.2 (a), the majority of the differences between the reference and the *LPS* for crown width are negative. Apart from low detection rate, the tree parameters yielded by *PWLM* and *FLM* are not promising, which is validated by large absolute values of  $E_{CW}$ ,  $MAE_H$ ,  $RMSE_H$ , and  $RMSE_{CW}$ . *PWLM* cannot segment tree crown accurately because the algorithm is mostly suitable for conifer forest as stated in McGauchey (2016). As a result, the trees identified by  $PWLM_I$  suffer from oversegmentation and  $E_{CW}$  has a negative value. In contrast, due to the fixed window size, *FLM* suffers from undersegmentation in dense canopies, especially when the tree canopies overlap heavily. As a result, the  $E_{CW}$  for  $FLM_I$  is larger than various window size based algorithms such as *VLM* and *ITCD*, which is validated by Figure 6.2 (b) that a large number of the differences range from 2 m to 4 m. Although the absolute value of  $E_H$  for  $FLM_I$  is much smaller than that for  $PWLM_I$ , the corresponding  $MAE_H$  and  $RMSE_H$  are larger. According to Figure 6.1 (b), the differences of tree height between the *FLM* results and the reference are evenly distributed, which causes the small absolute value of  $E_H$  for  $FLM_I$ . However, according to Figure 6.1(b)-(c), the majority of the tree height differences between the *PWLM* results and the reference range from -1 m to 1 m while about 12% of the tree height differences between the *FLM* results and the reference are larger than -1 m. The comparisons of Figure 6.1(b)-(c) indicate a small absolute value of mean error does not necessarily mean better accuracy and multiple criteria should be considered when analysing the accuracy. For instance, two of the tree height differences between  $FLM_I$  and the references are 1 m and -1 m whereas two of the tree height differences between  $PWLM_I$  and the references are 0.5 m and 0.5 m. Although the average of the two differences for *FLM* is smaller than that for  $PWLM_I$ , the results derived from *PWLM* are more accurate. Thanks to the strategy of an adaptive moving window, the results of  $ITCD_I$  are promising. According to Figure 6.1 (e), the differences of the tree height between the  $ITCD_I$  and the reference are evenly distributed. Meanwhile, the majority of the differences of the crown width for  $ITCD_I$  are between -2 m and 2 m, as shown in Figure 6.2 (e). Although  $VLM_I$  achieves the most accurate results in terms of  $E_{CW}$ , the tree heights derived from  $VLM_I$  are not promising. Because *VLM* applies MST to reduce commission errors, some LM with low elevation values may be misclassified as false positives and removed, which occurs commonly in dense forests. Consequently,  $N_{DT}$  and  $N_{TP}$  are low and the heights of extracted individual trees are much larger than the corresponding reference trees.

Table 6.1 The Analysis of the results for various algorithms

	$LPS$	$FLM_1$	$PWLM_1$	$VLM_1$	$ITCD_1$
$DR$ (%)	73.86	61.93	57.95	42.05	74.43
$E_{om}$ (%)	26.14	38.07	42.05	57.95	25.57
$E_{com}$ (%)	11.56	17.42	18.40	18.68	12.67
$E_H$ (m)	0.292	-0.048	0.355	0.341	0.022
$MAE_H$ (m)	0.420	0.603	0.547	0.556	0.521
$E_{CW}$ (m)	-1.979	1.505	-1.866	0.001	0.085
$MAE_{CW}$ (m)	2.799	2.707	2.365	1.139	1.969
$RMSE_H$ (m)	0.597	0.742	0.710	0.718	0.672
$RMSE_{CW}$ (m)	3.484	3.230	3.046	1.473	2.475

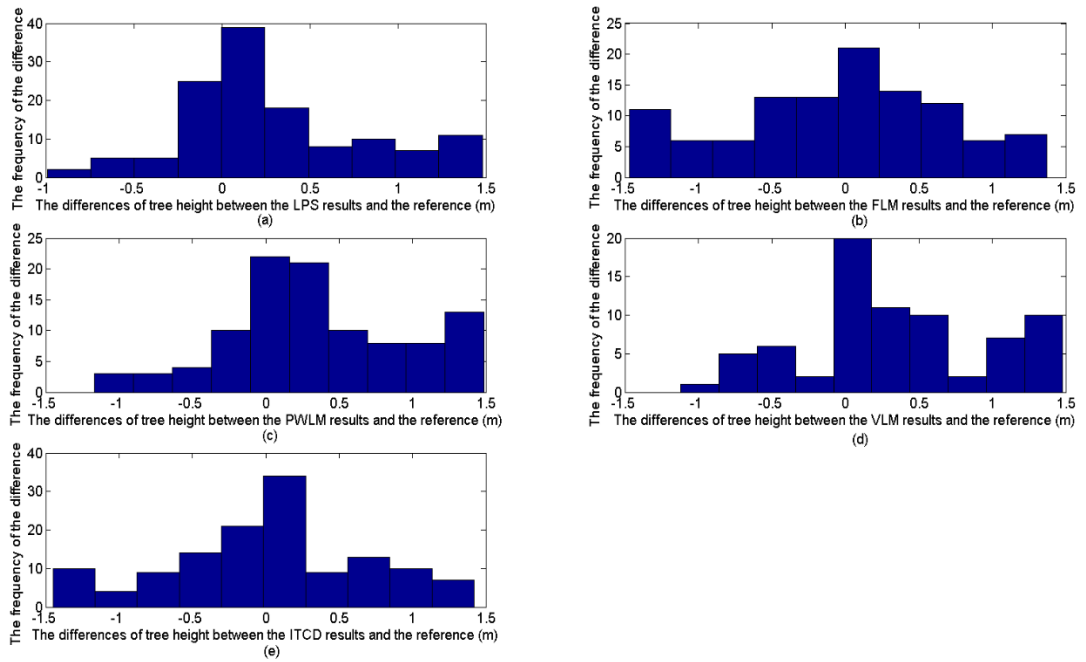


Figure 6.1 The differences of tree height for various algorithms

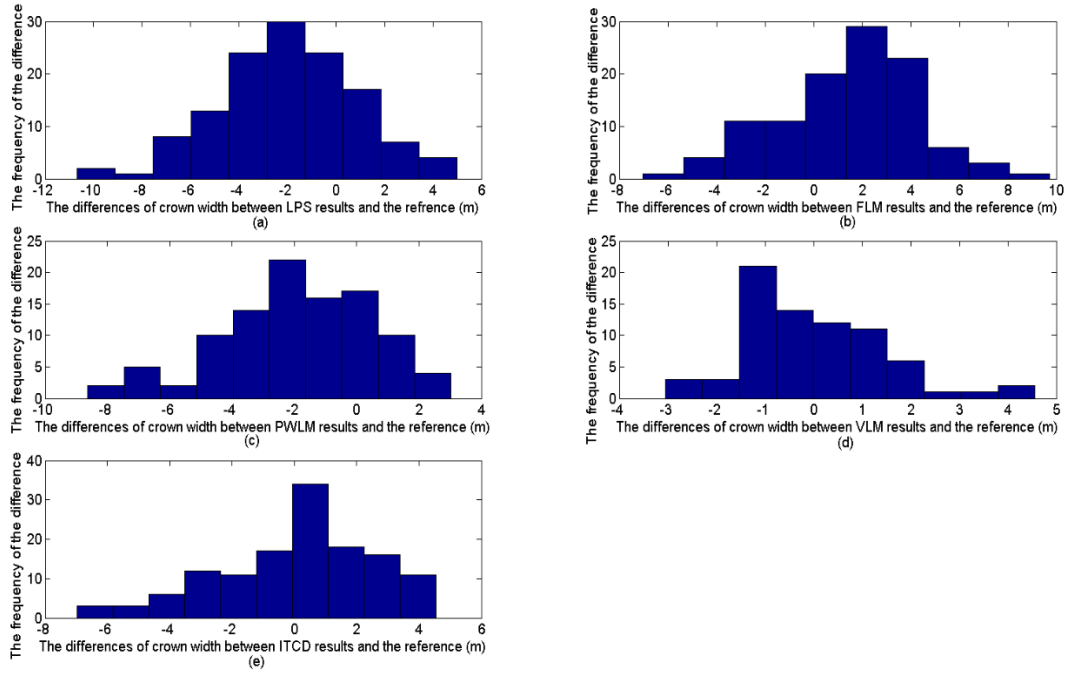


Figure 6.2 The differences of crown width for various algorithms

To verify if CHMs with better resolution promote the accuracy of the final results, FLM, PWLM, VLM, and ITCD were applied to  $CHM_{0.5}$  and  $CHM_2$ , respectively. The window sizes to identify LM in FLM were set to  $3 \times 3$  for  $CHM_2$  and  $7 \times 7$  for  $CHM_{0.5}$ , separately. A large window size may fail to detect small tree crowns, while a small window size may lead to large commission errors as well as compromising computational efficiency. Given the spatial resolution of the CHM, the window size is set to  $3 \times 3$  for  $CHM_2$  and  $7 \times 7$  for  $CHM_{0.5}$ . For straightforward comparison, ACR was set to 0.25 as well when VLM was applied to  $CHM_{0.5}$  and  $CHM_2$ , separately. The spacing threshold in ITCD was set as the same value for  $CHM_1$  during the procession of  $CHM_{0.5}$  and  $CHM_2$ , respectively. The results of  $CHM_{0.5}$  and  $CHM_2$  for FLM are denoted by  $FLM_{0.5}$  and  $FLM_2$ ,  $PWLM_{0.5}$  and  $PWLM_2$  for PWLM,  $VLM_{0.5}$  and  $VLM_2$  for VLM, and  $ITCD_{0.5}$  and  $ITCD_2$  for ITCD, respectively. The  $N_{DTS}$  for  $FLM_{0.5}$ ,  $FLM_2$ ,  $PWLM_{0.5}$ ,  $PWLM_2$ ,  $VLM_{0.5}$ ,  $VLM_2$ ,  $ITCD_{0.5}$  and  $ITCD_2$  were 3196, 6585, 35455, 19527, 60173, 6961, 61229 and 7622, separately. The corresponding  $N_{TPs}$  were 28, 25, 110, 59, 137, 20, 154 and 30, separately whereas the corresponding  $N_{FPs}$  were 11, 4, 22, 17, 13, 2, 10 and 6, respectively. The results for various algorithms are also compared with the reference data and demonstrated in Table 6.2.

Table 6.2 The Analysis of the impact of resolution on the accuracy of the results

	$FLM_{0.5}$	$FLM_2$	$PWLM_{0.5}$	$PWLM_2$	$VLM_{0.5}$	$VLM_2$	$ITC_{0.5}$	$ITC_2$
$DR$ (%)	15.91	14.20	62.50	33.52	77.84	11.36	87.50	17.05
$E_{om}$ (%)	84.09	85.80	37.50	66.48	22.16	88.64	12.50	82.95
$E_{com}$ (%)	28.21	13.79	16.67	22.37	8.67	9.09	6.10	16.67
$E_H$ (m)	0.229	0.370	0.254	0.325	0.094	0.355	0.108	0.256
$MAE_H$ (m)	0.781	0.460	0.506	0.605	0.344	0.431	0.295	0.567
$E_{CW}$ (m)	3.692	3.922	-3.846	0.463	-2.200	2.119	-2.914	1.382
$MAE_{CW}$ (m)	4.171	4.236	3.890	2.739	2.720	3.598	3.025	2.899
$RMSE_H$ (m)	0.897	0.630	0.659	0.773	0.513	0.601	0.457	0.701
$RMSE_{CW}$ (m)	5.127	4.953	4.538	3.271	3.487	5.054	3.874	3.651

The comparisons of the results indicate both  $N_{DT}$  and  $N_{TP}$  will decrease when the cell size of the CHM increases. One exception is that  $FLM_{0.5}$  has less amount of  $N_{DT}$  and  $N_{TP}$  than that of  $FLM_1$ , which may result from the fixed window size. In addition, most algorithms achieve the most accurate tree heights when the resolution of the CHM is 0.5 m. For instance, despite a larger value of  $E_H$  for  $ITCD_{0.5}$  than that for  $ITCD_1$ , the corresponding  $MAE_H$  and  $RMSE_H$  for  $ITCD_{0.5}$  are much smaller than that for  $ITCD_1$ . According to Figure 6.3, 79.22% of the tree height differences between  $ITCD_{0.5}$  and the reference range from -0.5 m to 0.5 m whereas 43.51% of the tree height differences between  $ITCD_1$  and the reference are out of the range between -0.5 m and 0.5 m, which indicates the tree heights derived from  $ITCD_{0.5}$  are more accurate. This is because, in a dense forest, it is more accurate to identify LM within a small surrounding. Although the values of  $E_{CW}$  generally increase when the value of the resolution increases, different algorithms achieve the optimal results at different resolutions. For instance, for PWLM, crown widths are most accurate when the resolution of the CHM is 2 m while for VLM and ITCD, they extract the most accurate crown widths at the resolution of 1 m. Generally, ITCD outperforms other algorithms because ITCD can segment individual trees accurately with a high detection rate while other algorithms fail to achieve these two goals (i.e. segment individual tree accurately and maintain a high detection rate) simultaneously.

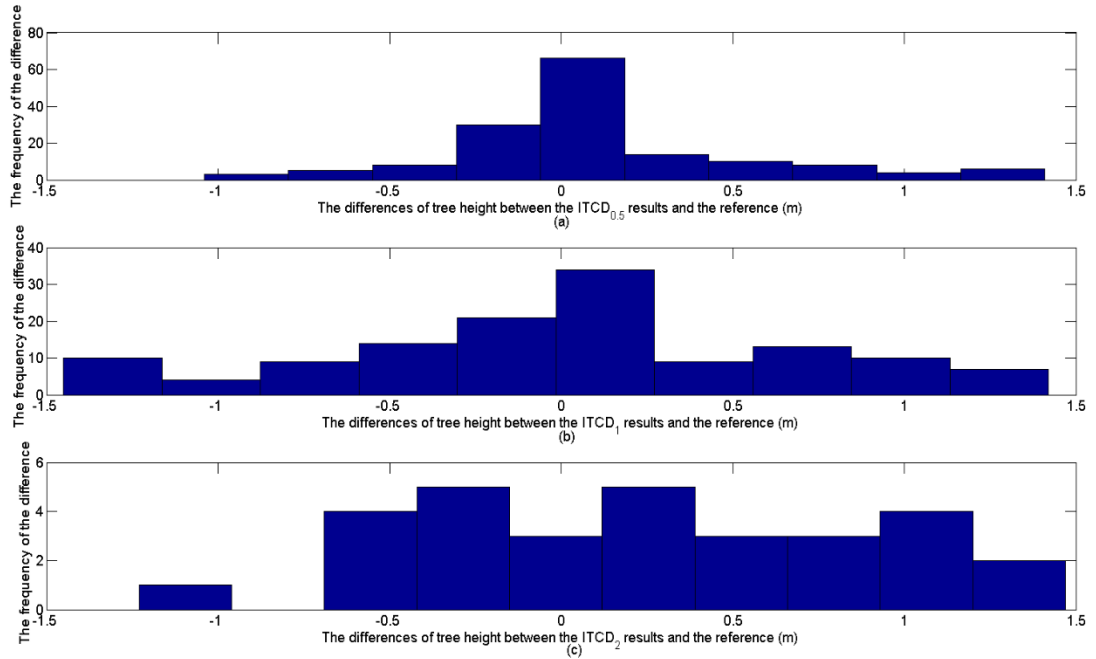


Figure 6.3 The tree height differences between various ITCD results and the reference

## 6.5 Summary

To verify which existing approach generates most accurate results, this chapter compares the fixed-window local maxima algorithm, Popescu and Wynne’s local maxima algorithm, variable area local maxima algorithm, individual-tree-crown delineation algorithm and Li’s point-based segmentation algorithm. The comparisons of the results with the reference data indicate that Li’s point-based segmentation algorithm succeeds in extracting the largest number of individual trees but the extracted tree heights and crown widths are less accurate since the algorithm suffers from oversegmentation. Because of an adaptive window size, the individual-tree-crown delineation algorithm achieves the most accurate tree height and crown width. The CHM-based algorithms are also applied to the CHMs with different resolutions to testify if CHMs with better resolution promote the accuracy of the results. The results show CHMs with better spatial resolution cannot guarantee high accurate crown width. The individual-tree-crown delineation algorithm can be used in the future work because of its good performance in achieving accurate tree tops and crown widths but it cannot detect understory trees. Moreover, for the individual-tree-crown delineation algorithm, it is difficult to achieve the optimal results of the tree height and crown width based on the CHM with a specific grid cell size. For instance, the tree

heights yielded by  $CHM_{0.5}$  are the most accurate because of the lowest  $MAE_H$  and  $RMSE_H$  whereas the crown widths yielded by  $CHM_1$  have better accuracy but the associated LM may produce high omission errors. To obtain high accurate tree heights and crown widths simultaneously and to be able to identify understory trees, a hybrid individual tree segmentation algorithm is proposed by integrating the modified individual-tree-crown delineation algorithm with a point-based algorithm. The details will be present in Chapter 7.

## Chapter 7 : A Hybrid Method for Segmenting Individual Trees from Airborne Lidar Data

The assessment of five existing individual tree segmentation algorithms in Chapter 6 demonstrates that the individual-tree-crown delineation algorithm can yield accurate tree heights and crown widths, which is validated by low values of  $E_H$  and  $E_{CW}$ . However, it is hard to achieve optimal results of tree heights and crown widths simultaneously at one specific spatial resolution. For example, the ITCD algorithm generates the most accurate tree height when it is applied to  $CHM_{0.5}$  whereas it generates the most accurate crown width when applied to  $CHM_1$ . In addition, the CHM-based ITCD algorithm cannot identify understory trees. To obtain highly accurate tree tops and crown width simultaneously and to identify understory trees, a hybrid method for individual tree segmentation from airborne lidar data is present in this chapter. The core of the hybrid tree segmentation algorithm is that a modified ITCD algorithm is proposed to make use of the fact that CHM-based algorithms are easy to implement to identify highly accurate tree tops and the LM from the modified ITCD method will serve as the initial input to the point-based method to identify understory trees and achieve promising results. The chapter is structured as follows: Section 7.1 shows the details of the methodology while Section 7.2 presents the experiment results and discussion with a brief summary in Section 7.3.

### 7.1 Methodology

As stated above, although CHM-based algorithms are efficient to identify LM, the results depend on the spatial resolution of the CHM. To tackle this issue, a modified multiscale ITCD algorithm is presented to recognise the LM that are strongly correlated with tree apices. Different from existing multiscale analyses that explore multiscale LM identification at a particular spatial resolution, a multiscale LM analysis is applied at different spatial resolutions and a local maxima index and its threshold are introduced to decide whether or not an identified local maximum is appropriate as an input for further processing. Since LM derived from CHM-based algorithms may suffer from underestimation, lidar points whose horizontal distances are within 3 m from the LM and whose vertical distances are within 50 cm, are searched and treated as the tree apices. Once the final tree apices are determined, a point-based vertical profile analysis algorithm is applied to segment lidar points into individual trees. Various rules are set to identify the boundaries of the crown of a tree, including gap identification, crown boundaries identification and largest elevation change identification. In case of the presence of understory trees, once the vertical profile analysis is done, a histogram analysis is applied to each cluster of tree points to detect understorey trees and finalise the segmentation of trees. Each step of the proposed method

is described in detail in the following subsections. The flowchart of the proposed method is illustrated in Figure 7.1.

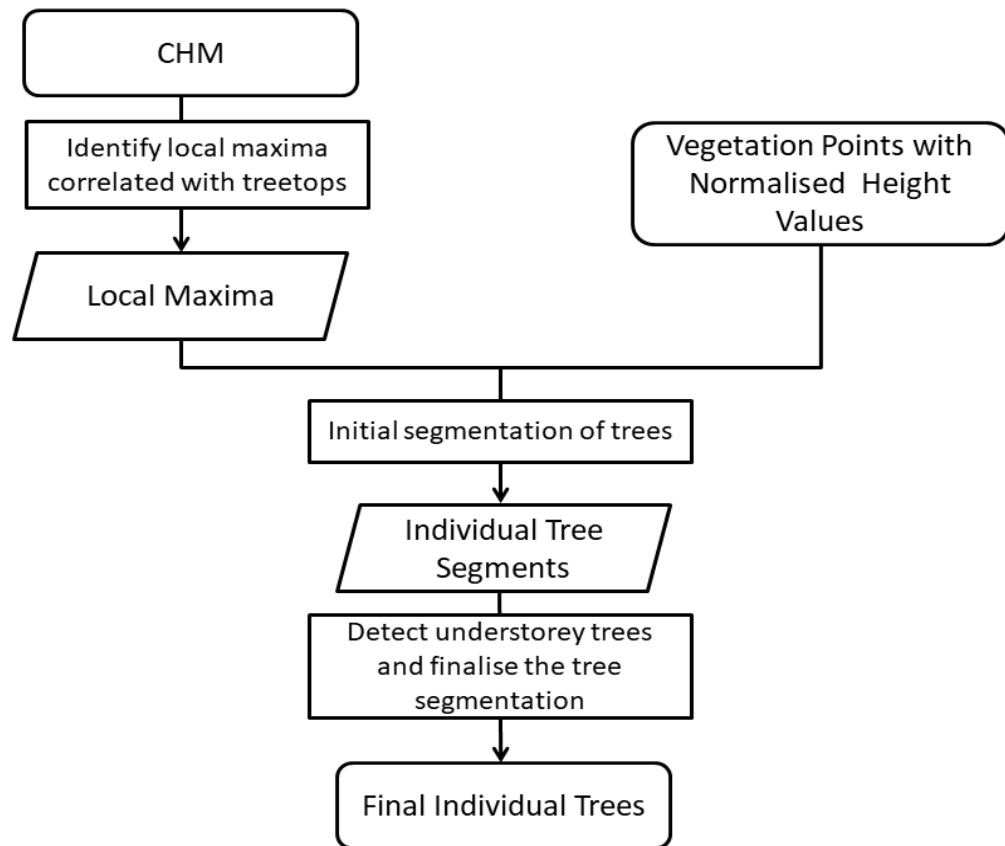


Figure 7.1 The flowchart of the proposed method

### 7.1.1 Identification of LM

The ITCD algorithm (Coomes et al., 2017) is a well-designed CHM-based segmentation method, which locates LM using a moving window with a set of user-defined sizes and segments tree crowns based on the LM. However, a large segmentation scale may lead to the omission of small tree apices, whereas a small scale may result in the misclassification of LM as tree apices. According to the results in Chapter 6, a high spatial resolution of a CHM does not always guarantee accurate tree heights and crown widths. Therefore, instead of finding an optimal spatial resolution, the ITCD algorithm was modified by applying various spatial resolutions and selecting the highest accuracy LM from the derived LM at each spatial resolution. The derived LM at the spatial resolution  $R$  is denoted by  $LM_R$ . To determine the highest accuracy LM, a local maxima index (denoted by  $I_{LM}$ ) is introduced. That is, for each local maximum in  $LM_R$ , if a lidar point  $i$  is within a 3-m horizontal distance and a 50-cm vertical distance from the local maximum, then  $I_{LM}$  of the point will increase by the spatial resolution value. The initial value of  $I_{LM}$  is set to 0.

The maximum horizontal distance between the local maximum and the point  $i$  is set to 3 m because of the accuracy of the GPS device. The maximum vertical distance is set to 50 cm based on experimental results, considering the point density as well as the variance of height values for LM derived from CHMs with different spatial resolutions. The mathematical model is shown as Eq. (7.1). Instead of using the LM identified by the ITCD algorithm directly, lidar points that are within a 3-m buffer of the LM and whose height values are 50-cm deviated from the corresponding LM are taken as tree apices in further processing because tree heights obtained from a CHM are usually lower than the actual values (Chasmer et al., 2006). The incremental index should be carefully chosen because LM generated by the CHM with a small cell size may produce high commission errors, whereas LM created by the CHM with a large cell size may have high omission errors. Misidentification of LM is more challenging than omission error since the misclassified LM are more difficult to be removed when the final LM are determined. Considering these factors, the spatial resolution value is selected as the incremental index. Once the computation of  $I_{LM}$  for all points is complete, an Otsu segmentation (Otsu, 1978) is used to obtain the threshold of the  $I_{LM}$ . The main idea of the Otsu segmentation is that the derived threshold should maximise the variance between distinctive local maxima indices. The details of the identification of LM are provided below:

Step 1. Establish a set of spatial resolution values, set the minimum value in the set of spatial resolution values as the current spatial resolution  $R_c$  and set the initial value of  $I_{LM}$  for all the lidar points to 0;

Step 2. Apply the segmentation algorithm to the CHM of the spatial resolution  $R_c$  (denoted by  $CHM_{R_c}$ ) to identify LM;

For each local maximum in  $LM_{R_c}$  derived from Step 2, if the horizontal distance between a lidar point  $i$  and the local maximum is within 3 m and the point  $i$  is vertically 50-cm deviated from the corresponding local maximum, the point  $i$  is considered to be identical to a local maximum. In case that more than one lidar points meet the criteria, only the  $I_{LM}$  of the point whose height value is the least deviated from the height value of the local maximum increases by the spatial resolution of  $R_c$  as shown in Eq. (7.1):

$$I_{LM_i} = I_{LM_i} + R_c \quad \text{if} \quad \begin{cases} \sqrt{(x_{LM(R_c,b)} - x_i)^2 + (y_{LM(R_c,b)} - y_i)^2} \leq 3 \text{ m} \\ |z_{LM(R_c,b)} - z_i| < 0.5 \text{ m} \\ |z_{LM(R_c,b)} - z_i| = \min(|z_{LM(R_c,b)} - z_j|) \end{cases} \quad (7.1)$$

where  $i$  is the serial number of the lidar points;  $(x_{LM(R_C,b)}, y_{LM(R_C,b)}, z_{LM(R_C,b)})$  and  $(x_i, y_i, z_i)$  are the 3D coordinates of  $LM_{(R_C,b)}$  and the point  $i$ , respectively;  $(x_{LM(R_C,b)}, y_{LM(R_C,b)}, z_{LM(R_C,b)})$  are derived from the ITCD algorithm in Step 2;  $LM_{(R_C,b)}$  is the  $b^{\text{th}}$  local maximum generated by applying the ITCD algorithm to the CHM of the spatial resolution  $R_C$ ;  $b$  is the serial number of the local maximum;  $j=1,2,\dots,s$ ;  $s$  denotes the total number of lidar points which meet the criteria of first two conditions.

Step 3. Take the next larger spatial resolution value in the set of predefined spatial resolution values as  $R_C$  and repeat Steps 2-3 until the spatial resolution value reaches the maximum; otherwise, go to Step 5;

Step 4. Sort and rank all the LM indices in ascending order and, for the lidar points with the same LM index, they are treated equally without ordering within the same LM index;

Step 5. Apply the Otsu segmentation to the sorted LM indices to compute the threshold for the  $I_{LM}$  according to Eq. (7.2); the threshold for the  $I_{LM}$  should maximise the variance of index values, therefore have the largest  $\theta^2$  as illustrated in Figure 7.2, and lidar points with  $I_{LM}$  larger than the threshold are regarded as the final LM serving as initial seeds in further processing;

$$\begin{cases} \theta^2 = \omega_0(\varepsilon_0 - \varepsilon_L)^2 + \omega_1(\varepsilon_1 - \varepsilon_L)^2 \\ \omega_0 = \sum_{r=1}^k P_{I_{LM}^r}; \text{ where: } P_{I_{LM}^r} = g_{I_{LM}^r}/n \\ \omega_1 = \sum_{r=k+1}^L P_{I_{LM}^r}; \\ \varepsilon_0 = \sum_{r=1}^k I_{LM}^r P_{I_{LM}^r} / \omega_0; \\ \varepsilon_1 = \sum_{r=k+1}^L I_{LM}^r P_{I_{LM}^r} / \omega_1; \\ \varepsilon_L = \sum_{r=1}^L I_{LM}^r P_{I_{LM}^r}; \end{cases} \quad (7.2)$$

where  $k$  indicates the rank of current LM index value;  $r = 1, \dots, k, \dots, L$ ;  $L$  denotes the rank of the maximum LM index value;  $I_{LM}^r$  indicates the LM index value when the associated rank is  $r$ ;  $\theta^2$  denotes the class variance when the rank value is  $k$ ;  $\omega_0$  is the fraction of the presence of LM values with ranks ranging from 1 to  $k$ ;  $\omega_1$  is the fraction of the presence of LM index values with ranks ranging from  $k + 1$  to  $L$ ;  $P_{I_{LM}^r}$  is the fraction of the presence of the LM index value when the corresponding rank is  $r$ ;  $g_{I_{LM}^r}$  indicates the total number of points with a LM index value of rank  $r$ ;  $n$  represents the total number of lidar points;  $\varepsilon_0$  is the weighted average of LM indices with ranks ranging from 1 to  $k$ ;  $\varepsilon_1$  is the weighted average of LM indices with ranks ranging from  $k + 1$  to  $L$ ; and  $\varepsilon_L$  is the weighted average of the all LM indices.

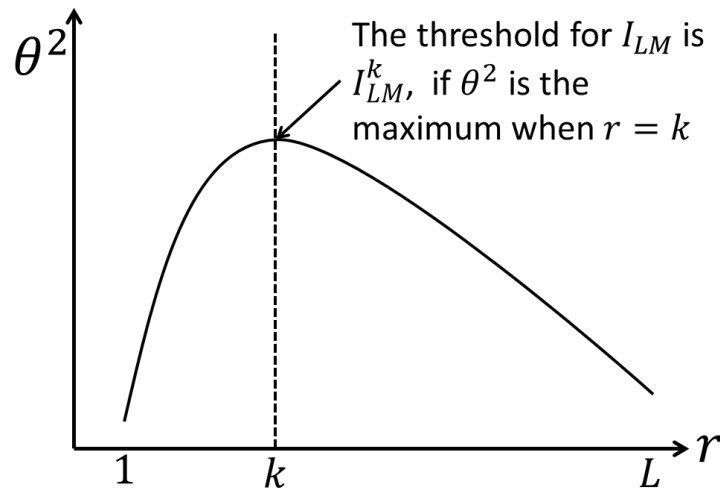


Figure 7.2 The concept of Otsu segmentation

The set of spatial resolution values in Step 1 should be carefully selected. If the minimum resolution value is too small, it may falsely recognise many LM as tree apices. If the minimum is too large, it may omit some LM. On the other hand, if the maximum is too large, it increases the computation time because more iterations are needed to recognise the LM at each spatial resolution; and if the maximum is too small, it may fail to identify some LM. Another factor that needs to be taken into consideration is the size of the forest and the type of forest. If the forest covers a large area, a small value for the minimum will lead to heavy computation, whereas a large value for the maximum may compromise the accuracy of the segmentation results. For the maximum spatial resolution value, the segmentation algorithm was applied to CHMs with different spatial resolution values ranging from 1 m to 10 m, increased by 1 m. The experimental results indicate that the results are not good when the spatial resolution is larger than 2 m. For the minimum spatial resolution value, a set of resolutions are investigated including 0.1 m, 0.2 m and 0.5 m, and the experiments indicate the computational time increases greatly if the segmentation algorithm is applied to a CHM with a smaller cell size ranging from 0.1 m and 0.5 m. Base on the experimental results, the minimum and maximum resolutions are set to 0.5 m and 2 m, respectively.

### 7.1.2 Segmentation of individual trees

Once LM are identified, a moving window-based vertical profile analysis is conducted to segment individual trees from lidar points. The vertical profile analysis is widely used for identifying the borders of a tree crown because of its simplicity and ease of use (Duncanson et al., 2014; Paris et al., 2016; Hamraz et al., 2016). During the generation of the vertical profile, a maximum crown radius is usually set. However, a pre-defined crown radius cannot ensure

whether or not the vertical profile covers the tree crown in case the tree is huge. In contrast, for a local maximum selected after the previous steps, the closest LM in terms of horizontal distance in eight directions (from  $0^\circ$  to  $360^\circ$ , at  $45^\circ$  spacing) are searched to ensure that the vertical profile can characterise the height variations of the entire tree crown. For a local maximum,  $0^\circ$  is defined as the direction where the x coordinates increase whereas the y coordinates remain stable.  $90^\circ$  is defined as the direction where the y coordinates increase whereas the x coordinates remain stable. Considering the fact that other LM may not be in the eight directions exactly, a 1-m buffer parallel to each direction is set as illustrated in Figure 7.3. For a local maximum  $LM_C$ , if another local maximum  $LM_j$  ( $LM_j \neq LM_C, j = 1, 2, \dots, q, q = \text{the total number of LM after the selection of highly accurate LM}$ ) is found within the buffer in direction  $V$  ( $V = 0^\circ + 45^\circ * t, t = 1, 2, \dots, 8$ ) and the horizontal distance between  $LM_C$  and  $LM_j$  is smaller than the horizontal distances between  $LM_C$  and other LM in the buffer,  $LM_j$  is regarded as the nearest local maximum in direction  $V$ . As stated above, no radius is pre-set for the search for the nearest LM in the eight directions to make ensure that the generated vertical profile can cover the whole crown regions. However, if no local maximum is identified as the nearest local maximum in direction  $V$ , the nearest local maximum in direction  $V$  will set as null. When the nearest LM in all eight directions are searched and identified, if the total number of the nearest LM is less than 4, the local maximum  $LM_C$  is discarded to ensure the accurate delineation of a tree crown. The vertical profile in direction  $V$  is generated by the points between  $LM_j$  and  $LM_C$ . Given the lidar points with the same horizontal coordinates but different height values, only the point with the largest height value is used. To expedite the computation process, two moving windows are introduced to move from the endpoints towards the middle, alongside the vertical profile between the two LM, respectively. The details of the two moving windows will be explained in Rule 2 in the following section. The main steps are described below and are illustrated in Figure 7.4:

- Step 1. For a local maximum ( $LM_C$ ), search the nearest LM in eight directions ranging from  $0^\circ$  to  $360^\circ$  increased by  $45^\circ$ ;
- Step 2. Generate the vertical profile of the lidar points between  $LM_C$  and  $LM_j$  ;
- Step 3. Each of two moving windows moves from one endpoint towards the middle of the vertical profile, and the boundary points of a tree crown are identified based on Rules 1-3 as explained in details in the following section;
- Step 4. Repeat Steps 2-3 until all eight vertical profiles are examined;

- Step 5. Generate a convex hull based on the derived boundary points, and take lidar points with all height values within the convex hull as part of the tree; the labelled lidar points will not be processed in the further steps;
- Step 6. Randomly select another local maximum and repeat Steps 1–5 until all LM are visited;
- Step 7. Check if all points are assigned as part of a tree segment; if not, sort out these points according to their elevation values in descending order and go to Step 8;
- Step 8. Set the point with the largest elevation value as the current local maximum and repeat Steps 1–5;
- Step 9. Remove the labelled points from the list and repeat Steps 7–8 until all points are labelled.

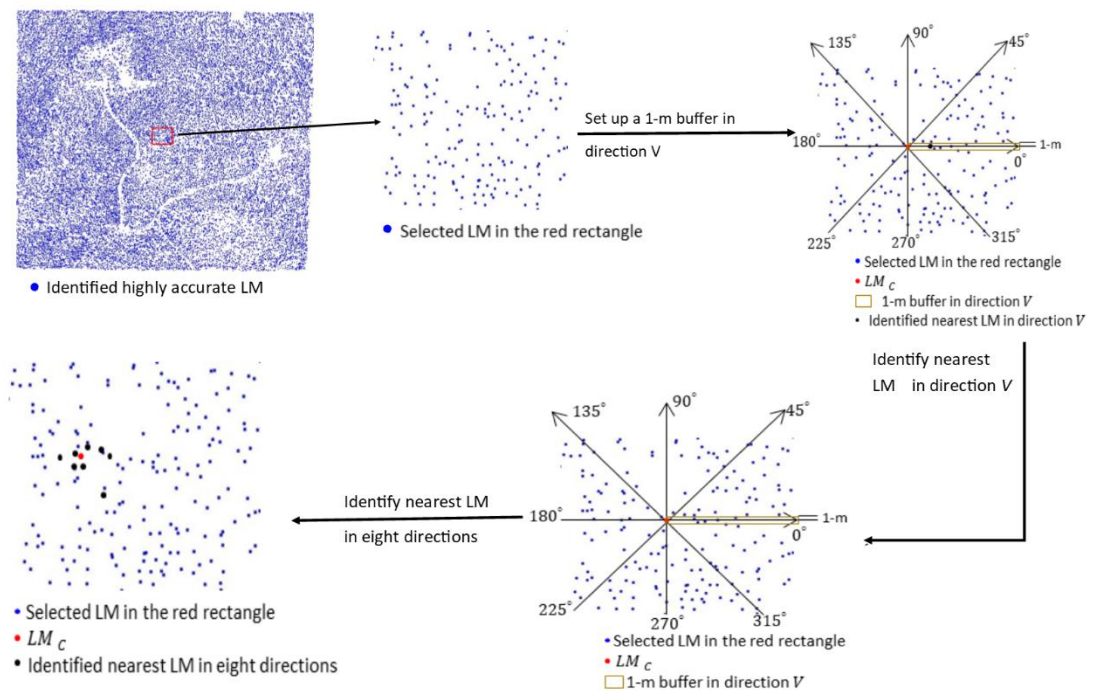


Figure 7.3 The identification of nearest local maxima in eight directions

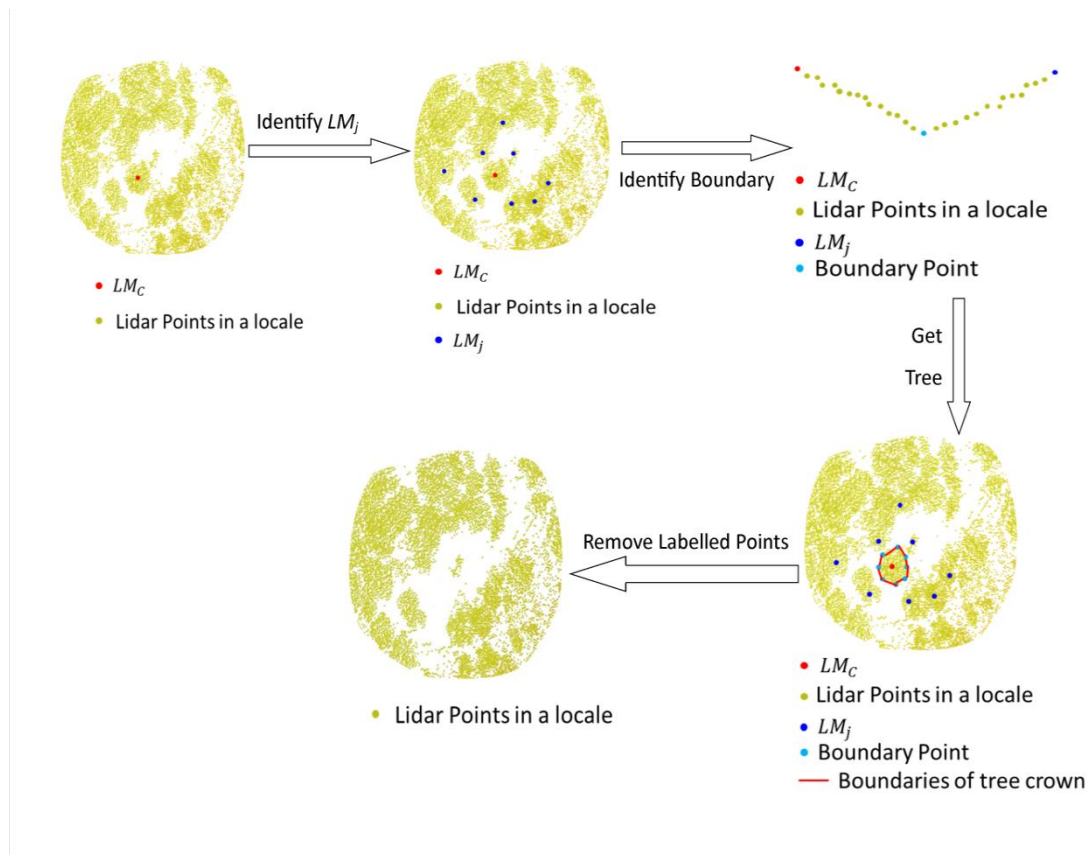


Figure 7.4 The concept of segmenting individual trees

To decide whether a point is a boundary point or not, three rules are proposed: (1) given the presence of a horizontal gap in the vertical profile because of the empty space between two trees, the point nearest to the gap is treated as a crown boundary point; (2) if a point is lower than the surroundings, it is regarded as a crown boundary point; (3) because of multiple returns within the canopy, more than one point with the lowest elevation may be present. In this case, the point with the largest elevation change is labelled as a crown boundary point.

#### Rule 1: Gap Identification

Since empty space between two trees may be present, there will be a horizontal gap in the vertical profiles. Therefore, the point nearest to the horizontal gap can be a crown boundary point. A Poisson distribution (Kingman, 2005) can be found in the Euclidean distances between two adjacent points. The Poisson distribution will become an approximately normal distribution after transforming the Euclidean distances to their square root (Thacker and Bromiley, 2001). If the square root of the Euclidean distance between two adjacent points is larger than three times the standard deviation from the square root of the mean value, the two points are assumed to have a gap, as shown in Eq. (7.3). Once a gap is identified, the point closest to the gap is labelled as a boundary point as demonstrated in Figure 7.5.

$$\begin{cases} \sqrt{D_{i,i+1}} > 3\delta + \sqrt{D_{mean}} \\ D_{mean} = (\sum_1^{p-1} \sqrt{(x_i - x_{i+1})^2 + (y_i - y_{i+1})^2}) / (p - 1) \\ \delta = \sqrt{\sum_1^{p-1} (\sqrt{(x_i - x_{i+1})^2 + (y_i - y_{i+1})^2} - D_{mean})^2} / (p - 1) \end{cases} \quad (7.3)$$

where  $D_{i,i+1}$  is the Euclidean distance between the point  $i$  and the point  $i + 1$ ;  $p$  is the total number of points in the vertical profile;  $\delta$  is the standard deviation of the Euclidean distances; and  $D_{mean}$  is the mean value of the Euclidean distances.

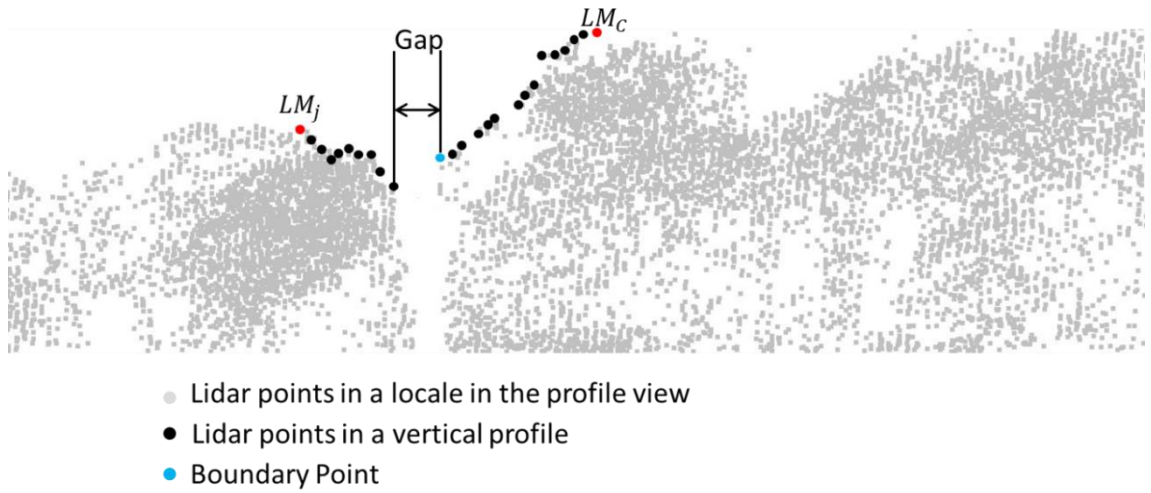


Figure 7.5 Gap identification

Rule 2: Identification of crown boundary points

As for a crown boundary point, its elevation is usually lower than the adjacent neighbours. Hence the elevation of a crown boundary point should meet the criteria given in Eq. (7.4).

$$\begin{cases} H_i < H_{i+1} + \alpha \\ H_i < H_{i-1} + \alpha \\ H_i < (H_{i+1} + H_{i-1})/2 \end{cases} \quad (7.4)$$

where  $H_i$ ,  $H_{i+1}$ ,  $H_{i-1}$  are the elevation values of the points  $i$ ,  $i + 1$ ,  $i - 1$ , respectively; and  $\alpha$  is a small value in case of natural variations in height values in the canopy since the height values of the points in a vertical profile do not always decrease continuously. If  $\alpha$  is set too large, it may fail to detect the boundary points. If  $\alpha$  is set too small, it may leads to the misclassification of non-boundary points because of the natural variations in height values. Based on trial and error,  $\alpha$  is set to 0.5 m.

As stated, two moving windows are used to accelerate the computation process and each window is wide enough to cover three consecutive points considering the variations in tree conditions. A moving window ( $W_1$ ) is used to analyse the points starting from  $LM_C$ . If a point satisfies the

criteria of Eq. (7.4), it is labelled as the start point. Meanwhile, another moving window ( $W_2$ ) is used to analyse the points starting from  $LM_j$ . A point is labelled as the end point once it meets the criteria of Eq. (7.4). If the start point and the end point are the same, the point is treated as a crown boundary point. The flowchart of Rule 2 is illustrated in Figure 7.6.

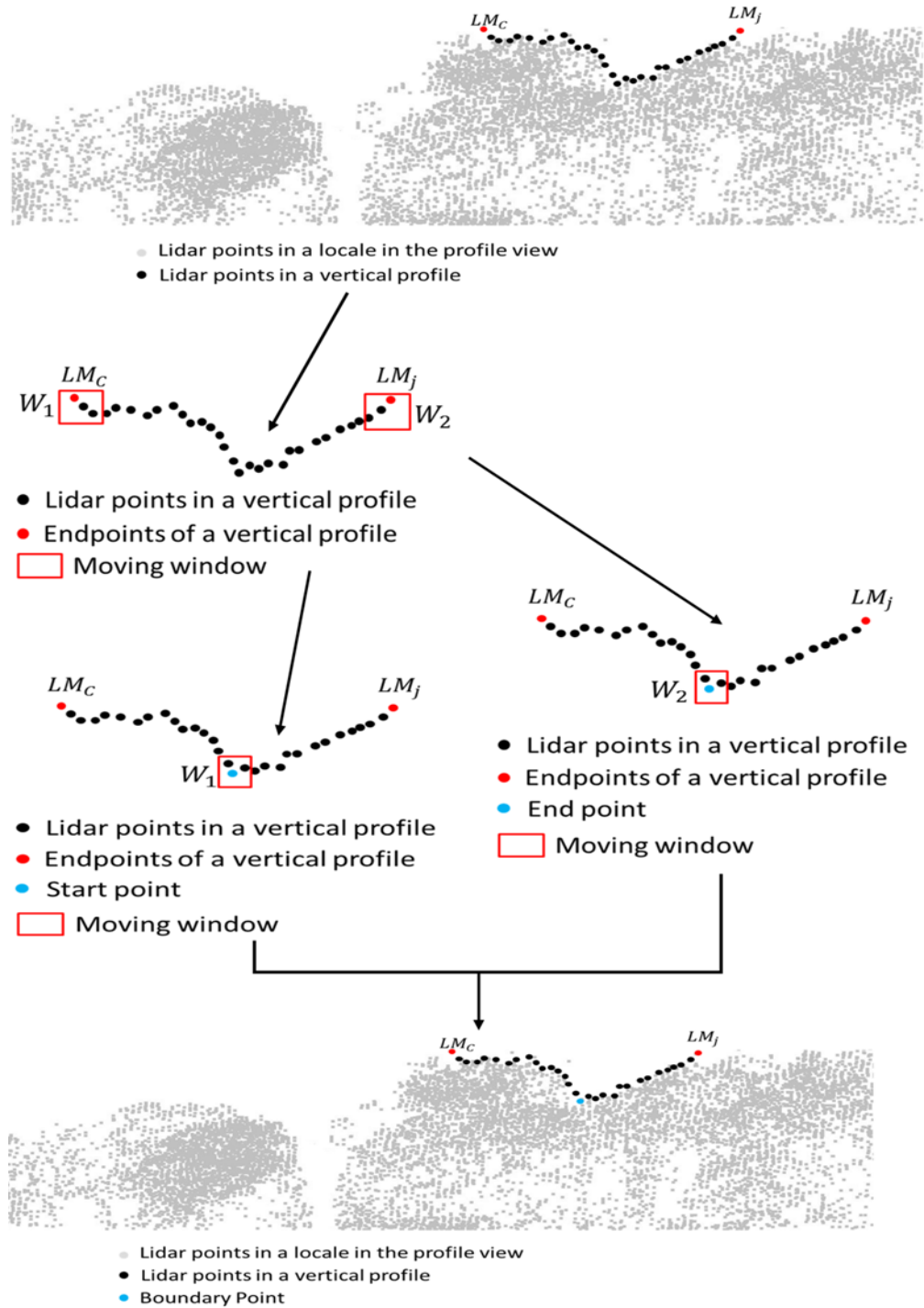


Figure 7.6 The identification of crown boundary points.

Rule 3: Identification of the largest elevation change

Due to the variation of vegetation height within the crown, the start point and the end point may be different. In this case, the third rule is applied. That is, the lowest point between the start point and the end point is considered as a boundary point. If there exist more than one lowest point, the elevation changes between the lowest points and the corresponding adjacent points are calculated. The removal of noises in lidar points is done at the data preparation stage, hence the lowest points with the largest elevation change are not noises and should be identified as boundary points.

### 7.1.3 *Detection of understory trees*

In this thesis, understory trees refer to the trees that are not entirely blocked by upper canopies because lidar pulses may not penetrate dense upper canopies. According to Popescu and Zhao (2008), a salient curve in a smoothed histogram generated by the histogram bins represents a canopy layer if the second derivatives of the histogram bins are negative. Therefore, the histogram of each segmented individual tree (which is referred to as tree segment hereafter) is analysed using the associated lidar points to examine the presence of understory trees. The bin width is set to 0.5 m to ensure enough points in each bin and meanwhile enough bins to detect the negative values in the second derivatives. The histogram analysis can be applicable to different tree species regardless of the crown size or the crown shape because it has no presumptions about the trees. The major steps are described below and are shown in Figure 7.7:

- Step 1. A height histogram is generated from the points in a tree segment;
- Step 2. A 3×3 Gaussian filter is applied to smooth the height histogram to reduce the impact of amplitude movement because of irregular lidar returns on the analysis results (Wang et al., 2008), and the window size is set to 3×3 to avoid oversmoothing;
- Step 3. Compute the second derivatives of the smoothed histogram;
- Step 4. If there are more than one negative values in the second derivatives, it indicates the presence of an understory tree. If so, go to Step 5; otherwise, go to Step 7;
- Step 5. Set the middle point of the interval between the top canopy layer and the second top canopy layer as the threshold to remove the top canopy layer, namely the points with height values above the threshold belong to the top canopy layer and will not be processed in the following steps, the top canopy layer is defined as the canopy layer with the highest elevation value among all the canopy layers as illustrated in Figure 7.7;

- Step 6. Set the second top layer as the current top layer and repeat Step 5 until all negative values are detected and examined;
- Step 7. Repeat Steps 1–6 until all tree segments are visited.

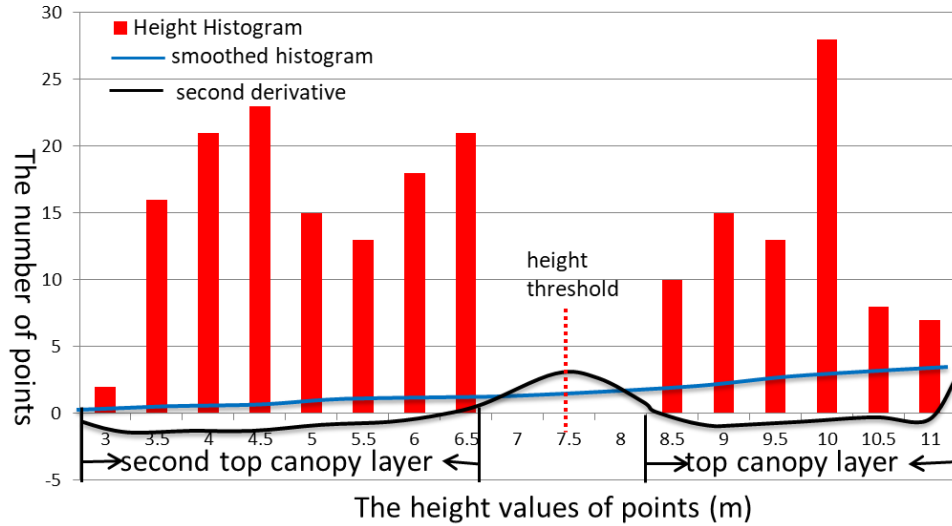


Figure 7.7 Height histogram analysis of a tree segment

As some branches extend outward, they can be misidentified as a layer if no constraints are applied. To reduce the risk of misclassification of branches as an understory tree, three constraints are proposed, namely, the number of points in a layer ( $N$ ), the maximum height of the layer ( $H_L$ ), and the ratio of the overlapped area to the area of the top layer ( $R_A$ ). The mathematical model is shown as Eq. (7.5).

$$\begin{cases} N \geq N_t \\ H_L \geq H_t \\ R_A \leq R_t \end{cases} \quad (7.5)$$

where  $N_t$ ,  $H_t$ ,  $R_t$  are the thresholds for  $N$ ,  $H_L$ ,  $R_A$ , respectively.

The principles of these constraints are: 1) there should be enough points in an understory tree; 2) the height of the understory tree should be high enough to avoid being totally blocked by the dominant tree; and 3) the overlap between the understory tree and the dominant tree should be small. Hence, if  $N$  of a sublayer exceeds  $N_t$ , the corresponding  $H_L$  is larger than  $H_t$ , and  $R_A$  is below  $R_t$ , then the sublayer is labelled as an understory tree. Although the algorithm is applicable to different tree species, the thresholds should be carefully chosen to obtain optimal results. For instance, a major branch can be misrecognised as an understory tree if a small  $N_t$ , a small  $H_t$  and a large  $R_t$  are used. In contrast, given a large  $N_t$ , some understory trees may fail to be identified because there may exist only a few points that belong to the understory trees. Based on experimental results,  $N_t$  is set to 100,  $H_t$  to 3 m and  $R_t$  to 25% for this study region.

## 7.2 Results and discussion

After applying the proposed method to the lidar data over the study region in Matlab R2013b (MathWorks, 2015), the total number of extracted individual trees ( $N_{DT}$ ) was 42,063 and the number of recognised understorey trees ( $N_{UT}$ ) was 5,803. Based on Eq. (6.4),  $N_{TP}$  was 152,  $N_{FN}$  was 24 and  $N_{FP}$  was 16; hence  $DR$  was 86.36%,  $E_{om}$  was 13.64% and  $E_{com}$  was 9.52%. According to Eq. (6.5),  $E_H$  and  $E_{CW}$  were 0.147 m and -0.004 m, respectively.  $MAE_H$  and  $MAE_{CW}$  were 0.416 m and 1.515 m, respectively.  $RMSE_H$  and  $RMSE_{CW}$  were 0.565 m and 1.988 m, respectively. To investigate the performance of proposed hybrid individual tree segmentation algorithm, tree segmentation results are also visualised at individual tree level because it is impractical to visualise more than 40,000 trees over the study region meanwhile demonstrating clearly if the individual tree segments suffer from oversegmentation or undersegmentation. According to Figure 7.8, the three tree segments delineate the trees accurately. However, because of few points presented in the red rectangle in Figure 7.8(b), it is difficult to determine whether these points belong to subdominant trees or not. Hence, these points are treated as part of the dominant tree.

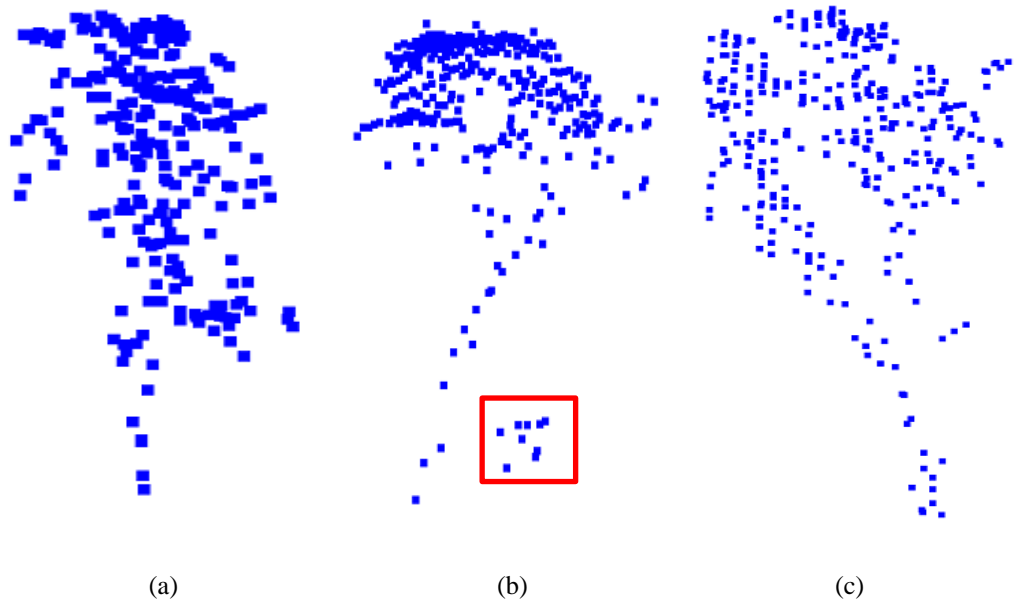


Figure 7.8 Three tree segments at individual tree level

To investigate the effect of the three constraints ( $N$ ,  $H_L$ ,  $R_A$ ) in the detection of understorey trees, an experiment without applying the three constraints was conducted. As a result,  $N_{DT}$  was 139,980 while  $N_{UT}$  was 103,270. The associated  $N_{TP}$  was 176,  $N_{FN}$  was 0 and  $N_{FP}$  was 1, hence  $DR$  was 100%,  $E_{om}$  was 0% and  $E_{com}$  was 0.56%. The corresponding  $E_H$  and  $E_{CW}$  were 0.011 m and -0.405 m, respectively,  $MAE_H$  and  $MAE_{CW}$  were 0.155 m and 1.673 m, respectively, and

$RMSE_H$  and  $RMSE_{CW}$  were 0.249 m and 2.269 m, respectively. To investigate the performance of the detection of understory trees, an analysis without applying the identification of understory trees was also conducted. According to the results,  $N_{DT}$  was 36,260,  $N_{TP}$  was 148,  $N_{FN}$  was 28 while  $N_{FP}$  was 18. Consequently,  $DR$  was 84.09%,  $E_{om}$  was 15.91% and  $E_{com}$  was 10.84%. The corresponding  $E_H$  and  $E_{CW}$  were 0.151 m and 0.181 m, respectively,  $MAE_H$  and  $MAE_{CW}$  were 0.442 m and 1.539 m, respectively and  $RMSE_H$  and  $RMSE_{CW}$  were 0.592 m and 2.014 m, respectively. The distributions of the differences of tree height and crown width for various conditions are shown in Figure 7.9. According to Figure 7.9(b), without the detection of understory trees, the majority of the differences of crown width between the results and the reference data range from -2 m to 4 m. In contrast, after the detection of understory trees, the differences of crown width between the results and the reference data mostly are between -2 m and 2 m. The comparison of Figure 7.9(b) and (d) indicates without the detection of understory trees, the extracted trees may suffer from undersegmentation whereas the detection of understory trees can isolate the understory trees from dominant trees, therefore obtaining accurate tree crowns. However, if the three constraints are not applied during the detection of understory trees, most of the differences of crown width between the extracted results and the reference data are from -4 m to 0 m, which indicates the results may suffer from oversegmentation. The statement is validated by the fact that, according to Table 7.1, without the application of the three constraints, the corresponding  $E_{CW}$  is negative and the absolute value is much larger than that of  $E_{CW}$  when applying the three constraints. Although the oversegmentation results in the increase of  $N_{DT}$  and  $N_{UT}$ , therefore leading to the better detection rate and smaller omission errors, the performance of the algorithm without the application of three constraints is worse since the absolute values of the  $MAE_{CW}$  and  $E_{CW}$  are larger, especially the  $E_{CW}$ . Conversely, without the detection of understory trees,  $N_{DT}$  and  $N_{TP}$  both decrease. Hence the  $DR$  decreases while the  $E_{om}$  increases. Moreover, the corresponding  $E_H$  and  $E_{CW}$  become larger since the understory trees are misidentified as parts of the dominant trees. Overall, the detection of understory trees enhances the detection rate, reduces omission error and commission error, and improves the accuracy of extracted tree height and crown width.

Table 7.1 The results of the proposed method in various conditions

	Without the detection of understory trees	With the application of three constraints	Without the application of three constraints
$N_{DT}$	36,260	42,063	139,980
$N_{UT}$	-	5,803	103,270
$N_{TP}$	148	152	176
$N_{FN}$	28	24	0
$N_{FP}$	18	16	1
$DR$ (%)	84.09	86.36	100
$E_{om}$ (%)	15.91	13.64	0
$E_{com}$ (%)	10.84	9.52	0.56
$E_H$ (m)	0.151	0.147	0.011
$MAE_H$ (m)	0.442	0.416	0.155
$E_{CW}$ (m)	0.181	-0.004	-0.405
$MAE_{CW}$ (m)	1.539	1.515	1.673
$RMSE_H$ (m)	0.592	0.565	0.249
$RMSE_{CW}$ (m)	2.014	1.988	2.269

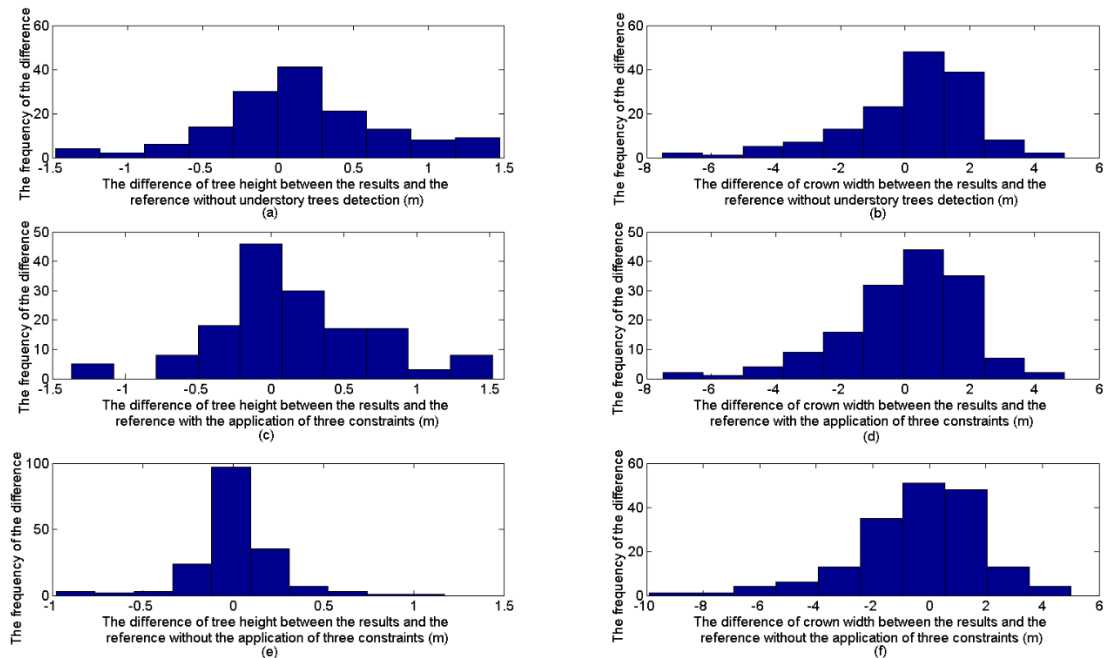


Figure 7.9 The distributions of the differences of tree height and crown width for various conditions

When compared with the results derived from existing individual tree segmentation algorithms in Table 6.1, the proposed method produced the highest number of correctly located trees, the highest detection rate and the smallest omission error and commission error because of the detection of understory trees as well as the introduction of the three constraints in the identification of understory trees. In addition, because of the balance between the commission and omission errors of LM by applying a modified ITCD algorithm and introducing the  $I_{LM}$  to select highly accurate LM, the proposed hybrid method produced the smallest commission error and omission error of identified individual trees. Although its absolute value of  $E_H$  is larger than that of  $ITCD_1$  and  $FLM_1$ , the corresponding  $RMSE_H$  and  $MAE_H$  are smaller, which indicates that the extracted tree heights, in general, deviate less from the reference values. Moreover, according to Figure 7.9, 69.74% of the tree height differences between the proposed algorithm and the reference are between -0.5 m and 0.5 m. In contrast, according to Figure 6.2, only 56.49% of the tree height differences between the  $ITCD_1$  and the reference range from -0.5 m to 0.5 m. The comparisons validate the tree heights derived from our proposed algorithm are the most accurate. In terms of the crown width, our proposed algorithm obtain promising results as well, which is proven by small absolute values of  $MAE_{CW}$ ,  $E_{CW}$ , and  $RMSE_{CW}$ . Although the absolute values of  $MAE_{CW}$ ,  $E_{CW}$ , and  $RMSE_{CW}$  for the proposed algorithm are slightly larger than that of  $VLM_1$ , the proposed algorithm outperforms VLM when measured in terms of tree height, detection rate, commission error, and omission error. Overall, the proposed algorithm has the best performance.

### 7.3 Summary

In this chapter, a hybrid method is present to segment individual trees from airborne lidar data by modifying a CHM-based algorithm and integrating it into a point-based vertical profile analysis algorithm. The main idea is to take advantage of the efficiency of local maxima identification from the CHM-based algorithm and the ability of capturing accurate tree heights and identifying understory trees from the point-based algorithm. More specifically, a multiscale local maxima algorithm is applied to the CHMs at various spatial resolutions and a local maxima index is introduced to select the highest accuracy local maxima from the identified local maxima at each spatial resolution, which is one novelty of the proposed method. This method provides a better balance between the commission and omission errors of the identified local maxima in comparison with other algorithms. Since tree heights yielded by CHM-based tree segmentation methods may be lower than the actual values, seed points which are close to and have identical height values with the final local maxima are used instead of the final local maxima directly. Once the seed points are found, a vertical profile analysis is exploited to recognise the crown boundaries of a tree and segment lidar points. To detect the understory trees, a histogram analysis is applied

to check if an understory tree exists in a tree segment. To reduce the misclassification of the outward extending branches as a separate tree, three constraints are proposed, including the number of points in a layer, the maximum height of the layer, and the ratio of the overlapped area between a sublayer and the top layer to the area of the top layer. The introduction of these three constraints is another novelty of the proposed method. Field measurements of tree heights and crown widths are used to compare with the extracted individual tree parameters. The comparisons demonstrate that the mean errors and the RMSEs between the estimated and ground truth heights are 0.147 m and 0.565 m, respectively, and the mean errors and the RMSEs for the crown widths are -0.004 m and 1.988 m, respectively. The presented results suggest that the proposed method can extract individual treetops and crown widths accurately. The results are also compared with the results in Chapter 6 generated by five commonly-used single tree extraction methods. The comparison results exhibit that the proposed method outperforms others in terms of detection rate, omission error, commission error, mean absolute error of height, and RMSE of height. Although the crown widths generated by the proposed algorithm are less accurate than that of VLM, the proposed algorithm has overall the best performance, correctly segmenting a large amount of individual trees meanwhile maintaining a good accuracy in terms of tree height and crown width.

However, because no understory trees are recorded in the field measurements, it is impossible to investigate the accuracy of identified understory trees separately so that the overall accuracy of all extracted individual trees were examined instead. In addition, the proposed approach requires a certain amount of points to represent an understory tree so that the understory tree can be detected. If an understory tree is heavily blocked by some dominant trees and only a few points belong to the understory canopy, the algorithm may fail to identify it. Another weakness of the proposed method is associated with the computational time. Although a modified CHM-based algorithm is applied to capture local maxima and a moving-window based vertical profile analysis to accelerate the computational process, the proposed hybrid method is still time-consuming. Once the extraction of individual tree parameters is done, the final step of the framework is the generation of the AGB regression model. DBH is a conventional parameter for AGB estimation, which is explored by many scholars (Williams et al., 2005; Paul et al., 2015). However, because of the lack of points at the breast height of a tree in lidar data, it is impossible to extract DBH directly from segmented individual trees. Hence, in Chapter 8, a DBH regression model will be firstly generated based on extracted tree height and crown width since the DBH is a function of tree height and crown width (Verma, et al., 2014). Because the field measurements of the AGB for individual trees are not available in the study region, the existing generalised AGB allometric models will be utilised to compute the AGB and the computed AGB estimates will be used as the reference to generate the AGB regression model. Different machine learning algorithms will also

be explored since the acquired regression method has an impact on the accuracy of the generated regression model. The details will be shown in Chapter 8.

## **Chapter 8 : The Generation of Aboveground Biomass Regression Model for Individual Trees**

Once the individual trees are segmented from airborne lidar data and the corresponding individual tree parameters are extracted, the final step of the framework of the AGB estimation for individual trees from airborne lidar data is to generate the AGB regression model based on field measurements of AGB estimates and lidar-based metrics. To generate an AGB regression model, field samples of AGB for individual trees are required as a reference. Although these localised AGB regression models generate the most accurate AGB estimations for the regions where the models have been developed; they can yield substantial biases when applied to a different study region (Paul et al., 2015). Moreover, reference data on AGB is not always available, and it is difficult to collect at some inaccessible forests. Hence, some scholars have tackled the issue by building generalised AGB models based on the assumption of representing the AGB estimation by one allometric relationship, irrespective of site or species. These generalised AGB allometric models have been developed with a large number of field tree samples in different locations and species and can minimise the uncertainties in AGB estimation (Chave et al., 2004; Van Breugel et al., 2011) compared to the majority of localised AGB allometric models (Paul et al., 2015). Hence, in this chapter, three generalised AGB allometric models will be used to compute the AGB estimates as the reference since the field sampled AGB estimates are not available in the study region. For each set of AGB estimates generated by different existing generalised AGB allometric models, four machine learning techniques will be applied to generate the AGB regression model, including random forest, support vector regression, multilayer perceptron and radial basis function. To distinguish existing allometric models from newly generated models, the existing allometric models are referred to as allometric models whereas the newly generated models are referred to as regression models in this chapter. The chapter is structured as follows: Section 8.1 describes the details of the method of AGB regression model generation; the results of the AGB regression model generation are present in Section 8.2 and Section 8.3 summarises the chapter and discusses the pros and cons of the method of the generation of AGB regression model.

### **8.1 Methodology**

DBH is a widely-used variable for AGB estimation for individual trees, which is used by many scholars (Williams et al., 2005; Paul et al., 2015). However, there are not enough lidar points at the breast height level of a tree, hence it is difficult to retrieve the DBH based on airborne lidar data. To tackle this issue, a DBH regression model is generated based on the obtained tree

height and crown width because the DBH of a tree is strongly related to the corresponding tree height and crown width (Verma et al., 2014). Since there is no consensus on the statistical method used to generate regression models and the acquired statistical method will influence the accuracy of the generated regression models, different machine learning algorithms are explored including random forest, support vector regression, multilayer perceptron multilayer perceptron and radial basis function. The DBH results yielded by various machine learning techniques are compared to the reference DBH records to analyse the accuracy of the derived DBH results. The most accurate DBH results are selected as input for the generation of the AGB regression model for individual trees. Because field samples of the AGB for individual trees are not available for the study region, three existing generalised AGB allometric models are applied to compute the AGB estimates as the reference, respectively. For each set of the calculated AGB estimates, the four aforementioned machine learning techniques are applied to generate the AGB regression model, separately. The flowchart of the methodology is shown in Figure 8.1.

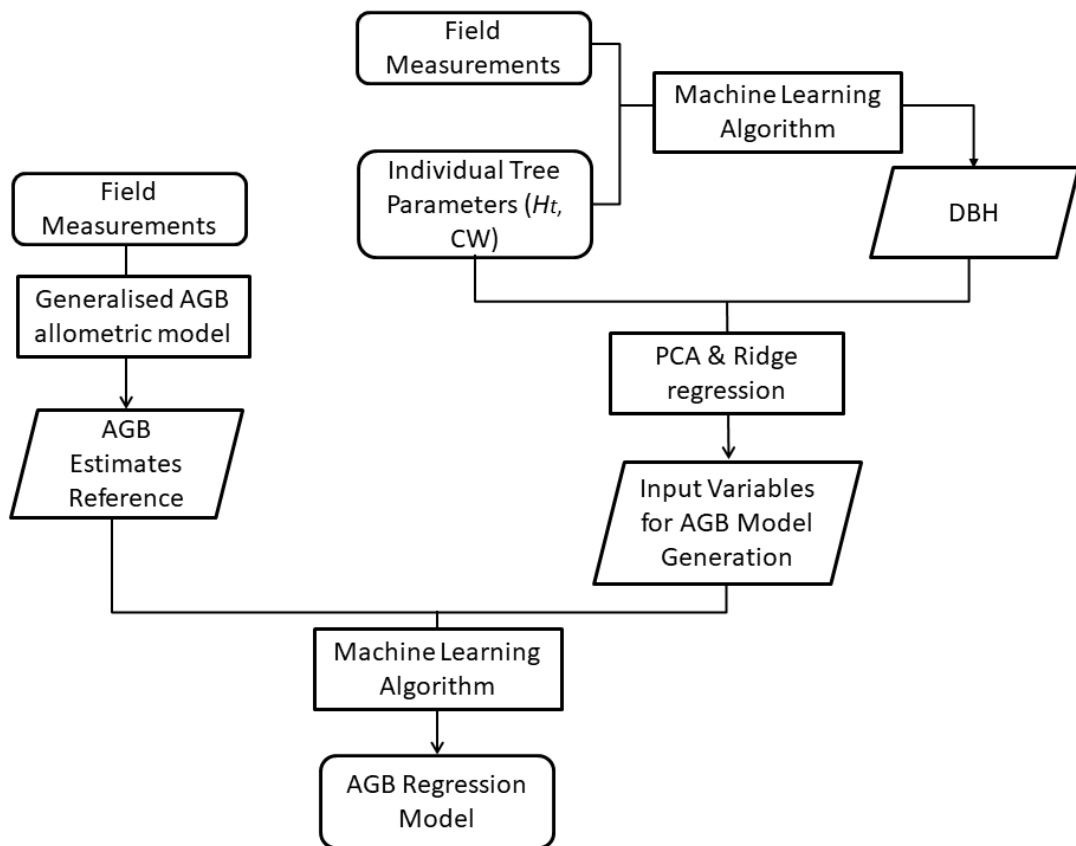


Figure 8.1 Flowchart of the methodology

### 8.1.1 Generating the DBH allometric model

DBH is an important tree parameter which can be used to infer canopy attributes and estimate the AGB of the tree (Verma et al., 2014). However, it is difficult to obtain accurate DBH of individual trees based on lidar points since few lidar points are present at 1.30 m from the ground for each segmented individual tree. To obtain the DBH of individual trees, a DBH regression model is generated based on the lidar-based tree height and crown width, because the DBH of a tree is correlated to the corresponding tree height and crown width, which has been examined in numerous studies (Hall et al., 1989; Gering and May, 1995; Arzai and Aliyu, 2010; Verma et al., 2014). To remove the impact of outliers in the field measurements, DBH records are checked manually before the generation of the DBH regression models and two records of field DBH observations are removed because their values are obviously deviated from other records even though the corresponding values of tree heights and crown widths are similar. Once the manual check of outliers is finished, the lidar-derived tree parameters are calibrated with the corresponding field DBH observations to generate the regression model of the DBH. Lu (2006) pointed out that the regression techniques could influence the accuracy of the generated model. To get the most accurate DBH, thus enhancing the results of the AGB estimation, the DBH regression model is generated by using four commonly applied machine learning techniques, including random forest, support vector regression, multilayer perceptron and radial basis function. Random forest is selected because of its robustness and the ability to handle data with multicollinearity. Support vector regression is selected because it was proven to be useful in AGB estimation (Gleason and Im, 2012). Multilayer perceptron, a deep learning technique, remains a hot-topic because of the great interest in deep learning and the selection of the multilayer perceptron can demonstrate if the estimation of AGB can benefit from deep learning. Like deep learning techniques, radial basis function network is also trained by a two-step algorithm, the unsupervised learning in the first step and the supervised learning in the second step. It is chosen because it has the advantages of easy design, high tolerance to noises and good generalisation (Hu et al., 2011). These machine learning techniques were operated in Matlab R2013b (MathWorks, 2015) with a CPU of Intel (R) Core(TM) i7-472 4900 and a 16 GB installed memory.

Random forest is insensitive to overfitting and credited for its ability to handle data with high dimensionality and multicollinearity (Hudak et al., 2008; Falkowski et al., 2009; Korpela et al., 2009) and has been explored intensively to estimate the DBH (Wu et al., 2015) and the AGB (Avitabile et al, 2012). The concept of random forest is that a set of binary rule-based decision trees are generated to determine the relationship between the input variables and the predictor variable. If splitting a single rule into multiple rules produces lower errors than using a single rule, the regression tree will grow more rules. Once the minimum error versus the input data is achieved, the decision tree will stop growing. These decision trees can depict complicated relationships

among variables at different scales accurately (Walton, 2008), thus leading to better performance when these decision trees are aggregated. However, since each decision tree is set randomly, it may generate different results every time the model is running (Walton, 2008). To solve this problem, the leave-one-out cross-validation is applied to demonstrate how the selection of training datasets in the training phase would influence and verify the results of the model. Namely, each time, one observation is left out as the testing dataset to validate the model created by the remaining (n-1) observations as the training dataset until all the observations are visited. Hence, each time, the random forest will generate a regression model and a prediction will be made based on the corresponding test dataset. This procedure is repeated until all the observations are processed. The model with the minimal difference ( $D_{min}$ ) between the prediction value ( $PV$ ) and the corresponding test observation value ( $OV$ ) is selected as the finalised regression model. The average of the squares of the differences ( $ASD$ ) between the prediction values and the corresponding test observation values is used to assess the robustness of the machine learning method as shown in Eq. (8.1).

$$ASD = \frac{1}{n} \sum_{i=1}^n (e_i)^2 \quad (8.1)$$

where:  $e_i$  is the difference between the prediction value and the corresponding test observation value in step  $i$ ; and  $i$  is the serial number of the repeating step.

As an application of support vector machines (SVM), support vector regression has been successfully used to estimate leaf area index (LAI, Durbha et al., 2007), to predict soil properties (Ballabio, 2009), and to estimate AGB (Gleason and Im, 2012). Support vector regression assumes that each set of input parameters is related to its response variable, and grouping the predictors can identify rules for predicting the response variable from a set of inputs. To identify the rules, support vector regression assumes that input data can be separated in feature space and separates the data among multidimensional hyperplanes. Hyperplanes are existing features in feature space, which is a multidimensional space built from input variables. Based on the value of the predictor variable, every response variable can be located in the hyperplanes, and similar responses will be spatially clustered in the feature space. To allocate each observation to the hyperplanes, support vector regression uses “support vectors” and iteratively adjusts the hyperplanes based on the errors until the optimal results are achieved. In the implementation of the support vector regression, the radial basis kernel function is chosen because of its good performance on forest parameter estimation and because few parameters are needed to be defined (Huang et al., 2008; Kavzoglu & Colkesen, 2009; Kuemmerle et al., 2009). The classic grid search is employed to optimise the parameters. The aforementioned leave-one-out cross-validation is

also applied in the support vector regression network training to select the finalised regression model and test the robustness of the support vector regression method.

Multilayer perceptron is one of the most commonly used feed-forward networks and is famous for solving sophisticated image classification problems. It typically contains three types of layers, namely the input layer, the hidden layer and the output layer. These layers are made up of neurons. The neurons in the input layer serve to transfer the input data into the neurons in the hidden layers. Each of the neurons in the hidden layers estimates the weights of the inputs by analysing the strengths of connections of the input data from the input layer, sums up the weighted input data, and computes the output of the hidden layers. The neurons in the output layers work similarly. Multilayer perceptron uses a gradient descent algorithm to adjust the weight of the connection between neurons  $s$  and  $t$  (denoted by  $\Delta\omega_{(s,t)}$ ) as shown in Eq. (8.2). Starting with the output layer, multilayer perceptron determines the weight of the connections iteratively until the optimal results are achieved. To select the regression model with the best quality, the strategy of leave-one-out cross-validation is also applied in the training of the multilayer perceptron neural network because the selection of training samples and test samples has a critical effect on the generated regression model. To avoid overfitting resulted from the small size of samples, widely-used approaches include early-stopping, noise injection, and optimization approximation algorithm (Piotrowski and Napiorkowski, 2013). In this research, the early-stopping strategy is adopted by lowering the pre-set goal of accuracy, limiting the number of epochs and the number of neurons because of the ease of implementation.

$$\begin{cases} \Delta\omega_{(s,t)} = R\delta_t x_s \\ \delta_t = (\partial f / \partial \text{sum}_t) (y_t^P - y_t) \text{ if } t \text{ is the output neuron} \\ \delta_t = (\partial f / \partial \text{sum}_t) (\sum_q \omega_{(q,t)} \delta_q) \text{ if } t \text{ is the hidden neuron} \end{cases} \quad (8.2)$$

where:  $R$  is the learning rate which affects the coverage rate of the weight;  $x_s$  is the input of neuron  $s$ ;  $\partial$  is the function to obtain the derivative of the input;  $f$  is the function to transfer the sum of the weighted input to the output;  $\text{sum}_t$  is the total sum of the weighted input to  $t$ ;  $y_t^P$  is the predicted value of the output of  $t$ ,  $y_t$  is the target output of  $t$ ; there is no target output if  $t$  is the hidden neuron, and  $(y_t^P - y_t)$  is therefore replaced by the weighted sum of  $\delta_q$  that has already been obtained for neuron  $q$  connected to neuron  $t$ , and  $\omega_{(q,t)}$  is the weight between the neuron  $t$  and  $q$ .

By contrast with multilayer perceptron, radial basis function neural network processes the neurons in the input layer with a linear function and then passes the input to the hidden layers. Moreover, the connections between the neurons in the input and hidden layers are not weighted. Radial basis

function neural network uses a radial basis function to process the hidden layers and the output layer is the summing procedure to compute the weighted sum of the hidden layer output as the final output. In the implementation of the function, the classic Gaussian kernel is selected. The leave-one-out cross-validation strategy is also applied to select the finalised regression model and to test robustness of the algorithm and the early-stopping strategy is used to avoid overfitting by lowering the pre-set goal of accuracy, limiting the number of epochs and the number of neurons.

For each site-specifically generated DBH regression model, the corresponding predicted DBH results are compared with the field DBH measurements to compute the mean absolute error ( $MAE_{DBH}$ ),  $RMSE_{DBH}$  and standard deviation ( $\sigma_{DBH}$ ) to further assess the accuracy of the model-based DBH results. The mathematical models of the three metrics are shown in Eq. (8.3). Two existing generalised DBH allometric models (Jucker et al., 2017) are also compared with the newly-generated DBH regression models in terms of the  $MAE_{DBH}$ ,  $RMSE_{DBH}$  and  $\sigma_{DBH}$  to investigate the performance of these generated DBH regression models. The two generalised DBH allometric models include one designed for the angiosperm trees in mixed forests in Australasia shown in Eq. (8.4) and another designed for all global tree species shown in Eq. (8.5). Comparisons of the two generalised DBH models and site-specific DBH models can also demonstrate if the generalised DBH models can be useful when a medium accuracy is sufficient and if a globally generalised model performs the worst. The predicted DBH values with the highest accuracy measured in terms of  $MAE_{DBH}$ ,  $RMSE_{DBH}$  and  $\sigma_{DBH}$  will be used as one of the input parameters in the AGB regression model generation in the following steps.

$$\begin{cases} MAE_{DBH} = \frac{1}{n} \sum_{m=1}^n |PV_{DBH_m} - OV_{DBH_m}| \\ ME_{DBH} = \frac{1}{n} \sum_{m=1}^n (PV_{DBH_m} - OV_{DBH_m}) \\ RMSE_{DBH} = \sqrt{\frac{1}{n} \sum_{m=1}^n (PV_{DBH_m} - OV_{DBH_m})^2} \\ \sigma_{DBH} = \sqrt{\frac{1}{n} \sum_{m=1}^n (PV_{DBH_m} - OV_{DBH_m} - ME_{DBH})^2} \end{cases} \quad (8.3)$$

where:  $m=1,2,\dots,n$ ;  $PV_{DBH_m}$  and  $OV_{DBH_m}$  are the predicted value and the observation value of the  $m^{\text{th}}$  observation datasets, respectively;  $ME_{DBH}$  is the mean value of the differences between the predicted values and the observation values.

$$\ln(\text{DBH}) = 0.769 + 0.811 \times \ln(H \times CW) \quad (8.4)$$

$$\text{DBH} = 0.557 \times (H \times CW)^{0.809} \times \exp(0.056^2/2) \quad (8.5)$$

where:  $\exp$  is the exponential function.

### 8.1.2 Generating the AGB regression model

As stated above, to generate the AGB regression model for individual trees in a study area, it requires field sampling of AGB as a reference to calibrate with lidar-based metrics so that they can be used to predict the AGB for all the individual trees in the study region. However, field measurements of AGB are not always available because of the inaccessibility of the forest. Hence, some scholars refer to generalised AGB allometric models to compute the AGB estimates when medium accuracy is required. Since the field measurements of AGB are not available in this study, the existing generalised AGB allometric models are exploited to compute the AGB estimates of individual trees as the reference and generate the AGB regression models for individual trees based on computed AGB estimates and corresponding individual tree parameters. The core steps are as follows: firstly, the AGB estimates of individual trees are computed as the reference based on the models of Paul, Williams and Jucker; the mathematical models are shown in Eqs. (8.6)-(8.8), respectively. Secondly, for each set of reference AGB estimates, four machine learning techniques are applied to generate the AGB regression models. Thirdly, the accuracy of the generated AGB regression models is investigated based on the adjusted coefficient of determination ( $\bar{R}^2$ ), ASD, Akaike information criterion (AIC, Akaike, 1974), normalised-mean-square-error of the AGB estimates ( $NMSE_{AGB}$ , Poli and Cirillo, 1993) and model efficiency index (EI, Soares et al., 1995).

$$\ln(\text{AGB}) = 2.375\ln(\text{DBH}) - 2.016 \quad (8.6)$$

$$\ln(\text{AGB}) = -2.0596 + 2.1561\ln(\text{DBH}) + 0.1362(\ln(H))^2 \quad (8.7)$$

$$\text{AGB} = (0.016) \times (H \times CW)^{2.013} \times \exp\left(\frac{0.204^2}{2}\right) \quad (8.8)$$

#### 8.1.2.1 Selecting input variables

When generating the AGB regression models, the selection of variables is crucial. Typical variables for the estimation of AGB include  $DBH$ ,  $H$ ,  $DBH^2 \times H$ ,  $DBH \times H$ ,  $DBH^2$ ,  $DBH \times H^2$  and some scholars have used  $DBH$  or  $H$  only, or used combinations of variables to generate the model. Since in this study  $DBH$  is computed based on the function of tree height and crown width instead of being obtained from lidar points directly,  $CW$  is also chosen as a variable in the generation of the AGB regression model. Principal component analysis (PCA, Lever et al., 2017) is also conducted before the regression process to check if there is multicollinearity in the seven variables. If the eigenvalues of some variables are close to 0, multicollinearity is shown in these variables. To remove the multicollinearity, ridge regression is applied to show the ridge traces of each variable. Details of the ridge regression can be found in Hoerl and Kennard (1970). Two

rules are set as follows: (1) remove the variable whose ridge trace is stable when the biasing parameter changes; (2) remove the variable whose ridge trace never converges. The processes of PCA and ridge regression also enhance the selection of variables, which will accelerate the regression process when less important variables are removed. Once the input variables are selected, for each set of reference AGB estimates, the aforementioned four machine learning techniques are applied to generate the AGB regression model, separately. The parameters of the four algorithms are determined based on trial and error to ensure the optimal results, since there is no common guidance for selecting the parameters.

### 8.1.2.2 Assessing the generated AGB regression model

After the generation of the AGB regression models, these models are assessed based on the five metrics, namely,  $\bar{R}^2$ , ASD, AIC,  $NMSE_{AGB}$ , and EI. The mathematical models of  $\bar{R}^2$ , AIC,  $NMSE_{AGB}$  and EI are as shown in Eq. (8.9). Rather than using classic  $R$ -squared,  $\bar{R}^2$  is used so that adding irrelevant independent variables to the model will be penalised. The ASD results can show the robustness of the model. AIC provides a method to select the model by estimating the relevant information lost by a model. It makes a trade-off between the fitness and the simplicity of the model and assumes that a model has a good quality if it loses less information. Since the accuracy of the AGB estimates derived from existing generalised AGB allometric models is unknown, traditional RMSE and the mean of the absolute differences between the predictions and the observations cannot demonstrate the quality of the generated AGB regression model if the three sets of AGB estimation reference are not at the same scale. Hence,  $NMSE_{AGB}$  is selected to normalise the differences between the predictions and the observations and demonstrate how the predictions deviate from the observations. EI can measure the fitness of the model. When EI is 0, this means that using the average of the observation values is more accurate than using the predicted values, whereas a value of 1.0 indicates a perfect fit.

$$\left\{ \begin{array}{l} \bar{R}^2 = 1 - (1 - R^2) \frac{n-1}{n-p-1} \\ AIC = 2p + n \times \ln(\sum_{m=1}^n (PV_{AGB_m} - OV_{AGB_m})^2 / n) \\ NMSE_{AGB} = \frac{n \times \sum_{m=1}^n (PV_{AGB_m} - OV_{AGB_m})^2}{\sum_{m=1}^n PV_{AGB_m} \times \sum_{m=1}^n OV_{AGB_m}} \\ \delta_{AGB} = \sqrt{\frac{1}{n} \sum_{m=1}^n (PV_{AGB_m} - OV_{AGB_m})^2} \\ EI = 1 - \frac{(\delta_{AGB})^2}{\sigma^2} \end{array} \right. \quad (8.9)$$

where:  $R^2$  is the coefficient of the determination of the generated model;  $p$  is the number of variables in the model;  $\ln$  is the function to get the natural logarithm of the input;  $PV_{AGB_m}$  and  $OV_{AGB_m}$  are the predicted value and the observation value of the  $m^{th}$  observation dataset;  $\delta_{AGB}$  is

the root-mean-square differences between predicted values and the corresponding observation values;  $\sigma^2$  is the mean square differences between each observation and the mean of the observations.

## 8.2 Results and discussion

As stated above, after the manual check of outliers, two records of DBH field observations were treated as outliers and removed. Hence, the total number of DBH field observations used in the generation of DBH regression model was 150. After applying the machine learning algorithms to generate the DBH regression model, the accuracy of the predicted DBH values derived from the various DBH regression models is shown in Table 8.1. Figure 8.2 illustrates the relationship between the predicted DBH values and field DBH observations for each machine learning method and shows the variety of predictions across the different site-specifically generated DBH regression models. The analysis of the results in Table 8.1 demonstrates that random forest performed the best since the corresponding  $MAE_{DBH}$ ,  $RMSE_{DBH}$  and  $\sigma_{DBH}$  were the smallest. In contrast, radial basis function yielded the largest  $MAE_{DBH}$  and  $\sigma_{DBH}$  when compared with the other machine learning techniques. A further investigation indicates that, while the value of  $MAE_{DBH}$  for radial basis function was the largest, the  $ME_{DBH}$  of radial basis function was 0, which means that the DBH regression model generated by radial basis function suffered from overfitting. The problem of overfitting also occurred in the DBH regression model derived from multilayer perceptron since the corresponding  $ME_{DBH}$  was even smaller than that of random forest. One plausible explanation is that radial basis function and multilayer perceptron are designed for solving more sophisticated problems, whereas the total number of observations used in the generation of the DBH models was relatively small. In terms of the performances of the two existing generalised DBH allometric models, they were worse than the site-specifically generated DBH regression models. It is obvious that localised models yield more accurate results than generalised models. When comparing the performance of these two generalised DBH allometric models, the globally generalised DBH allometric model underperformed the DBH allometric model designed based on samples in Australasia. The bad performance of the globally generalised DBH allometric model may be caused by the fact that the many forest conditions are considered when generating the model and some of the forests conditions are different from the study region, which may degrade the accuracy of the results. However, the Australasian generalised model only takes forest samples in the Australasian region into account so that its performance improves to some extent. Overall, the predicted DBH results yielded by random forest were served as the input in the following processes because of the high accuracy measured by  $MAE_{DBH}$ ,  $RMSE_{DBH}$  and  $\sigma_{DBH}$ .

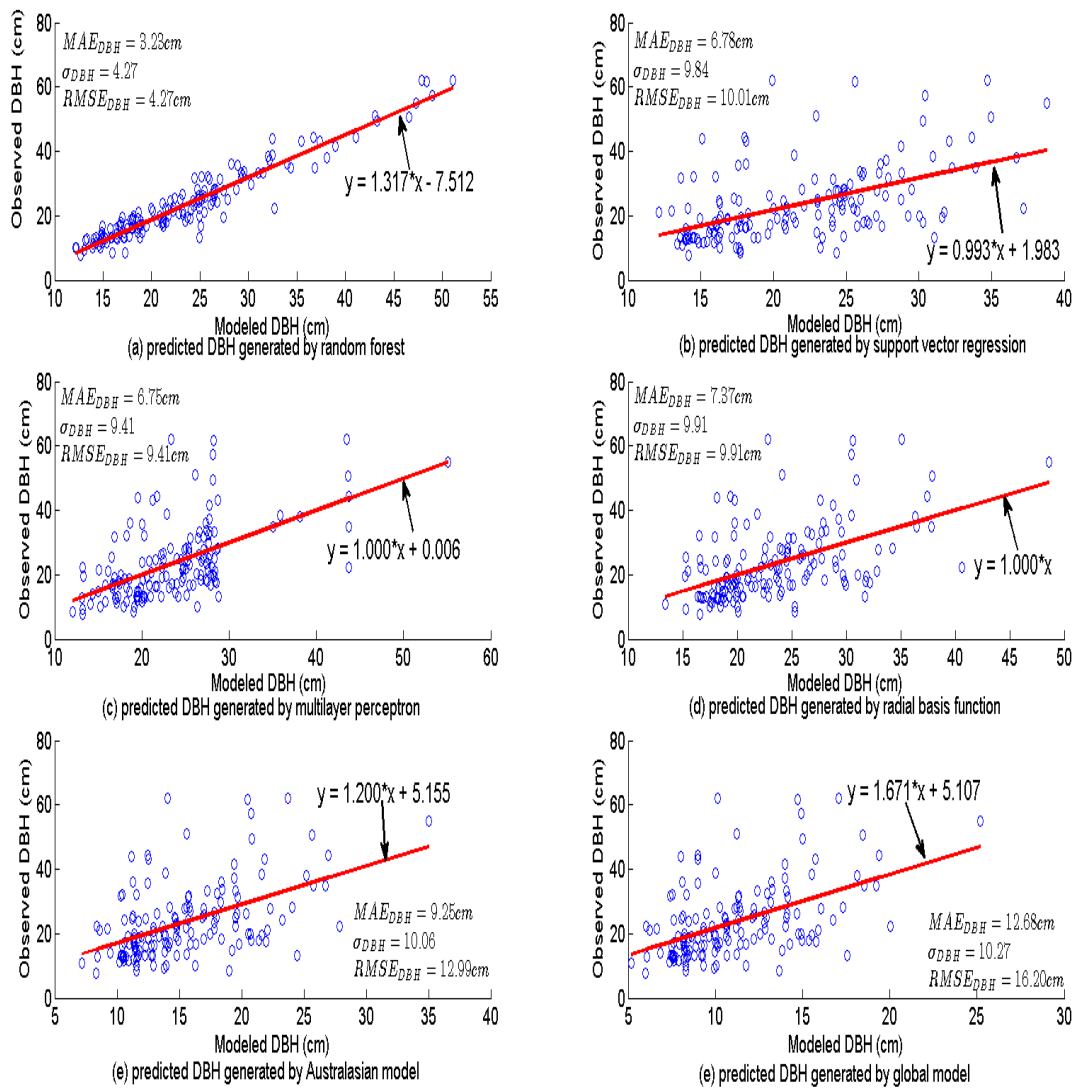


Figure 8.2 The relationship between predicted DBH values and field DBH observations for various models

Table 8.1 The accuracy analysis of the predicted DBH values generated by various models

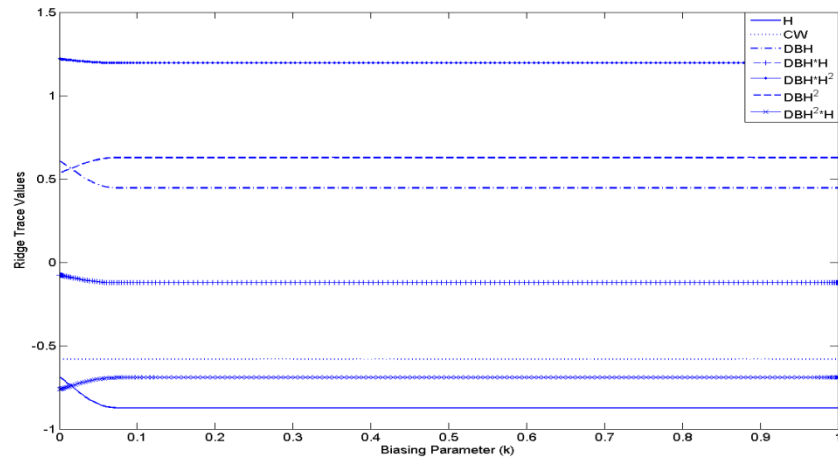
Various Models	$MAE_{DBH}$ (cm)	$RMSE_{DBH}$ (cm)	$\sigma_{DBH}$	Time (min)
(1)	3.23	4.27	4.27	18.2
(2)	6.78	10.01	9.84	15.7
(3)	6.75	9.41	9.41	32.3
(4)	7.37	9.91	9.91	7.5
(5)	12.68	16.20	10.27	0.4
(6)	9.25	12.99	10.06	0.4

Note: (1)-(4) is the DBH regression models developed by random forest, support vector regression, multilayer perceptron, and radial basis function, respectively; (5) is the globally-generalised DBH allometric model while (6) is the generalised Australasian DBH allometric model.

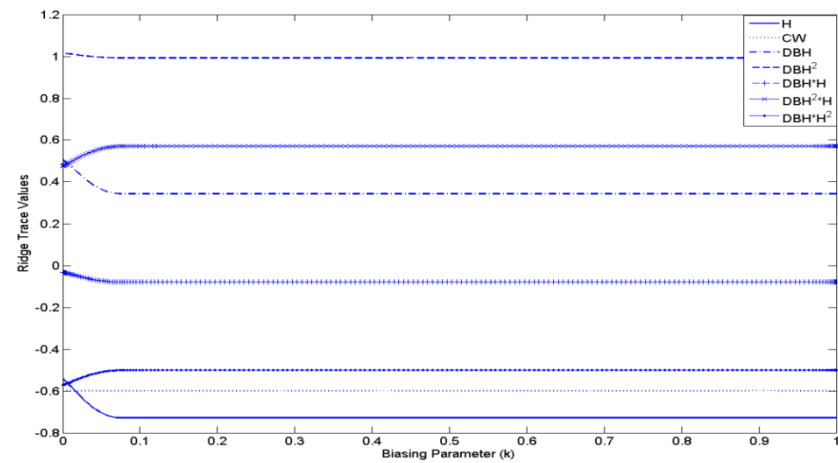
As mentioned above, PCA analysis was conducted before the generation of the AGB regression models to check if multicollinearity was present in the input variables because the DBH of a tree was derived from the corresponding  $H$  and  $CW$ . According to Table 8.2, the eigenvalues of  $H$  and  $CW$  were too small, so ridge regression was conducted to determine which variables should be deleted. Based on the experimental results, ridge regression was conducted in a logistic form using different sets of reference AGB estimates generated by the three existing generalised AGB allometric models as the dependent variable as shown in Figure 8.3. According to the two rules,  $CW$ ,  $DBH \times H$ , and  $DBH^2$  were removed regardless of which set of reference AGB estimates was used. The relationships between different reference AGB estimates and the corresponding predicted AGB estimates by various machine learning algorithms are illustrated in Figures 8.4–8.6. The qualities of the various generated AGB regression models are shown in Table 8.2. According to Table 8.2, when using the AGB estimates yielded by Williams’ model as the reference, the generated AGB regression models have the best qualities, regardless of the regression technique adopted because of the low values of AIC and  $NMSE_{AGB}$  and high values of  $\bar{R}^2$  and EI. Conversely, the AGB regression models using Jucker’s model to compute the AGB estimates as the reference are of bad quality, which is validated by the high values of  $NMSE_{AGB}$  and low values of  $\bar{R}^2$  and EI. The bad performance of Jucker’s model is because only a small portion of the samples used in Jucker’s model are located in Australia and the forest conditions of the samples in Australia are also different from the study region. In contrast, both Paul’s model and Williams’ model are designed for eucalyptus in Australia. In particular, the study region in Williams’ model has similar temperature and forest conditions to our study area, so the performance of this model is generally superior to Paul’s model. In terms of the machine learning techniques, random forest generally outperforms the other methods because of the high quality of the AGB regression models generated. Apart from the good performance on the generation of AGB regression models, random forest is also the most robust overall, which is validated by the low values of ASD. Multilayer perceptron also generates AGB regression models with high quality. However, when setting the pre-set goal of accuracy to an extremely small value, multilayer perceptron will lead to overfitting and some of the predicted AGB values are negative. To solve this problem, the pre-set goal of accuracy was lowered, the maximum number of neurons and the maximum number of epoch were reduced, therefore worsening the performance of multilayer perceptron. This is also the cause of the poor performance of radial basis function. Another vulnerability of multilayer perceptron is the robustness of the method. According to the results, the values of ASD for multilayer perceptron are largest when using the different existing generalised AGB allometric models to compute the reference AGB estimates, which indicates that multilayer perceptron is not robust when selecting different training samples. In contrast,

support vector regression generates the AGB regression models with the worst quality, which is proven by the large values of  $NMSE_{AGB}$  and small values of EI and  $\bar{R}^2$ .

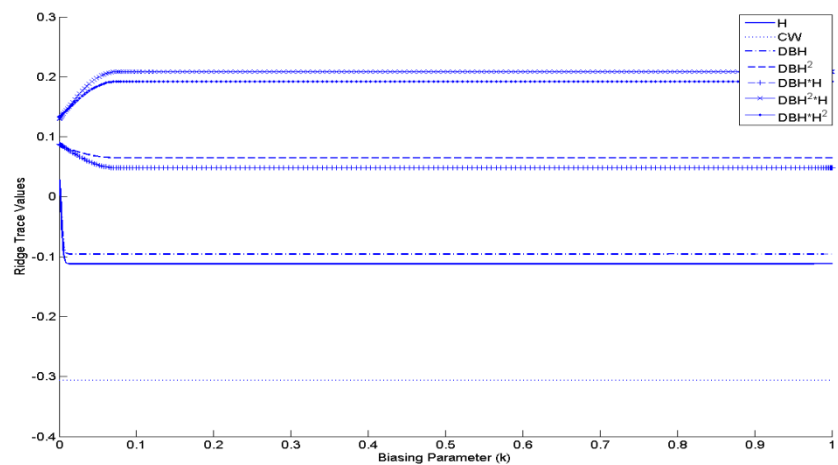
Overall, the AGB estimates generated by Willams' model are strongly correlated to lidar-based tree metrics such as  $DBH$  and  $H$ . The  $\bar{R}^2$ s are generally over 94% and the  $NMSE_{AGB}$  is as low as 1.40%, which indicates that Willams' generalised AGB allometric models can be used to predict AGB estimates in the study region. Our results also indicate generalised allometric models can also yield highly accurate results if the forest conditions in which the generalised allometric models are generated resemble the study region. In terms of the machine learning techniques, random forest outperforms other methods in the generation of both  $DBH$  regression models and AGB regression models and it is also the most robust. In addition, multilayer perceptron and radial basis function may suffer from overfitting when generating different regression models.



(a) ridge trace values of different input variables using reference AGB estimates by Paul's model



(b) ridge trace values of different input variables using reference AGB estimates by Williams' model



(c) ridge trace values of different input variables using reference AGB estimates by Jucker's model

Figure 8.3 The ridge trace values of different input variables

Table 8.2 Eigen values of the original input variables

Eigen Values	$H$	$CW$	$DBH$	$DBH^2$	$DBH \times H$	$DBH \times H^2$	$DBH^2 \times H$
$\gamma$	$3.82 \times 10^{-3}$	$7.54 \times 10^{-3}$	0.14	0.84	4.31	7.42	125.10

Table 8.3 The analysis of the qualities of various generated AGB regression models

Machine Learning Techniques		$\bar{R}^2$ (%)	ASD	AIC	$NMSE_{AGB}$ (%)	EI (%)	Time (min)
random forest	Paul's Model	99.06	$1.70 \times 10^4$	$1.16 \times 10^3$	1.60	99.09	20.2
	Williams' Model	99.10	$1.26 \times 10^4$	$1.12 \times 10^3$	1.40	99.13	21.3
	Jucker's Model	90.41	$2.59 \times 10^3$	883.71	17.26	90.66	20.7
support vector regression	Paul's Model	94.90	$2.43 \times 10^4$	$1.41 \times 10^3$	8.90	95.04	17.9
	Williams' Model	94.43	$1.85 \times 10^4$	$1.39 \times 10^3$	8.92	94.58	18.4
	Jucker's Model	37.09	$2.54 \times 10^3$	$1.17 \times 10^3$	150.37	38.78	18.9
multilayer perceptron	Paul's Model	98.74	$7.34 \times 10^6$	$1.20 \times 10^3$	2.17	98.77	37.3
	Williams' Model	99.06	$2.76 \times 10^7$	$1.13 \times 10^3$	1.48	99.09	36.5
	Jucker's Model	74.87	$9.58 \times 10^6$	$1.03 \times 10^3$	45.70	75.55	41.2
radial basis function	Paul's Model	95.89	$1.78 \times 10^4$	$1.38 \times 10^3$	7.04	96.01	7.5
	Williams' Model	96.38	$2.04 \times 10^4$	$1.33 \times 10^3$	5.70	96.47	7.4
	Jucker's Model	36.29	$2.56 \times 10^3$	$1.17 \times 10^3$	115.91	38.00	9.3

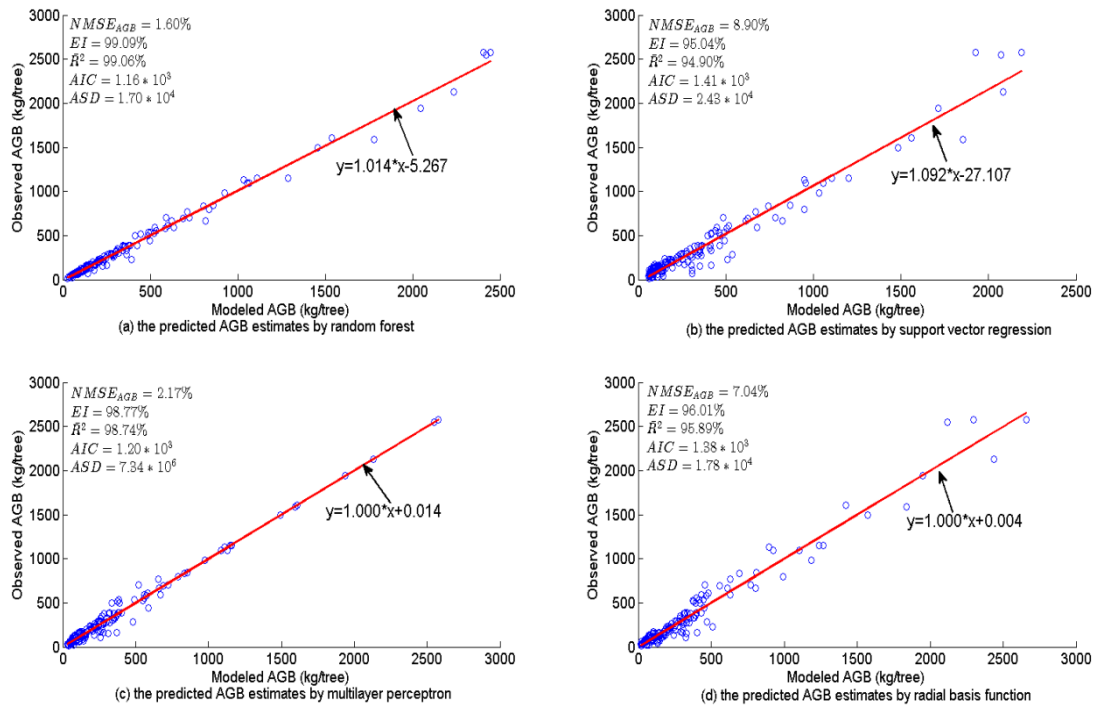


Figure 8.4 The relationships between the predicted AGB estimates by various approaches and the reference AGB estimates from Paul's Model

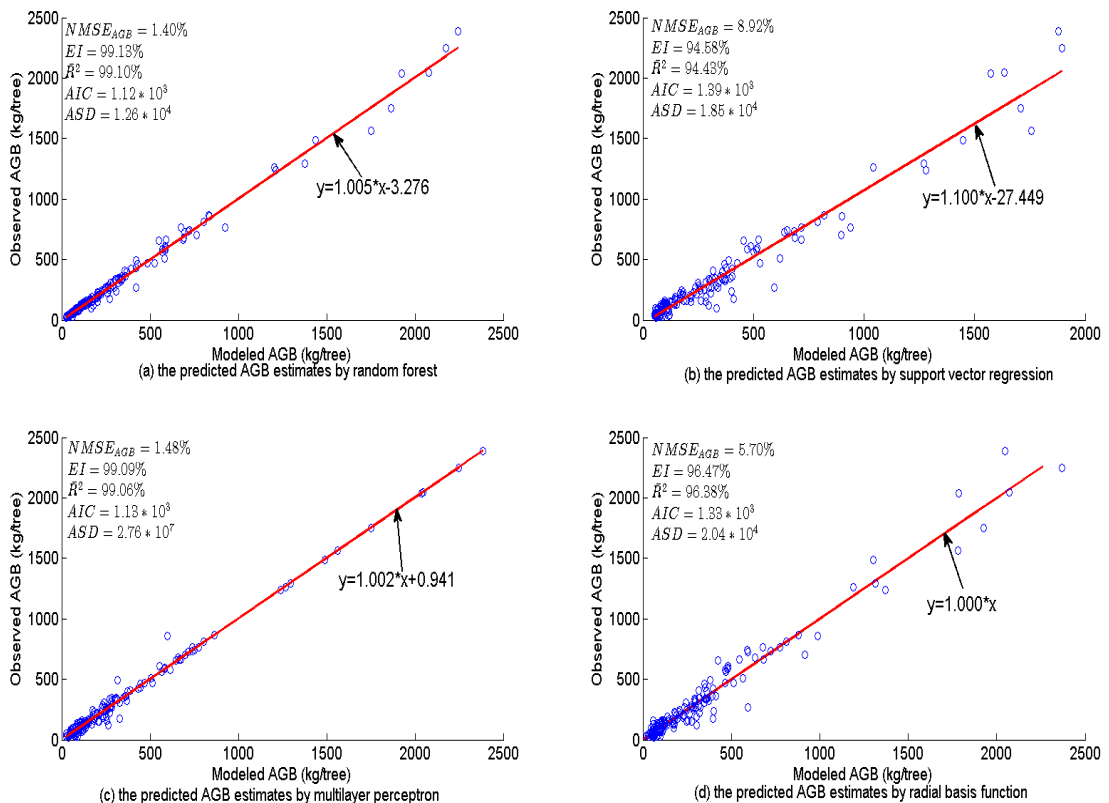


Figure 8.5 The relationships between the predicted AGB estimates by various approaches and the reference AGB estimates from Williams' Model

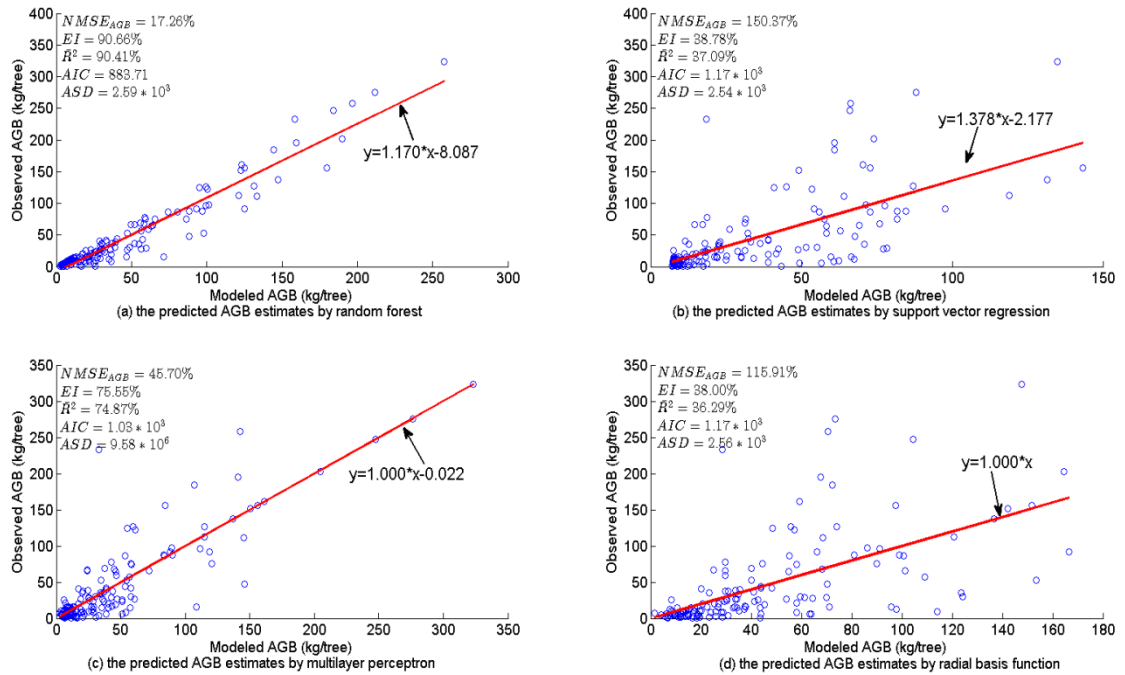


Figure 8.6 The relationships between the predicted AGB estimates by various approaches and the reference AGB estimates from Jucker's Model

### 8.3 Summary

In this chapter, the method of the generation of the AGB regression models for individual trees is presented. In comparison with localised AGB allometric models, generalised AGB allometric models are generated with numerous AGB field samples in various locations and species, therefore minimising uncertainties in AGB estimation. These generalised AGB allometric models are meaningful in study regions where the field observations of AGB estimates are not available. In the study, three existing generalised AGB allometric models (i.e. Paul's model, Williams' model and Jucker's model) were used to compute the AGB estimates as the reference, separately because field samples of AGB estimates were not recorded during the field measurement collection. Since the DBH of a tree is a crucial parameter to estimate the AGB and there are few lidar points present at the breast height of a tree to retrieve the associated DBH directly, the author takes advantage of the fact that the DBH of a tree is correlated to its height and crown width to generate the DBH regression model based on the lidar-based height and crown width. Four machine learning techniques are applied to generate the DBH regression model, separately, since the adopted regression method can influence the accuracy of the generated model. The four machine learning techniques include random forest, support vector regression, multilayer perceptron and radial basis function. The predicted DBH values derived from the different machine learning techniques are compared with the reference DBH values to compute the differences between the predictive values and the corresponding field observations. The

accuracy of the DBH results is measured in terms of the average of the absolute differences, the standard deviation of the differences, and the root-mean-square-errors. Two existing generalised DBH allometric models by Jucker et al. (2017) are also investigated and compared with the site-specifically generated DBH regression models in terms of  $MAE_{DBH}$ ,  $RMSE_{DBH}$  and  $\sigma_{DBH}$ . The most accurate DBH predictive values will be used in the following generation of the AGB regression model. Commonly used variables for AGB estimation are the  $DBH$ ,  $H$ ,  $DBH^2 \times H$ ,  $DBH \times H$ ,  $DBH^2$ , and  $DBH \times H^2$  and  $CW$  is also included in our study because the  $DBH$  is generated based on  $H$  and  $CW$ . PCA analysis and ridge regression are applied to examine the presence of multicollinearity and remove the less important variables. If the ridge trace of a variable is stable or hardly converges when the biasing parameter varies from 0 to 1, the corresponding variable will be removed. After the selection of the input variables, for each set of AGB estimates yielded by the three existing generalised AGB allometric models, the four aforementioned regression techniques are applied to generate the AGB model, respectively. The quality of the generated AGB regression models is assessed by adjusted coefficient of determination, the average of the squares of the differences between the prediction values and the corresponding test observation values, Akaike information criterion, normalised mean square errors of the AGB estimates, and model efficiency index.

The quantitative analysis of the machine learning techniques in generating the DBH regression model indicates that random forest outperforms other methods since the predicted DBH values created by random forest have the smallest values of  $MAE_{DBH}$ ,  $RMSE_{DBH}$  and  $\sigma_{DBH}$ . Conversely, radial basis function and multilayer perceptron suffer from overfitting since both of their results have large values of  $MAE_{DBH}$ ,  $RMSE_{DBH}$  and  $\sigma_{DBH}$  but the corresponding  $ME_{DBH}$ s are very small. The comparisons of the DBH regression models generated by the machine learning techniques and two generalised DBH allometric models indicate that the localised DBH regression models perform better than the generalised DBH allometric models. However, the Australasian generalised DBH allometric model performs better than the globally-generalised DBH allometric model. One plausible reason is that the majority of the tree samples used in the globally-generalised DBH allometric model are located outside the Australasian region, where the forest conditions are different from the study region in Australia. In comparison, the Australasian generalised DBH allometric model only uses tree samples in the Australasian region. Hence, the DBH results derived from random forest are used in the generation of AGB regression models. When comparing the three generalised AGB allometric models, the models using the AGB estimates created by Williams' model as the reference have the best quality because of the high values of  $\bar{R}^2$ , EI, and low values of  $NMSE_{AGB}$ . In contrast, the models using the AGB estimates created by Jucker's model as the reference have the worst quality. This can be explained by the

fact that a large amount of the field samples of trees explored in Williams' model are located in the east of Australia where the living conditions of trees resemble the study region. In contrast, Jucker's model utilises worldwide tree samples with a small portions of tree samples in Australia. Although Paul's model also uses field samples of trees in the east of Australia, a large amount of the tree samples are located in Western Australia where the climate is quite different from the study area. In terms of the performance of the four machine learning techniques in the generation of AGB regression models, random forest generally yields the AGB regression models with the highest quality and is also the most robust when selecting different training samples. Overall, random forest is robust in the generation of different regression models and can produce highly accurate predicted values. Although the AGB regression models generally have high accuracy with most of the values of  $\bar{R}^2$  above 90%, there are some drawbacks in the framework of the generation of AGB regression model for individual trees. For instance, the coverage of the study region is small and the forest is homogenous. In Chapter 9, the whole framework of the generation of AGB regression model for individual trees will be summarised with a focus on the pros and cons of the framework. Based on the errors of the results and the drawback of the design of the study, the associated recommendations will be made.

## **Chapter 9 : Concluding Remarks and Recommendations**

The main aim of this research was to develop a framework for the AGB estimation of individual trees for a forest in Australia with airborne lidar data. To achieve AGB estimates with good accuracy, error sources that may be present in the framework were examined, including the misclassification of vegetation points as ground points and the omission of ground points during the lidar filtering processing, the presence of pits in the CHM, the misidentification of subdominant trees as a portion of dominant trees and the use of improper modelling techniques. To reduce these errors, the author developed a voxel-based multiscale morphological airborne lidar filtering algorithm for forest regions (Chapter 4), a multiscale morphological algorithm to replace the pits in the CHM (Chapter 5), a hybrid algorithm to segment individual trees (Chapter 7), a DBH regression model and an AGB regression model to examine the performance of different machine learning techniques in regression model generation (Chapter 8). Various tests have been conducted to validate these algorithms.

This chapter presents a summary of the research, with the proposed algorithms being reviewed briefly, and the strengths and weaknesses of each algorithm being discussed comprehensively. This chapter also provides a brief discussion about the future outlook for research, and two potential approaches that may yield promising AGB estimates are provided.

### **9.1 Concluding remarks**

As lidar points contain both ground points and object points, it is essential to segment ground points first, then identify vegetation points from object points and normalise the height values of the identified vegetation points. However, it is difficult to classify ground points in the forest, leading to high omission errors. To achieve a balance between the omission errors of ground points and commission errors of object points, a voxel-based multiscale morphological airborne lidar filtering algorithm was presented in Chapter 4. The main concept of this algorithm is to identify object points at multispatial scales using height distribution analysis, convexity constraints, a morphological filter and a moving window-based voxel filter. To minimise the misclassification problem, an object index was introduced to label the identified object points rather than removing them at each iteration. An Otsu segmentation algorithm was applied to compute the threshold for the object indices automatically.

After applying the voxel-based multiscale morphological airborne lidar filtering algorithm to the lidar data in the study region, a 1-m resolution DTM was created by interpolating the identified ground points within every each  $1\text{ m} \times 1\text{ m}$  grid cell. Since the only objects in the study region are vegetation, the recognised object points were regarded as vegetation points without further

classification. Among these object points, the points with the highest elevation values in each grid were selected to be rasterised into a 1-m resolution DSM. A 1-m resolution CHM was generated by the subtraction from the DSM of the corresponding DTM pixel by pixel. However, the accuracy of the CHM suffers from the presence of the pit pixels that demonstrate abnormal lower elevation values than the surroundings. These pit pixels, caused by the penetration of lidar pulses into the canopy, may degrade the accuracy of the CHM and have an impact on the results when an individual-tree segmentation algorithm is applied. To identify and replace these pit pixels with correct values, a multiscale morphological algorithm was proposed in Chapter 5. The algorithm assumes that: 1) the majority of pits are in the canopy regions; 2) trees in the study regions have various sizes and species; 3) the canopy shape of a tree is circular from the top view. Based on these assumptions, a multiscale Laplacian operator, a multiscale morphological closing operator and a multiscale median filter were applied to recognise and replace the pits with correct values. Since the sizes of the trees in the study area vary, multiscale operators were proposed in each step to deal with various tree conditions and fused the results generated by the multiscale operators in each step to limit the influence of the improper choice of the window sizes on the final results.

After replacing the pits with correct values, the next step is to segment individual trees. Commonly used techniques include CHM-based and point-based algorithms to segment individual trees from airborne lidar data. In Chapter 6, five existing algorithms were tested to investigate which one yields the most accurate results, including FLM, PWLM, VLM, ITCD and LPS. The results were compared in terms of the mean errors of tree height and crown width, root-mean-square-errors of tree height and crown width, detection rate, commission error and omission error. According to the results, ITCD outperformed other individual tree segmentation algorithms because it takes the strategy of multiscale analysis to segment the crowns. In addition, although LPS yielded the largest number of individual trees, it suffered from oversegmentation which is validated by the negative value of the mean error of the crown width. We also investigated whether the CHM with a finer spatial resolution could generate more accurate tree parameters. For this, CHM-based algorithms were applied to the CHM with different spatial resolutions. Based on the results, the conclusion can be drawn that when the CHM-based algorithms are applied to a CHM with a finer spatial resolution, the generated crown widths are not necessarily more accurate.

The analysis of the existing algorithms in Chapter 6 indicates that CHM-based algorithms cannot detect understorey trees, whereas point-based algorithms are inefficient. In addition, for the CHM-based algorithms, the most accurate tree heights and crown widths may not be achieved at one specific grid cell simultaneously. To obtain accurate tree height and crown width simultaneously and recognise the understorey trees, in Chapter 7, a hybrid tree segmentation algorithm was

proposed to segment airborne lidar points into individual trees by integrating a CHM-based tree segmentation algorithm with a point-based algorithm. The ITCD was firstly applied to CHMs with various spatial resolutions to identify the highly accurate LM, which were used as seeds in the point-based vertical profile analysis algorithm to delineate the crown boundaries of individual trees. To identify the presence of subdominant trees, for each segmented individual tree, a histogram analysis was applied. Three metrics were introduced to limit the misclassification of large outwardly extended tree branches as individual trees, namely the number of points in a canopy layer, the maximum height of the canopy layer, and the ratio of the overlapped area between a sublayer and the top canopy layer to the area of the top canopy layer.

The DBH is a significant parameter for AGB estimation but the proposed individual tree segmentation algorithm failed to extract the DBHs of individual trees from lidar points directly because of the few points available at the breast height of a tree from the ground. To tackle this issue, in Chapter 8, a localised DBH regression model was generated based on lidar-based tree heights and crown widths and field observations of the DBH. Four machine learning techniques were applied to generate the DBH regression model, respectively, since the regression method may influence the quality of the generated regression model. The four machine learning techniques are random forest, support vector regression, multilayer perceptron and radial basis function. The predicted values of the DBH generated by the different DBH regression models were compared with the reference to compute the differences. The predicted DBH values that deviated the least from the reference were used as the input variables for AGB estimation. Since the DBHs were computed based on a function of tree height and crown width, principal component analysis was applied to investigate if multicollinearity occurred and ridge regression was explored to remove the less important input variables. Three existing generalised AGB allometric models were used respectively to compute the AGB estimates of individual trees as the reference, since the field measurements of the AGB were not available. After the determination of the input variables, for each set of AGB estimates generated by the existing generalised AGB allometric models, the aforementioned four machine learning techniques were applied respectively to generate the AGB regression model. The quality of each of the generated AGB regression models was measured in terms of  $\bar{R}^2$ , EI, AIC, CV and  $NMSE_{AGB}$ . According to the result, random forest worked better than the other machine learning techniques in the generation of the AGB regression models because of the small values of  $NMSE_{AGB}$  and large values of  $\bar{R}^2$  and EI. Moreover, the AGB estimates created by Williams' model had a stronger correlation with the lidar-based input variables in the study region.

Based on the results, the concluding remarks include:

- I. The proposed voxel-based multiscale morphological airborne lidar filtering algorithm manages to achieve a balance between the omission errors of ground points and commission errors of object points and the performance of the proposed lidar filtering algorithm is comparable to other commercially available lidar filtering algorithm when applied to forest regions.
- II. The proposed multiscale morphological algorithm can replace pits with meaningful values, and improve the accuracy of the CHM and the improvement of the CHM can promote the accuracy of individual tree segmentation.
- III. The hybrid tree segmentation algorithm can segment individual trees accurately meanwhile detecting understory trees.
- IV. Random forest yields AGB regression models with the best quality among the four machine learning algorithms and it also works more robust than other machine learning algorithms.

## 9.2 Recommendations

Based on analyses of the drawbacks of the proposed algorithms presented in this thesis, the research topics that are recommended for future work are as follows:

- I. Making use of the available knowledge of topography

The knowledge of the topography in the study region can be used to generate a highly accurate DTM. Although the proposed voxel-based multiscale morphological filtering algorithm can maintain a balance between the omission errors and commission errors and succeed in removing the majority of object points, it removes many ground points as well and some object points remain, which will have an impact on the accuracy of the CHM. Although the proposed CHM improvement algorithm can improve the accuracy of the CHM to some extent by replacing the pits in the canopy regions, the accuracy of a CHM is closely related to the accuracy of the associated DSM and DTM. If knowledge of the topography in the study region is available, the accuracy of the CHM can be further improved. In addition, the accuracy of the normalised height values of lidar points can be enhanced as well since the height values of the lidar points are normalised by subtracting the height values of the lidar points from the corresponding DTM. Consequently, the tree heights derived from the proposed hybrid individual tree segmentation algorithm can be promoted, which will increase the accuracy of the AGB estimates. Hence, it is recommended to use knowledge of the topography, if available, to enhance the accuracy of the AGB estimation for individual trees.

## II. Exploiting AGB estimation for individual trees based on unmanned aerial vehicle (UAV)-based lidar data

In this study, the DBHs of individual trees are obtained based on lidar-based tree heights and crown widths, since the presence of few points at the breast height of a tree makes it difficult to get accurate DBHs from points directly. Consequently, the errors in lidar-based tree heights and crown widths will be propagated to the DBHs, influencing the accuracy of the AGB estimation further. It may be beneficial to obtain DBHs of trees directly from much denser lidar points. The miniaturisation of sensors and positioning systems has paved the way for UAV as a powerful alternative to acquiring high-resolution data (Wallace et al., 2012a). Data collected from UAV-based lidar has similar characteristics to full-scale airborne lidar data (Wallace et al., 2012b). However, in comparison with airborne lidar, UAV-based lidar can capture much denser point clouds because of the ability to capture data from close range with various viewing angles (i.e. nadir and oblique). In addition, UAV-based lidar allows for frequent missions due to the ease of deployment and low cost, yielding datasets with high spatial and temporal resolution (Harwin and Lucieer, 2012), can get access to inaccessible and hazardous regions, and requires little ground on site. Hence, it is recommended to take advantage of the high point density of UAV-based lidar points for AGB estimation for individual trees.

## III. Applying deep learning techniques to the segmentation of individual trees from airborne lidar data and the generation of regression models

Deep learning techniques have been credited for image classification, feature extraction and segmentation. Some deep learning neural networks such as CNN, have been successfully applied for tree segmentation (Windrim and Bryson, 2018; Weinstein et al., 2019), building segmentation (Wu et al., 2018), and road detection (Caltagirone et al., 2017). Compared to traditional feature extraction, deep learning techniques contribute to simplifying the feature extraction process. Deep learning neural networks can learn feature patterns during the data training phase and work as feature estimators during the classification stage, which can manage complex scenarios and be used for different datasets. Hence, it is recommended to apply deep learning techniques to the segmentation of individual trees from airborne lidar data and the generation of regression models when the study region is large and complex.

## IV. Applying the proposed framework of AGB estimation for individual trees to a larger forest with various tree species

Although the proposed framework of AGB estimation for individual trees yields promising results in the study region, the main issue is that the coverage of the study region is

relatively small compared with other studies. Meanwhile, the tree species in the region are dominated by eucalyptus and the homogeneity of a forest makes it less difficult to achieve good results. To test the robustness of the framework, it is recommended to apply the proposed framework of AGB estimation for individual trees to a heterogeneous forest with a larger area of coverage.

## References

- Achard, F., Eva, H.D., Mayaux, P., Stibig, H., Belward, A., 2004. Improved estimates of net carbon emissions from land cover change in the tropics for the 1990s. *Global Biogeochemical Cycles*, 18:GB2008.
- Alexander, C., Korstjens, A.H., Hill, R.A., 2018. Influence of micro-topography and crown characteristics on tree height estimations in tropical forests based on LiDAR canopy height models. *International Journal of Applied Earth Observation and Geoinformation*, 65:105-113.
- Axelsson, P., 1999. Processing of laser scanner data-algorithms and applications. *ISPRS Journal of Photogrammetry and Remote Sensing*, 54:138-147.
- Axelsson, P., 2000. DEM generation from laser scanner data using adaptive TIN models. in *IAPRS*, 33: 111-118.
- Anderson, J., Martin, M.E., Smith, M., Dubayah, R.O., Hofton, M.A., Hyde, P., Peterson, B.E., Blair, J.B., Knox, R.G., 2006. The use of waveform lidar to measure northern temperate mixed conifer and deciduous forest structure in New Hampshire. *Remote Sensing Of Environment*, 105:248-261.
- Anderson, J.E., Plourde, L.C., Martin, M.E., Braswell, B.H., Smith, M.L., Dubayah, R.O., Hofton, M.A., Blair, J.B., 2008. Integrating Waveform Lidar with Hyperspectral Imagery for Inventory of a Northern Temperate Forest. *Remote Sensing Of Environment*, 112 (4): 1856-1870.
- Akaike, H., 1974. A new look at the statistical model identification. *IEEE Transactions on Automatic Control*, 19 (6):716-723.
- Ali, I., Greifeneder, F., Stamenkovic, J., Neumann, M., Notarnicola, C., 2015. Review of Machine Learning Approaches for Biomass and Soil Moisture Retrievals from Remote Sensing Data. *Remote Sensing*, 7:16398-16421.
- Arzai, A., Aliyu, B., 2010. The relationship between canopy width, height and trunk size in some tree species growing in the savana zone of Nigeria. *Bajopas*, 3(1): 260-263.
- Asner, G.P., Hughes, R.F., Mascaro, J., Uowolo, A.L., Knapp, D.E., Jacobson, J., Kennedy-Bowdoin, T., Clark, J. K., 2011. High-resolution Carbon Mapping on the Million-hectare Island of Hawaii. *Frontiers in Ecology and the Environment*, 9: 434-439.

Asner, G.P., Hughes, R.F., Varga, T., Knapp, D., Kennedy-Bowdoin, T., 2009. Environmental and Biotic Controls over Aboveground Biomass throughout a Tropical Rain Forest. *Ecosystems*, 12: 261-278.

Asner, G.P., Mascaro, J., 2014. Mapping Tropical Forest Carbon: Calibrating Plot Estimates to a Simple LiDAR Metric. *Remote Sensing Of Environment*, 140: 614-624.

Asner, G.P., Mascaro, J., Muller-Landau, H., Vieilledent, G., Vaudry, R., Rasamoelina, M., Hall, J., Breugel, M., 2012. A Universal Airborne Lidar Approach for Tropical Forest Carbon Mapping. *Oecologia*, 168 (4): 1147-1160.

Avitabile, V., Baccini, A., Friedl, M., Schmillius, C., 2012. Capabilities and limitations of Landsat and land cover data for aboveground woody biomass estimation of Uganda. *Remote Sensing Of Environment*, 117: 366-380.

Baccini, A., Friedl, M.A., Woodcock, C.E., Warbington, R., 2004. Forest biomass estimation over regional scales using multisource data. *Geophysical Research Letters*, 31:1-4.

Ballabio, C., 2009. Spatial prediction of soil properties in temperate mountain regions using support vector regression. *Geoderma*, 151:338-350.

Balzter, H., 2001. Forest mapping and monitoring with interferometric synthetic aperture radar (InSAR). *Progress in Physical Geography*, 25: 159-177.

Balzter, H., Rowland, C.S., Saich, P., 2007. Forest canopy height and carbon estimation at Monks Wood National Nature Reserve, UK, using dual-wavelength SAR interferometry. *Remote Sensing Of Environment*, 108: 224-239.

Bao Y.F., Li, G.P., Cao, C.X., Li, X.W., Zhang, H., He, Q.S., Bai, L.Y., Chang, C.Y., 2008. Classification of Lidar Point Cloud and Generation of DTM From Lidar Height and Intensity Data In Forested Area. In: *IAPRSIS, XXXVII(B3b)*, Beijing, 2008.

Bartels, M., Hong, W., 2006. Segmentation of Lidar Data Using Measures of Distribution. In: *ISPRS Journal of Photogrammetry and Remote Sensing, WG V11/4 Advanced Classification Techniques*, Enschede, Netherlands.

Bartels, M., Hong, W., 2010. Threshold-free object and ground point separation in LIDAR data. *Pattern Recognition Letters*, 31(10):1089-1099.

Bartels, M., Hong, W., Mason, D.C., 2006. DTM Generation from LIDAR Data using Skewness Balancing. In: *ICPR, Hong Kong*, 566 - 569.

- Beaudoin, A., Le Toan, T., Goze, S., Nezry, E., Lopes, A., Mougin, E., Hsu, C.C., Han, H.C., Kong, J.A., Shin, R.T., 1994. Retrieval of forest biomass from SAR data. *International Journal of Remote Sensing*, 15: 2777-2796.
- Ben-Aire, J.R., Hay, G.J., Powers, R.P., Castilla, G., St-Onge, B., 2009. Development of a pit filling algorithm for lidar canopy height models. *Computers & Geosciences*, 35:1940-1949.
- Beven, K., Freer, J., 2001. Equifinality, data assimilation, and uncertainty estimation in mechanistic modeling of complex environmental systems using the GLUE methodology. *Journal of Hydrology*. 249, 11-29.
- Biosca, J., Lerma, J., 2008. Unsupervised robust planar segmentation of terrestrial laser scanner point clouds based on fuzzy clustering methods. *ISPRS Journal of Photogrammetry and Remote Sensing*, 63(1):84-98.
- Boyd, D.S., Foody, G.M., Curran, P.J., 1999. The relationship between the biomass of Cameroonian tropical forests and radiation reflected in middle infrared wavelengths (3.0–5.0 mm). *International Journal of Remote Sensing*, 20: 1017-1023.
- Brandtberg, T., Warner, T.A., Landenberger, R.E., McGraw, J.B., 2003. Detection and analysis of individual leaf-off tree crowns in small footprint, high sampling density lidar data from the eastern deciduous forest in North America. *Remote Sensing Of Environment*, 85(3):290–303.
- Brovelli, M.A., Cannata, M., Longoni, U.M., 2004. LiDAR data filtering and DTM interpolation within GRASS. *Transactions in GIS*, 8: 155-174.
- Brown, J.H., West, G.B., Enquist, B.J., 2005. Yes, West, Brown and Enquist's Model of Allometric Scaling is Both Mathematically Correct and Biologically Relevant. *Functional Ecology*, 19: 735-738.
- Bunting, P., Lucas, R.M., 2006. The Delineation of Tree Crowns in Australian Mixed Species Forests Using Hyperspectral Compact Airborne Spectrographic Imager (CASI) Data. *Remote Sensing Of Environment*, 101(2):230–248.
- Burrows, S., Gower, S., Norman, J., Diak, G., Mackay, D., Ahl, D., Clayton, M., 2003. Spatial variability of aboveground net primary production for a forested landscape in northern Wisconsin. *Canadian Journal of Remote Sensing*. 33 (10):2007-2018.

Cao, L.D., Pan, J.J., Li, R.J., Li, J.L., Li, Z.F., 2018. Integrating Airborne LiDAR and Optical Data to Estimate Forest Aboveground Biomass in Arid and Semi-Arid Regions of China. *Remote Sensing*, 10(4):532.

Castel, T., Guerra, F., Caraglio, Y., Houllier, F., 2002. Retrieval biomass of a large Venezuelan pine plantation using JERS-1 SAR data: analysis of forest structure impact on radar signature. *Remote Sensing Of Environment*, 79: 30-41.

Chasmer, L., Hopkinson, C., Treitz, P., 2006. Investigating Laser Pulse Penetration Through a Conifer 358 Canopy by Integrating Airborne and Terrestrial LiDAR. *Canadian Journal of Remote Sensing*, 32:115-125.

Chave, J., Condit, R., Aguilar, S., Hernandez, A., Lao, S., Perez, R., 2004. Error propagation and scaling for tropical forest biomass estimates. *Philosophical Transactions of the Royal Society B*, 359:409-420.

Chen, C., Li, Y., Li, W., Dai, H., 2013. A multiresolution hierarchical classification algorithm for filtering airborne LiDAR data. *ISPRS Journal of Photogrammetry and Remote Sensing*, 82: 1-9.

Chen, Q., 2013. Lidar Remote Sensing of Vegetation Biomass. *Remote Sensing of Natural Resources*, 399-420. Boca Raton, FL: CRC Press and Taylor & Francis Group.

Chen, Q., Baldocchi, D., Gong, P., Kelly, M., 2006. Isolating individual trees in a savanna woodland using small footprint lidar data. *Photogrammetric Engineering&Remote Sensing*, 72:923-932.

Chen, Q., Gong, P., Baldocchi, D., Tian, Y.Q., 2007. Estimating basal area and stem volume for individual trees from lidar data. *Photogrammetric Engineering&Remote Sensing*, 73:1355-1365.

Chen, Q., Gong, P., Baldocchi, D., Xie, G., 2007. Filtering airborne laser scanning data with morphological methods. *Photogrammetric Engineering&Remote Sensing*, 73(2):175-185.

Chen, Q., Vaglio Laurin, G., Battles, J.J., Saah, D., 2012. Integration of Airborne Lidar and Vegetation Types Derived from Aerial Photography for Mapping Aboveground Live Biomass. *Remote Sensing Of Environment*, 121:108-117.

Chen, W., Chen, J., Liu, J., Cihlar, J., 2000. Approaches for Reducing Uncertainties in Regional Forest Carbon Balance. *Global Biogeochemical Cycles*, 14: 827-838.

Chen, Y., Zhu, X., 2013. An Integrated GIS Tool for Automatic Forest Inventory Estimates of *Pinus Radiata* from Lidar Data. *GIScience&Remote Sensing*, 50(6):667-689.

- Cho, W., Jwa, Y.S., Chang, H.J., Lee, S.H., 2004. Pseudo-grid based building extraction using airborne LIDAR data. In: IAPRS, 35 (B3):378-381
- Clark, M.L., Roberts, D.A., Ewel, J.J., Clark, D.B., 2011. Estimation of Tropical Rain Forest Aboveground Biomass with Small-footprint Lidar and Hyperspectral Sensors. *Remote Sensing Of Environment*, 115: 2931-2942.
- Claverie, M., Demarez, V., Duchemin, B., Hagolle, O., Ducrot, D., Marais-Sicre, C., Dejoux, J., Huc, M., Keravec, P., Béziat, P., Fieuzal, R., Ceschia, E., Dedieu, G., 2012. Maize and sunflower biomass estimation in southwest France using high spatial and temporal resolution remote sensing data. *Remote Sensing Of Environment*, 124 :844-857.
- Coomes, D.A., Dalponte, M., Jucker, T., Asner, G.P., Banin, L.F., Burslem, D., Lewis, S.L., Nilus, R., Phillips, O.L., Phua, M.-H., Qie, L., 2017. Area-based vs tree-centric approaches to mapping forest carbon in Southeast Asian forests from airborne laser scanning data. *Remote Sensing Of Environment*, 194:77-88.
- Cohen, J., 1960. A coefficient of agreement for nominal scales. *Educational and Psychological Measurement*, 20 (1): 37-46.
- Crosilla, F., Macorig, D., Scaioni, M., Sebastianutti, I., Visintini, D., 2013. Lidar data filtering and classification by skewness and kurtosis iterative analysis of multiple point cloud data categories. *Applied Geomatics*, 5(3): 225-240.
- Crow, T., 1978. Biomass and production in three contiguous forests in northern Wisconsin. *Ecology*, 265–273.
- Culvenor, D.S., 2002. TIDA: an algorithm for the delineation of tree crowns in high spatial resolution remotely sensed imagery. *Computers & Geosciences*, 28(1):33-44.
- Dalponte, M., Reyes, F., Kandare, K., Gianelle, D., 2015. Delineation of Individual Tree Crowns from ALS and Hyperspectral data: a comparison among four methods. *European Journal of Remote Sensing*, 48:365-382.
- Dalponte, M., 2017. Package “itcSegment”, accessed in July 2017.
- DeGrandi, G.D., Lucas, R.M., Kropacek, J., 2009. Analysis by Wavelet Frames of Spatial Statistics in SAR Data for Characterizing Structural Properties of Forests. *IEEE Transactions on Geoscience and Remote Sensing*, 47: 494-507.

Dobson, M., Ulaby, F., Pierce, L., Sharik, T., Bergen, K., Kellndorfer, J., Kendra, J., Li, E., Lin, Y., Nashashibi, A., Sarabandi, K., 1995. Estimation of Forest Biomass Characteristics in Northern Michigan with SIR-C/XSAR Data. *IEEE Transactions on Geoscience and Remote Sensing*, 33:877-894.

Dang, A., Nandy, S., Srinet, R., Luong, N.V., Ghosh, S.A., Kumar, S., 2019. Forest aboveground biomass estimation using machine learning regression algorithm in Yok Don National Park, Vietnam, *Ecological Informatics*, 50: 24-32.

Donoghue, D.N.M., Watt, P.J., Cox, N.J., Wilson, J., 2007. Remote sensing of species mixtures in conifer plantations using LiDAR height and intensity data. *Remote Sensing Of Environment*, 110:509-522.

Drake, J.B., Knox, R.G., Dubayah, R.O., Clark, D.B., Condit, R., Blair, B.J., Hofton, M., 2003. Above-ground biomass estimation in closed canopy Neotropical forests using lidar remote sensing: factors affecting the generality of relationships. *Global Ecology and Biogeography*, 12:147-159.

Du, L., Zhou, T., Zou, Z., Zhao, X., Huang, K., Wu, H., 2014. Mapping Forest Biomass Using Remote Sensing and National Forest Inventory Data. *Forests*, 5:1267-1283.

Duncanson, L., Cook, B., Hurtt, G., Dubayah, R., 2014. An efficient, multi-layered crown delineation algorithm for mapping individual tree structure across multiple ecosystems. *Remote Sensing Of Environment*, 154:378-386.

Durbha, S., King, R., Younan, N., 2007. Support vector machines regression for retrieval of leaf area index from multiangle imaging spectroradiometer. *Remote Sensing Of Environment*, 107:348-361.

Evans, J.S., Hudak, A.T., 2007. A Multiscale Curvature Algorithm for Classifying Discrete Return LiDAR in Forested Environments. *IEEE Transactions on Geoscience and Remote Sensing*, 45(4):1029-1038.

Falkowski, M., Evans, J., Martinuzzi, S., Gessler, P., Hudak, A., 2009. Characterizing forest succession with lidar data: An evaluation for the Inland Northwest, USA. *Remote Sensing Of Environment*, 113: 946-956.

Falkowski, M.J., Smith, A.M., Gessler, P.E., Hudak, A.T., Vierling, L.A., Evans, J.S., 2008. The influence of conifer forest canopy cover on the accuracy of two individual tree measurement algorithms using lidar data. *Canadian Journal of Remote Sensing*, 34:S338-S350.

- Falkowski, M.J., Smith, A.M., Hudak, A.T., Gessler, P.E., Vierling, L.A., Crookston, N.L., 2006. Automated estimation of individual conifer tree height and crown diameter via two-dimensional spatial wavelet analysis of lidar data. *Canadian Journal of Remote Sensing*, 32:153-161.
- Fang, F., Im, J.H., Lee, J.H., Kim, K.M., 2016. An improved tree crown delineation method based on live crown ratios from airborne LiDAR data, *GIScience.&Remote Sensing*, 53(3):402-419.
- Fang, J., Chen, A., Peng, C., Zhao, S., Ci, L., 2001. Changes in forest biomass carbon storage in China between 1949 and 1998. *Science*, 292 (5525):2320-2322.
- Ferraz, A., Bretar, F., Jacquemoud, S., Goncalves, G., Pereira, L., Tomé, M., Soares, P., 2012. 3-D mapping of a multi-layered Mediterranean forest using ALS data. *Remote Sensing Of Environment*, 121:210–223.
- Filin, S., Pfeifer, N., 2006. Segmentation of airborne laser scanning data using a slope adaptive neighbourhood. *ISPRS Journal of Photogrammetry and Remote Sensing*, 60(2):71-80.
- Foody, G.M., Boyd, D.S., Cutler, M.E., 2003. Predictive relations of tropical forest biomass from Landsat TM data and their transferability between regions. *Remote Sensing Of Environment*, 85 (4):463-474.
- Forzieri, G., Guarnieri, L., Vivoni, E.R., Castelli, F., Preti, F., 2009. Multiple attribute decision making for individual tree detection using high-resolution laser scanning. *Forest Ecology and Management*, 258:2501-2510.
- Fuchs, H., Magdon, P., Kleinn, C., Flessa, H., 2009. Estimating Aboveground Carbon in a Catchment of the Siberian Forest Tundra: Combining Satellite Imagery and Field Inventory. *Remote Sensing Of Environment*, 113: 518-531.
- Gaulton, R., Malthus, T.J., 2010. Lidar mapping of canopy gaps in continuous cover forests: A comparison of canopy height model and point cloud based techniques. *International Journal of Remote Sensing*, 31:1193-1211.
- Gaveau, D.L.A., Hill, R.A., 2003. Quantifying canopy height underestimation by laser pulse penetration in small-footprint airborne laser scanning data. *Canadian Journal of Remote Sensing*, 29: 650-657.
- Gering, L.R., May, D.M., 1995. The relationship of diameter at breast height and crown diameter for four species groups in Hardin county, Tennessee. *Southern Journal of Applied Forestry*, 19 (4):177-181.

- Gleason, C., Im, J.H., 2012. Forest biomass estimation from airborne LiDAR data using machine learning approaches. *Remote Sensing Of Environment*, 125: 80-91.
- Gong, J.Y., Li, Q., Zhu, H.S., Zhou, Y., 2000. Effects of various factors on the accuracy of DEMs: An intensive experimental investigation. *ISPRS Journal of Photogrammetry and Remote Sensing*, 66:1113-1117.
- Gong, P., Sheng, Y., Biging, G.S., 2002. 3D model-based tree measurement from high-resolution aerial imagery. *Photogrammetric Engineering&Remote Sensing*, 68(11):1203–1212.
- Gougeon, F., 1995. A crown-following approach to the automatic delineation of individual tree crowns in high spatial resolution aerial images. *Canadian Journal of Remote Sensing*, 21(3):274–284.
- Guan, H., Li, J., Yu, J., Zhong, L., 2014. DEM generation from lidar data in wooded mountain areas by cross section plane analysis. *International Journal of Remote Sensing*, 35(3): 927 948.
- Habib, A., Ghanma, M., Morgan, M., Al-Ruzouq, R., 2005. Photogrammetric and LiDAR data registration using linear features. *Photogrammetric Engineering&Remote Sensing*, 71: 699-707.
- Hall, R.J., Morton, R.T., Nesby, R.N., 1989. A Comparison of existing models for DBH estimation for large scale photos. *Forestry Chronicle*, 114-116.
- Häme, T., Salli, A., Andersson, K., Lohi, A., 1997. A new methodology for estimation of biomass of conifer-dominated boreal forest using NOAA AVHRR data. *International Journal of Remote Sensing*, 18:3211-3243.
- Hamraz, H., Contreras, M.A., Zhang, J., 2016. A robust approach for tree segmentation in deciduous forests using small-footprint airborne LiDAR data. *International Journal of Applied Earth Observation and Geoinformation*, 52:532–541.
- Hamraz, H., Contreras, M.A., Zhang, J., 2017. Vertical stratification of forest canopy for segmentation of understory trees within small-footprint airborne LiDAR point clouds. *ISPRS Journal of Photogrammetry and Remote Sensing*, 130:385-392.
- Hansen, M., Potapov, P., Moore, R., Hancher, M., Turubanova, S., Tyukavina, A., Thau, D., Stehman, S., Goetz, S., Loveland, T., Kommareddy, A., Egorov, A., Chini, L., Justice, C., Townshend, J., 2013. High-resolution Global Maps of 21st-century Forest Cover Change. *Science*, 342: 850-853.

- Harikumar, A., Bovolo, F., Bruzzone, L., 2017. Subdominant Tree Detection In Multi-Layered Forests By A Local Projection Of Airborne Lidar Data. In: IGARSS 2017, pp:2760-2763.
- Harrell, P.A., Kasischke, E.S., Bourgeau-Chavez, L.L., Haney, E.M., Christensen, N.L., 1997. Evaluation of approaches to estimating aboveground biomass in southern pine forests using SIR-C data. *Remote Sensing Of Environment*, 59: 223-233.
- Harwin, S., Lucieer, A., 2012. Assessing the accuracy of georeferenced point clouds produced via multi-view stereopsis from unmanned aerial vehicle (UAV) imagery. *Remote Sensing*, 4 (6): 1573-1599.
- Hawbaker, T.J., Gobakken, T., Lesak, A., Trømborg, E., Contrucci, K., Radeloff, V., 2010. Light detection and ranging-based measures of mixed hardwood forest structure. *Forest Science*, 56:313-326.
- Heath, L.S., Smith, J.E., 2000. An Assessment of Uncertainty in Aboveground Forest Carbon Budget Projections. *Environmental Science & Policy*, 3: 73-82.
- Hengl, T., 2006. Finding the right pixel size. *Computers & Geosciences*, 32(9):1283-1298.
- Hese, S., Lucht, W., Schmullius, C., Barnsley, M., Dubayah, R., Knorr, D., Neumann, K., Riedel, T., Schröter, K., 2005, Global biomass mapping for an improved understanding of the CO<sub>2</sub> balance-the Earth observation mission Carbon-3D. *Remote Sensing Of Environment*, 94: 94-104.
- Hoerl, A., Kennard, R., 1970. Ridge regression: Biased estimation for nonorthogonal problems. *Technometrics*, 12 (1): 55-67.
- Holmgren, J., Barth, A., Larsson, H., Olsson, H., 2010. Prediction of stem attributes by combining airborne laser scanning and measurements from harvesting machinery. In: *SilviLaser 2010 10th International Conference on LiDAR Applications for Assessing Forest Ecosystems*, Freiburg, Germany.
- Hosoi, F., Matsugami, H., Watanuki, K., Shimizu, Y., Omasa, K., 2012. Accurate detection of tree apexes in coniferous canopies from airborne scanning light detection and ranging images based on crown-extraction filtering. *Journal of Applied Remote Sensing*, 6: 063502-1.
- Houghton, R.A., 2005, Aboveground forest biomass and the global carbon balance. *Global Change Biology*, 11: 945-958.

- Houghton, R., Skole, D., Nobre, C.A., Hackler, J., Lawrence, K., Chomentowski, W.H., 2000. Annual fluxes of carbon from deforestation and regrowth in the Brazilian Amazon. *Nature*, 403 (6767):301-304.
- Hu, B., Li, J., Jing, L., Judah, A., 2014. Improving the efficiency and accuracy of individual tree crown delineation from high-density LiDAR data. *International Journal of Applied Earth Observation and Geoinformation*, 01(26):145-155.
- Hu, X.Y., and Yuan Y., 2016. Deep Learning Based Classification for DTM Extraction from ALS Point Cloud. *Remote Sensing*, 8(9):730, <https://doi.org/10.3390/rs8090730>.
- Huang, C., Song, K., Kim, S., Townshend, J., Davis, P., Masek, J., Goward, S., 2008. Use of a dark object concept and support vector machines to automate forest cover change analysis. *Remote Sensing Of Environment*, 112:970-985.
- Huang, Y., Chen, J., 2013. Advances in the Estimation of Forest Biomass Based on SAR Data. *Remote Sensing For Land & Resources*, 25: 7-13.
- Hudak, A., Crookston, N., Evans, J., Hall, D., Falkowski, M., 2008. Nearest neighbor imputation of species-level, plot-scale forest structure attributes from LiDAR data. *remote Sensing Of Environment*, 112: 2232-2245.
- Hudak, A., Strand, E.K., Vierling, L.A., Byrne, J.C., Eitel, J.U.H., Martinuzzi, S., Falkowski, M.J., 2012. Quantifying aboveground forest carbon pools and fluxes from repeat LiDAR surveys. *Remote Sensing Of Environment*, 123: 25-40.
- Huete, A., Didan, K., Miura, T., Rodriguez, E.P., Gao, X., Ferreira, L.G., 2002. Overview of the radiometric and biophysical performance of the MODIS vegetation indices. *Remote Sensing Of Environment*, 83:195-213.
- Hussin, Y., Reich, R., Hoffer, R., 1991. Estimating slash pine biomass using radar backscatter. *IEEE Transactions on Geoscience and Remote Sensing*, 29:427-431.
- Hyypä, H.J., Hyypä, J.M., 2001. Effects of stand size on the accuracy of remote sensing-based forest inventory. *IEEE Transactions on Geoscience and Remote Sensing*, 39 (12):2613-2621.
- Hyypä, J., Hyypä, H., Leckie, D., Gougeon, F., Yu, X., Maltamo, M., 2008. Review of methods of small-footprint airborne laser scanning for extracting forest inventory data in boreal forests. *International Journal of Remote Sensing*, 29(5):1339-1366.

- Hyypä, J., Inkinen, M., 1999. Detecting and estimating attributes for single trees using laser scanner. *The Photogrammetric Journal of Finland*, 16: 27-42.
- Hyypä, J., Kelle, O., Lehikoinen, M., Inkinen, M., 2001. A segmentation based method to retrieve stem volume estimates from 3-D tree height models produced by laser scanners. *IEEE Transactions on Geoscience and Remote Sensing*, 39(5):969-975.
- Hyypä, J., Mielonen, T., Hyypä, H., Maltamo, M., Yu, X., Honkavaara, E., Kaartinen, H., 2005. Using individual tree crown approach for forest volume extraction with aerial images and laser point clouds, In: *Proceedings of ISPRS workshop laser scanning*. Citeseer, pp.12-14.
- Ikeda, H., Okamoto, K., Fukuhara, M., 1999. Estimation of aboveground grassland phytomass with a growth model using Landsat TM and climate data. *International Journal of Remote Sensing*, 20(11): 2283-2294.
- Imhoff, M.L., 1995. Radar backscatter and biomass saturation: Ramifications for global biomass inventory. *IEEE Transactions on Geoscience and Remote Sensing*, 33(511).
- Ioki, K., Imanishi, J., Sasaki, T., Morimoto, Y., Kitada, K., 2010. Estimating stand volume in broad-leaved forest using discrete-return LiDAR: Plot-based approach. *Landscape and Ecological Engineering*, 6:29-36.
- IPCC, 2003. *Good Practice Guidance for Land Use, Land-Use Change and Forestry*. In: Penman, J., Gytarsky, M., Hiraishi, T., Krug, T., Kruger, D., Pipatti, R., Buendia, L., Miwa, K., Ngara, T., Tanabe, K. and Wagner, F., (Eds.), Institute for Global Environmental Strategies (IGES), Kanagawa.
- ISPRS, 2003. Available online: <http://www.itc.nl/isprswgiii-3/filtertest>; accessed on May. 21, 2017.
- Jacobsen, K., Lohmann, P., 2003. Segmented filtering of laser scanner DSMs. In: *IAPRSS*, 34(3/W13).
- Jahromi, A.B., Zoj, M.J.V., Mohammadzadeh, A., Sadeghian, S., 2011. A novel filtering algorithm for bare-earth extraction from airborne laser scanning data using an artificial neural network. *IEEE Journal Of Selected Topics In Applied Earth Observations And Remote Sensing*, 4 (4):836-843.
- Ji, L., Wylie, B.K., Nossor, D.R., Peterson, B., Waldrop, M.P., McFarland, J.W., Rover, J., Hollingsworth, T.N., 2012. Estimating aboveground biomass in interior Alaska with Landsat data

and field measurements. *International Journal of Applied Earth Observation and Geoinformation*, 18: 451-461.

Jing, L., Hu, B., Li, J., Norland, T., 2012. Automated delineation of individual tree crowns from LiDAR data by multi-scale analysis and segmentation. *Photogrammetric Engineering & Remote Sensing*, 78(12):1275-1284.

Jucker, T., Caspersen, J., Chave, J., Antin, C., Barbier, N., Bongers, F., Dalponte, M., van Ewijk, K., Forrester, D., Haeni, M., Higgins, S., Holdaway, R., Iida, Y., Lorimer, C., Marshall, P., Momo, S., Moncrieff, G., Ploton, P., Poorter, L., Rahman, K., Schlund, M., Sonke, B., Sterck, F., Trugman, A., Usoltsev, V., Vanderwel, M., Waldner, P., Wedeux, B., Wirth, C., Woell, H., Woods, M., Xiang, W., Zimmermann, N., Coomes, D., 2017. Allometric equations for integrating remote sensing imagery into forest monitoring programs. *Global Change Biology*, 23(1):177-190,

Kasischke, E., Melack, J., Dobson, M., 1997. The Use of Imaging Radars for Ecological Applications: A Review. *Remote Sensing Of Environment*, 59 (2): 141-156.

Kavzoglu, T., Colkesen, I., 2009. A kernel functions analysis for support vector machines for land cover classification. *International Journal of Applied Earth Observation and Geoinformation*, 11:352-359.

Kayitakire, F., Hamel, C., Defourny, P., 2006. Retrieving Forest Structure Variables Based on Image Texture Analysis and IKONOS-2 Imagery. *Remote Sensing Of Environment*, 102 (3-4):390-401.

Ke, Y., Quackenbush, L.J., 2011. A Review of Methods for Automatic Individual Tree-Crown Detection and Delineation from Passive Remote Sensing. *International Journal of Remote Sensing*, 32(17): 4725–4747.

Keller, M., Palace, M., Hurtt, G., 2001. Biomass Estimation in the Tapajos National Forest, Brazil: Examination of Sampling and Allometric Uncertainties. *Forest Ecology and Management*, 154: 371-382.

Kellndorfer, J., Walker, W., Pierce, L., Dobson, C., Fites, J.A., Hunsaker, C., Vona, J., Clutter, M., 2004. Vegetation Height Estimation from Shuttle Radar Topography Mission and National Elevation Datasets. *Remote Sensing Of Environment*, 93 (3): 339-358.

Khosravipour, A., Skidmore, A.K., Isenburg, M., Wang, T.J., Hussin, Y.A., 2014. Generating Pit-free Canopy Height Models from Airborne Lidar. *Photogrammetric Engineering & Remote Sensing*, 80(9):863-872.

- Kingman, J., 2005. Poisson Processes. Encyclopedia of Biostatistics. 6. DOI: 10.1002/0470011815.b2a07042
- Koch, B., Heyder, U., Weinacker, H., 2006. Detection of individual tree crowns in airborne lidar data. *Photogrammetric Engineering & Remote Sensing*, 72(4):357-363.
- Korpela, I., Koskinen, M., Vasander, H., Holopainen, M., Minkkinen, K., 2009. Airborne small-footprint discrete-return LiDAR data in the assessment of boreal mire surface patterns, vegetation, and habitats. *Forest Ecology and Management*, 258:1549-1566.
- Korpela, I., Tuomola, T., Välimäki, E., 2007. Mapping forest plots: an efficient method combining photogrammetry and field triangulation. *Silva Fenn.* 41(3):457–469.
- Krankina, O., Harmon, M., Cohen, W., Oetter, D., Zyrina, O., Duane, M., 2004. Carbon stores, sinks, and sources in forests of Northwestern Russia: Can we reconcile forest inventories with remote sensing results? *Climatic Change*, 67:257-272.
- Kraus, K., Pfeifer, N., 1998. Determination of terrain models in wooded areas with aerial laser scanner data. *ISPRS Journal of Photogrammetry and Remote Sensing*, 53:193-203.
- Krofcheck, D.J., Litvak, M.E., Lippitt, C.D., Neuenschwander, A., 2016. Woody Biomass Estimation in a Southwestern U.S. Juniper Savanna Using LiDAR-Derived Clumped Tree Segmentation and Existing Allometries. *Remote Sensing*, 8(453).
- Kronseder, K., Ballhorn, U., Böhm, V., Siegert, F., 2012. Above ground biomass estimation across forest types at different degradation levels in Central Kalimantan using LiDAR data. *International Journal of Applied Earth Observation and Geoinformation*, 18:37-48.
- Kuplich, T.M., Salvatori, V., Curran, P.J., 2000. JERS-1/SAR backscatter and its relationship with biomass of regenerating forests. *International Journal of Remote Sensing*, 21: 2513-2518.
- Kuemmerle, T., Chaskovskyy, O., Knorn, J., Radeloff, V., Kruhlov, I., Keeton, W., Hostert, P., 2009. Forest cover change and illegal logging in the Ukrainian Carpathians in the transition period from 1988 to 2007. *Remote Sensing Of Environment*, 113:1194-1207.
- Kurvonen, L., Pulliainen, J., Hallikainen, M., 1999. Retrieval of biomass in boreal forests from multitemporal ERS-1 and JERS-1 SAR data. *IEEE Transactions on Geoscience and Remote Sensing*, 37: 198-205.
- Kwak, D.-H., Lee, W.-K., Lee, J.H., Biging, G.S., Gong, P., 2007. Detection of individual trees and estimation of tree height using LiDAR data. *Journal of Forest Research*, 12:425-434.

Larocque, G., Bhatti, J., Boutin, R., Chertov, O., 2008. Uncertainty Analysis in Carbon Cycle Models of Forest Ecosystems: Research Needs and Development of a Theoretical Framework to Estimate Error Propagation. *Ecological Modelling*, 219 (3–4): 400–412.

Lastools, 2016. Available online: <http://www.cs.unc.edu/~isenburg/lastools/> (accessed on Aug. 3rd, 2016).

Le Toan, T., Beaudoin, A., Riom, J., Guyon, D., 1991, Relating forest parameters to SAR data, In: *Proceedings of IGARSS'91*. Helsinki University of Technology. Espoo, Finland, 3-6 June, 2:689-692.

Le Toan, T., Beaudoin, A., Guyon, D., 1992. Relating forest biomass to SAR data. *IEEE Transactions on Geoscience and Remote Sensing*, 30: 403-411.

Le Toan, T., Quegan, S., Davidson, M., Balzter, H., Paillou, P., Papathanassiou, K., Plummer, S., Rocca, F., Saatchi, S., Shugart, H., Ulander, L., 2011. The BIOMASS Mission: Mapping Global Forest Biomass to Better Understand the Terrestrial Carbon Cycle. *Remote Sensing Of Environment*, 115 (11): 2850-2860.

Leckie, D.G., 1998. Forestry applications using imaging radar. In *Principles and Applications of Imaging Radar, Manual of Remote Sensing*, 3rd edn, vol. 2, F.M. Henderson and A.J. Lewis (Eds), 437-509 (Chichester: John Wiley & Sons).

Leckie, D., Gougeon, F., Hill, D., Quinn, R., Armstrong, L., Shreenan, R., 2003. Combined high-density lidar and multispectral imagery for individual tree crown analysis. *Canadian Journal of Remote Sensing*, 29: 633-649.

Lee, H., Slatton, K.C., Roth, B.E., Cropper, W.P., 2010. Adaptive clustering of airborne LiDAR data to segment individual tree crowns in managed pine forests. *International Journal of Remote Sensing*, 31(1):117-139.

Lefsky, M.A., Cohen, W.B., Harding, D.J., Parker, G.G., Acker, S.A., Gower, S.T., 2002. Lidar Remote Sensing of Above-ground Biomass in Three Biomes. *Global Ecology and Biogeography*, 11 (5): 393-399.

Lefsky, M.A., Cohen, W.B., Acker, S.A., Parker, G.G., Spies, T.A., Harding, D., 1999. Lidar Remote Sensing of the Canopy Structure and Biophysical Properties of Douglas-Fir Western Hemlock Forests. *Remote Sensing Of Environment*, 70 (3): 339-361.

- Lever, J., Krzywinski, M., Altman, N., 2017. Principal component analysis, *Nature Methods*, 14:641-642.
- Li, W.K., Guo, Q.H., Jakubowski, M.K., Kelly, M., 2012. A New Method for Segmenting Individual Trees from the Lidar Point Cloud. *Photogrammetric Engineering&Remote Sensing*. 78:75-84.
- Liu, L., Lim, S., 2015. A voxel-based skewness and kurtosis balancing algorithm for updating road networks from airborne lidar data. In: *CEUR Workshop Proceedings*, Brisbane, Australia. 21- 33.
- Liu, X.Y., 2008. Airborne LiDAR for DEM generation: some critical issues. *Progress in Physical Geography*, 32(1):31-49.
- Lodha, S.K., Fitzpatrick, D.M., Helmbold, D.P., 2007. Aerial Lidar Data Classification using AdaBoost. In: *6<sup>th</sup> 3DIM*, 435-442.
- Lu, D., 2005. Aboveground Biomass Estimation Using Landsat TM Data in the Brazilian Amazon. *International Journal of Remote Sensing*, 26: 2509-2525.
- Lu, D., 2006. The potential and challenge of remote sensing-based biomass estimation. *International Journal of Remote Sensing*, 27:1297-1328.
- Lu, D., Batistella, M., 2005. Exploring TM image texture and its relationships with biomass estimation in Rondônia, Brazilian Amazon. *Acta Amazonica*, 35:261-268.
- Lu, D., Chen, Q., Wang, G., Liu, L., Li G., Moran E., 2016. A survey of remote sensing-based aboveground biomass estimation methods in forest ecosystems, *International Journal of Digital Earth*, 9(1): 63-105.
- Lu, D., Chen, Q., Wang, G., Moran, E., Batistella, M., Zhang, M., Vaglio Laurin, G., Saah, D., 2012. Aboveground Forest Biomass Estimation with Landsat and LiDAR Data and Uncertainty Analysis of the Estimates. *International Journal of Remote Sensing*, 2012:16.
- Lu, N., Zhou, J., Han, Z.X., Li, D., Cao, Q., Yao, X., Tian, Y.C., Zhu, Y., Cao, W.X., Cheng, T., 2019. Improved estimation of aboveground biomass in wheat from RGB imagery and point cloud data acquired with a low cost unmanned aerial vehicle system, *Plant Methods*, 15:17. <https://doi.org/10.1186/s13007-019-0402-3>

- Lu, W.L., Murphy, K.P., Little, J.J., Sheffer, A., Fu, H., 2009. A hybrid conditional random field for estimating the underlying ground surface from airborne LiDAR data. *IEEE Transactions on Geoscience and Remote Sensing*, 47(8):2913-2922.
- Lucas, R.M., Mitchell, A.L., Rosenqvist, A., Proisy, C., Melius, A., Ticehurst, C., 2007. The Potential of L-band SAR for Quantifying Mangrove Characteristics and Change: Case Studies from the Tropics. *Aquatic Conservation: Marine and Freshwater Ecosystems*, 17: 245-264.
- Luckman, A., Baker, J.R., Kuplich, T.M., Yanasse, C.C.F., Frery, A.C., 1997. A study of the relationship between radar backscatter and regenerating forest biomass for space borne SAR instrument. *Remote Sensing Of Environment*, 60: 1-13.
- Luther, J., Fournier, R., Piercey, D., Guindon, L., Hall, R., 2006. Biomass Mapping Using Forest Type and Structure Derived from Landsat TM Imagery. *International Journal of Applied Earth Observation and Geoinformation*, 8: 173-187.
- Mascaro, J., Detto, M., Asner, G.P., Muller-Landau, H.C., 2011. Evaluating Uncertainty in Mapping Forest Carbon with Airborne LiDAR. *Remote Sensing Of Environment*, 115 (12):3770-3774.
- MathWorks, 2015. Matlab R2013b user guide. The MathWorks, Inc., Natick, Massachusetts, United States, [https://au.mathworks.com/help/releases/R2013a/pdf\\_doc/matlab/getstart.pdf](https://au.mathworks.com/help/releases/R2013a/pdf_doc/matlab/getstart.pdf), accessed in December 2015.
- Mauya, E.W., Ene, L.T., Bollandås, O.M., Gobakken, T., Næsset, E., Malimbwi, R. E., Zahabu, E., 2015. Modelling aboveground forest biomass using airborne laser scanner data in the miombo woodlands of Tanzania. *Carbon Balance and Management*, 10:28.
- McGauchey, R.J., 2016. FUSION/LDV: Software for LiDAR Data Analysis and Visualization. Forest Service Pacific Northwest Research Station USDA, Seattle, accessed in April 2016.
- McRoberts, R. E., Næsset, E., Gobakken, T., 2013. Inference for Lidar-assisted Estimation of Forest Growing Stock Volume. *Remote Sensing Of Environment*, 128: 268-275.
- Meng, X.L., Currit, N., Zhao, K.G., 2010. Ground Filtering Algorithms for Airborne LiDAR Data: A Review of Critical Issues. *Remote Sensing*, 2: 833-860, doi:10.3390/rs2030833.
- Meng, X.L., Wang, L., Currit, N., 2009. Morphology-based building detection from airborne LIDAR data. *Photogrammetric Engineering&Remote Sensing*, 75:427-442.

- Mongus, D., Lukač, N., Žalik, B., 2014. Ground and building extraction from LiDAR data based on differential morphological profiles and locally fitted surfaces. *ISPRS Journal of Photogrammetry and Remote Sensing*, 93:145-156.
- Mongus, D., Žalik, B., 2012. Parameter-free ground filtering of LiDAR data for automatic DTM generation. *ISPRS Journal of Photogrammetry and Remote Sensing*, 67(1):1-12.
- Montesano, P.M., Nelson, R.F., Dubayah, R.O., Sun, G., Cook, B.D., Ranson, K.J.R., Næsset, E., Kharuk, V., 2014. The Uncertainty of Biomass Estimates from LiDAR and SAR Across a Boreal Forest Structure Gradient. *Remote Sensing Of Environment*, 154: 398-407.
- Morsdorf, F., Meier, E., Kötz, B., Itten, K.I., Dobbertin, M., Allgöwer, B., 2004. LIDAR-based geometric reconstruction of boreal type forest stands at single tree level for forest and wildland fire management. *Remote Sensing Of Environment*, 92(3):353-362.
- Mountrakis, G., Im, J., Ogole, C., 2011. Support vector machines in remote sensing: A review. *ISPRS Journal of Photogrammetry and Remote Sensing*, 66:247-259.
- Mutanga, O., Skidmore, A.K., 2004. Narrow band vegetation indices overcome the saturation problem in biomass estimation. *International Journal of Remote Sensing*, 25 (19):3999-4014.
- Mutanga, O., Adam, E., Cho, M.A., 2012. High density biomass estimation for wetland vegetation using WorldView-2 imagery and random forest regression algorithm. *International Journal of Applied Earth Observation and Geoinformation*, 18: 399-406.
- Muukkonen, P., Heiskanen, J., 2007. Biomass estimation over a large area based on standwise forest inventory data and ASTER and MODIS satellite data: A possibility to verify carbon inventories. *Remote Sensing Of Environment*, 107:617-624.
- Nabuurs, G.J., van Putten, B., Knippers, T.S., Mohren, G., 2008. Comparison of Uncertainties in Carbon Sequestration Estimates for a Tropical and a Temperate Forest. *Forest Ecology and Management*, 256 (3): 237-245.
- Næsset, E., 2004. Effects of different flying altitudes on biophysical stand properties estimated from canopy height and density measured with a small-footprint airborne scanning laser. *Remote Sensing Of Environment*, 91:243-255.
- Næsset, E., 2005. Assessing sensor effects and effects of leaf-off and leaf-on canopy conditions on biophysical stand properties derived from small-footprint airborne laser data. *Remote Sensing Of Environment*, 98:356-370.

- Næsset, E., Gobakken, T., Solberg, S., Gregoire, T.G., Nelson, R., Ståhl, G., Weydahl, D., 2011. Model-assisted regional forest biomass estimation using LiDAR and InSAR as auxiliary data: A case study from a boreal forest area. *Remote Sensing Of Environment*, 115:3599-3614.
- Næsset, E., Økland, T., 2002. Estimating tree height and tree crown properties using airborne scanning laser in a boreal nature reserve. *Remote Sensing Of Environment*, 79:105-115.
- Nafiseh, G., Reza, S.M., Ali, M., 2011. A Review on Biomass Estimation Methods Using Synthetic Aperture Radar Data. *International Journal Of Geomatics And Geosciences*, 1:776-788.
- Nie, S., Wang, C., Dong, P.L., Xi, X.H., Luo, S.Z., Qin, H.M., 2017. A revised progressive TIN densification for filtering airborne LiDAR data. *Measurement*, 104:70-77.
- Niemeyer, J., Rottensteiner, F., Soergel, U., 2014. Contextual classification of lidar data and building object detection in urban areas. *ISPRS Journal of Photogrammetry and Remote Sensing*, 87:152-165.
- Otsu, N., 1979. A threshold selection method from gray-level histograms. *IEEE Transactions on Systems, Man, and Cybernetics*, 9(1):62-66.
- Özcan, A.H., Ünsalan, C., 2016. LiDAR Data Filtering and DTM Generation Using Empirical Mode Decomposition. *IEEE Journal Of Selected Topics In Applied Earth Observations And Remote Sensing*. DOI: 10.1109/JSTARS.2016. 2543464.
- Paris, C., Valdug, D., Bruzzone, L., 2016. A Hierarchical Approach to Three-Dimensional Segmentation of LiDAR Data at Single-Tree Level in a Multilayered Forest. *IEEE Transactions on Geoscience and Remote Sensing*, 54(7): 4190-4203.
- Patenaude, G., Milne, R., Dawson, T.P., 2005. Synthesis of Remote Sensing Approaches for Forest Carbon Estimation: Reporting to the Kyoto Protocol. *Environmental Science & Policy*, 8:161-178.
- Paul, K., Roxburgh, S., Chave, J., England, J., Zerihun, A., Specht, A., Lewis, T., Bennett, L., Baker, T., Adams, M., Huxtable, D., Montagu, K., Falster, D., Feller, M., Sochacki, S, Ritson, P., Bastin, G., Bartle, J., Wildy, D., Hobbs, T., Larmour, J., Waterworth, R., Stewart, H., Jonson, J., Forrester, D., Applegate, G., Mendham, D., Bradford, M., O'grady, A., Green, D., Sudmeyer, R., Rance, S., Turner, J., Barton, C., Wenk, E., Grove, T., Attiwill, P., Pinkard, E., Butler, D., Brooksbank, K., Spencer, B., Snowdon, P., O'brien, N., Battaglia, M., Cameron, D., Hamilton, S., Mcauthor, G., Sinclair, J., 2015. Testing the generality of above-ground biomass allometry across plant functional types at the continent scale. *Global Change Biology*, 22:2106-2124.

- Persson, A., Holmgren, J., Soderman, U., 2002. Detecting and measuring individual trees using an airborne laser scanner. *Photogrammetric Engineering&Remote Sensing*, 68(9):925-932.
- Pfeifer, N., Kostli, A., Kraus, K., 1998. Interpolation and filtering of laser scanner data implementation and first results. in: *IAPRSSI*, 32(3/1):153-159
- Phua, M.-H., Johari, S., Wong, O.-C., Ioki, K., Mahali, M., Nilus, R., Coomes, D., Maycock, C., Hashim, M., 2017. Synergistic use of Landsat 8 OLI image and airborne LiDAR data for above-ground biomass estimation in tropical lowland rainforests. *Forest Ecology and Management*, 406:163-171.
- Pingel, T.J., Clarke, K.C., McBride, W.A., 2013. An improved simple morphological filter for the terrain classification of airborne LiDAR data. *ISPRS Journal of Photogrammetry and Remote Sensing*, 77: 21-30.
- Piotrowski, A., Napiorkowski, J., 2013. A comparison of methods to avoid overfitting in neural networks training in the case of catchment runoff modelling. *Journal of Hydrology*, 476:97-111.
- Polat, N., Uysal, M., 2015. Investigating performance of Airborne LiDAR data filtering algorithms for DTM generation. *Measurement*, 63:61-68.
- Poli, A., Cirillo, M., 1993. On the use of the normalized mean square error in evaluating dispersion model performance. *Atmospheric Environment. Part A. General Topics*, 27(15):2427-2434.
- Popescu, S.C., Wynne, R.H., 2004. Seeing the trees in the forest: Using lidar and multispectral data fusion with local filtering and variable window size for estimating tree height. *Photogrammetric Engineering&Remote Sensing*, 70:589-604.
- Popescu, S., Wynne, R., Nelson, R., 2002. Estimating plot-level tree heights with lidar: Local filtering with a canopy-height based variable window size. *Computers and Electronics in Agriculture*, 37:71-95.
- Popescu, S., Wynne, R., Nelson, R., 2003. Measuring Individual Tree Crown Diameter with Lidar and Assessing Its Influence on Estimating Forest Volume and Biomass. *Canadian Journal of Remote Sensing*, 29 (5): 564-577.
- Popescu, S., Zhao, K., 2008. A voxel-based lidar method for estimating crown base height for deciduous and pine trees. *Remote Sensing Of Environment*, 112:767-781.

- Powell, S.L., Cohen, W.B., Healey, S.P., Kennedy, R.E., Moisen, G.G., Pierce, K.B., Ohmann, J.L., 2010. Quantification of live aboveground forest biomass dynamics with Landsat time-series and field inventory data: A comparison of empirical modeling approaches. *Remote Sensing Of Environment*, 114:1053-1068
- Pukelsheim, F., 1994. The Three Sigma Rule. *The American Statistician*, 48(2):88-91.
- Pullianen, J., Engdahl, M., Hallikainen, M., 2003. Feasibility of Multi-temporal Interferometric SAR Data for Stand-level Estimation of Boreal Forest Stem Volume. *Remote Sensing Of Environment*, 85 (4): 397-409.
- R: A Language and Environment for Statistical Computing, 2016. R Foundation for Statistical Computing, Vienna, Austria, accessed in April 2016,
- Rahman, M.M., Sumantyo, J.T.S., 2013. Retrieval of Tropical Forest Biomass Information from ALOS PALSAR Data. *Geocarto International*, 28 (5): 382-403.
- Rauste, Y., Hame, T., Pullianen, J., Heiska, K., Hallikainen, M., 1994. Radar-based forest biomass estimation. *International Journal of Remote Sensing*, 15(14):2797-2808.
- Reitberger, J., Schnorr, C., Krzystek, P., Stilla, U., 2009. 3D segmentation of singletrees exploiting full waveform LIDAR data. *ISPRS Journal of Photogrammetry and Remote Sensing*, 64(6):561-574.
- Rivington, M., Matthews, K., Bellocchi, G., Buchan, K., 2006. Evaluating Uncertainty Introduced to Process-based Simulation Model Estimates by Alternative Sources of Meteorological Data. *Agricultural Systems*, 88 (2-3): 451-471.
- Roggero, M., 2001. Airborne laser scanning: clustering in raw data. in: *IAPRSSI*, 34(3/W4):227-232.
- Saatchi, S.S., Moghaddam, M., 1999. Estimation of boreal forest biomass using spaceborne SAR systems. IN: *Proceedings of the IGARSS99 Symposium, Hamburg, Germany, 28 June-2 July 1999*.
- Saatchi, S.S., Houghton, R.A., Alvalá, R.C., Soares, J.V., Yu, Y., 2007. Distribution of Aboveground Live Biomass in the Amazon Basin. *Global Change Biology*, 13 (4): 816-837.
- Saatchi, S., Marlier, M., Chazdon, R.L., Clark, D.B., Russell, A.E., 2011. Impact of Spatial Variability of Tropical Forest Structure on Radar Estimation of Aboveground Biomass. *Remote Sensing Of Environment*, 115 (11): 2836-2849.

- Sader, S.A., 1987. Forest biomass, canopy structure, and species composition relationships with multipolarization L-band synthetic aperture radar data. *Photogrammetric Engineering&Remote Sensing*, 53: 193-202.
- Salas, C., Ene, L., Gregoire, T.G., Næsset, E., Gobakken, T., 2010. Modelling tree diameter from airborne laser scanning derived variables: A comparison of spatial statistical models. *Remote Sensing Of Environment*, 114:1277-1285.
- Sandberg, G., Ulander, L.M.H., Fransson, J.E.S., Holmgren, J., Le Toan, T., 2011. L- and P-band Backscatter Intensity for Biomass Retrieval in Hemiboreal Forest. *Remote Sensing Of Environment*, 115 (11): 2874-2886.
- Santhi, V., Acharjya, D.P., Ezhilarasan, M., 2016. *Emerging Technologies in Intelligent Applications for Image and Video Processing*. IGI Global, Hershey, PA, USA.
- Santos, J.R., Pardi Lacruz, M.S., Araujo, L.S. Keil, M., 2002. Savanna and tropical rainforest biomass estimation and spatialization using JERS-1 data. *International Journal of Remote Sensing*, 23: 1217-1229.
- Sarker, M., Nichol, J., Ahmad, B., Busu, I., Rahman, A., 2012. Potential of Texture Measurements of Two-date Dual Polarization PALSAR Data for the Improvement of Forest Biomass Estimation. *ISPRS Journal of Photogrammetry and Remote Sensing*, 69: 146-166.
- Sačkov, I., Hlásny, T., Bucha, T., Juriš, M., 2017. Integration of tree allometry rules to treetops detection and tree crowns delineation using airborne lidar data. *iForest-Biogeosci. Forestry*, 10, 459.
- Seidel, D., Fleck, S., Leuschner, C., Hammett, T., 2011. Review of Ground-based Methods to Measure the Distribution of Biomass in Forest Canopies. *Annals of Forest Science*, 68 (2): 225-244.
- Segura, M., Kanninen, M., 2005, Allometric models for tree volume and total aboveground biomass in a tropical humid forest in Costa Rica. *Biotropica*, 37:2-8.
- Shamsoddini, A., Turner, R., Trinder, J.C., 2013. Improving lidar-based forest structure mapping with crown-level pit removal. *Journal of Spatial Science*, 58(1):29-51.
- Shan, J., Sampath, A., 2005. Urban DEM generation from raw LiDAR data: a labeling algorithm and its performance. *Photogrammetric Engineering&Remote Sensing*, 71:217-226.

- Sibson, R., 1981. A brief description of natural neighbor interpolation. In: *Interpreting Multivariate Data*, Chichester: John Wiley & Sons, New York, USA. 21-36.
- Sierra, C.A., del Valle, J.I., Orrego, S.A., Moreno, F.H., Harmon, M.E., Zapata, M., Colorado, G.J., Herrera, M., Lara, W., Restrepo, D., Berrouet, L., Loaiza, L., Benjumea, J., 2007. Total Carbon Stocks in a Tropical Forest Landscape of the Porce Region, Colombia. *Forest Ecology and Management*, 243 (2-3): 299-309.
- Sithole, G., 2001. Filtering of laser altimetry data using a slope adaptive filter. In: *IAPRSSI*, 34(3/W4):203-210.
- Sithole, G., 2005. Segmentation and classification of airborne laser scanner data. PhD thesis, Delft University of Technology, Delft, the Netherlands.
- Sithole, G., Vosselman, G., 2004. Experimental comparison of filter algorithms for bare-Earth extraction from airborne laser scanning point clouds. *ISPRS Journal of Photogrammetry and Remote Sensing*. 59: 85-101.
- Sithole, G., Vosselman, G., 2005. Filtering of airborne laser scanner data based on segmented point clouds. in *Proc. of ISPRS Workshop Laser Scanning*, Enschede, the Netherlands. 66-71.
- Silva, C.A., Crookston, N.L., Hudak, A.T., Vierling, L.A., 2017. rLiDAR: An R package for reading, processing and visualizing LiDAR data, version 0.1.1, accessed in July 2017.
- Silva, C.A., Klauberg, C., Hentz, Â., Corte, A., Ribeiro, U., Liesenberg, V., 2018. Comparing the performance of ground filtering algorithms for terrain modeling in a forest environment using airborne lidar data. *Floresta e Ambiente*, 25(2) :e20160150.
- SMRF, 2011. Available online: <http://tpingel.org/code/smrf/smrf.html> (accessed on Oct. 15, 2016).
- Smyth, C., Kurz, W., Neilson, E., Stinson, G., 2013. National - scale Estimates of Forest Root Biomass Carbon Stocks and Associated Carbon Fluxes in Canada. *Global Biogeochemical Cycles*, 27 (4): 1262–1273.
- Soares, P., Tome, M., Skovsgaard, J., Vanclay, J., 1995. Evaluating a growth model for forest management using continuous forest inventory data. *Forest Ecology and Management*, 71:251-265.

- Sohn, G., Dowman, I., 2002. Terrain surface reconstruction by the use of tetrahedron model with the MDL Criterion. In: Proc. of PCV 02, ISPRS Commission III, Symposium, Graz, Austria. 336-344
- Solberg, S., Næsset, E., Gobakken, T., Bollandsås, O., 2014. Forest Biomass Change Estimated from Height Change in Interferometric SAR Height Models. *Carbon Balance and Management*, 9(5).
- Song, C., 2013. Optical Remote Sensing of Forest Leaf Area Index and Biomass. *Progress in Physical Geography*, 37 (1): 98-113.
- Statistical Tables, 2018. <https://home.ubalt.edu/ntsbarsh/Business-stat/StatisticalTables.pdf>. accessed on 26th September 2018.
- Su, Y.-J., Guo, Q.-H., Xue, B.-L., Hu, T.-Y., Alvarez, O., Tao, S.-L., Fang, J.-Y., 2016. Spatial distribution of forest aboveground biomass in China: Estimation through combination of spaceborne lidar, optical imagery, and forest inventory data. *Remote Sensing Of Environment*, 173:187-199.
- Sun, G., Ranson, K.J., Kharuk, V.I., 2002. Radiometric slope correction for forest biomass estimation from SAR data in the western Sayani Mountains, Siberia. *Remote Sensing Of Environment*, 79: 279-287.
- Sun, X.F., Li, G.C., Wang, M., and Fan, Z.M., 2019. Analyzing the Uncertainty of Estimating Forest Aboveground Biomass Using Optical Imagery and Spaceborne LiDAR, *Remote Sensing*, 11:722 doi:10.3390/rs11060722.
- Swetnam, T.L., Falk, D.A., 2014. Application of Metabolic Scaling Theory to reduce error in local maxima tree segmentation from aerial LiDAR. *Forest Ecology and Management*, 323:158-167.
- Terrasolid, 2016. TerraScan User's Guide. Available online: <http://www.terrasolid.com/download/tscan.pdf> (accessed on Oct. 25th, 2016).
- Thacker, N.A., Bromiley, P.A., 2001. The effects of a square root transform on a Poisson distributed quantity. *Tina Memo* 10.
- Tian X., Yan, M., van der Tol, C., Li, Z.Y., Su, Z.B., Chen, E.X., Li, X., Li, L.H., Wang, X.F., Pan, X.D., Gao, L.S., Han, Z.T., 2017. Modeling forest above ground biomass dynamics using

multi source data and incorporated models: A case study over the Qilian Mountains. *Agricultural and Forest Meteorology*, 246: 1-14.

Todd, S.W., Hoffer, R.M., Milchunas, D.G., 1998. Biomass estimation on grazed and ungrazed rangelands using spectral indices. *International Journal of Remote Sensing*, 19:427-438.

Tomppo, E., Nilsson, M., Rosengren, M., Aalto, P., Kennedy, P., 2002. Simultaneous use of Landsat-TM and IRS-1C WiFS data in estimating large area tree stem volume and aboveground biomass. *Remote Sensing Of Environment*, 82:156-171.

Tóvári, D., Pfeifer, N., 2005. Segmentation based robust interpolation – a new approach to laser filtering. In: *IAPRSS*, 36(3/W19):79-84.

Turner, D., Guzy, M., Lefsky, M., Ritts, W., van Tuyl, S., Law, B.E., 2004. Monitoring forest carbon sequestration with remote sensing and carbon cycle modeling. *Environmental Management*, 33: 457-466.

Twomey, S., 1997. *Introduction to the Mathematics of Inversion in Remote Sensing and Indirect Measurements*; Dover Publications: Mineola, NY, USA.

Ulaby, F.T., Moore, R.K., Fung, A.K., 1986. *Microwave Remote Sensing: Active and Passive, Volume I: Fundamentals and Radiometry*; Artech House Publishers: Norwood, MA, USA.

Ural, S., Shan, J., 2016. A Min-cut Based Filter for Airborne LIDAR Data. In: *IAPRSSI, XXIII ISPRS Congress, Prague, Czech Republic. XLI-B3*.

Vaglio Laurin, G., Chen, Q., Lindsell, J.A., Coomes, D.A., Frate, F., Del Guerriero, L., Pirotti, F., Valentini, R., 2014. Aboveground Biomass Estimation in an African Tropical Forest with Lidar and Hyperspectral Data. *ISPRS Journal of Photogrammetry and Remote Sensing*, 89: 49-58.

Van Aardt, J.A.N., Wynne, R.H., Oderwald, R.G., 2006. Forest Volume and Biomass Estimation Using Small-Footprint Lidar-Distributional Parameters on a Per-Segment Basis. *Forest Science*, 2(6):636-649.

Van Breugel, M., Ransijn, J., Craen, D., Bongers, F., Hall, J., 2011. Estimating carbon stock in secondary forests: decisions and uncertainties associated with allometric biomass models. *Forest Ecology and Management*, 262:1648-1657.

Vastaranta, M., Holopainen, M., Yu, X., Hyypä, J., Mäkinen, A., Rasinmäki, J., Melkas, T., Kaartinen, H., Hyypä, H., 2011. Effects of individual tree detection error sources on forest management planning calculations. *Remote Sensing*, 3:1614-1626.

- Vauhkonen, J., Ene, L., Gupta, S., Heinzl, J., Holmgren, J., Pitkänen, J., Solberg, S., Wang, Y., Weinacker, H., Hauglin, K., Lien, V., Packalén, P., Gobakken, T., Koch, B., Næsset, E., Tokola, T., Maltamo, M., 2010. Comparative testing of single-tree detection algorithms. In: *SilviLaser 2010 10th International Conference on LiDAR Applications for Assessing Forest Ecosystems*, Freiburg, Germany.
- Vega, C., Hamrouni, A., El Mokhtari, S., Morel, J., Bock, J., Renaud, J.P., Bouvier, M., Durrieu, S., 2014. PTrees: A point-based approach to forest tree extraction from lidar data. *International Journal of Applied Earth Observation and Geoinformation*, 33:98–108.
- Verma, N., Lamb, D., Reid, N., Wilson, B., 2014. An allometric model for estimating DBH of isolated and clustered Eucalyptus trees from measurements of crown projection area. *Forest Ecology and Management*, 326:125-132.
- Verbesselt, J., Somers, B., Van Aardt, J., Jonckheere, I., Coppin, P., 2006. Monitoring herbaceous biomass and water content with SPOT VEGETATION time-series to improve fire risk assessment in savanna ecosystems. *Remote Sensing Of Environment*, 101:399-414.
- Vosselman, G., 2000. Slope based filtering of Laser altimetry data. In: *IAPRSSI*, 33: 935-942.
- Vosselman, G., Gorte, B.G.H., Sithole, G., Rabbani, T., 2004. Recognizing structure in laser scanner point clouds. In: *IAPRSSI*, 46(8):33-38.
- Wallace, L., Lucieer, A., Watson, C. S., 2012(b). Assessing the feasibility of UAV-based LiDAR for high resolution forest change detection,” in *Proc. ISPRS, IAPASS*, 38(B7):499-504.
- Wallace, L., Lucieer, A., Watson, C.S., 2014. Evaluating tree detection and segmentation routines on very high resolution UAV lidar data. *IEEE Transactions on Geoscience and Remote Sensing*, 52(12):7619-7628.
- Wallace, L., Lucieer, A., Watson, C. S., Turner, D., 2012(a). Development of a UAV-LiDAR System with Application to Forest Inventory. *Remote Sensing*, 4:1519-1543.
- Walton, J., 2008. Subpixel urban land cover estimation: Comparing cubist, random forests, and support vector regression. *Photogrammetric Engineering&Remote Sensing*, 74:1213-1222.
- Wang, G., Oyana, T., Zhang, M., Adu-Prah, S., Zeng, S., Lin, H., Se. J., 2009. Mapping and Spatial Uncertainty Analysis of Forest Vegetation Carbon by Combining National Forest Inventory Data and Satellite Images. *Forest Ecology and Management*, 258 (7): 1275-1283.

- Wang, G., Zhang, M., Gertner, G., Oyana, T., McRoberts, R., Ge, H., 2011. Uncertainties of Mapping Aboveground Forest Carbon Due to Plot Locations Using National Forest Inventory Plot and Remotely Sensed Data. *Scandinavian Journal of Forest Research*, 26 (4): 360-373.
- Wang, Y., Weinacker, H., Koch, B., 2008. A Lidar point cloud based procedure for vertical canopy structure analysis and 3D single tree modelling in forest. *Sensors*, 8:3938-3951.
- Warner, T.A., Yeol Lee, J., McGraw, J.B., 1998. In: Hill, D.A., Leckie, D.G. (Eds.), *Delineation and identification of individual trees in the eastern deciduous forest*. Victoria, BC, pp. 81–92.
- Weinstein, G., Marconi, S., Bohlman, S., Zare, A., White, E., 2019. Individual Tree-Crown Detection in RGB Imagery Using Semi-Supervised Deep Learning Neural Networks. *Remote Sensing*, 11:1309. 10.3390/rs11111309.
- Williams, R., Zerihun, A., Montagu, K., Hoffman, M., Hutley, L., Chen, X.Y., 2005. Allometry for estimating aboveground tree biomass in tropical and subtropical eucalypt woodlands: towards general predictive equations. *Australian Journal of Botany*, 53:607-619.
- Windrim, L., Bryson, M., 2018. Forest Tree Detection and Segmentation using High Resolution Airborne LiDAR. Manuscript submitted for publication. (<https://arxiv.org/abs/1810.12536>)
- Wolf, B.M., Heipke, C., 2007. Automatic extraction and delineation of single trees from remote sensing data. *Machine Vision and Applications*, 18(5):317–330.
- Wu, J.W., Yao, W., Choi, S-H., Park, T-J., Myneni, R.B., 2015. A Comparative Study of Predicting DBH and Stem Volume of Individual Trees in a Temperate Forest Using Airborne Waveform LiDAR. *IEEE Geoscience And Remotesensing Letters*, 12:2267-2271.
- Wulder, M.A., White, J.C., Nelson, R.F., Næsset, E., Ørka, H.O., Coops, N.C., Hilker, T., Bater, C.W., Gobakken, T., 2012. Lidar sampling for large-area forest characterization: a review. *Remote Sensing Of Environment*, 121:196-209.
- Yan, F., Wu, B., Wang, Y.J., 2015. Estimating spatiotemporal patterns of aboveground biomass using Landsat TM and MODIS images in the Mu Us Sandy Land, China. *Agricultural and Forest Meteorology*, 200:119-128.
- Yin, D.M., Wang, L., 2016. How to assess the accuracy of the individual tree-based forest inventory derived from remotely sensed data: a review. *International Journal of Remote Sensing*, 37(19):4521-4553.

- Yu, H., Xie, T., Paszczynski, S., Wilamowski, B.M., 2011. Advantages of Radial Basis Function Networks for Dynamic System Design. *IEEE Transactions on Industrial Electronics*, 58(12): 5438-5450.
- Zhang, K., Chen, S., Whitman, D., Shyu, M.A., 2003. Progressive morphological filter for removing non-ground measurements from airborne LiDAR data. *IEEE Transactions on Geoscience and Remote Sensing*, 41:872-882.
- Zhang, L., Yu, G., Gu, F., He, H., Zhang, L., Han, S., 2012. Uncertainty Analysis of Modeled Carbon Fluxes for a Broad-leaved Korean Pine Mixed Forest Using a Process-based Ecosystem Model. *Journal of Forest Research*, 17 (3): 268-282.
- Zhang, M., Lin, H., Zeng, S., Li, J., Shi, J., Wang, G., 2013. Impacts of Plot Location Errors on Accuracy of Mapping and Scaling up Aboveground Forest Carbon Using Sample Plot and Landsat TM Data. *IEEE Geoscience and Remote Sensing Letters*, 10 (6): 1483-1487.
- Zhang, Z., Gerke, M., Vosselman, G., Yang, M.Y., 2018. Filtering photogrammetric point clouds using standard lidar filters towards DTM generation. *ISPRS Annals of Photogrammetry, Remote Sensing & Spatial Information Sciences*, 4(2):319-326.
- Zhao, D., Pang, Y., Li, Z.Y., Sun, G.Q., 2013. Filling pit pixels in a lidar-derived canopy height model with morphological crown control. *International Journal of Remote Sensing*, 34(13): 4636-4654.
- Zhao, F., Guo, Q., Kelly, M., 2012. Allometric equation choice impacts lidar-based forest biomass estimates: A case study from the Sierra National Forest, CA. *Agricultural and Forest Meteorology*, 165:64-72.
- Zhao, J.P., You, S.Y., 2012. Road network extraction from airborne lidar data using scene context. In: *CV&PR*, Providence, Rhode Island, USA. 9-16.
- Zhao, K.G., Popescu, S.C., 2007. Hierarchical watershed segmentation of canopy height model for multi-scale forest inventory. In: *ISPRS Workshop on Laser Scanning and SilviLaser*, Espoo, September 12-14, Finland, 436-441.
- Zhao, K., Popescu, S., Nelson, R., 2009. Lidar remote sensing of forest biomass: A scale-invariant estimation approach using airborne lasers. *Remote Sensing Of Environment*, 113:182-196.

Zhao, X.Q., Guo, Q.H., Su, Y.J., Xue, B.L., 2016. Improved progressive TIN densification filtering algorithm for airborne LiDAR data in forested areas, *ISPRS Journal of Photogrammetry and Remote Sensing*, 117:79-91.

Zhen, Z., Quackenbush, L.J., Zhang, L., 2014. Impact of Tree-oriented Growth Order in Marker-controlled Region Growing for Individual Tree Crown Delineation Using Airborne Laser Scanner (ALS) Data. *Remote Sensing*, 6 (1): 555-579.

Zhen, Z., Quackenbush, L.J., Zhang, L.J., 2016. Trends in Automatic Individual Tree Crown Detection and Delineation—Evolution of LiDAR Data. *Remote Sensing*, 8(333),doi:10.3390/rs8040333.

Zheng, D., Rademacher, J., Chen, J., Crow, T., Bresee, M., Le Moine, J., Ryu, S., 2004. Estimating aboveground biomass using Landsat 7 ETM+ data across a managed landscape in northern Wisconsin, USA. *Remote Sensing Of Environment*, 93:402-411.

Zolkos, S.G., Goetz, S.J., Dubayah, R., 2013. A meta-analysis of terrestrial aboveground biomass estimation using lidar remote sensing. *Remote Sensing Of Environment*, 128 :289-298.